University of Nottingham

The University of Nottingham
UNITED KINGDOM · CHINA · MALAYSIA

School of Mathematical Sciences

An *in vitro* and *in silico* study of altered airway smooth muscle structure and function in a remodelled asthmatic airway

Sarah Kirsty Brown

A thesis submitted to the University of Nottingham for the degree of
Doctor of Philosophy

March 2023

Abstract

Inflammatory processes in the airway lead to altered extracellular matrix (ECM) and increased airway smooth muscle (ASM), which is responsible for the rapid contraction of asthmatic airways during exacerbations. Increased ASM contributes substantially to the thickening of airways (airway remodelling), and a higher likelihood of experiencing potentially fatal attacks. In culture, ASM cells exhibit changes in shape and contractile ability between a spindle-shaped contractile phenotype and a more rounded proliferative phenotype with synthetic properties capable of depositing ECM. The link between phenotype switching and corresponding changes in structure, function and relative bio-mechanical abilities *in vivo* is unclear, but key in understanding remodelling. The aim of this project is to combine *in silico* and *in vitro* techniques in order to develop models that contribute to the identification of key mechanisms involved in airway remodelling and provide a framework for predicting dynamic mechanical changes in airway tissue.

We first summarise and extend our previously developed ODE model accounting for ASM phenotype and ECM changes triggered by environmental stimuli, based on a newly discovered pathway of remodelling (Chapter 2). Bifurcation analysis of this model identifies a mechanism by which irreversible increases in ECM and ASM mass could occur, given a particular parameter range. We therefore develop two novel experimental serum deprivation protocols using cultured human ASM and microscopy to more accurately quantify the cell phenotype switching rates, as these are the parameters to which the model is most sensitive (Chapter 3). Our experimental results suggest that ASM contractility is increased and that there are structural changes in ASM cells upon switching to a contractile phenotype.

Using this temporal data, we demonstrate the use of a Bayesian inference approach to estimate model parameters and inform future experimental design (Chapter 4).

We then extend this work through the development of a new bio-mechanical vertex-based cell model represented by a network of damped springs and contractile elements, in combination with spatial traction force microscopy data, to investigate changes in mechanical properties of the altered tissue (Chapter 5). We incorporate a physical and functional change in contractile cells and find that the model replicates the elongation, stress and strain properties that we would expect of this cell phenotype. In order to replicate the ASM phenotype switching that we initiate experimentally through serum deprivation, we then further develop this model by adding the random switching of cell phenotypes over the simulation period. This allows us to explore the hypothesis that the mechanical environment of ASM cells and their neighbours drives changes in the structure and function of the tissue, and hence is key in the phenotype switching process (Chapter 6).

The vertex-based bio-mechanical model is also used to test the impact of simulating an asthmatic exacerbation and, much like with the ODE model, results show a mechanism by which long-term changes to ASM cells could occur (Chapter 7). Having tested the impact of a single exacerbation event in isolation, we then mimic the full traction force microscopy experimental protocol using this model and appropriate cell numbers. We find that the model qualitatively agrees well with the dynamics displayed in the experimental results. This computational framework could be exploited to investigate whether cell signalling changes the alignment of internal contractile machinery (increases cell elongation) first, which then drives phenotype change, or vice versa. Understanding more about these processes and their impact on asthma development is key for the ultimate aim of finding new

therapeutic targets. This and other scope for future work is discussed in Chapter 8.

Acknowledgements

I would first like to thank my supervisors Bindi Brook and Reuben O'Dea for their help, guidance and dedicated time throughout this project. I am also grateful for their continued understanding and patience during difficult times and upon deciding to do my PhD part time. Without Bindi's influence for promoting outreach and engagement in maths, I may not have discovered my passion for this area; a realisation that has led to my career in science communication and marketing.

I thank the MRC for funding this project and everyone involved with the organisation of my doctoral training programme. I thank Simon Johnson, Christopher Philp, Debbie Clements, Marlies Fischer and Charlotte Billington from the Division of Respiratory Medicine at the University of Nottingham as well as Ramaswamy Krishnan and Sumati Ram-Mohan from the Department of Emergency Medicine at Harvard University, for their experimental expertise, direction and assistance. I thank Dr Gary Mirrams from the School of Mathematical Sciences at the University of Nottingham for his help with understanding Bayesian statistics.

My thanks extend to my family, especially my parents, for providing me the opportunities to get where I am today, for always supporting me, and for encouraging me to do the best that I can do. I am also thankful for having great friends. Thanks especially to Katie, Abigail and the "synchro girls" for being a constant support. Thank you to my amazing dog Alfie for all the love and happiness you provide. Last but by no means least, I would like to thank James for his love, care and understanding over the past 5 years. I honestly do not think I would have got this far without your kindness, reassurance and silliness.

CONTENTS

1

INTRODUCTION

In this chapter we begin by first describing the biological context of this project including the key hallmarks of asthma (Section 1.1), the main characteristics of airway smooth muscle (ASM) cells (Section 1.2.1), the role of extracellular matrix (ECM) (Section 1.2.2), and the recent discovery of a signalling pathway of airway remodelling involving the activation of the enzyme Matrix Metalloproteinase-1 (MMP-1) (Section 1.3). We follow this by explaining the use of *in vitro* experimentation (Section 1.4) in particular the techniques of Immunocytochemistry (Section 1.4.1) and Traction Force Microscopy (TFM) (Section 1.4.2), that we use in Chapter 3. We also explore the literature for mathematical models of airway dynamics (Section 1.5). We detail examples of both continuum models and cell-based models, the two formulations we use to develop models in this project. Finally, we give an overview of the content and structure of this thesis (Section 1.6).

1.1 ASTHMA, EXACERBATIONS AND AIRWAY REMODELLING

Asthma is a chronic lung disease that affects approximately 5.4 million people in the UK. Around 200,000 of these people are severely affected by this disease, experiencing frequent exacerbations and hospitalisation, with significant burden to the NHS. Furthermore, severe asthma often co-occurs with a further collection of lung conditions: chronic obstructive pulmonary disease (COPD). Although asthma is not always seen as being a serious dis-

ease, in the UK there are an average of three deaths each day as a direct impact of asthma [4, 48]. No prevention strategies or cure have yet been identified for asthma, in part because its pathogenesis is not yet fully understood. Treatment only addresses the symptoms and is based on combining regular corticosteroid inhalation (to reduce inflammation), bronchodilators (to reopen airways during an exacerbation) and environmental controls (to reduce exposure to triggers) [48]. Many researchers are currently working to enhance both the diagnosis and treatment methods, and to ultimately find a cure [4].

Asthma is characterised by inflammation, airway hyper-responsiveness and airway remodelling (described in more detail below), which account for occurrences of wheezing and loss of breath. Asthma patients experience recurrent exacerbations (or asthma attacks) in which their airways are narrowed as an effect of contraction of ASM. Exacerbations occur in response to triggers including aero-allergens such as dust mites and histamine-inducing pollen [49]. While these stimuli are non-pathogenic, in asthmatic airways they result in an aberrant immune response. Exposure to allergens first results in the endocytosis of any allergens by antigen presenting cells (APCs). This then leads to the activation of Th2 (T-helper 2) cells and the production of the allergy antibody IgE [54]. Further exposure to the allergen elicits an acute inflammatory response, increasing the number of inflammatory cells such as eosinophils and basophils. IgE activates mast cells resident in the airway tissue, causing their de-granulation and the release of mediators such as histamines, proteases and cytokines, as well as many growth factors [48, 17]. These inflammatory mediators act as contractile agonists, causing the ASM cells lining the airways to contract, and so eliciting acute constriction of the airways [54].

The lungs of an asthmatic are dysfunctional in that they exhibit a significant increase in the responsiveness of contracting airways. This rapid contrac-

tion of the airways occurs at much lower doses of contractile agonist and is known as hyper-responsiveness [54]. ASM causes this contraction and hence the cells that make up this tissue exhibit both hypersensitivity, such that there is an increase in response to a smaller stimuli, and hyperactivity, where the contractile force produced in reaction to any stimuli increases [39].

The accumulation of mediators released from immune cells during inflammation promotes airway remodelling. Examples of such mediators are transforming growth factor beta (TGF-β) and mast cell tryptase, which both induce remodelling through a range of mechanisms, including ECM synthesis [54]. It is thought that the process of airway remodelling begins in patients early in life and is irreversible. Remodelling progresses through each exacerbation event, leading to the advancement of the disease and can eventually cause severe breathing difficulties [56]. A remodelled airway is characterised by epithelial desquamation (shedding of the airway epithelial cell layer), hyperplasia of goblet cells (increases in the number of cells which secrete mucus) and increases in reticular basement membrane (RBM) thickness, together with increases in the amount of ECM and ASM [49, 56, 79]. The differences between a healthy airway and a remodelled airway of a severe asthmatic patient are shown in Figure 1.1. The overall thickening of the airway wall during remodelling is associated with an increase in hyper-responsiveness. In this project we focus on the increase in ASM mass and the changes in ECM, as well as the mechanisms underlying airway remodelling.

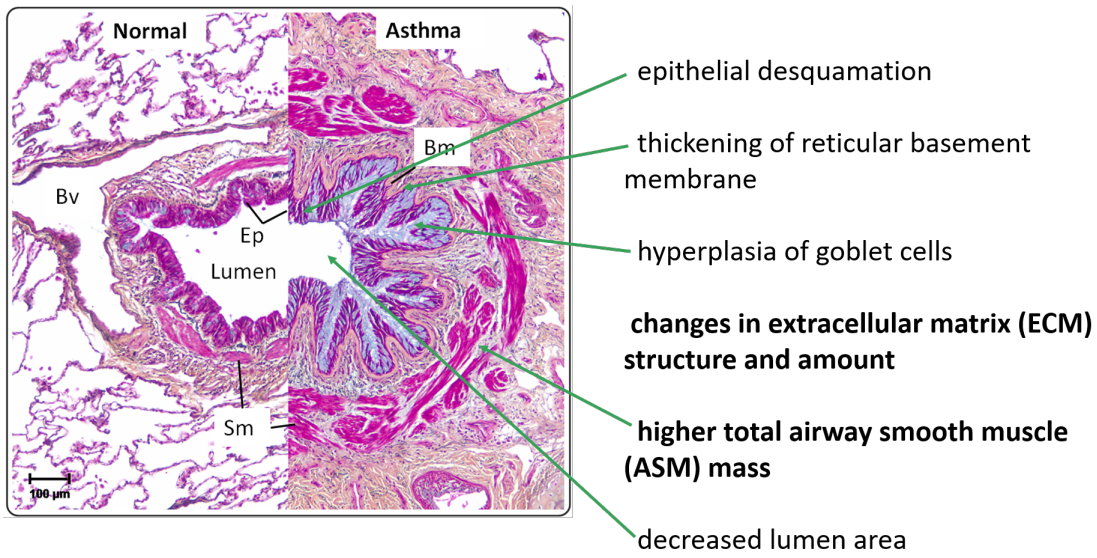

Figure 1.1: Cross-sectional image of a stained healthy airway (left) and a remodelled airway of a severe asthmatic patient (right). This is an open sourced image taken from [79]. The characteristics labelled in bold are focused on the most in this thesis.

1.2 AIRWAY COMPONENTS

1.2.1 *Airway Smooth Muscle*

Smooth muscle cells contract in response to many extracellular messengers, therefore accounting for the overall changes in constriction and relaxation of the airways. ASM is a component of the airway that plays a major role in airway remodelling in asthma (shown in Figure 1.1). As mentioned in Section 1.1, asthmatic ASM recruits inflammatory cells, is hyper-responsive and is affected by airway remodelling, hence is involved in all three of the major characteristics of asthma [39]. With multiple exacerbations over an extended length of time, there is a change in the amount of, and function of, ASM cells. Specifically, there is an increase in ASM mass, which not only contributes to the thickening of the airway wall tissue (and respective

narrowing of the airway lumen) but also increases the rate at which the airways contract, thereby creating a positive feedback loop. ASM cells are hence responsible for and impacted by airway remodelling [39].

ASM cells can be thought of as existing somewhere on a spectrum between two phenotypes, a proliferative or synthetic phenotype that is able to undergo cell division and a contractile phenotype that has a higher contractile ability. *In vivo*, smooth muscle cells have been found to exist normally in a state towards the contractile end of the spectrum, switching to a state towards the proliferative end of the spectrum only during cell division. Furthermore, these phenotypes also differ in their morphology, organisation and protein content [30, 31, 84]. Contractile ASM cells are seen to be elongated and spindle-shaped, with a parallel alignment of actin filaments in the circumferential direction. This organisation is highly regulated by the ECM structure, since ECM components play an important role in force transfer between ASM cells [16, 3]. Contractile markers such as calponin, desmin, sm-alpha-actin and sm-MHC are found to be up to 75% higher in cells of the contractile phenotype compared to those of the proliferative phenotype [30]. When ASM cells are cultured for experimental use, the addition of serum in the growth medium drives them to a proliferative phenotype. Chang *et al.* [16], found that vascular smooth muscle cells, when driven to their proliferative phenotype in culture, lose their parallel actin filament organisation and the fibres become more randomly distributed. This phenotype is hence recognised by its less elongated, broader and flatter morphology, as well as increased proliferation as measured by proliferation markers (such as Ki67 and PCNA) [32]. The difference in the shape and actin alignment of these cell phenotypes can be seen in Figure 1.2. It has been shown that if cultured cells undergo an extended period of serum deprivation (up to 19 days), this allows at least a sub-population of these cells to switch back to having the shortening ability, morphology and protein constituents of an *in vivo* contractile phenotype [30].

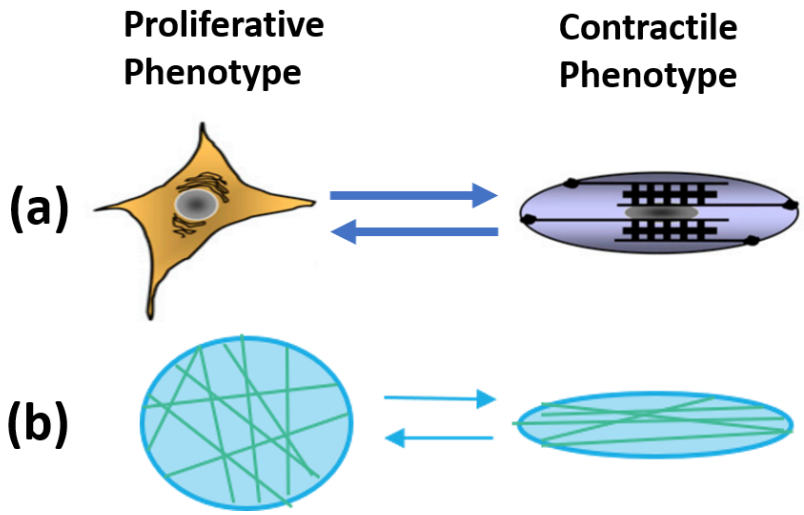

Figure 1.2: Schematics illustrating (a) differences in the cell shape of proliferative ASM cells (left) and contractile ASM cells (right) [31] and (b) differences in the alignment of actin filaments in proliferative ASM cells (left) and contractile ASM cells (right).

1.2.2 *Extracellular Matrix*

Another structure that is highly relevant in the process of airway remodelling is the extracellular matrix (ECM). The ECM forms an elaborate network that provide cells with both structure and ability to signal through the cooperation of adhesion receptors [77]. ECM is laid down by ASM cells and therefore an increase in ASM mass through remodelling, results in a corresponding increase in ECM. The ECM of an asthmatic patient differs from a healthy ECM in its structure and amount [69]. There are significant differences in the quantities of several proteins; fibronectin, lumican, collagen I II and V and tenasin C are found in higher quantities, whereas elastin and collagen IV are found in lower quantities in asthmatic ECM [45]. This altered ECM profile has a crucial impact on ASM cell function, including both higher migration and proliferation of ASM cells [45]. Higher amounts of collagen and fibronectin also lead to enhanced synthetic function [15] and differences in contractile capacity [1]. These differences in ASM cells in

turn increase bronchial hyper-responsiveness and, therefore, the likelihood of an exacerbation [56]. Additionally, Freyer *et al.* [25] discovered that ASM cells are more resistant to apoptosis as a result of a survival signal released to them from interacting ECM and β1-integrins. They found that the proteins that are more abundant in the remodelled ECM are most important in the production of this signal. They therefore conclude that asthmatic ASM growth is partially explained by this strong signal produced by the altered ECM, and that the increase in ASM cells leads to further production of ECM and hence a cycle which eventually results in the remodelling of the airways.

1.3 MMP-1 ASSOCIATED SIGNALLING PATHWAY OF AIRWAY REMODELLING

In this section we describe the findings of Naveed *et al.* [56], that provide new insights on the role of the enzyme Matrix Metalloproteinase-1 (MMP-1) in the remodelling of ECM in an ASM bundle. Naveed *et al.* [56] discovered that MMP-1 (which is secreted by ASM cells) is activated by mast cell tryptase, an enzyme released by inflammatory mast cells. In addition, it was found that there is more MMP-1 in the airways of asthmatic patients compared to healthy controls. Under the inflammatory conditions present during an exacerbation, it was demonstrated that there is an increase in the number of mast cells in the airway, and therefore more mast cell tryptase present for the activation of pro-MMP-1 (the inactivated form of MMP-1). Naveed *et al.* also showed that an exacerbation led to a significant increase in active MMP-1. This active form of MMP-1 changes the structure of the ECM into the altered pro-proliferative form described in Section 1.1. It was confirmed that activated MMP-1 is the factor driving the pro-proliferative form of ECM via the following observations: directly adding activated MMP-1 to ECM led to increased proliferative ability, and silencing MMP-1 no longer led to increased proliferative ability. Activated MMP-1 has also been shown

to enhance ASM proliferation in several other papers [66, 67]. The altered ECM contains a substrate which promotes the proliferative form of ASM, hence resulting in a significant increase in the size of the total ASM cell population. Furthermore, it was shown that there is a strong association between the expression of activated MMP-1 and the reduction of airway calibre [56].

These discoveries can be summarised as follows:

- MMP-1 is more highly expressed in the airways of asthmatic patients than in healthy controls,
- MMP-1 is activated by mast cell tryptase during exacerbations,
- Active MMP-1 remodels ECM to a pro-proliferative form which enhances remodelling.

The evidence for the these discoveries was first obtained through *in vitro* studies and was later confirmed in human airways using asthmatic and control groups [56]. The findings listed above illustrate an important pathway of airway remodelling that results in the changes in ECM and ASM structure and function that we have discussed. This pathway (encapsulated in the diagram in Figure 1.3) is the basis of a mathematical model that we have previously developed (Appendix A), which is summarised and extended in Chapter 2. We choose to explore this pathway because it has not previously been studied and it could teach us more about the process of airway remodelling. Ultimately, preventing interactions between certain components of an ASM bundle, for example mast cells and ASM derived products such as pro-MMP-1, could reduce airway remodelling and therefore asthma severity [56].

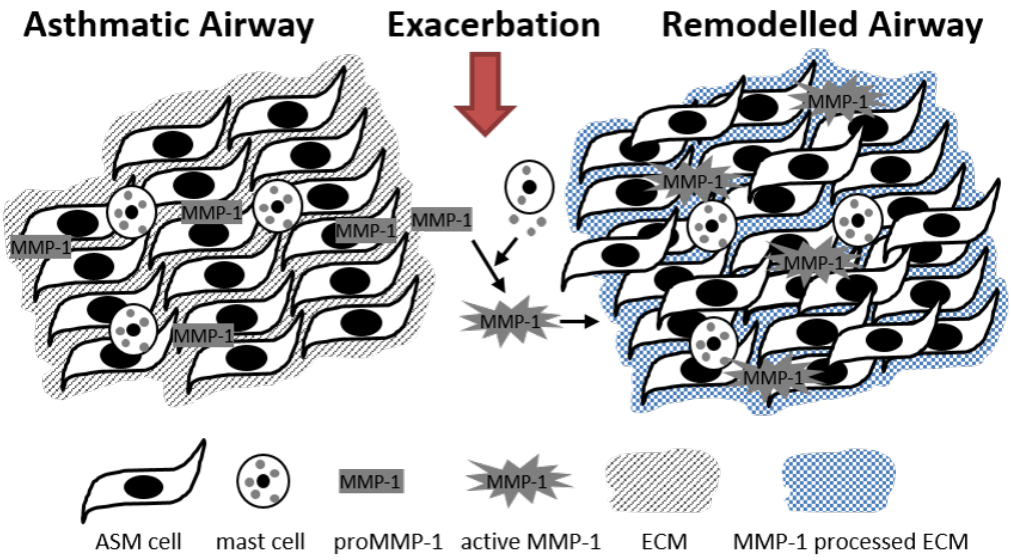

Figure 1.3: Schematic diagram summarising the MMP-1 associated signalling pathway of airway remodelling [56]. The diagram shows the interaction of mast cell mediators (released during an exacerbation) with pro-MMP-1, leading to the activation of MMP-1 and therefore the alteration of the ECM structure. This results in an increase in ASM tissue mass in the remodelled airway. This schematic is edited from [56].

1.4 *in vitro* EXPERIMENTATION

In vitro is defined as taking place outside of a living organism, such as in the process of tissue or cell culture. Cell culture is used widely to simplify the disease system and gain an understanding of interactions between specific components. In this section, we discuss the process of *in vitro* cell culture as well as the advantages and disadvantages of *in vitro* experimentation compared to *in vivo* experiments in asthma. We then go on to describe two examples of experimental methods that we make use of later in this project (Chapter 3).

While *in vivo* ("within the living") experiments are common in analysing the mechanisms involved in asthma, these studies have significant limitations. Animal models that are often used to learn about asthma include mice, rats, cats, dogs and primates, although none of these animals are known to naturally develop this disease. Where therapeutics have been developed based on a new understanding of the immune pathways using animal models, few of these pass clinical trials due to lack of efficacy for the human disease. A mouse, for example, is different to a human in its anatomy, physiology and immunology. Mice are small, quadrupeds, unable to cough and do not have bronchodilatory nerves, all of which make translating experimental findings to fit the human disease extremely difficult. Additionally, we have already seen that mast cells are important in the immune response (Section 1.1), but mice and human mast cells release different mediators when activated [7]. Finally, the ethical implications involved with these *in vivo* experiments are extensive and the replacement, reduction and refinement (3Rs) of animal models are encouraged [70].

Access to human airway tissue through a bronchoscopy has enabled *in vitro* studies of asthmatic mechanisms. The protocol we use in this project for human smooth muscle cell culture is described in detail in Appendix

B.1. Briefly, the cells are grown in sterile conditions in flasks containing Dulbecco's Modified Eagle Medium (DMEM), a liquid which supports the growth and survival of the cells. Fetal Bovine Serum (FBS) is also added to this medium as a source of growth factors. Cells are incubated at $37^{\circ}C$ for optimal growth. When a flask is 70-90% confluent (proportion of surface covered with cells), the cells are passaged. Passaging involves splitting the population of cells into several different flasks such that they have room to keep growing. In isolating these cells and growing them in culture, we are able to reduce the complexity of the system and test interactions between specific components. A comparison of the responses between primary human asthmatic and non-asthmatic cells in culture allows the exploration of pathways which could contribute to disease progression. *In vitro* experimentation is also fast and relatively inexpensive. Disadvantages of this method, however, include differences in gene expressions compared to *in vivo* cells and a lack of interactions between different cell types. Primary cells can also lose certain characteristics or become senescent at high passage numbers [7].

1.4.1 *Immunocytochemistry*

Immunocytochemistry is a technique that is widely used in the literature in order to identify protein expression and localisation within cultured cells. This process involves the use of immunoglobulins, more commonly know as antibodies. Antibodies are Y shaped proteins made up of a variable region called the Fab portion and a constant region called the Fc portion (Figure 1.4). Cells are fixed such that they are preserved in their current state without any further biochemical reactions occurring. This means that antibodies are able to access intracellular structures in their current state in order to detect antigens. The fixed cells are then initially exposed to a primary antibody. The Fab portion of this primary antibody will bind to the protein or antigen of interest within the cell. Once bound, the complex is detected through the use of a secondary antibody which binds to the Fc

portion and is labelled with a fluorescent marker [13]. The cells can then be imaged using a fluorescent microscope.

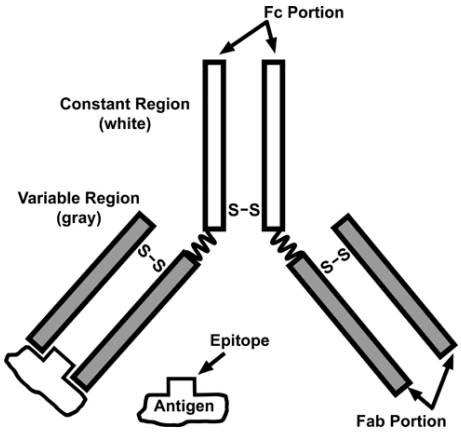

Figure 1.4: Immunoglobulin G (IgG) antibody, with the Fab and Fc portions labelled. Taken from [13].

1.4.2 *Traction Force Microscopy*

ASM cells exert tractions on their surroundings when they contract. While these forces are generally not directly accessible in experimentation, traction force microscopy (TFM) is a technique that measures these tractions through the displacement of fluorescent beads that are embedded at the surface of an underlying gel substrate to which the cells are adhered. This gel substrate acts as a gauge for the amount of strain, since the forces that the cells exert are able to deform the gel in an amount proportional to the applied force, and this is realised through the movement of fluorescent markers (Figure 1.5). The gel also has known material properties and can be approximated as being a semi-infinite solid [14, 71].

The displacements are measured through the comparison of images taken of the plates (using confocal microscopy) before and after the addition of a contractile agonist, compared to a reference image in which the cells have

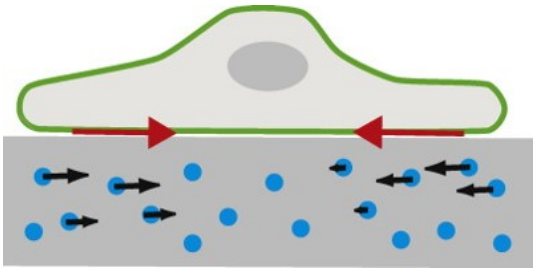

Figure 1.5: Schematic representation of TFM theory. This shows gel deformation and therefore bead displacement due to the contraction of an adherent cell. Taken from [71].

been detached. In following the displacement of individual beads between these images, a substrate displacement field can be produced with spatial resolution based on the density of fluorescent markers [61]. The tractions are calculated from these displacement field data using Fourier transform traction cytometry (FTTC), a method described by Butler *et al.* in [14] and summarised as follows. The Green's function, with 2×2 matrix tensor $K = K(\|\mathbf{r} - \mathbf{r'}\|)$ at a point $\mathbf{r}$ due to a force exerted at point $\mathbf{r'}$, is used to map tractions to displacements. Displacements $\mathbf{u}(\mathbf{r})$ are given by $\mathbf{u}(r) = K \otimes \mathbf{T}$, where $\otimes$ denotes integration over $\mathbf{r'}$ and $\mathbf{T}$ is the traction vector at $\mathbf{r'}$. Inverting this equation (so that tractions can be obtained from displacements) is difficult since K is not diagonal in real space and tractions at a single point can cause displacements at several different points. K is diagonal in Fourier space, however, and hence the FTTC method is used. The Faltung theorem states that the Fourier transform of a convolution (the integral defining the area of overlap between a function and the spatial reverse of another function) is the product of the Fourier transforms of the respective functions convolved. This theorem is used to find the forward problem $\tilde{\mathbf{u}}(\mathbf{k}) = \tilde{K}(\mathbf{k})\tilde{\mathbf{T}}(\mathbf{k})$, where $\mathbf{k}$ is a wave vector and Fourier transforms are denoted by a tilde bar.

Here, as required, $\tilde{K}$ is diagonal and so the solution is readily calculated as follows:

$$\mathbf{T} = FT_2^{-1}(\tilde{K}^{-1}\tilde{\mathbf{u}}) \tag{1.1}$$

where FT_2^{-1} is the 2D inverse Fourier transform [14]. In order to use this equation, an explicit formula for $K(\mathbf{r})$ is found in Fourier space (see [14] for further details). Furthermore, the total strain energy (U) exerted by the cells to cause the displacement of beads seen is given as

$$U = \frac{1}{2}\int \mathbf{T}(\mathbf{r}) \cdot \mathbf{u}(\mathbf{r}) dxdy, \tag{1.2}$$

for a point $\mathbf{r}$ in the 2D coordinate system (x, y). The above process for finding the displacement field and corresponding traction map given fluorescent images is undertaken computationally in MATLAB. The displacements are found using a cross-correlation function followed by calculation of corresponding tractions using Equation (1.1) as described above. An example of a phase-contrast image of a single cell and the corresponding fluorescent bead image, displacement field and traction map are shown in Figure 1.6 [14].

1.5 EXISTING AIRWAY MATHEMATICAL MODELS

As discussed in Section 1.4, there are many limitations to both *in vivo* and *in vitro* experimentation in asthma research. These issues highlight the uncertainty in the value of these methods of experimentation alone, and hence the need for more combinations with *in silico* solutions that are risk free, cheaper and faster (given a fully validated model) [49]. Such models are also useful for determining mechanisms and predicting future outcomes. Here, we discuss some previous mathematical models of the airways, focusing in particular on a model by Chernyavsky *et al.* [17] and its extension by Hill *et al.* [33], since these models take into account the inflammation

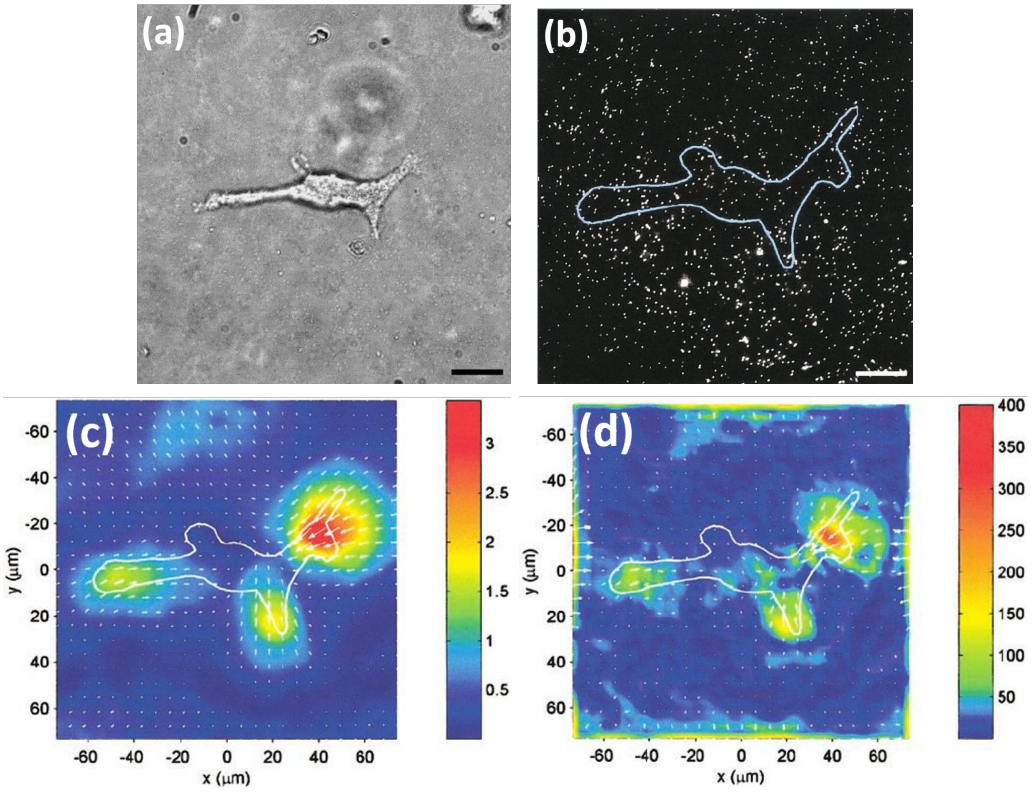

Figure 1.6: Phase-contrast image (a), fluorescent bead image (b), bead displacement field (c) and cell traction field (d) of a single human ASM cell using TFM. The magnitude and directions of displacements and tractions are represented by arrows in (c) and (d) respectively. Images taken from [14].

involved in an asthmatic exacerbation and its effect on the accumulation of ASM mass.

There have been relatively few attempts to develop mathematical models for asthmatic airway remodelling. Until fairly recently, the majority of airway models have focussed on expiratory airflow interacting with structural properties, for example as in [47]. The Hai-Murphy cross bridge model [29], was the first model of smooth muscle contraction to include the "latch state" (described below). Muscle contraction is fuelled by actin-activated myosin adenosinetriphosphatase (ATPase) activity. This activity occurs as an effect of phosphorlylation of the 20-kDa myosin light chain and results in cross-bridge cycling between actin and myosin filaments, generating force. The maintenance of a steady state, with reduced levels of this phosphorylation (and therefore cross-bridge cycling); is known as the "latch state". The model developed by Hai *et al.* [29], is made up of four differential equations that describe the kinetics of this contractile force development in smooth muscle. This model is the basis of many other cross-bridge models in the study of contracting airways.

In the past 20 years, there has been a rise in the number of models to predict functional changes in the airways as an impact of ASM contraction. In 2008, Wang *et al.* [81] published a model based on the Hai-Murphy cross bridge model, which explores the effect of changes in calcium concentrations on the contraction of ASM cells and airway hyper-responsiveness. These molecular level dynamics were later incorporated in a multiscale model to examine the impact of hyper-responsiveness on the lung as a whole [63]. Brook *et al.* [11] also present a model that focuses on the mechanics of airways through development of an elastic axisymmetric model that considers the amount of connective tissue relative to ASM and the resultant contractile forces produced. Results from this model agree well with data from experimentation of agonist-induced contraction of lung slices. The model allows

for predictions of the contractile force distributions through varying layers of the airway wall. Furthermore, this model shows the increase in ASM mass through remodelling as well as the resulting increase in the heterogeneity of local stress patterns. This is the first model which incorporates the changes in the airway response as an effect of cellular events and structural remodelling by considering associations between local stress and the proliferation of ASM cells [11]. While we go on to discuss some specific models in more detail, we are aware that there are many asthma models not discussed in this thesis and we recommend that the interested reader take a look at the review by Irons *et al.* [37].

1.5.1 *Continuum Models*

We now discuss an ODE model developed by Chernyavsky *et al.* [17] and a mechanical continuation of this model by Hill *et al.* [33] using partial differential equations (PDEs). Some of the modelling ideas presented in these studies were previously used to develop our own ODE model (Appendix A), which we summarise and extend in Chapter 2.

In 2014, Chernyavsky *et al.* [17] developed an ODE model which examines specifically the impact of inflammation on the accumulation of ASM mass. This model uses the assumption that ASM cells can exist in two different phenotypes, proliferative or contractile (non-proliferative), $p(t)$ and $c(t)$ respectively (as seen in Section 1.2.1). The model states that contractile ASM cells can switch to the proliferative phenotype with an associated rate λ_{cp}, and visa versa with the rate λ_{pc} (see Figure 1.7). Only the p population proliferates and it does so logistically, with a rate λ_p and carrying capacity V. It is assumed that the switching rate λ_{pc} is much faster than the proliferation rate λ_p, hence the cells only exist in a state p for a short length of time. Cellular apoptosis is only associated with the c population. This occurs with

a rate λ_a which is assumed to be significantly slower than the proliferation rate. As illustrated in Figure 1.7, another variable $\mu(t)$ accounts for the inflammation involved in an exacerbation and this variable modifies the value of the switching rate from phenotype c to p: λ_{cp}. The system of ODEs for this model is given below [17]:

$$\frac{dp}{dt} = \lambda_p p\left(1 - \frac{p+c}{V}\right) - \lambda_{pc}p + \lambda_{cp}c, \tag{1.3}$$

$$\frac{dc}{dt} = \lambda_{pc}p - (\lambda_{cp} + \lambda_a)c, \tag{1.4}$$

$$\frac{d\mu}{dt} = -\lambda_d \mu + af(t; w), \tag{1.5}$$

where

$$f(t; w) = \sum_i \delta(t - t_i), \quad w = \frac{1}{E[t_{i+1} - t_i]}. \tag{1.6}$$

In Equation (1.5), λ_d is the resolution rate of the inflammation and a represents the magnitude of each peak in inflammation given by the function $f(t; w)$, an environmental stimulus. An exacerbation occurs at a time t_i and w gives the rate of recurrence for these events [17].

This model predicts that the increase in the number of ASM cells is reliant on the normalised parameters representing inflammation magnitude, frequency and resolution rate. The latter of these is shown to be the parameter of the highest importance in airway remodelling. This is due to the fact that slow resolution can lead to a build-up of inflammation from previous exacerbation events, thereby producing a larger impact on total ASM growth. Furthermore, results of this model show that the primary goal of research efforts should be to increase this resolution speed in asthmatic patients before decreasing frequency and magnitude of exacerbation events [17].

Hill *et al.* [33], combine the above ODE model with a finite-thickness continuum based mechanical model which accounts for cell level contractile

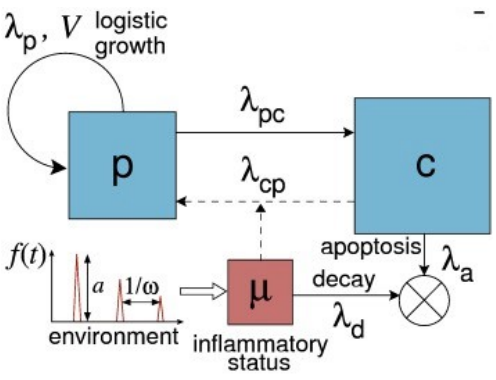

Figure 1.7: Schematic representation of the ASM growth model developed by Chernyavsky *et al.* taken from [17], showing the interactions between the three variables c, p and μ and the relevance of the environmental stimulus $f(t)$.

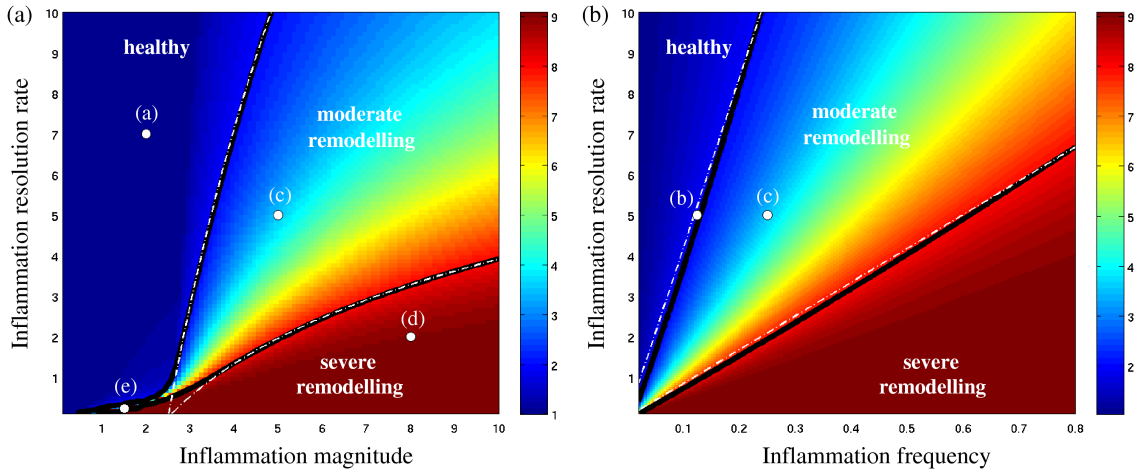

Figure 1.8: Assessing ASM growth as a function of inflammation resolution rate and inflammation magnitude (a) or frequency (b) using the model developed by Chernyavsky *et al.* [17]. This is used to predict which parameters have the highest impact on the increase in ASM mass during airway remodelling. Image taken from [17].

force [35] and further extends this combination to include two-way feedback between the structural change in the remodelled airway and the consequential mechanochemical impact. In this, the airway is represented by a two-layered cylinder (an inner layer of the sub-epithelial basement membrane and an outer layer of ASM). Initially the system is assumed to lie in its stress-free resting configuration (κ_0) with inner, interface and outer radii given by R_1, R_{int} and R_2 respectively, and the location of a particle denoted by X. The growth of the airway wall leads to a different configuration (κ_g) where the position of the particle previously at X is now $\xi(X,t)$. This grown configuration results in an airway wall deformation into a stressed state (κ) with inner, interface and outer radii given by r_1, r_{int} and r_2 respectively and the particle previously positioned at ξ is now given by $X(\xi)$. The mapping between the grown and stressed position is given by the elastic deformation gradient tensor F as follows:

$$F = diag\left[\frac{\partial r}{\partial \xi}, \frac{r}{\xi}, \lambda_z\right]. \tag{1.7}$$

The mechanical tissue response is then modelled through the additive decoupling of the Cauchy stress tensors. As in the previous model [17], variables in this model include proliferative and contractile ASM cells, however here ECM is another variable and the mechanical responses of each of these variables are de-coupled. The system is challenged by events $f(t)$, resulting in the increase in both inflammatory cells and contractile agonists. Hence the model has a variable μ, which describes the inflammatory status of the airway given by Equation (1.5) above, where $f(t)$ is given by a series of time dependent Gaussian peaks. The contractile agonist (k) induces contraction of ASM and therefore stress in the airway wall; k evolves under the following equation:

$$\frac{dk}{dt} = a_k f(t) - c_{dk}k + a_{k\mu} + a_c \tau H(\tau), \tag{1.8}$$

where a_k is the magnitude of agonist added, c_{dk} is the agonist decay rate, a_{ku} is the rate of agonist activation by inflammatory cells and a_c is the rate

at which agonist is released as a result of the local fibre tensile stress τ (with Heaviside step function H). τ additionally drives the switch in ASM phenotype previously seen (Figure 1.7) along with μ . ECM turnover evolves through synthesis by proliferative ASM cells, modification by mediators released by inflammatory cells and decay. A schematic of the biochemical mechanisms in this system is shown in Figure 1.9. Considering both the change in local density of each variable over time (as function of ξ) and the assumption that each variable is thought of as being intrinsically incompressible, gives the mass balance equation for the growth of each layer of the airway [33].

Results from this model show that stresses in airway wall tissue, as an impact of challenges of inflammation and contractile agonist, create a mechanotransductive feedback loop. ASM cells contract in the presence of an agonist, leading to the generation of mechanical stress which further drives the release of contraction inducing mediators. Hill *et al.* [33] therefore found that an increase in hyper-responsiveness to an agonist gives more remodelling, bronchoconstriction and a chronic presence of contractile agonist.

1.5.2 *Cell-based Models*

The ability to quantify mechanical forces exerted by cells (such as described in Section 1.4.2) has led to the development of many numerical approaches which incorporate interactions between the cells that make up a tissue. While many models of tissue development are continuum based, these models assume homogeneity across the tissue and rely on averages over areas typically larger than a cell, so can not easily capture cell level effects. Moreover, a system must contain a large number of cells to justify the use of this method. Discrete, cell-based approaches are therefore often more realistic when modelling mechanics such as cell-cell adhesion [24].

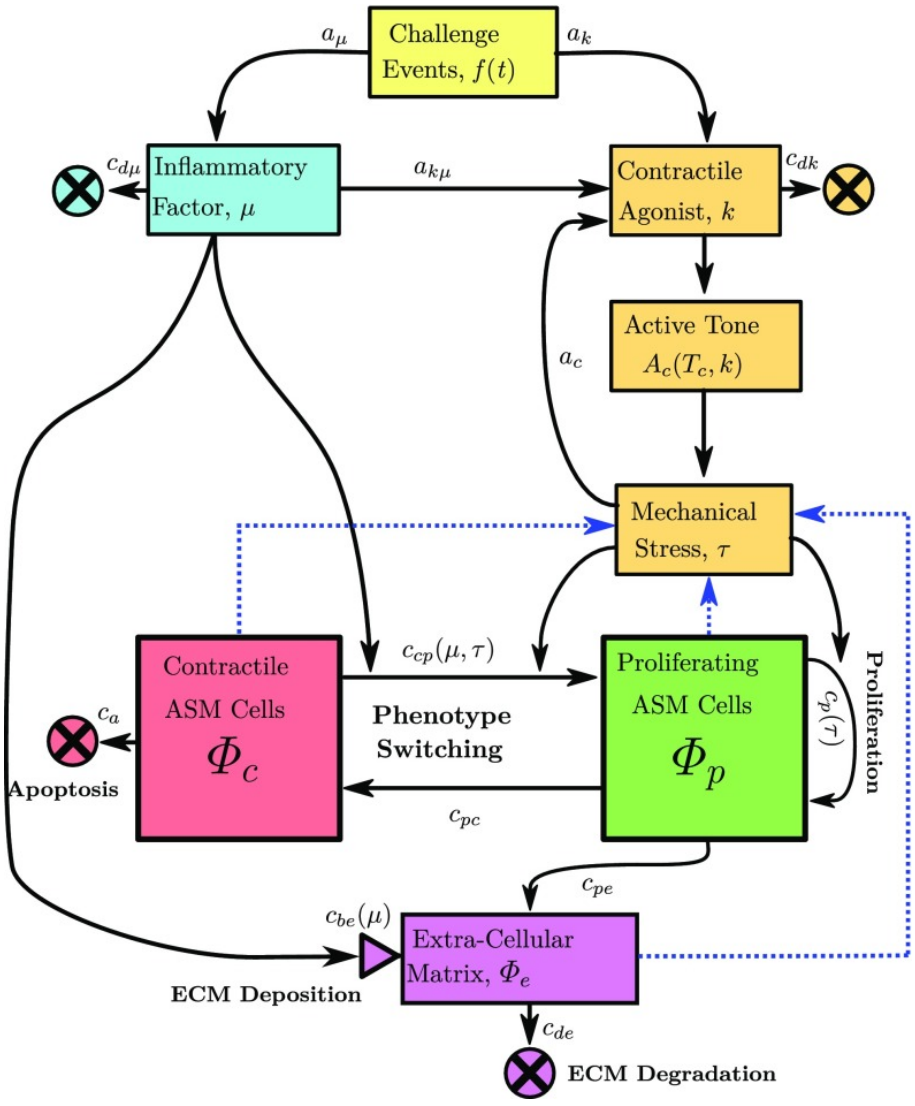

Figure 1.9: Schematic representation of the biochemical mechanisms in the model developed by Hill *et al.*, taken from [33].

Initially, lattice based models were developed, in which cells are represented by points on a grid such as in [64]. In these, movement is restricted to grid points and incorporating cell division is difficult without breaking connections between cells. Lattice-free models allow the continuous movement of cells within the domain and so can more easily incorporate proliferation of cells. Off-lattice models are used extensively in order to model processes such as wound healing, tissue growth, collective cell motility and cell-substrate interactions [74]. Most of the literature focuses on using these methods to describe epithelial cells, which are closely packed in a monolayer. These models are often formulated in one of two ways; cell-centred models or vertex-based models [24, 53].

For vertex-based models and some cell-centred models, cells are modelled as polygons of varying shape created through the formulation of a Voronoi tessellation and the corresponding Delaunay triangulation. A set a points are first chosen to represent the cell centres, these are called generating points. A Voronoi tessellation [78] (shown by the black lines in Figure 1.10) creates the polygons by drawing lines to divide the plane into regions so that every coordinate in a certain region is closest to the same generating point, located somewhere inside of that region. These lines, which each bisect two such generating points, become the boundaries or edges of each cell within the population. The locations where these lines meet are equidistant from three or more points. This defines a cell vertex, where the degree of the vertex is given by the number of edges that come together [19]. It has been shown that Voronoi domains describe cultured epithelial cells packed into a sheet or monolayer reasonably well, through comparisons with photographs of cells in plates [36].

The Delaunay triangulation (red lines in Figure 1.10) is then used to give the connections between cell-centres of neighbouring cells. This is found through the dual of the Voronoi tessellation. The dual is a formulation

where the cell centres become vertices that are connected if the cells of the Voronoi tessellation share an edge. The Delaunay triangulation is unique and each vertex of the corresponding Voronoi tessellation is distinct and so will all have a degree of three (as opposed to the degenerate case, where vertices coincide leading to vertices with a higher degree).

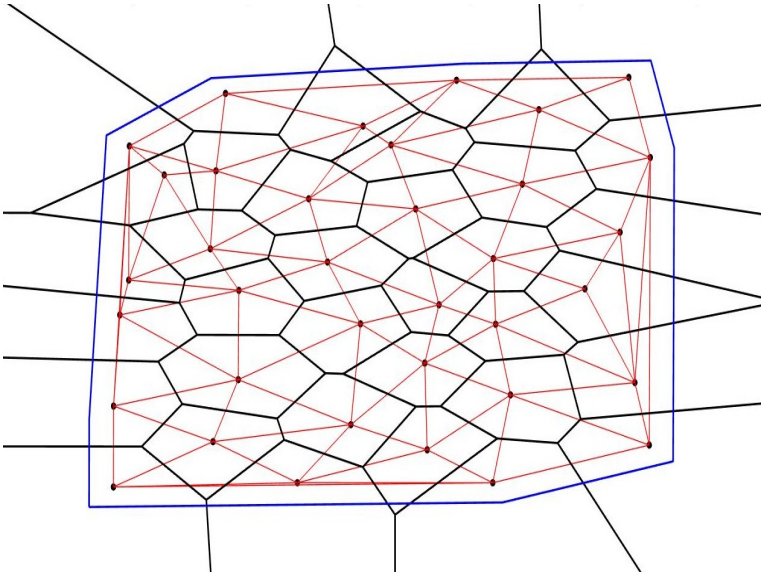

Figure 1.10: Cellular network created by generator points (black circles), a Voronoi tessellation of these points (black lines), the corresponding Delaunay triangulation (red lines) and an enlarged convex hull (blue border).

A Voronoi tessellation will always contain some infinitely large faces, since points that are on the boundary will never be enclosed by a Voronoi edge. This issue is typically solved by closing the cells using the convex hull of all generator points. The convex hull is the smallest set which contains all these points and is also convex. If this set is enlarged so that our definitions of cell centres and cell edges still apply, this can be used to define a boundary for our simulated monolayer (blue line in Figure 1.10).

Cell-centred Model

An early model of the cell-centred type was developed by Meineke *et al.* [50] and describes epithelial cells in the mouse intestinal crypt. The cells in this model are represented by convex polygons formed using a Voronoi tessellation and the corresponding Delaunay triangulation as described above. In this cell-centred model, the triangulation generates a network connecting neighbouring cell centres, the edges of which are damped linear springs that each have a constant resting length r_0. Each cell centre moves as a result of local elastic forces. The total force acting on a cell is therefore the sum of all the forces from the springs connected to neighbouring cells. A force balance is then calculated using Newton's Second law leading to the displacement of cell centres.

For a cell α, the position of its centre (one of the points used to generate the network of polygons) is denoted

$$\mathbf{r}_\alpha(t) = (x_\alpha(t), y_\alpha(t)) \tag{1.9}$$

at a given time t, and thus the force exerted on cell α by a neighbouring cell β is

$$\mathbf{f}_{\alpha\beta} = k\left(1 - \frac{\mathbf{r}_0}{|\,\mathbf{r}_{\alpha\beta}\,|}\right)\mathbf{r}_{\alpha\beta}, \tag{1.10}$$

where k is the spring constant and $\mathbf{r}_{\alpha\beta} = \mathbf{r}_\beta - \mathbf{r}_\alpha$. This means that if we consider a small time interval Δt, the displacement of the cell centre is given by

$$\mathbf{r}_\alpha(t + \Delta t) = \mathbf{r}_\alpha(t) + \frac{\mathbf{F}_\alpha(t)\Delta t}{\gamma}, \tag{1.11}$$

where γ is a damping constant and

$$\mathbf{F}_\alpha = \sum_{\beta \in N_i} \mathbf{f}_{\alpha\beta} \tag{1.12}$$

for all neighbours, N_α, of each cell α.

Following each displacement in positions of cell centres, Meineke *et al.* re-triangulate to dynamically evolve the system such that the shape of each cell is always purely dependent on the distance between its centre and that of its neighbours. This approach easily allows for variation in the cell number through cell proliferation or death [50]. There are some issues with this approach, however, including that following re-meshing, the cell edges are redefined and so their neighbours and polygonal class can change significantly between single time steps. This is not very biologically realistic and does not consider the high importance of cell-cell junctional mechanics.

Vertex-based Models

In contrast to this approach, vertex-based models are able to represent cell-cell junctional mechanics, which are imperative in defining the properties of cell monolayers [53]. The mesh of polygons representing cells in a vertex model is formed in the same way as in the cell-centred model (Figure 1.10); however, the tessellation (not the triangulation), now represents the spring network. The network springs therefore join the vertices of each cell and hence represent the cell edges. The majority of vertex-based formulations in the literature use the assumption that cells are displaced as an effect of mechanical forces and that this movement is over-damped. The position of a vertex $\mathbf{r}_i$ is hence given by

$$\eta_i \frac{d\mathbf{r}_i}{dt} = \mathbf{F}_i, \tag{1.13}$$

for vertex i, with drag coefficient η_i [24]. There are several methods that can be used to define $\mathbf{F}_i$ but for the purpose of this project we review the well established model used by Staddon *et al.* [74]. Here, cells are assumed to have a mechanical energy E as follows:

$$E = \frac{1}{2}\sum_{\alpha} K(A_\alpha - A_0)^2 + \frac{1}{2}\sum_{\alpha} T(P_\alpha - P_0)^2, \tag{1.14}$$

where K is the cell stiffness (assumed the same for all cells), A_α is the area of a given cell α and A_0 is the target area. The first term in E therefore represents the incompressibility of cells. The second term characterises the contractility of the cell cortex, where T is the constant of elasticity, P_α is the perimeter of a given cell and P_0 is the target perimeter obtained given all springs at resting length [74]. $\mathbf{F}_i$ can be calculated directly from E using the fact that $\mathbf{F}_i = -\nabla_i E$, where $\nabla_i E = \nabla E|_{\mathbf{r}=\mathbf{r}_i}$ [24].

Vertex-based Model Evolution

The network of springs is constantly aiming for the arrangement where the springs are at their resting length and hence in the lowest energy state. To implement this energy minimisation in our model we first explored using the Matlab function `fminsearch`, which starts at a given estimate of the solution x_0 and looks for the local minimum x using the Nelder-Mead simplex algorithm [57].

Figures 1.11 and 1.12 show the issues that arise when using this approach. Figure 1.11 shows a simple test case using a single triangle with zero, one or two fixed vertices, while Figure 1.12 shows an example of a minimisation for four connected polygons with none of the vertices fixed. We can see in both cases that there can be a significant displacement of the whole shape using this method, particularly in the examples where no vertices are fixed. While in cellular monolayers, we would not consider vertices to be fixed, we would consider that cells are all connected to one another thus providing additional constraints on their movements. We also notice that, so long as the energy is minimised based on the given resting quantities, there are no constraints on the resultant shape that is produced using this method and so this could lead to cells in our model becoming overlapped or concave.

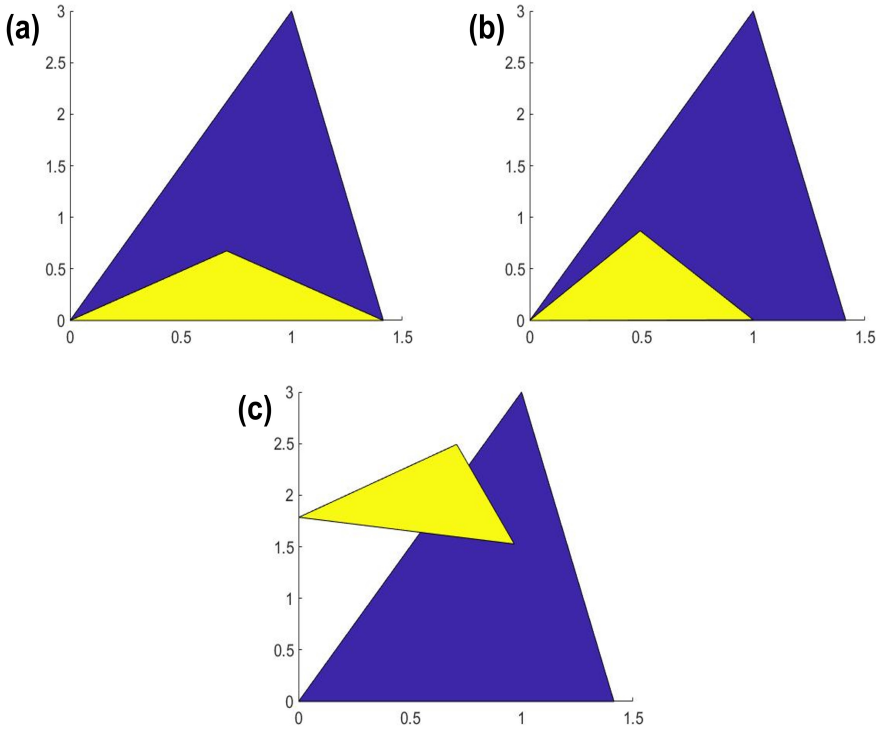

Figure 1.11: Energy minimisation from the blue triangle to the yellow triangle given $\tilde{L}_0 = 3$ and $\tilde{A}_0 = 0.433$, using `fminsearch` in Matlab. The triangle in (a) has two fixed vertices, in (b) has one fixed vertex and in (c) has no fixed vertices.

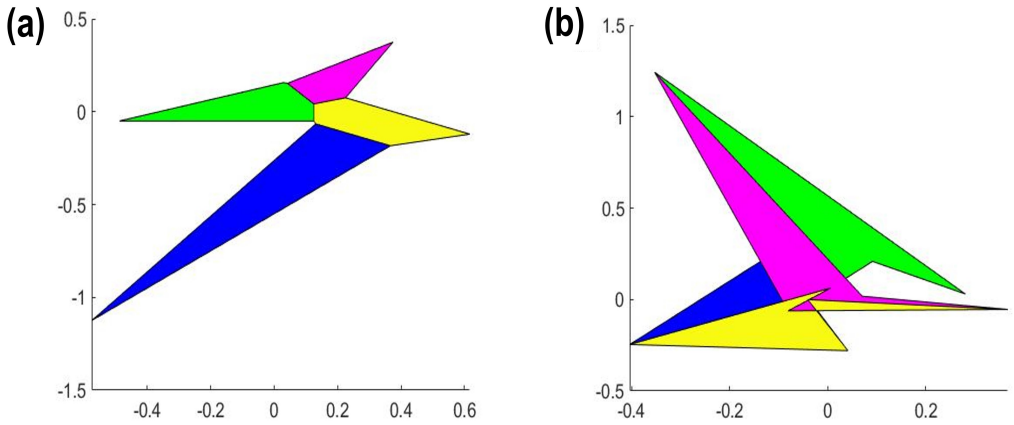

Figure 1.12: Energy minimisation from (a) to (b) using `fminsearch` in Matlab. Self intersecting and overlapping cells result.

We instead choose to implement a more gradual evolution in cell vertex positions over time. This can be calculated by numerically solving Equation (1.13) using a forward Euler discretization to give the following [24]:

$$\mathbf{r}_i(t+\delta t) = \mathbf{r}_i(t) + \frac{\delta t}{\eta_i}\mathbf{F}_i(t), \tag{1.15}$$

which we go on to derive for our specific model in Chapter 5.

In recent work by Nestor-Bergmann *et al.* [58], a vertex-based approach is used to investigate the association between an epithelial cell's morphology and the mechanical properties of the tissue. This is done through the exploration of the alignment of both stress and shape tensors. By fitting parameters of the model to experimental data using Xenopus embroyonic tissue, the model shows how the mechanics of the system can create mesoscopic patterns of cell shape [58].

Vertex-based Model Operations

Vertex-based models are also able to represent cellular events such as proliferation and apoptosis. Below we note some operations commonly used to to put mechanisms like this into place and to maintain a monolayer of non-intersecting cells, each with the realistic polygonal shape.

It is assumed that when cell division occurs, the cell is split into two equally sized areas. The dividing edge passes directly through the centroid of the cell and ends at the cell perimeter on either side, where new vertices are placed (Figure 1.13) [10, 24]. A T1 swap (Figure 1.14(a–b)) is an operation which rearranges edges when two vertices are too close to each other (given a minimum threshold distance). This entails moving these vertices to be a length of $d_{sep} = k_{sep} d_{min}$ apart, where k_{sep} is a separation ratio and d_{min} and d_{sep} are the distances between the vertices before and after being separated respectively. T1 swaps ensure that vertices are always contained in exactly

three elements (cells) when not on the boundary and that all cells keep their polygonal shape. T2 swaps are then put in place to remove cells that have become triangular (through the application of several T1 swaps) and are smaller than a certain area threshold (Figure 1.14(c–d)). This operation accounts for cell apoptosis [24, 55].

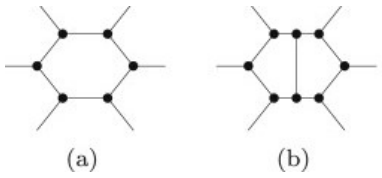

Figure 1.13: Operation for cell division in a vertex-based model. The single cell shown in (a) divides to form two cells with an equal area in (b). Taken from [24].

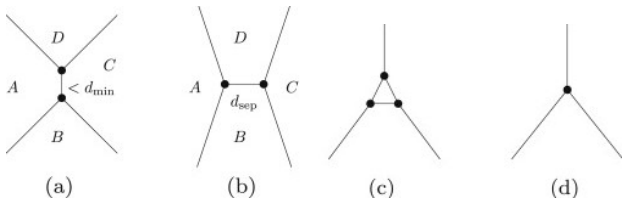

Figure 1.14: T1 and T2 swap operations in a vertex-based model. The edge separating cells A and C is $< d_{min}$ (a) therefore a new edge is created between cells B and D with length d_{sep} (b). A small triangular element (c) is removed so that every vertex is contained in three elements (d). Taken from [24].

Hybrid Cell-based Model

A hybrid model has additionally been developed by Mosaffa *et al.* [53] to include cell–cell interactions between both cell centres and cell junctions. A difference in this model compared to other cell-based models is that a Barycentric tessellation is used, where vertices are formed at the barycentre

of each triangle in the Delaunay triangulation. This is to ensure that vertices stay within the triangles, and so cells do not overlap. An energy minimisation is once again used. However, here it includes the total energy of both the nodal (cell centres) and vertex networks. This hybrid method allows the separate regulation of properties of cell interiors and cell boundaries [53].

1.6 THESIS OVERVIEW AND STRUCTURE

Our goal is to use *in vitro* and *in silico* techniques in complement to improve our understanding of structural and functional changes in the ASM of remodelled asthmatic airways. We have previously developed an ODE model accounting for ASM phenotype and ECM changes triggered by environmental stimuli (Appendix A). In Chapter 2, we start with a summary of important insights obtained from that model, including the illustration of a mechanism of airway remodelling identified through a post-stimulation irreversible increase in ASM mass. We then add some further biological accuracy to the model and find that the model is most sensitive to changes in the parameters associated with ASM phenotype switching rates.

In Chapter 3, we aim to more accurately quantify phenotype switching rates through the design and undertaking of two novel experimental protocols using Human ASM cells. In both experiments, the phenotype switch (from proliferative to contractile) is initiated though the long-term removal of serum. Experiment 1 uses immunocytochemistry to track changes in fluorescence of stains for both proliferative and contractile markers at different time points throughout this period. Experiment 2 uses TFM to track the change in the contractile force exerted by cells pre and post stimulation at different time points throughout this period. The data collected from these experiments allows us to infer the proportion of each phenotype out of the whole cell population at each time point. Using this along with a reduced version of the ODE model (to match the experimental protocol),

we undertake a least squares fit for parameter values associated with phenotype switching. There is a lack of accuracy in this fit, however, as a result of a small number of time points. In Chapter 4 therefore, we use a Bayesian statistical approach to find the optimal number of experimental time points and repeats needed so that future results will provide sufficient data to give an accurate and robust model fit.

In Chapters 5–7, we develop and test a vertex-based bio-mechanical model of an ASM cell monolayer with the aim of both replicating TFM spatial-temporal results and exploring how phenotype-associated changes in cell shape and mechanics combine to influence cell population dynamics. Chapter 5 introduces the vertex-based modelling approach and time dependent network evolution that we implement. Cell phenotypes are incorporated into the model through assigning cells with differences in their shape and contractile machinery. In Chapter 6, we extend the model to account for random phenotype switching over the simulation period (to match the period of serum deprivation within experiments). This allows us to explore the hypothesis that ASM cell shape change is driven by the mechanical environment and is key in the phenotype switching process. In Chapter 7, we use our model to investigate the population dynamics following a contractile stimulus by considering three test cases involving different conditions. The test case in Section 7.4 mimics our TFM experimental protocol (described in Section 3.2) so that we can qualitatively compare results.

We summarise our main findings and conclusions in Chapter 8, and discuss the scope for future work.

2

ODE MODEL OF MMP-1 ASSOCIATED REMODELLING

As discussed in Section 1.5, mathematical models enable us to explore pathways, determine mechanisms and make future predictions about a system in question. When compared to experimental approaches, they have the advantage of being risk free, cheap and fast (given a fully validated model).

In this chapter, we first summarise our previously developed (Appendix A) ODE model of a specific pathway of airway remodelling involving the enzyme Matrix Metalloproteinase-1 (MMP-1), including the most significant results from this previous study (Section 2.1). In Section 2.2, we then extend the model to add further biological realism and to learn more about the mechanisms involved in this pathway of airway remodelling. Insights from the model discussed in this chapter provide the motivation for the focus of the rest of this thesis, with the ultimate goal to find ways to reduce remodelling and therefore asthma severity.

2.1 SUMMARY OF A PREVIOUSLY DEVELOPED ODE MODEL

We previously developed an ODE model based on the findings from Naveed *et al.* [56] of a pathway of airway remodelling involving MMP-1 (Appendix A). The main results from this paper, described in more detail in Section 1.3, include:

1. Asthmatic patients produce more MMP-1 than healthy controls,
2. MMP-1 (produced by ASM cells) is activated by mast cell tryptase during an exacerbation,
3. Active MMP-1 alters ECM (including the protein structure and quantity) leading to higher ASM proliferation and therefore enhanced airway remodelling.

This information is summarised in the diagram in Figure 1.3 and, along with modelling ideas from Chernyavsky *et al.*[17] (discussed in Section 1.5.1), was the basis of our previous model formulation. As described fully in Appendix A, the mathematical model was therefore formulated based on the following four steps, with the letter representing each of our model variables given in brackets.

1. The increase in mast cell tryptase (Y) during the inflammation involved in an exacerbation event,
2. The activation of pro MMP-1 (M) by mast cell tryptase,
3. The effect of active MMP-1 (Q) on altering the ECM (E),
4. The impact that the altered ECM (A) has on the switching rate of ASM cells from a contractile (C) to a proliferative (P) phenotype, the rate of ASM proliferation and the survival of ASM cells.

A schematic diagram of this pathway is shown in Figure 2.1 and the respective parameter descriptions are given in Figure 2.2.

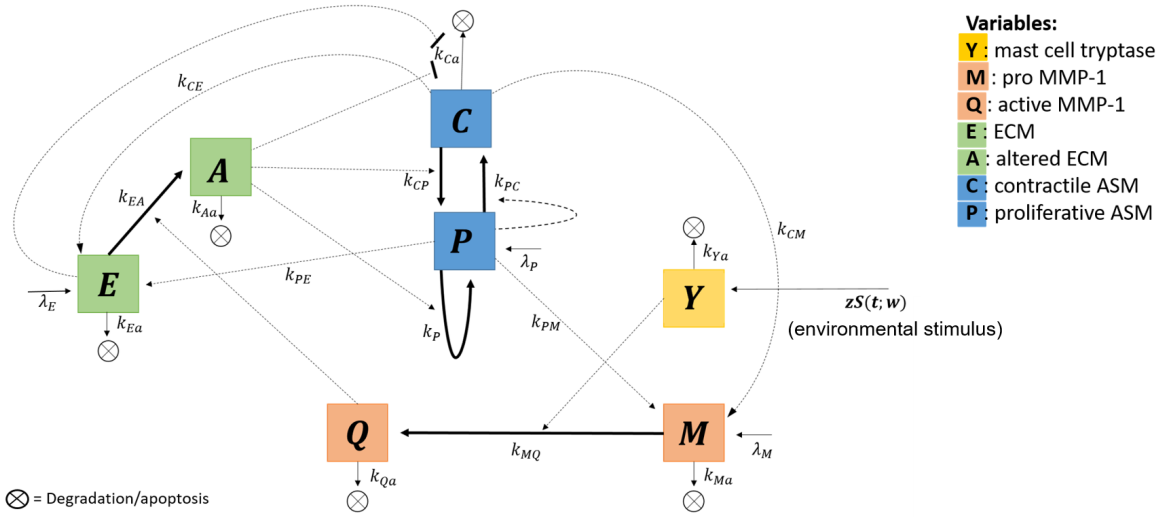

Figure 2.1: Schematic representation of the model formulation showing the interactions between all 7 variables in this system, as well as the impact of the environmental stimulus $zS(t;w)$, which accounts for the inflammation involved in an exacerbation event. Thick solid arrows represent a variable being converted to another variable, thin solid arrows represent baseline productions and degradations, arrows with a flat head represent inhibition and dashed lines show variables that enhance the production of other variables without being lost themselves.

Parameter	Description
k_{Ya}	Decay rate of mast cell tryptase
k_{PM}	Rate of production of pro-MMP-1 by proliferative ASM cells
k_{CM}	Rate of production of pro MMP-1 by contractile ASM cells
k_{Ma}	Decay rate of mast pro MMP-1
k_{Qa}	Decay rate of active MMP-1
k_{PE}	Rate of production of ECM by proliferative ASM cells
k_{CE}	Rate of production of ECM by contractile ASM cells
k_{Ea}	Decay rate of ECM
k_{Aa}	Decay rate of altered ECM
k_{PC}	Rate of switch from a proliferative ASM phenotype to a contractile phenotype
k_{Ca}	Decay rate of contractile ASM
$\hat{k}_{CP}$	Base rate of switch from a contractile ASM phenotype to a proliferative phenotype
$\hat{k}_P$	Base rate of proliferation of ASM cells

Parameter	Description
J_{MQ}	Maximum rate of activation of pro MMP-1
J_{EA}	Maximum rate of change of ECM to altered ECM
J_{CP}	Maximum rate of change of contractile ASM to proliferative ASM
J_P	Maximum proliferation rate
α	Threshold value of the Hill function for $k_P(A)$
β	Threshold value of the Hill function for $k_{CP}(A)$
γ	Threshold value of the Hill function for $k_{EA}(A)$
μ	Threshold value of the Hill function for $k_{MQ}(A)$
n	Hill exponent
λ_M	Baseline value of pro MMP-1
λ_E	Baseline value of ECM
λ_P	Baseline value of proliferative ASM
V	Total capacity of ASM cells

Figure 2.2: Descriptions of the parameters in the dimensional system based on the schematic in Figure 2.1.

Using the schematic diagram in Figure 2.1, a system of seven ODEs was constructed, using mass action and Hill functions to describe the activation

and binding of components in the pathway. The model in dimensionless form is:

$$\frac{dy}{dT} = \hat{z}S(T;w) - K_1 y, \tag{2.1}$$

$$\frac{dm}{dT} = K_2\sigma_1 p + K_3\sigma_2 c - j_1\left(\frac{y^n}{\phi_1 + y^n}\right)m - K_4 m + \psi_1, \tag{2.2}$$

$$\frac{dq}{dT} = j_1\sigma_3\left(\frac{y^n}{\phi_1 + y^n}\right)m - K_5 q, \tag{2.3}$$

$$\frac{de}{dT} = K_6\sigma_4 p + K_7\sigma_5 c - j_2\left(\frac{q^n}{\phi_2 + q^n}\right)e - K_8 e + \psi_2, \tag{2.4}$$

$$\frac{da}{dT} = j_2\sigma_6\left(\frac{q^n}{\phi_2 + q^n}\right)e - K_9 a, \tag{2.5}$$

$$\begin{aligned}\frac{dc}{dT} = {} & \sigma_7 p + j_5\sigma_7\left(\frac{p^n}{\phi_5 + p^n}\right)p - K_{10}c - j_3\left(\frac{a^n}{\phi_3 + a^n}\right)c - K_{13}c \\ & - j_6\left(\frac{1}{1+\frac{e^n}{\phi_6}}\right)\left(\frac{1}{1+\frac{a^{n+1}}{\phi_7}}\right)c,\end{aligned} \tag{2.6}$$

$$\begin{aligned}\frac{dp}{dT} = {} & K_{10}\sigma_8 c + j_3\sigma_8\left(\frac{a^n}{\phi_3 + a^n}\right)c - p - j_5\left(\frac{p^n}{\phi_5 + p^n}\right)p \\ & + p\left(K_{12} + j_4\left(\frac{a^n}{\phi_4 + a^n}\right)\right)\left(1 - \frac{p + \sigma_8 c}{\sigma_9}\right) + \psi_3,\end{aligned} \tag{2.7}$$

where we have non-dimensionalised using the scalings $t = \frac{T}{k_{PC}}$ and $X = x\bar{X}$, where x represents each variable and $\bar{X}$ represents the corresponding scaling constant. Here, lower case letters represent the dimensionless variables and an upper case T is used for dimensionless time (see Appendix A for full details). We explore the occurrence of an asthmatic exacerbation in this model through the addition of an environmental time dependant stimulus $\hat{z}S(T;w)$ which, as discussed in Section 1.1, leads to an increase in mast cell tryptase. This is modelled using a Gaussian function as follows:

$$S(T;w) = \sum_i \exp\left(-\sigma(T - T_i)^2/2\right), \tag{2.8}$$

where $\sigma = 0.01$ and each exacerbation event has a magnitude of $\hat{z}$ and a recurrence time of $1/w$, as shown in Figure 2.3. Dimensionless parameter

descriptions and values are given in Appendix A. These values were assigned using order of magnitude estimates where possible, based on data from [56] and other literature.

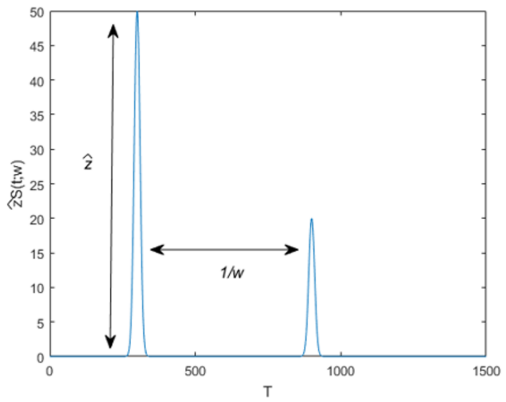

Figure 2.3: Dynamics of the environmental stimulus $\hat{z}S(T;w)$ over time using Equation 2.1 with $i = 2$. $\hat{z} = 50$ for the first stimulation at $T_1 = 300$ and $\hat{z} = 20$ for the second stimulation at $T_2 = 900$.

A parameter sensitivity analysis found that the model is most sensitive to changes in the values of the dimensionless parameters K_{13}, K_{12} and K_{10} (Figure 2.4). These parameters represent: the rate of apoptosis of c cells relative to the switching rate from p to c, the proliferation rate relative to the switching rate from p to c and the switching rate from c to p relative to the switching rate from p to c, respectively. The phenotype switching rates, in particular from p to c, are therefore important to accurately quantify. Bifurcation analysis for these parameters and the steady state of different model variables showed regions of bistability. An example of this, illustrating the change in the steady state of c when varying parameter K_{12} is shown in Figure 2.5.

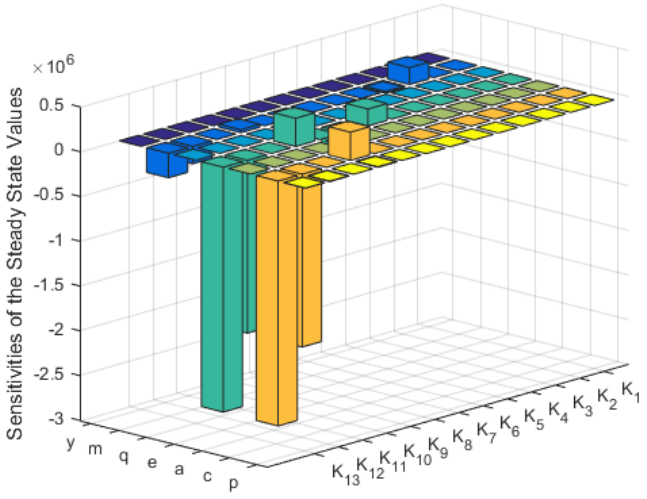

Figure 2.4: Bar graph showing the sensitivity of each of the steady states of the model given by Equations (2.1-2.7) to a 0.1% change in the parameter values $K_1 - K_{13}$. These sensitivities were calculated using COPASI.

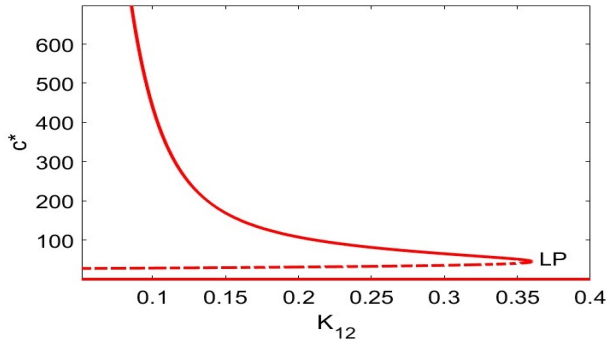

Figure 2.5: Bifurcation diagram for the steady state c^* as the parameter K_{12} is altered, using the model given by Equations (2.1-2.7). The other parameters remain as stated in the parameter tables of Appendix A. The red solid line represents a stable steady state and the dashed line an unstable steady state. Saddle-node bifurcations can be seen, where LP represents the limit point.

Figure 2.6 shows a time course simulation with an exacerbation at $T = 5$ (simulated through a time dependant stimulus that increases y). We see that immediately following the increase in y there is a large and rapid increase in q, a and p, as well as a much smaller increase in m, e and c. The density of all variables then remains at a temporary pathological steady state until y has decayed to zero, where q, a and p then rapidly decline back to zero, while m, e and c rapidly increase. As the density of q, a and p reaches zero, the density of m, e and c begins to decline until they saturate at their new, larger steady state.

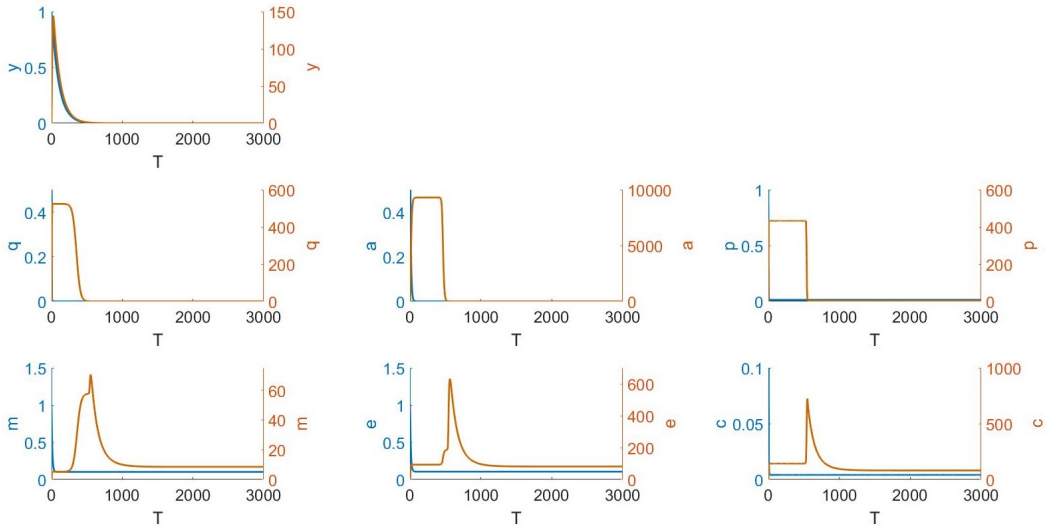

Figure 2.6: Time course simulations using the system of ODEs given by Equations (2.1-2.7) with initial conditions $[y_0, m_0, q_0, e_0, a_0, c_0, p_0] = [1, 1, 1, 1, 1, 1, 1]$ and no further stimulus (blue) and with a single stimulus $\hat{z}S(T; w)$ at $T = 5$ with $\hat{z} = 10$ (orange). Parameters remain as stated in the parameter tables of Appendix A except for $K_{12} = 0.25$.

The model hence shows a change in steady state resulting in an increase in both ECM and total ASM mass, which is consistent with the literature on airway remodelling. Analysis of this ODE model therefore suggests a possible mechanism by which the irreversible remodelling of airways in

severe asthmatics may occur. With a more accurate model of this type, the results could be used to help prevent the critical rate at which bistability occurs from being reached.

2.2 ODE MODEL DEVELOPMENTS

In this section, we now further develop the ODE model previously constructed and explored in Appendix A, as summarised above. In this model, the steady states of the pathological variables (mast cell tryptase, active MMP-1 and altered ECM) always return to zero, even if there has been an input which has caused a change in the steady state of the other variables. In exploring the biological literature further, however, it is found that mast cell tryptase has a constant baseline production rate in asthmatic patients, which increases during an exacerbation [86]. Healthy controls also have a baseline production rate of mast cell tryptase in their airways, though this is significantly lower. We therefore add this baseline production value to Equation 2.1 of the ODE model as follows:

$$\frac{dy}{dT} = \hat{z}S(T; w) - K_1 y + \psi_4. \tag{2.9}$$

Using this equation along with the rest of the system of ODEs which remain as stated in Equations (2.2-2.7), we undertake a bifurcation analysis once again. In doing so for the change in the steady state of c when varying parameter K_{12} (Figure 2.7), we can see that for a certain range values of K_{12}, there are now three stable steady states.

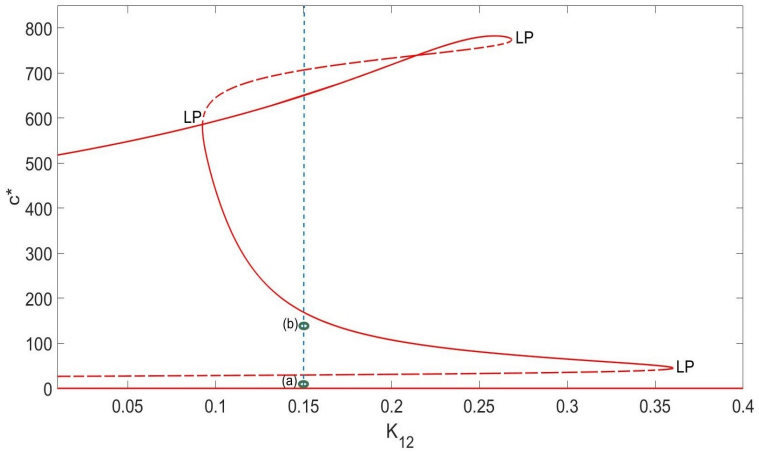

Figure 2.7: Bifurcation diagram for the steady state c^* as parameter K_{12} varies in the developed model given by Equation (2.9) and Equations (2.2-2.7). The solid red line represents a stable steady state and the dashed red line an unstable steady state. The blue dashed line shows a parameter set with $K_{12} = 0.15$, where three stable and two unstable steady states can be seen. In the simulations of Figure 2.8, three different initial conditions are used: $c_0 = 1$ (a; plus no stimulus), $c_0 = 145$ (b; plus no stimulus) and $c_0 = 1$ (a; with a single stimulus).

As before, we also simulate a time course with the addition of an environmental stimulus to model the impact of an asthmatic exacerbation (Figure 2.8). We find that, if the initial conditions are such that the system begins sufficiently close to the intermediate stable steady state and so tends to this state without an external stimulus, an exacerbation would drive the system to the highest stable steady state. If the system begins sufficiently close to the lower stable steady state, however, the exacerbation again drives the system to this highest stable steady state, rather than first increasing to the intermediate steady state.

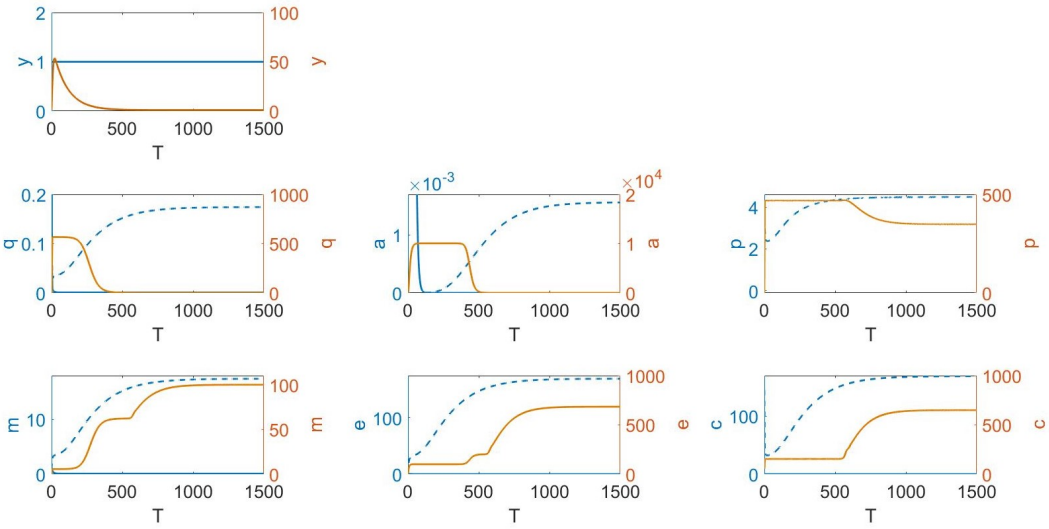

Figure 2.8: Time course simulations of the developed model given by Equation (2.9) and Equations (2.2-2.7) with initial conditions $[y_0, m_0, q_0, e_0, a_0, c_0, p_0] = [1, 1, 1, 1, 1, 1, 1]$ (point (a) in Figure 2.7) and no further stimulus (blue), $[y_0, m_0, q_0, e_0, a_0, c_0, p_0] = [1, 1, 1, 1, 1, 145, 1]$ (point (b) in Figure 2.7) and no further stimulus (blue dashed) and $[y_0, m_0, q_0, e_0, a_0, c_0, p_0] = [1, 1, 1, 1, 1, 1, 1]$ (point (a) in Figure 2.7) with the single exacerbation input $\hat{z}S(t; w)$ at $T_1 = 1$ with $\hat{z} = 5$ (orange). Parameter values are as before except for $K_{12} = 0.15$ and $\psi_4 = 0.01$.

Upon exploring the impact of some small changes in parameter values as a result of new insights from the literature [17], namely $K_{13} = \epsilon^4$ (previously ϵ^3), $j_3 = 1$ (previously 10) and $\phi_i = 100^n$ for all values of i (previously 10^n), we find some interesting limit cycle behaviour. Figure 2.9 shows bifurcation diagrams for the parameter values ψ_4, K_1 and K_4. We see that, for the lowest values of the parameter, there is a single stable steady state. A Hopf bifurcation then occurs such that the steady state becomes unstable and stable limit cycles surround it. There is then another Hopf bifurcation to end the limit cycle behaviour and return to a stable steady state again. We observe this behaviour in the time course simulations shown in Figure 2.10. While

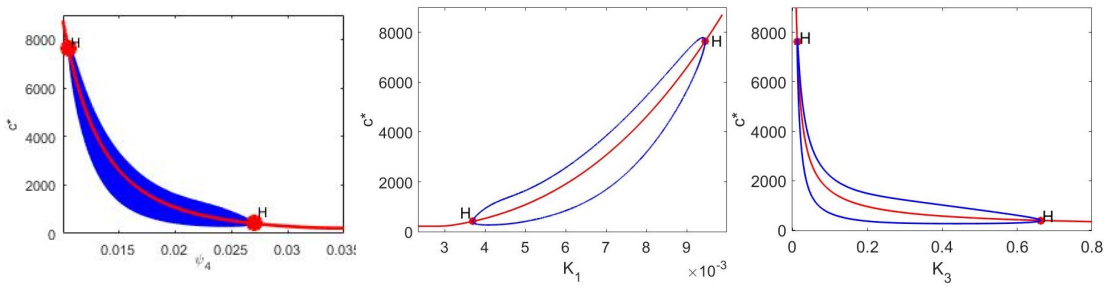

(a) (b) (c)

Figure 2.9: Bifurcation diagrams using the developed model given by Equation (2.9) and Equations (2.2-2.7) for the variable c as parameters ψ_4 (a), K_1 (b) and K_3 (c) are altered. Parameters remain as stated in the parameter tables of Appendix A except for $K_{13} = \epsilon^4$, $j_3 = 1$ and $\phi_i = 100^n$ for all i as discussed above. The red solid line represents a stable steady state until the Hopf bifurcation (H), where this state becomes unstable and stable limit cycles arise as seen in blue. (a) shows the full orbits while (b) and (c) just show the minimum and maximum values of these cycles.

there has been no experimental evidence that cycles in the quantity of each variable occurs like this in the airways, it could be that the period of these oscillations are so small that experimental measurements are not taken frequently enough to notice this behaviour. One could explore this further by collecting more experimental data and performing a more comprehensive bifurcation analysis on this model in order to deem if this behaviour is relevant.

2.3 SUMMARY

This chapter first gave a recap of an ODE model that we previously developed (Appendix A) for an MMP-1 activated pathway of airway remodelling in asthma patients. This model showed bistability so that, for a certain range of parameter values, an asthmatic exacerbation event leads to a change in

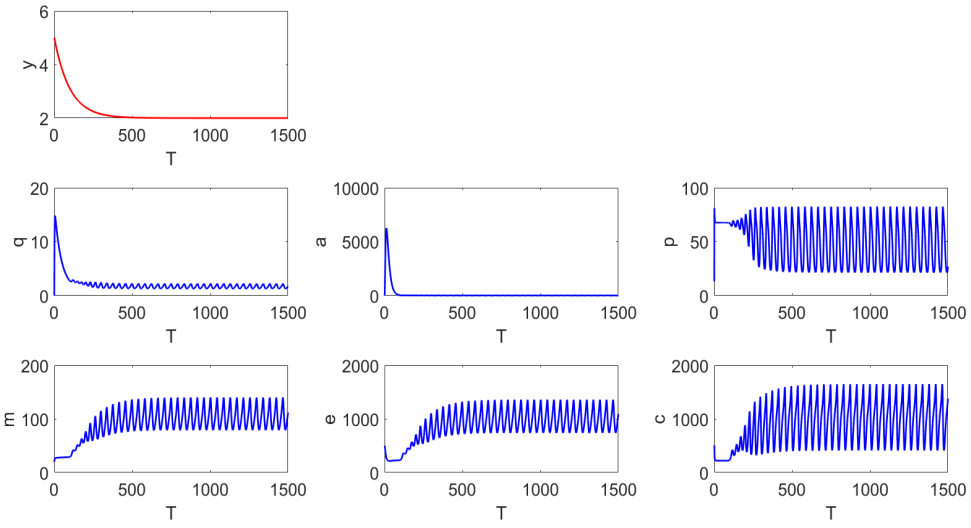

Figure 2.10: Time course simulations of the developed model given by Equation (2.9) and Equations (2.2-2.7) with initial conditions $[y_0, m_0, q_0, e_0, a_0, c_0, p_0] = [5, 20, 0, 500, 0, 500, 20]$ and no further stimulus. Parameters remain as stated in the parameter tables of Appendix A except for $K_{13} = \epsilon^4$, $j_3 = 1$ and $\phi_i = 100^n$ for all i as discussed above, as well as $\psi_4 = 0.02$ (determined from Figure 2.9 in order to observe limit cycle behaviour).

steady state resulting in an increase in both ECM and total ASM mass. The model therefore illustrates a mechanism of asthmatic airway remodelling. We then developed this model to add further biological realism. In doing so, we maintain the observation of this mechanism of remodelling for some parameter set, as well as finding some interesting possibilities of limit cycle behaviour.

This model, however, cannot reliably inform us about this system without us first accurately quantifying any rate parameters that we use. We use the model results from this chapter therefore, to tell us which of these parameters are most important to determine accurately, and then design experiments with this aim. We go forward with this project using modelling

and experimentation in complement to ultimately develop an accurate tool which could be used to identify new therapeutic targets.

3

IN VITRO EXPERIMENTS OF AIRWAY SMOOTH MUSCLE PHENOTYPE SWITCHING

In the previous chapter, we developed an ODE model for the occurrence of an asthmatic exacerbation triggered by an environmental stimulus. Bifurcation analysis of this theoretical model found a mechanism by which airway remodelling (irreversible increases in ECM and total ASM mass), could occur. In Section 2.1, we identified the parameters to which the model is most sensitive: the switching rates of ASM cell phenotypes, and in particular that from a proliferative to contractile phenotype (k_{pc}). Little is currently known about how this change in cell phenotype occurs *in vivo*; however, as described in Section 1.2.1, we know that the phenotypes have differences in their morphology, organisation (alignment of actin filaments) and quantities of certain proteins, as well as their ability to contract, synthesise proteins or proliferate. We also have evidence that, when cells undergo a long period of serum withdrawal *in vitro*, a sub-population of these cells display the increased contractile (shortening) ability, morphology and protein constituents of an *in vivo* contractile phenotype [30].

In this chapter, we design and undertake *in vitro* experiments to accurately quantify the switching rate parameters, by using serum withdrawal to initiate a switch in phenotype, and then measuring the resultant rate of change of various quantities. Primary human airway smooth muscle (HASM) cells of asthmatic patients and healthy controls were used in these experiments.

Bronchial tissue was obtained through biopsy during flexible bronchoscopies performed by Shams-un-nisa Naveed (Division of Respiratory Medicine, University of Nottingham). This tissue was then used for the culture of the ASM cells [56] that we have grown and used in the following experiments.

We have designed two novel experimental protocols that focus on different aspects of this phenotype switch initiated through the long term removal of serum. In the first experiment we use immunocytochemistry to track the presence of certain protein markers within the cells over a period of serum deprivation (Section 3.1). In this experiment, we measure both the number of cells undergoing cell division (through proliferation markers and a cell counting algorithm) and the changes in actin filament alignment. In the second experiment, we measure the direct change in contractile force exerted by the cells over a period of serum deprivation (Section 3.2). Using the results of both experiments, we quantify the change in numbers of contractile and proliferative cells over time after the switch is initiated. Using these data, we use a least squares method to fit parameter values for the switching rate k_{pc} and the proliferation rate k_p to a simplified version of our ODE model from Chapter 2 (Section 3.3), such that the model matches the experimental protocol. Table 1 summarises the experiments discussed in this Chapter.

Experiment number	Experimental technique	Brief description	Main results	Model application
1	Immunocytochemistry	Using stains to track changes in cell numbers (a measure of proliferation) and actin alignment (a measure of contractility) at different time points over a period of serum deprivation.	A 4-fold increase in anisotropy over the period of serum deprivation.	Results used to infer proportion of each ASM phenotype at each time point.
2	Traction Force Microscopy	Tracking changes in contractile forces exerted before and after stimulation with histamine at different time points over a period of serum deprivation (through the displacement of fluorescent beads).	Histamine induced contraction increased with cell culture time.	Results used to infer proportion of each ASM phenotype at each time point.

Table 1: Summary of the *in vitro* experiments described in Chapter 3 including the main results and how they can help to inform our mathematical models.

3.1 EXPERIMENT 1: IMMUNOCYTOCHEMISTRY

3.1.1 *Aims and Objectives*

As described in Section 1.4.1, immunocytochemistry is a technique which allows us to see specific proteins through the binding of an antibody which is labelled with a coloured stain. We chose four fluorescent stains: DAPI, Phalloidin, anti-Ki67 and anti-PCNA (examples of their effect are shown in Figure 3.1). DAPI stains all nuclear material with blue fluorescence allowing us to calculate the total number of cells in the image. Phalloidin (coloured red) binds to actin filaments. This stain allows us to identify elongated contractile cells through identification of their strongly anisotropic actin filaments. Finally both anti-Ki67 and anti-PCNA (coloured green) are antibodies that are expressed highly in cells that are undergoing proliferation. To initiate the phenotypic switch, we culture the HASM cells in serum-rich media (that causes cells take on a proliferative phenotype) and then remove serum from the media and leave for 0, 5, 7, 11 and 14 days before fixation. We fix the cells at each of these time points such that they are no longer alive but large molecules like antibodies are still able to find intracellular antigens [51]. We use the method of immunocytochemistry detailed below to quantify the potential change in phenotype by measuring levels of proliferation and anisotropy of actin filaments. The hypothesis is that serum-deprivation of the cells will lead to an increase in alignment of actin filaments and a relative decrease in proliferation as the cells switch from a proliferative to a contractile phenotype.

3.1.2 *Materials*

- Cultured HASM cells in Dulbecco's Modified Eagles's Medium (DMEM) +10% Foetal Bovine Serum (FBS)

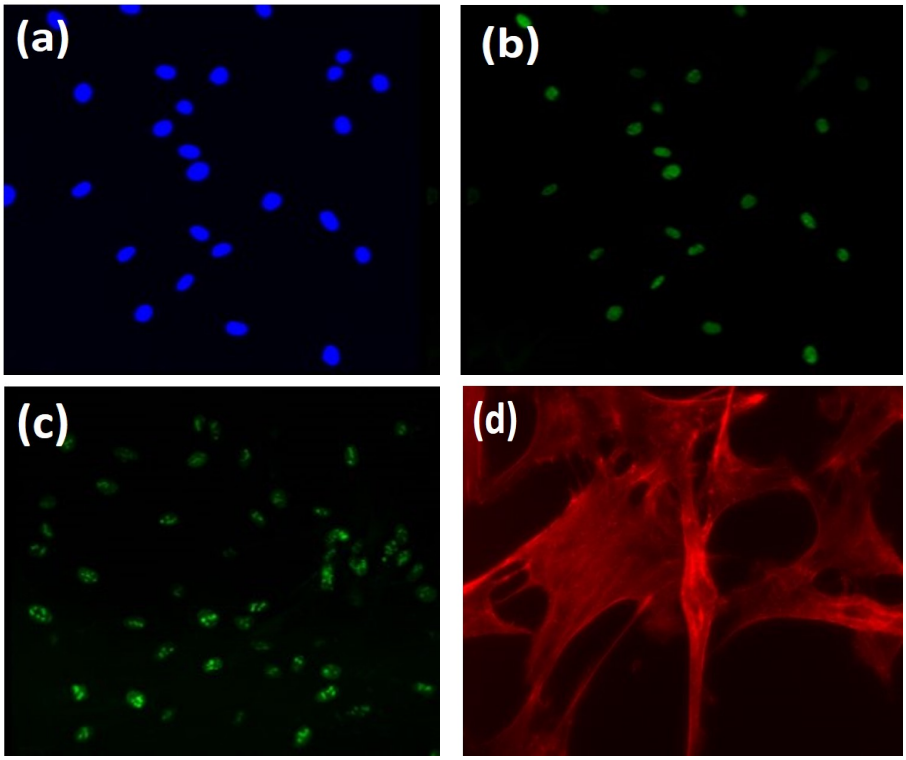

Figure 3.1: Examples of all four fluorescent stains used for the confocal microscopy in Experiment 1, (a) DAPI (nuclear stain), (b) anti-PCNA and (c) anti-Ki67 (both proliferation stains) and (d) Phalloidin (stain for actin filaments).

- Trypsin
- Polylysine coated chamber slides
- Phosphate-buffered saline (PBS)
- 4% formaldehyde (methanol free)
- 0.1% Triton X-100 in PBS
- Phalloidin-iFluor 555 Reagent - Cytopainter working solution (1μl of 1000X conjugate stock solution in 1ml of PBS +1% Bovine Serum Albumin)
- Ki67 (8D5) Mouse mAb (#9449)

- Alexa Fluor 488 goat anti-mouse secondary antibody
- 100% methanol
- Anti-PCNA PC10 (ab29)
- Vectormount DAPI mounting media
- Clear nail varnish

3.1.3 *Experimental Method*

This experiment was undertaken with the help of Dr Christopher Philp, Dr Debbie Clements, Dr Marlies Fischer and Dr Charlotte Billington (Centre for Respiratory Research, University of Nottingham). HASM cells from three healthy and five asthmatic donors were recovered in flasks with DMEM +10% FBS for two days. At this point the cells were trypsinised, spun down with a trypsin inhibitor and re-suspended in different amounts of media depending on the confluence of each flask and the required confluence for staining purposes. 500μl of the cell suspension from each donor was plated in duplicate in five different eight-well, polylysine-treated, chamber slides (since there are five time points). Four extra slides were also plated as controls which were kept in serum throughout the experimental time period. Two days after plating these cells, we fixed and stained each set of donor cells at time point t_0 and removed the serum from the remaining slides (except controls). The remaining slides for each set of donor cells were then fixed at t_1 = day 5, t_2 = day 7, t_3 = day 11 and t_4 = day 14 respectively. The fixation and staining protocol was as follows.

To allow fixation, the media was first aspirated and the cells were washed three times with PBS. The slides were then fixed and stained in two different ways, since during test experimental runs it was found that both the Phalloidin and Ki67 stains require formaldehyde fixation, however PCNA works

best when fixed in methanol. For the slides that require formaldehyde fixation, wells were covered with 4% formaldehyde for 15 minutes, then washed three times with PBS. Following this, these slides were permeablised with 0.1% Triton X in PBS for 10 minutes before a further three washes in PBS. Slides were then blocked in pre-made 2.5% goat serum for 20 minutes before another three washes with PBS. 100μl of the Phalloidin working solution was then added to each well before wrapping in foil and incubating at room temperature for 60 minutes. The slides were then washed in PBS three times. 200μl per well of a 1/1000 dilution of primary anti-Ki67 antibody was then added to the slides which were then left overnight at 4°C. The following day, we washed three times with PBS then added 250μl of secondary antibody to each well and left for 30 minutes. We washed a final three times with PBS then removed the chambers using a chamber slide key and any silicon that was stuck round the edge using tweezers. Five drops of aqueous mounting media with DAPI was added to the wells and the slide was slowly sealed with a cover slip. Once the mounting media had set, we sealed the edges of the cover slip with nail varnish. We could then observe the cells using a confocal microscope at Ex/Em = 493/517 nm for Phalloidin, 495/519 nm for anti-Ki67 antibody and 358/461 nm for DAPI. For the slides that required methanol fixation, these were submerged in methanol at -20°C for 10 minutes then washed three times with PBS. Slides were then blocked in pre-made 2.5% goat serum for 20 minutes before another three washes with PBS. We then added 200μl per well of 0.25mg/ml primary anti-PCNA antibody diluted in 10% goat serum and left in a dark box in the fridge overnight. The antibody was then taken off and the slides were washed with PBS three times before adding 250μl of secondary antibody to each well and leaving for 30 minutes. We then washed a final three times with PBS, removed the chambers, mounted with DAPI and imaged as above.

The protocol described above is the result of many optimisation steps. Tests were first done using different types of chamber slides, different densities

of cells per well, different combinations of fixation methods, different types of antibody and antibody dilutions and the use of secondary stains. These tests were also undertaken on both cells in serum and not in serum. Further details of this experimental optimisation process are given in Appendix B.2.

3.1.4 *Image Analysis Methods*

The protocol above generated hundreds of images. Analysis of these images required the counting of nuclei (for both DAPI and proliferative stains) and the measurement of the alignment of actin filaments stained with phalloidin. In order to do the former of these tasks efficiently, we developed a code in MATLAB in order to run through all the images and count nuclei automatically. This code works by reading through a file containing all the images and following the steps described in Algorithm 2.

This algorithm gave the number of nuclei in each image, along with each corresponding altered image showing which nuclei had been counted by their red outline. Variability in background noise meant that some nuclei were subjective in their positivity (i.e. showed some fluorescence but the signal was weak). We know that these nuclei are not counted by the algorithm since their perimeter is not outlined in red in the resultant altered image. Any images that have variability in background noise were therefore determined by an unusually low count; those not counted automatically were then manually added to the count. An example of an image before and after this process is shown in Figure 3.2. We divide the cell number by the area in order to obtain a cellular density per mm^2 for each image.

Anisotropy of actin filaments is measured using the FibrilTool in the image analysis program ImageJ, as described in [9]. This tool calculates the local

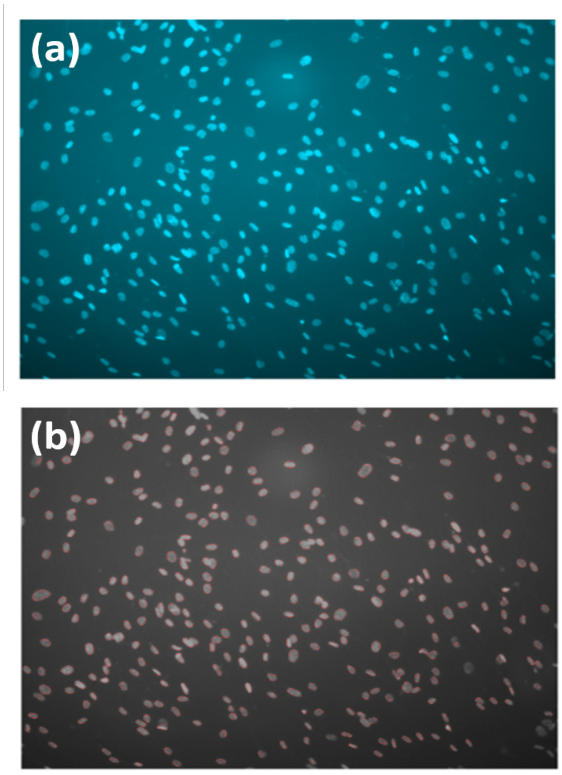

Figure 3.2: DAPI Stained HASM cells. (a) shows an area of DAPI stained cells obtained using confocal microscopy and (b) is the result of processing, where the image has been binarized for counting using thresholding (i.e. up to step 9 in Algorithm 2).

Algorithm 2: Nuclei counting method used on images in MATLAB

1. Read in image
2. Gray scale if colour image
3. Adjust the contrast
4. Remove objects on the border
5. Adaptively filter in order to reduce noise
6. Make the image binary
7. Fill in any holes
8. Remove connected points with fewer than 20 pixels
9. Overlay a red image of the perimeter pixels of each object remaining
10. Count the objects

nematic tensor $\mathbf{n} = \hat{t} \otimes \hat{t}$ where $\mathbf{n}_{x,x} = \hat{t}_x^2, \mathbf{n}_{x,y} = \mathbf{n}_{y,x} = \hat{t}_x \hat{t}_y, \mathbf{n}_{y,y} = \hat{t}_y^2$ and $\hat{t}$ is the unit vector which is tangent to the fibres, defined as follows:

$$\hat{t} = (\hat{t}_x, \hat{t}_y) = \frac{(\partial I/\partial y, -\partial I/\partial x)}{\sqrt{(\partial I/\partial x)^2 + (\partial I/\partial y)^2}}, \tag{3.1}$$

with $I(x, y)$ representing the pixel intensity at position (x, y). The nematic tensor over the region of interest is denoted $< \mathbf{n} >$ and is given by the average of $\mathbf{n}$ (over the region of interest, which is given by the whole image area in our case). The eigenvector of $< \mathbf{n} >$ corresponding to the largest eigenvalue then tells us the average orientation of the fibres. Similarly, the difference between the eigenvalues of this region gives us a measure of anisotropy. We therefore obtain a value of alignment between zero and one; zero being completely randomly aligned or isotropic (as in the proliferative phenotype) and one being strongly anisotropic (as they are when spindle-shaped and contractile). The output of the calculation above is shown in the image as

a line segment where the angle of this line is the average orientation of the fibres and the length of the line is proportional to the anisotropy score [9]. Figure 3.3 shows an example output using the FibrilTool on a image of cells in serum (Figure 3.3a) and without serum (Figure 3.3b) where the line segment is coloured green. As hypothesised, we see that the actin filaments of the cells in serum are randomly aligned and so have a small anistropy, whereas the cells that have been serum deprived show high anisotropy in their actin filaments.

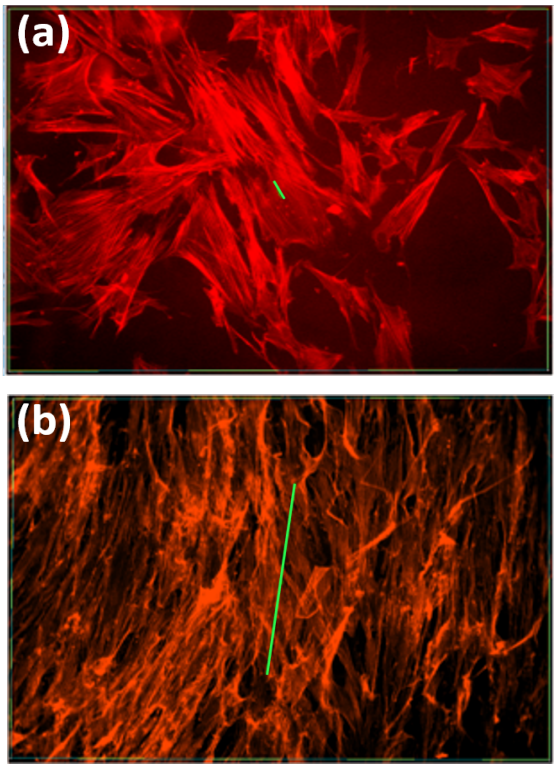

Figure 3.3: Phalloidin stained HASM cells. (a) shows the low anisotropy of actin filaments in cells in serum (represented by a single short green line) while (b) shows the high anisotropy of actin filaments in cells that have been serum deprived (represented by a single long green line in the direction of the average orientation of the fibres).

3.1.5 *Results*

The average density of all the cells (DAPI stained nuclei) per well, over the 14 day period of serum deprivation, is shown in Figure 3.4(a). We note that, while some cells continue to proliferate at day 5 giving a higher population at day 7, after this point the proliferation stops and the population size remains the same. At day 14 there is a drop in population size; this may be due to cell contact inhibition and apoptosis. Figure 3.4(b) illustrates the change in average anisotropy of actin filaments over the same time period. We see a strong (4-fold) increase in anisotropy over the 14 days. The results from the proliferation stains anti-PCNA and anti-Ki67 both showed approximately every cell as positive for proliferation at day 0 when serum was present and after the serum was removed this either dropped to zero or displayed just a few positive nuclei at day 5 and then dropped to zero for the remaining time points.

For the purpose of finding the rate of phenotype switching, we instead use the fact that we know the change in total population size S over time (via total cell density) and $S = c + p$. We can also infer the change in the size of the population c over time using the anisotropy data. To do this, we assume that when we obtain the highest value of anisotropy the cells are fully contractile at this point (since we observe almost fully parallel fibres when looking at the image by eye) and we normalise with respect to this highest value. This then gives us the proportion of the cells that are contractile at each time point. Using this and the value of S at each time point, we can infer the corresponding density of proliferative cells ($p = S - c$).

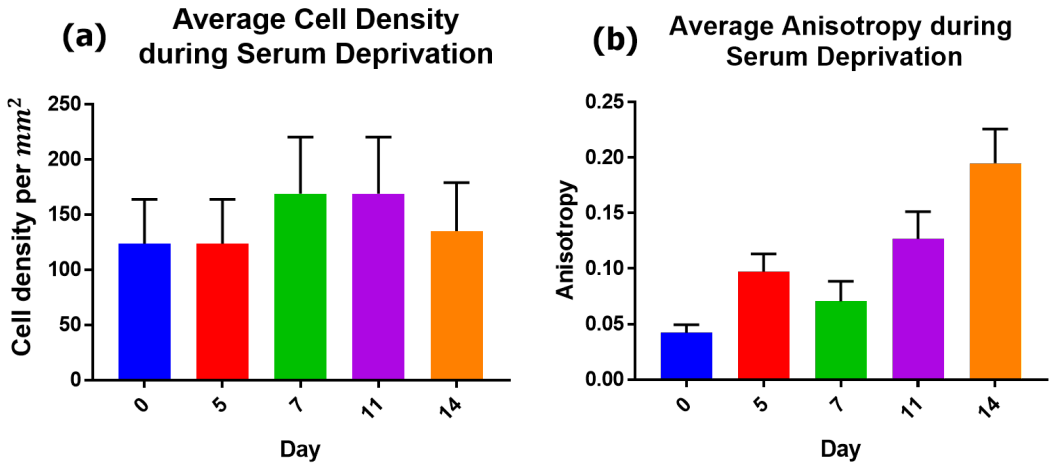

Figure 3.4: Immunocytochemistry results. (a) shows the change in average cell density over time using the DAPI counts, where a one-way ANOVA test gave an ANOVA coefficient of 0.2609 and a p-value of 0.9007. (b) shows the change in anisotropy of cell fibres over time using the phalloidin stained images, where a one-way ANOVA test gave an ANOVA coefficient of 9.201 and a p-value of < 0.0001. Error bars show standard error. As described above, the cell density results gives us $c + p$ (the whole population) and the anisotropy results give a measure for c out of this total cell population.

3.2 EXPERIMENT 2: TRACTION FORCE MICROSCOPY

3.2.1 *Aims and Objectives*

Experiment 1 allowed us to infer the rate of change of the populations c and p via changes in cell morphology and organisation as well as protein content. With this next experiment we aim to measure contractility directly using a technique called Traction Force Microscopy (TFM). As described in Section 1.4.2, TFM uses specially designed 96 well plates with a gel substrate of known material properties seeded with fluorescent beads such that

the traction forces exerted by the cells on the substrate can be determined using the displacements of these beads [59]. We use this approach to measure the contractile force generated by serum-deprived HASM cells when stimulated with a contractile agonist (histamine). For this experiment I travelled to Boston USA to work in the laboratory of Dr Ramaswamy Krishnan at Harvard Medical School. Here we developed an experimental protocol based on their optimised protocol of TFM. We measured the contractility of cells before and after the contractile agonist is added (day 0) then remove the serum and repeat this process on day 3, day 7 and day 10. The hypothesis is that the longer the cells are serum-deprived, the more will have switched to their contractile phenotype. Thus when a stimulus is added they would be expected to display greater contraction.

Upon activation, mast cells resident in the airway release several mediators (discussed in Section 1.1), an example of which is mast cell tryptase, an important variable in our original ODE model described in Chapter 2. We therefore additionally wished to observe the impact of activated mast cells as well as inactivated mast cells (as a control where mediators are not released) on the switching rate and contractility of the ASM cells in serum-deprived media. Mast cell supernatant is the fluid which remains on top of the cell pellet after centrifuging and it contains all soluble factors released by the dividing cells. We hypothesise that the addition of activated mast cell supernatant will enhance the switching rate, generating greater contractile force earlier in the time period of serum deprivation. The addition of inactivated mast cell supernantant as a control should, in theory, have the same effect as the study where no mast cell supernatant was added. The method for collecting both the activated and inactivated mast cell supernatant is given in Appendix B.3.

3.2.2 *Materials*

- Cultured confluent flask of HASM cells
- DMEM F-12 media + penicillin streptomycin + anti-fungal agent + glutamine + calcium with either 10% FBS or ITS
- 0.25% Trypsin
- 300 Pascal TFM plate
- 1M HEPES Buffer
- Sanpah powder
- DMSO
- Advanced Biomatrix Pure Col diluted to 0.05mg/ml in PBS
- PBS
- 10mM histamine
- 10mM methacholine (MCH)
- Buffer RLT (Qiagen)

3.2.3 *Experimental Method*

This experiment was undertaken with the help of Sumati Ram-Mohan (Department of Emergency Medicine, Harvard University). We used a bespoke glass bottomed plate with NuSil based gel substrates miniaturised in the bottom, seeded with fluorescent beads and functionalised with collagen (for details on how this is made see [85]). We chose a plate of stiffness 300Pa and cleaned the plate using 70% ethanol (once cleaned, the rest of the protocol was undertaken in sterile conditions). We added 40ml of 0.1M HEPES buffer into a universal, then added 100mg of SANPAH to 2ml DMSO and

added 160μl of this to the HEPES buffer. This solution was transferred to the plate such that it covered the surface of each well. The plate and lid were then placed under UV light for approximately 20 minutes in order to sterilise. We then removed the SANPAH solution without touching the bottom of the wells. 4oml of PBS was added to 650μl of collagen and then we transferred 200μl of this to each well. The lid was then replaced and the plate was left at 4°C for 48 hours.

When plating the cells, we first removed the collagen from the plate and discarded. We replaced this with 200μl of ITS media per well and incubated for 30 minutes. This media was removed and the cells were transferred from a confluent T75 flask to the plate, making sure that there were approximately 22,000 cells per well (we counted the number of cells in 10μl using a haemocytometer and then calculated how much IT media was needed to re-suspend the cell pellet for 85 wells). 200μl of this cell suspension was then added to each well before incubating over night.

The imaging process then began, whereby baseline (pre-treatment) and post-treatment images were taken on days 0, 3, 7 and 10 as described below. We imaged using an inverted Leica microscope with a heat chamber and motorized stage. The plate fit tightly into the insert on the stage such that the positions remained the same at each time-point. We imaged at 10× magnification for optimal bead size. A region of interest close to the centre of each well was chosen (traction is altered near the edges) with replicates per well non-overlapping. The rest of the process ran automatically, taking both fluorescent bead images and phase contrast images of the monolayer for each position in each well. After the baseline images were collected, treatments were prepared. A 10× dilution of histamine and methacholine were made, sterile filtered and added to their corresponding rows of wells (on top of the media already present). The same amount of extra media was added to the wells that were not treated as a vehicle control. We waited for 30 minutes

and then repeated the imaging process above to obtain post stimulation images. After imaging, we washed out the treatments with media. For the addition of mast cell supernatant, we needed 25% supernatant in media, and as usual 200μl was added to each well. This was applied to designated columns of wells after the imaging on days 0, 3 and 7.

At the final time point, after baseline and post-treatment images were taken, we did one more round of imaging to obtain a reference image without cells present. For this, we removed the contents of the plate and added 100μl of lysis buffer (buffer RLT) to each well before imaging once again.

3.2.4 *Image Analysis Method*

The many images collected during this experiment were compared to their reference image and analysed using a custom made program developed by Butler *et al.* [14] in Matlab, to produce images of the bead displacement maps and traction maps for each well. Figure 3.5 shows examples of all four images that we obtained for each position, at each time point, before and after stimulation. A text file was also created with the values of root mean squared traction (RMST), contractile moment (CM) and strain energy. The displacement map was computed from a comparison of the bead images throughout the experiment with a reference image taken at the end after lysing the cells. Using this, the traction map was computed using the constrained Fourier transform traction microscopy method for a cell monolayer (as described in Section 1.4.2) [42, 85]. In the results section below, we show the strain energy of the basal forces (before stimulation) and the histamine induced contraction (after stimulation) over the period of serum deprivation, where the data for histamine induced contraction has been normalised with respect to the basal force for that region of interest.

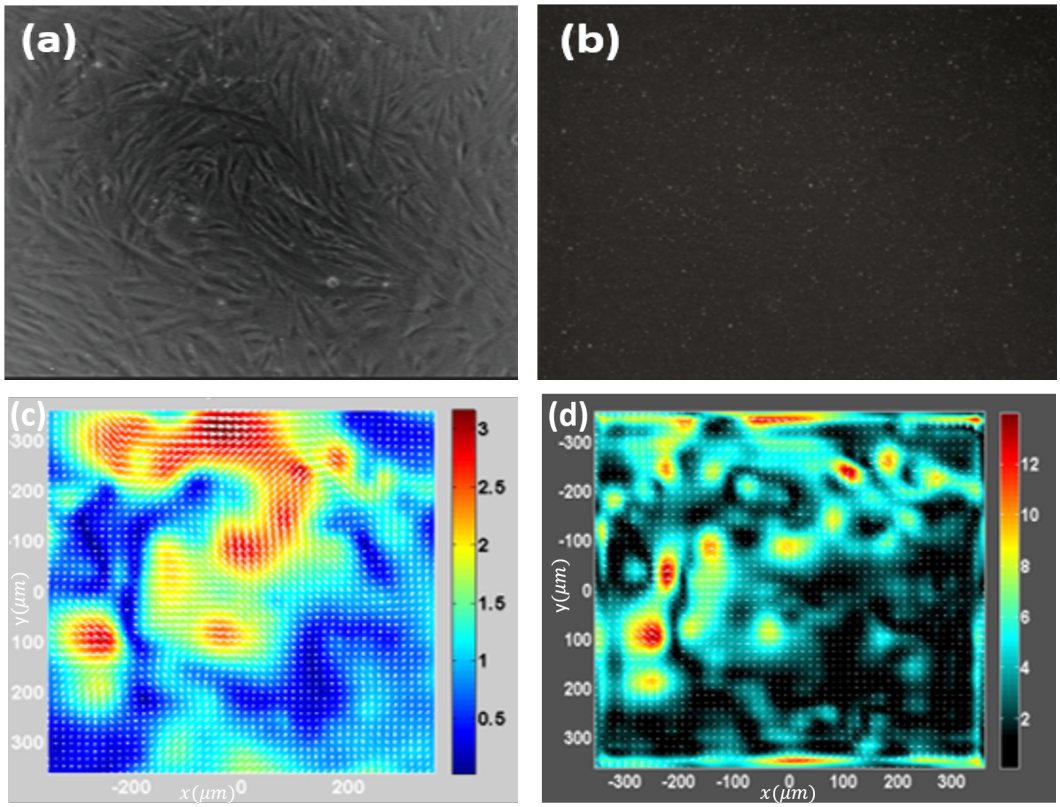

Figure 3.5: TFM Images of HASM monolayer: (a) A phase contrast cell image, (b) a fluorescent bead image, (c) a displacement map (the magnitude and direction of displacements are represented by arrows in the x, y plane) and (d) a traction force map (the magnitude and direction of tractions are shown by arrows), all obtained using TFM at Dr Krishnan's lab, Harvard Medical School.

3.2.5 *Results*

While much of this protocol has been pre-optimised [43], we found that when using these particular HASM cells, the response to histamine was much larger than that to MCh. We also found that we can plate directly into serum-free media and that most of the cells survived the disruption involved in the treatment and imaging process over a long 10 day period. The first result from this experiment is that basal HASM cell force decreased with cell culture time while histamine-induced contraction increased with culture time (Figure 3.6). We hence see that long term serum deprivation relaxes cells and that there is a greater effect of a contractile agonist. This is an important result that is consistent with the switch in phenotype from a proliferative cell population to a contractile one, with corresponding changes in protein content. We can therefore use the trend in basal traction forces as a measure of our variable p and the trend in histamine induced contraction as a measure of our variable c.

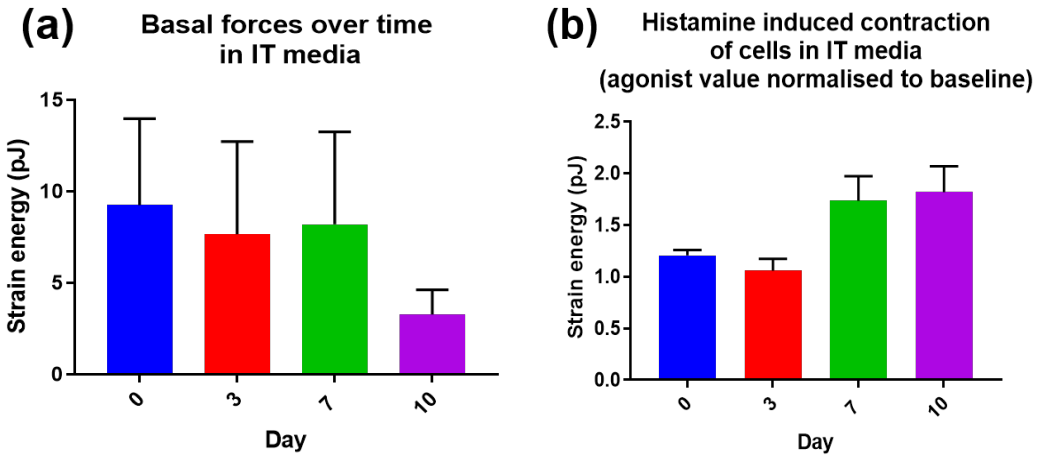

Figure 3.6: TFM results (no mast cell media). (a) shows the changes in cell basal forces over time in serum-deprived IT media, where a one-way ANOVA test gave an ANOVA coefficient of 0.724 and a p-value of 0.5403. (b) shows the changes in histamine induced contractile forces over time (with the agonist value normalised to baseline) in serum-deprived IT media, where a one-way ANOVA test gave an ANOVA coefficient of 4.382 and a p-value of 0.0111. Error bars show standard error.

The results for the activated mast cell supernatant experiment (Figure 3.7) showed that, while basal force did not decrease, histamine-induced contraction substantially increased over time with the activated mast cell supernatant. This may be explained by the impact that mast cell tryptase has on the activation of MMP-1 and the subsequent processing of the ECM as described in [56] (the pathway on which we based our ODE model development in Appendix A as described in Chapter 2). The fact that histamine-induced contraction in the activated mast cell media is higher than that without, also confirms the importance of mast cell tryptase in airway remodelling (Section 1.1) and further validates the results from [69] showing MMP-1 modulated promotion of ASM contraction. Cells in the control mast cell media (Figure 3.8) showed a similar trend in basal forces over time; how-

ever, there was little change in the histamine-induced contraction throughout.

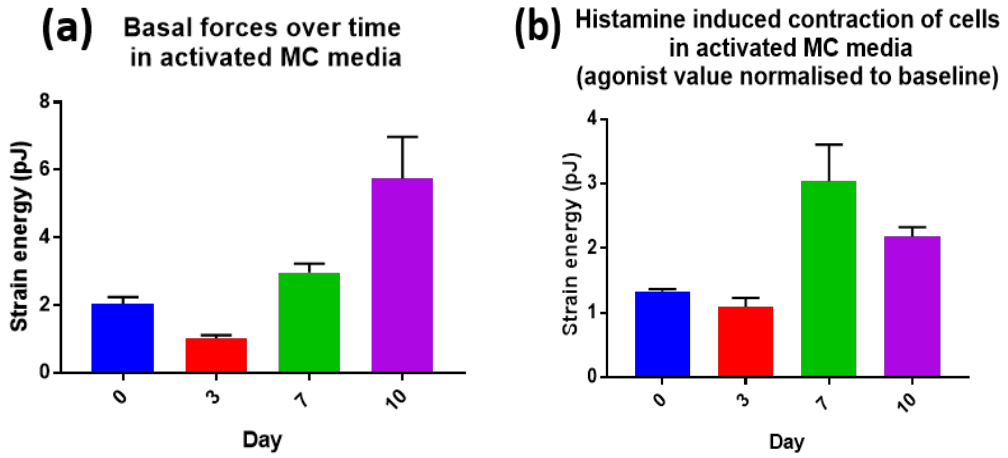

Figure 3.7: TFM results (activated mast cell media). (a) shows the changes in cell basal forces over time in activated MC media, where a one-way ANOVA test gave an ANOVA coefficient of 10.01 and a p-value of 0.0003. (b) shows the changes in histamine induced contractile forces over time (with the agonist value normalised to baseline) in activated MC media, where a one-way ANOVA test gave an ANOVA coefficient of 8.66 and a p-value of 0.0007. Error bars show standard error.

3.3 MODEL REDUCTION

Since the focus is on finding values for the ASM phenotype switching rates, these experiments do not account for the full remodelling pathway in Chapter 2. We therefore need to simplify the ODE model such that it matches the experimental system. In both experiment 1 and 2 (without mast cell media), we assume that only two subpopulations of ASM cells are present, and that there is no ECM deposition over this time scale. We reduce the model to just two variables c and p, where a p cell is able to switch to a c

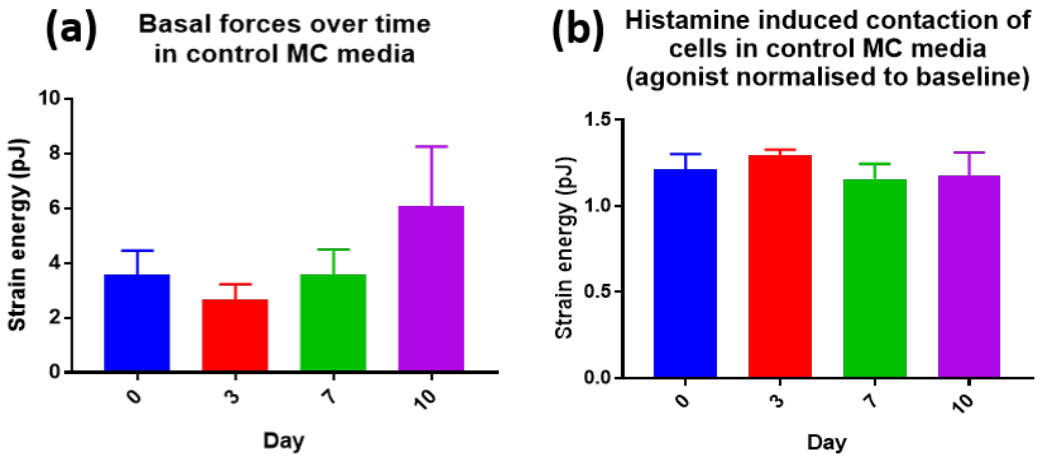

Figure 3.8: TFM results (inactivated mast cell media). (a) shows the changes in cell basal forces over time in inactivated MC media, where a one-way ANOVA test gave an ANOVA coefficient of 1.308 and a p-value of 0.2995. (b) shows the changes in histamine induced contractile forces over time (with the agonist value normalised to baseline) in inactivated MC media, where a one-way ANOVA test gave an ANOVA coefficient of 0.4115 and a p-value of 0.7465. Error bars show standard error.

cell (at rate k_{pc}) and proliferate (at rate k_p). We once again assume that the ASM cell apoptosis rate (k_{ca}) is negligible. Here, the ASM switching rate from a contractile to a proliferative phenotype (k_{cp}) is additionally assumed to be negligible since cells only switch to a proliferative phenotype in the presence of serum, which is removed during these experiments. The system is therefore reduced to the following:

$$\frac{dc}{dt} = k_{pc}p, \tag{3.2}$$

$$\frac{dp}{dt} = k_p p - k_{pc}p, \tag{3.3}$$

For experiment 2, where activated/inactivated mast cell supernatant is added to the cell media, we need to add mast cell supernatant as another variable M in addition to the two ASM cell subpopulations in the reduced model above. This variable is represented as a Gaussian time dependent input (since we added more supernatant to the media after imaging on days 0, 3 and 5) of magnitude β/u_M and with some decay rate k_{ma} as follows:

$$\frac{dM}{dt} = \frac{\beta}{u_M} e^{\frac{-(t-t_1)^2}{u_M^2}} + \frac{\beta}{u_M} e^{\frac{-(t-t_2)^2}{u_M^2}} + \frac{\beta}{u_M} e^{\frac{-(t-t_3)^2}{u_M^2}} - k_{ma}M, \tag{3.4}$$

where t_1, t_2 and t_3 are the days supernatant was added. u_M controls the time interval over which the bulk of M from each supernatant addition enters the media. A smaller value of u_M reduces this time interval; here we assume $u_M^2 = 0.5$. As Equation (3.4) is decoupled from Equation (3.2) and Equation (3.3), we are able integrate to solve for M. Since we assume that the rates k_p and k_{pc} are both functions of M, the equations for c and p are re-expressed as

$$\frac{dc}{dt} = \left(\hat{k}_{pc} + \frac{J_{pc}M^{n_1}}{\alpha + M^{n_1}}\right) p - k_{cp}c, \tag{3.5}$$

$$\frac{dp}{dt} = k_{cp}c - \left(\hat{k}_{pc} + \frac{J_{pc}M^{n_1}}{\alpha + M^{n_1}}\right) p + \left(\hat{k}_p + \frac{J_p M^{n_2}}{\alpha + M^{n_2}}\right) p, \tag{3.6}$$

where, (as in Chapter 2) we use Hill functions to describe the binding of variables with $\hat{k}_i$ as the baseline rate, J_i as the maximum rate, α the threshold at which M has an effect and Hill coefficients $n_1 = 8$, $n_2 = 4$ (under the

assumption that the change in rate k_{pc} with larger M is more sudden than the change in k_p) .

3.3.1 *Least Squares Fit*

We now have two sets of experimental data for which we have measures of the values of c and p at each time point, plus a reduced model for c and p to match these experiments. We can therefore use a least squares estimate in order to fit parameters to the simplified model. A non-linear least squares solver in Matlab (`lsqcurvefit`) is used for this purpose. In doing this for experiment 1 (described in Section 3.1), we obtain the results shown in Figure 3.9, with values for k_p and k_{pc} given in Table 2. Although the fit looks reasonable for the behaviour of $c(t)$ for the few points we have, it is likely that extra data points would alter the fit significantly. Note that the curves of Figure 3.9 are not straight lines, although they appear to be for the time period shown.

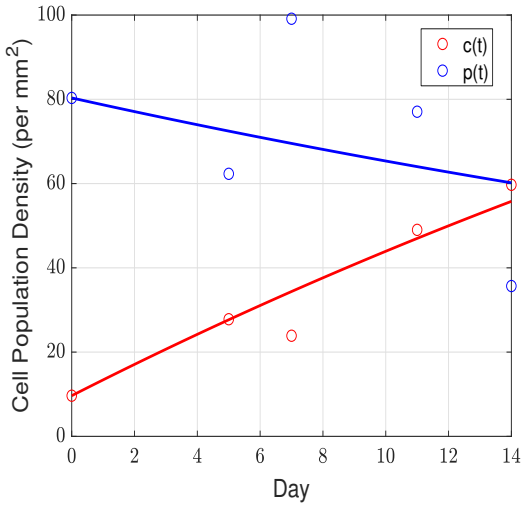

Figure 3.9: Least squares fit of the model given by Equations (3.2) and (3.3) (coloured lines) to data collected in experiment 1 and given in Figure 3.4 (coloured circles). The parameters being fitted are k_p and k_{pc}.

Results of fitting the model to the data collected in experiment 2 (described in Section 3.2), without mast cell supernatant, are shown in Figure 3.10(a) with values for k_p and k_{pc} given in Table 2. Again, the model fit is reasonable for the data that we have but is likely to be modified if more data were available.

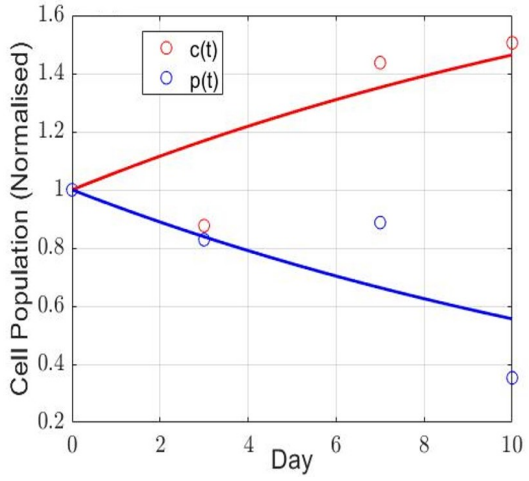

Figure 3.10: Least squares fit of the model given by Equations (3.2) and (3.3) (coloured lines) to data collected in experiment 2 and given in Figure 3.6 (coloured circles). The parameters being fitted are k_p and k_{pc}.

Finally the fit for the data with inactivated and activated mast cell supernatant added is shown in Figure 3.11(a) and 3.11(b) respectively. This system has a larger number of unknown parameters; however, results from fitting k_p and k_{pc} in the experiment without mast cell media (Figure 3.10) allow us to set these parameters as known. The fit to the data obtained when inactivated mast cell supernatant was used gives values of k_{ma}, k_{cp}, J_{pc} and J_p, as indicated in Table 2. We can then use the values obtained from the inactivated supernatant fit as known values for the fit to the activated mast cell data to obtain fits for the parameter values J_{pc} and J_p, as indicated in Table 2.

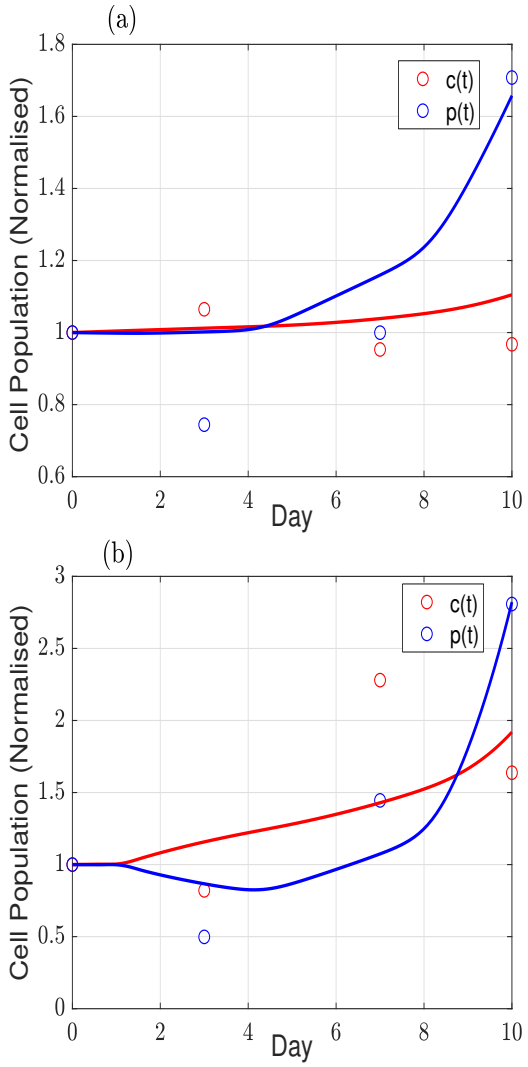

Figure 3.11: Least squares fit of the model given by equations (3.5) and (3.6) (coloured lines) to data collected in experiment 2 (coloured circles). (a) shows the fit for the data collected using inactivated mast cell supernatant (Figure 3.8). (b) shows the fit for the data collected using activated mast cell supernatant (Figure 3.7).

Parameter values given least square fit	Fit to Exp1 (Figure 3.9)	Fit to Exp 2 (Figure 3.10(a))	Fit to Exp 2 with inactivated mast cell media (Figure 3.11(a))	Fit to Exp 2 with activated mast cell media (Figure 3.11(b))
k_p	0.02659	0.00268	0.00268	0.00268
k_{pc}	0.04722	0.06134	0.06134	0.06134
k_{ma}	-	-	0.001	0.001
k_{cp}	-	-	0.05692	0.05692
J_p	-	-	0.36223	1.13671
J_{pc}	-	-	0	0.09472

Table 2: Summary of parameter values obtained in each of the model fits of Section 3.3.1.

3.4 SUMMARY

We began this chapter by proposing two novel *in vitro* experimental protocols that can be used to measure the switching rate from a proliferative phenotype (p) to a contractile phenotype (c) in human airway smooth muscle cells.

In the first experiment (Section 3.1), immunocytochemistry was used to quantify this rate through measuring the levels of both cell proliferation and alignment of actin filaments, over a period of serum deprivation. The results from this experiment (Section 3.1.5), showed that anisotropy of actin filaments (a measure of contractility) increased four-fold over the length of the experiment. We also found that, while there were few positive markers for proliferation after day 0, we were able to measure the change in average

total cell density over the 14 days through counting DAPI stained nuclei.

In the second experiment (Section 3.2), we applied traction force microscopy in order to measure the contractility of serum-deprived human airway smooth muscle cells when stimulated with a contractile agonist. We also undertook this process with cells incubated in mast cell medium. It was found that basal forces decreased with cell culture time, while histamine-induced contraction increased over time (Section 3.2.5). Furthermore, when cells were exposed to activated mast cell supernatant, this increase in contractile force was even more substantial.

The results from these experiments allowed us to quantify c and p at different time points. These values were then used in a least squares estimate to fit parameters to a simplified version of our ODE model from Chapter 2, such that it matches our experimental systems (Section 3.3). However, since we obtained data for very few time points, we are were unable to get a reliable fit. In the next chapter, therefore, we demonstrate the use of a Bayesian parameter estimation on simulated data, in order to optimise the reliability of further experiments.

4

BAYESIAN PARAMETER ESTIMATION USING MCMC

In Chapter 3, we designed and undertook two novel experiments with the aim of more accurately quantifying phenotype switching rates, the parameters for which the ODE model of Chapter 2 was most sensitive to changes. While we were then able to use a least squares estimate to fit parameters to a simplified version of the ODE model that matches the experimental protocol, having data at only a few time points within our experiment meant that the model was prone to over-fitting. This means that the model could be highly accurate for the specific data collected in the one experiment for which the model was trained; however if the experiment was repeated or new time points were collected, the model would be unlikely to fit the new data points (an over-fit model will not generalise well).

It would, therefore, be useful to have an understanding of the minimum number of repeats and time points needed to obtain a reliable and robust model fit. This would enable us to inform the design of our future experiments in terms of the optimal number of repeats and time points required to ensure model accuracy while still maintaining the logistic feasibility of the experiment. Our Traction Force Microscopy experiment, for example, can easily be adjusted to increase the number of repeats (since there are 96 wells to fill per plate of cells). However, it is more difficult to increase the number of time points, as taking measurements is a time consuming process that puts the cells at further risk with each additional time point. By using

a Bayesian statistical approach, we can obtain distributions for the optimal parameters based on n data points, rather than just point-estimates as in the least squares method. Bayesian methods also differ from the frequentist point-estimate approach in that they allow quantification of uncertainty for a given parameter set rather than fixed quantities.

In this chapter, we first explain the theory behind Bayesian statistics and why it is a useful technique for this purpose (Section 4.1). We go on to detail the reasons behind using an Markov Chain Monte Carlo (MCMC) method and the steps taken to do this (Section 4.2). In Section 4.3, we apply these processes to our simplified model (Equations (3.2) and (3.3)) and explore the impact of increasing the number of experimental time points on the distribution produced. We also modify our method to an adaptive Metropolis-Hastings approach in order to improve the mixing of random parameter guesses and, therefore, increase the speed of convergence. We use our data collected in both the Immunocytochemisty (experiment 1, Section 3.1) and Traction Force Microscopy (experiment 2, Section 3.2) experiments to find the set of parameter values that best represents these observed data. In Section 4.4, we consider both additional experimental time points and repeats in order to find the combination that best fits the data, while considering the practical feasibility of running these experiments. I thank Prof. Gary Mirams (School of Mathematical Sciences, University of Nottingham) for his help with the Bayesian theory in this Chapter.

4.1 THEORY OF BAYESIAN STATISTICS

While ODEs are a common method for modelling biological systems, rate parameters are seldom known or easily measured, hence parameter estimation techniques like Bayesian inference are crucial. Bayesian inference is based on the idea that, when an event occurs, there is usually some prior probability for how this happened and that, after further exploration of the

possibilities, this probability is updated. When we consider both the prior probability distribution and the new information about the probabilities of this event occurring (the data), we can obtain an updated or posterior distribution, which tells us the probabilities for a set of model parameters [44]. As such, for m parameters, we aim to find the region in m dimensional space that gives the highest likelihood of obtaining the data we observed. When this distribution is relatively narrow, the parameters that result in the peak of this posterior distribution are deemed to give the best fit.

Bayes rule [6] for calculating the posterior distribution is given by the following:

$$P(\theta|data) = \frac{P(data|\theta)P(\theta)}{P(data)} \tag{4.1}$$

where θ is some parameter set that is being explored for a model. Here, $P(\theta|data)$ is the posterior distribution, $P(data|\theta)$ is the likelihood, $P(\theta)$ is the prior and $P(data)$ is a normalisation term. Since θ is unknown, the prior distribution is based on this uncertainty before we collect any data. The posterior distribution, which tells us the probability of θ given some observed data, then tells us if a certain set of parameters for a model is a good fit for the data. Since $P(data)$ does not depend on θ, we can consider that

$$P(\theta|data) \propto P(data|\theta)P(\theta). \tag{4.2}$$

We consider $P(data|\theta)$ as the likelihood of observing the given data for varying θ. Note that we use likelihood and not probability, as probability would refer to the possibility of the data varying as opposed to θ varying, which is of interest to us [47, 40].

A common and sensible distribution to consider for the likelihood is a Gaussian distribution $N(\mu, \sigma^2)$ as follows [21, 75]:

$$L = P(data|\mu, \sigma^2) = \left(\frac{1}{\sqrt{2\pi\sigma^2}} e^{-\frac{(data-\mu)^2}{2\sigma^2}}\right)\left(\frac{1}{\sqrt{2\pi\sigma^2}} e^{-\frac{(data-\mu)^2}{2\sigma^2}}\right)... \tag{4.3}$$

$$= \frac{1}{(\sqrt{2\pi\sigma^2})^n} e^{-\frac{1}{2\sigma^2}\sum_{i=1}^{d}(data-\mu)^2}, \tag{4.4}$$

where d is given by the number of experimental time points multiplied by the number of experimental repeats. Given a uniform prior, which is sensible to use without prior knowledge of θ, the posterior probability is proportional to the likelihood.

In a non-Bayesian framework, we could find the maximum likelihood since this tells us the most probable estimate for θ. However, in the Bayesian framework, it is the posterior distribution for the parameters that is of interest. The mean of the posterior distribution tends to the value of the maximum likelihood estimation for large d. The precision is given by the reciprocal of the variance. With large d, the precision of a posterior distribution tends to d/σ^2 [44].

4.2 MARKOV CHAIN MONTE CARLO (MCMC) METHOD

In Section 3.3.1, we used a least squares estimate to fit parameters to a reduced version of our ODE model. We note; however, that this approach is limited due to the small number of data points. In order to use the Bayesian approach, we first need to increase the size of our data set by simulating additional data. We do this by adding noise from a Gaussian distribution (with mean $\mu = 0$ and a standard deviation of σ) to our reduced ODE model (Equations (3.2) and (3.3)). Since we have more than one unknown parameter, it would be extremely difficult to compute the shape of the posterior

distribution analytically. We instead estimate this shape through repeating a process with randomly generated numbers. In applying a Markov Chain Monte Carlo (MCMC) method [52], we follow a memoryless sequence of events given by set probabilities. While for few iterations this process does not provide us with accurate information (particularly if the starting point is far from the area of convergence), over a long time the distribution of parameter choices will converge to an average region with the highest likelihood. Sampling from the posterior distribution in this way, and then using statistics (such as the mean and variance), provides a good representation of the actual distribution.

Algorithm 3 describes the steps that we take to apply the MCMC technique [52, 12] using the additional simulated data. We use a uniform prior such that any positive value of θ is equally likely, since we assume no prior knowledge of these rate parameters. The first 50% of the total number of iterations are considered as "burn in" and are not included as samples of the posterior distribution.

4.3 APPLYING THE MCMC METHOD TO OUR MODEL PARAMETER INFERENCE

We first validate this MCMC method by testing that we see the expected convergence around our chosen parameters, as well as a change in the distribution given an increase in the number of time points. Applying this algorithm to our model governed by Equations (3.2) and (3.3) with $k_{pc} = 0.04$ and $k_p = 0.02$, we obtain the histograms and contour plots seen in Figures 4.1 and 4.2, respectively. Here, we have simulated a single experimental repeat using a given number of time points (n) in order to assess the impact that the number of time points alone has on the distribution of parameter estimates. We see that as n increases, the distribution gets tighter around the values $k_{pc} = 0.04$ and $k_p = 0.02$. In Figure 4.1, we note that this change

Algorithm 3: MCMC method

1. Pick a random set of values for the parameters ($\theta_{current}$).

2. Choose a new set of parameters ($\theta_{candidate}$) by sampling from a Gaussian distribution centered at the previous guess of the parameter value (i.e. $\theta_{current}$).

3. Given that they are positive, $\theta_{candidate}$ has a probability of $a = P(\theta_{candidate}|data)/P(\theta_{current}|data)$ for being chosen as the parameter which gives the better fit.

4. Compare a against b, a generated uniform random number between 0 and 1. If $b > a$ then keep $\theta_{current}$ as it is. If $a \geq b$ then $\theta_{candidate}$ will become the new $\theta_{current}$ (the bigger $P(\theta_{candidate}|data)$, the more probable it is that it will be selected as the better parameter candidate).

5. Repeat for several iterations or until the parameter values converge around their "best fit". We know that convergence has been reached when the trace plots (parameter value against iteration number) look like they are randomly scattered around a single stable value (however the more iterations taken, the more accurate the posterior distribution will be).

in distribution is significant between $n = 2$ and $n = 10$, but that the difference between $n = 10$ and $n = 20$ is small. Considering this, and the fact that this experimental technique is time consuming, we would say that $n = 10$ is a sufficient number of time points in order to get an accurate parameter fit for this 14 day experiment.

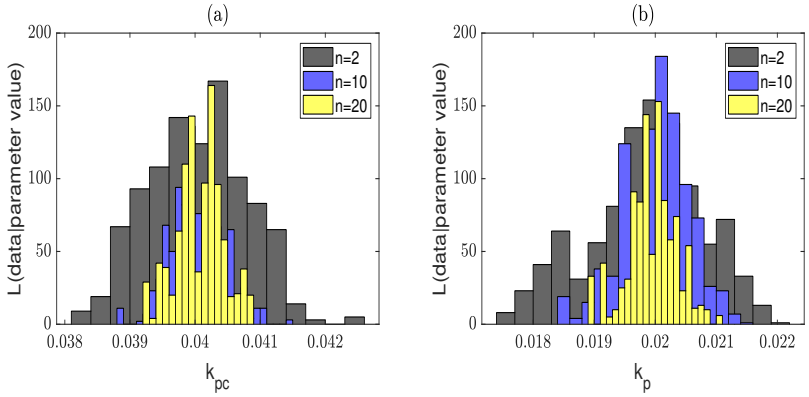

Figure 4.1: Histograms of the posterior distributions generated using the MCMC method for parameter values k_{pc} (a) and k_p (b). These results are based on simulated data from the model given by Equations (3.2) and (3.3) with $k_{pc} = 0.04$, $k_p = 0.02$ and random noise with $\mu = 0$ and $\sigma = 0.001$.

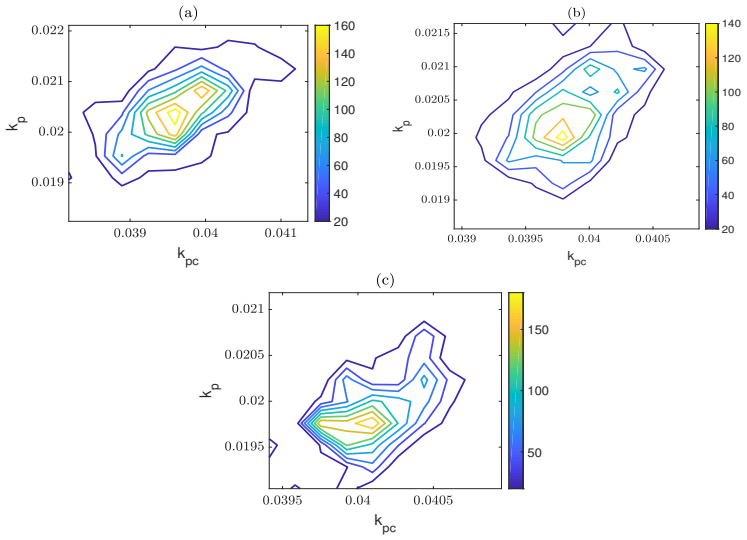

Figure 4.2: Contours showing the likelihood that the model is a good fit to the data given the combination of parameter values for k_{pc} and k_p using the MCMC approach with $n = 5$ (a), $n = 10$ (b) and $n = 20$ (c). These results are based on simulated data from the model given by Equations (3.2) and (3.3) with $k_{pc} = 0.04$, $k_p = 0.02$ and random noise with $\mu = 0$ and $\sigma = 0.001$. The colour bar indicates the likelihood, yellow being very likely and blue being very unlikely.

In addition to our model rate parameters, we are also interested in fitting the value for σ, the standard deviation of our noise for the simulated data. Knowing this would give us an idea about the number of experimental repeats required to give a reliable model fit. We therefore add σ as another parameter within the parameter set θ, so that it is also updated at each iteration of the MCMC process. When simulating this; however (Figure 4.3), the values of σ are not well mixed, meaning it takes a high number of iterations to converge around our chosen σ. This may be because, in this three-dimensional parameter space ($\theta = (k_{pc}, k_p, \sigma)$), there could be more than one local maxima that are not close to the global maximum. In the following, we therefore consider adaptations of MCMC algorithms in order to improve this mixing property.

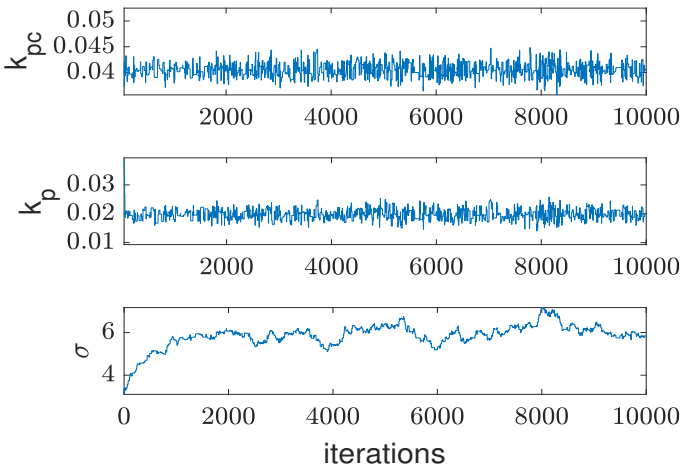

Figure 4.3: Trace plots showing the change in estimated values of k_{pc}, k_p and σ using the MCMC approach over 10000 iterations. These results are based on simulated data from the model given by Equations (3.2) and (3.3) with $k_{pc} = 0.04$, $k_p = 0.02$ and random noise with $\mu = 0$ and $\sigma = 5$. This plot shows that σ is not mixing well.

4.3.1 *Adaptive Covariance MCMC*

An adaptive Metropolis-Hastings algorithm [28] can be used to alter the way in which the candidate values for θ (step 2 in Algorithm 3) are proposed, such that the proposal distribution is skewed according to the percentage of candidate values that have been accepted, and where these values are in the state space. This can therefore give a faster convergence to the distribution around the chosen θ. We first run the algorithm as before for $1000 \times d_p$ iterations, where d_p is our number of parameters (the dimension of θ), in order to do a wider search before narrowing this down. Since good mixing corresponds to the percentage of proposed candidate values for θ that are accepted as the new $\theta_{current}$, the algorithm aims to maintain a "good acceptance rate" by changing the distances of each $\theta_{candidate}$ from $\theta_{current}$ [28, 38].

To implement this, the distribution used to sample our $\theta_{candidate}$ remains Gaussian, but now has an adaptive covariance that takes into consideration the previous values of $\theta_{current}$ through a scaling term based on the proportion of proposed $\theta_{candidate}$ values that have been accepted (as in Algorithm 1 of [38]). For example, if the acceptance rate is too low, the scaling term will shrink the covariance so that the distribution used to choose $\theta_{candidate}$ will be closer to $\theta_{current}$. If the acceptance rate is too high, then the scaling term will enlarge the covariance so that the distribution used to choose $\theta_{candidate}$ will be further away from $\theta_{current}$ [28, 38]. The scaling value is altered in each iteration to maintain an optimal acceptance rate, found by Roberts *et al.* [68] to be 23.4% (Corollary 1.2 in [68]).

The results of applying the adaptive covariance method are shown in Figures 4.4 and 4.5. As seen in the trace plots of Figure 4.4, the values of all parameters k_{pc}, k_p and σ are now well mixed. Since we are using simulated data, we can check that the MCMC is working properly by ensuring that the mean of each parameter from the posterior distributions matches the parameter values used to generate the simulated data. In the case of Figure 4.5, our data is simulated using the values $k_{pc} = 0.04$, $k_p = 0.02$ and $\sigma = 10$. We can see that the algorithm is working well since these numbers are (or are close to) the mean value of their respective distribution. Given a small value for σ in the simulated data and many experimental time points (n large), the distribution once again tightens around the mean of our given parameter values. This is shown in Figure 4.6 for increasing values of n. Given real experimental data, we can use this method to find the variance of the data from the model fit. We can then determine the number of times this experiment should be repeated in order for the model to give a reliable representation (Section 4.4).

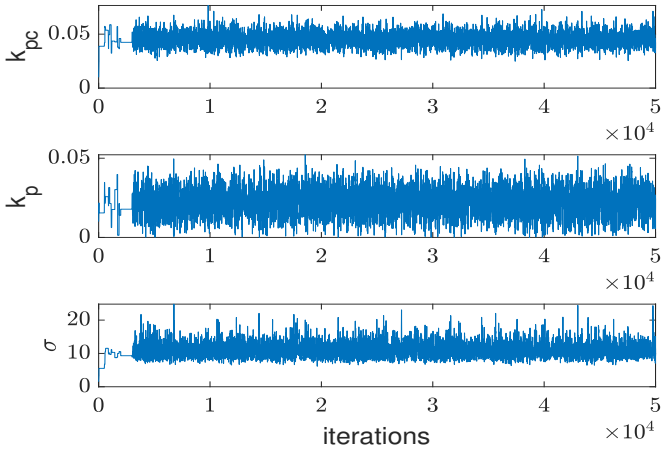

Figure 4.4: Trace plots showing the change in the estimated values of k_{pc}, k_p and σ using an adaptive covariance MCMC approach over 50000 iterations. These results are based on simulated data from the model given by Equations (3.2) and (3.3), with $k_{pc} = 0.04$, $k_p = 0.02$ and random noise with $\mu = 0$ and $\sigma = 10$. This plot shows that all parameters are now mixing well.

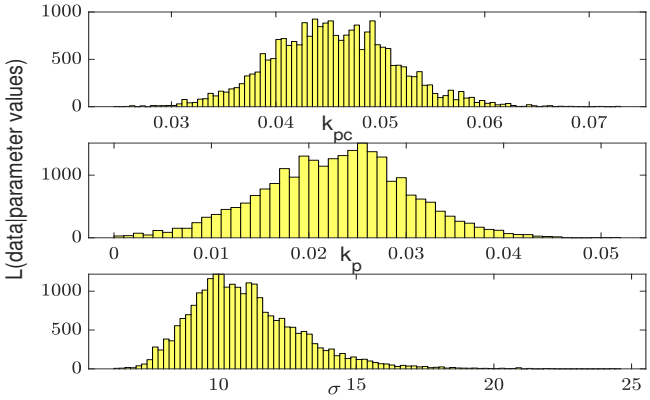

Figure 4.5: Histograms of the posterior distribution for $\theta = (k_{pc}, k_p, \sigma)$ with $n = 10$ using the adaptive covariance MCMC approach. These results are based on simulated data from the model given by Equations (3.2) and (3.3), with $k_{pc} = 0.04$, $k_p = 0.02$ and random noise with $\mu = 0$ and $\sigma = 10$.

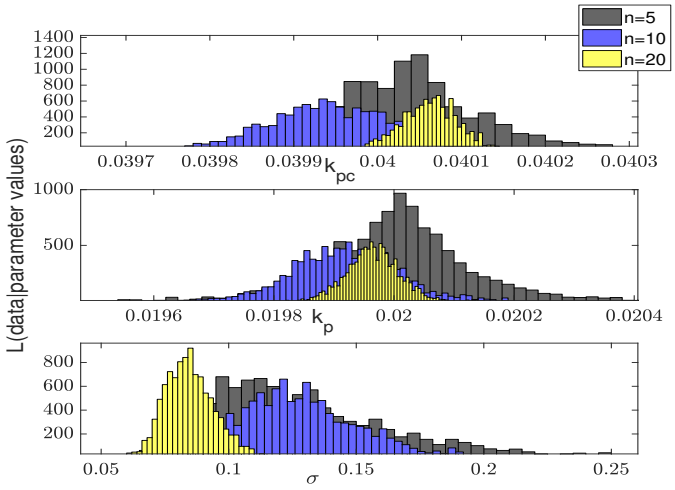

Figure 4.6: Histograms of the posterior distributions for for $\theta = (k_{pc}, k_p, \sigma)$ with $n = 5$ (black), $n = 10$ (blue) and $n = 20$ (yellow) using the adaptive covariance MCMC approach. These results are based on simulated data from the model given by Equations (3.2) and (3.3), with $k_{pc} = 0.04$, $k_p = 0.02$ and random noise with $\mu = 0$ and $\sigma = 0.1$.

4.3.2 *Using our Experimental Data*

Having validated the MCMC method with an adaptive covariance, we now use it to find the optimal parameter values (including the variance σ) of our own experimental data (for both experiment 1 and 2). A summary of these results, which are discussed separately below, is given in Table 3.

θ	Posterior Distribution Mean for Exp 1	Posterior Distribution Mean for Exp 2
k_{pc}	0.0497	0.0768
k_p	0.0267	0.023
σ	17.4105	0.2294

Table 3: Summary of parameter values obtained using Bayesian parameter estimations in Section 4.3.2.

Data from Experiment 1

Results of applying this method with the data obtained in experiment 1 are shown in Figure 4.7 with the mean value of each of these distributions given as $k_{pc} = 0.0497$, $k_p = 0.0267$ and $\sigma = 17.4105$. Using these three values to now simulate more realistic time points, we obtain the posterior distributions shown in Figure 4.8 for varying n. As before, the distribution tightens around the most accurate parameter value as n increases. Although $n = 10$, once again, gives an accurate enough distribution mean for k_{pc} and k_p, the mean for the σ distribution remains large until $n = 50$.

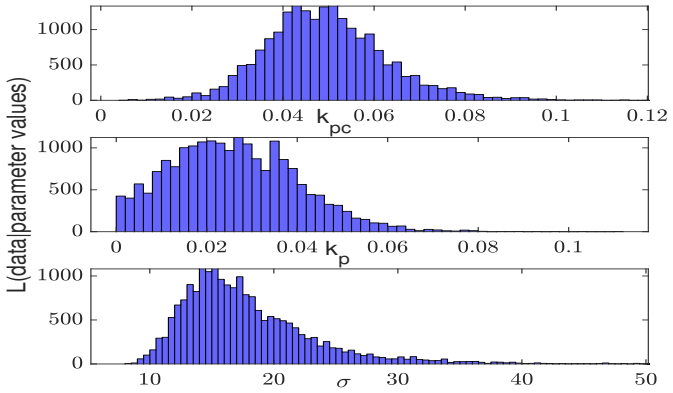

Figure 4.7: Histograms of the posterior distributions for $\theta = (k_{pc}, k_p, \sigma)$ with $n = 5$ using the adaptive covariance MCMC approach. These results are based on the model given by Equations (3.2) and (3.3) with our data set obtained in experiment 1 and shown in Figure 3.4.

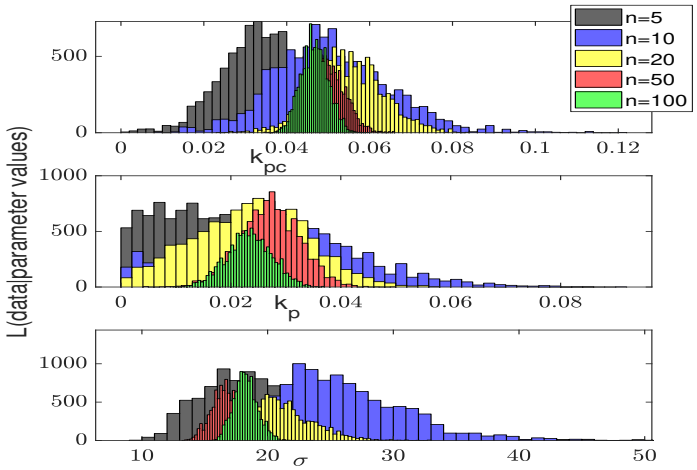

Figure 4.8: Histograms of the posterior distributions for for $\theta = (k_{pc}, k_p, \sigma)$ with $n = 5$, $n = 10$, $n = 20$, $n = 50$ and $n = 100$ using the adaptive covariance MCMC approach. These results are based on simulations using the model given by Equations (3.2) and (3.3) with the parameters given as the mean of the distributions shown in Figure 4.7 ($k_{pc} = 0.0497$, $k_p = 0.0267$ and $\sigma = 17.4105$).

Data from Experiment 2

Using this method with the data obtained in experiment 2 (without any mast cell supernatant), gives the results shown in Figure 4.9 with $k_{pc} = 0.0768$, $k_p = 0.023$ and $\sigma = 0.2294$ as the mean of each posterior distribution. Once again, using these values to simulate more data, we can see the impact of increasing the number of time points n in Figure 4.10. In this case, $n = 20$ gives a significantly more accurate value for k_p compared to when $n = 10$.

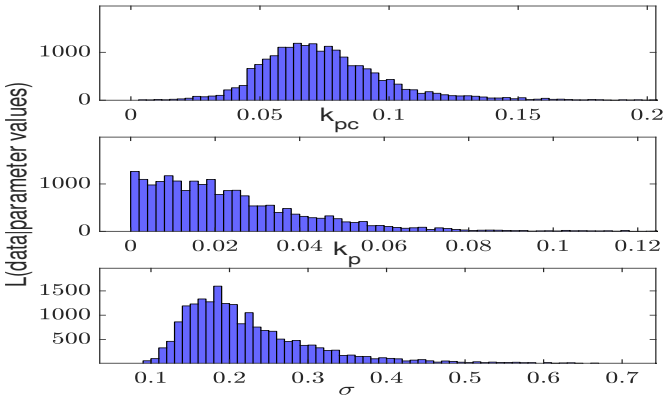

Figure 4.9: Histograms of the posterior distributions for $\theta = (k_{pc}, k_p, \sigma)$ with $n = 4$ using the adaptive covariance MCMC approach. These results are based on the model given by Equations (3.2) and (3.3) with our data set obtained in experiment 2 and shown in Figure 3.6.

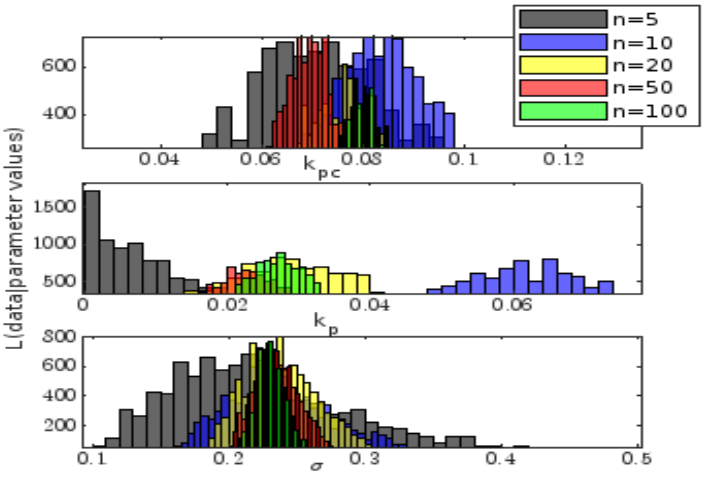

Figure 4.10: Histograms of the posterior distributions for $\theta = (k_{pc}, k_p, \sigma)$ with $n = 4$, $n = 10$, $n = 20$, $n = 50$ and $n = 100$ using the adaptive covariance MCMC approach. These results are based on simulations using the model given by Equations (3.2) and (3.3) with the parameters given as the mean of the distributions shown in Figure 4.9 ($k_{pc} = 0.0768$, $k_p = 0.023$ and $\sigma = 0.2294$).

4.4 OPTIMAL COMBINATION OF EXPERIMENTAL TIME POINTS AND REPEATS

In Section 4.3, we saw that increasing the number of time points to 10 or 20 significantly improves the model fit. However, given that this may be logistically infeasible, potential improvements could be made through increasing the number of experimental repeats either instead of, or in addition to, increasing the number of time points. Repeats are essential when conducting experiments in order to ensure reproducibility of results. We follow the same method as in Section 4.3.2; however, this time the data is simulated j times for each value of n (so that $j \times n = d$ the total number of data points). In addition to this, we repeat the whole process of simulating this single experiment given each combination of time points and repeats, 10 times. We

average the resulting statistics in order to learn about the average experimental run under each combination.

We first demonstrate how the histogram of the posterior distribution tightens around the true parameter value as the number of repeats is increased from 1 (a), to 10 (b), for $\sigma = 0.1$ (Figure 4.11), $\sigma = 1$ (Figure 4.12) and $\sigma = 10$ (Figure 4.13). With an increase in σ, we see that there is an increase in the variability around the true parameters and that the resultant statistics lose accuracy. As previously seen (Section 4.3.2), these figures also show the decrease in distribution width with an increase in the number of time points taken; this is illustrated through the different coloured histograms from blue (3 time points) through to yellow (10 time points).

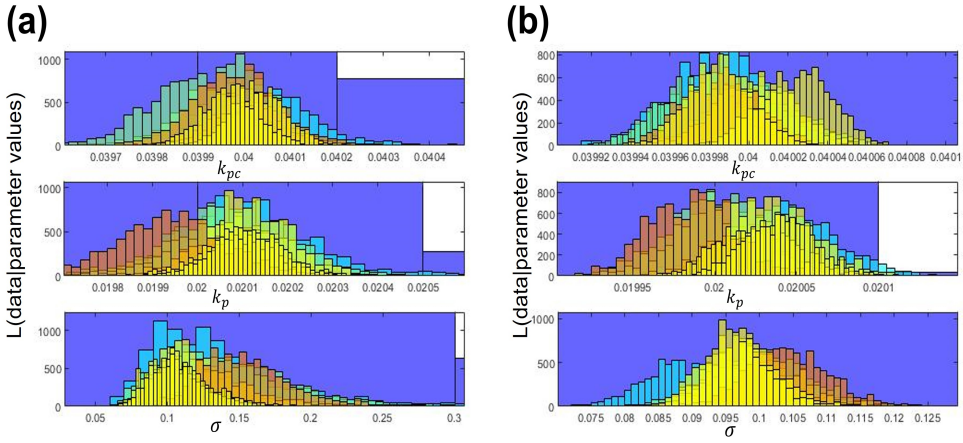

Figure 4.11: Histograms for the posterior distributions of $\theta = (k_{pc}, k_p, \sigma)$ where true values are given by $k_{pc} = 0.04$, $k_p = 0.02$ and $\sigma = 0.1$ with 1 repeat (a) and 10 repeats (b). Histograms of different colours were simulated given different numbers of time points, where the back most (blue) histogram was made with 3 time points and each of the histograms in front of this were made using 1 extra time point per colour, the front most (yellow) histogram using 10 time points.

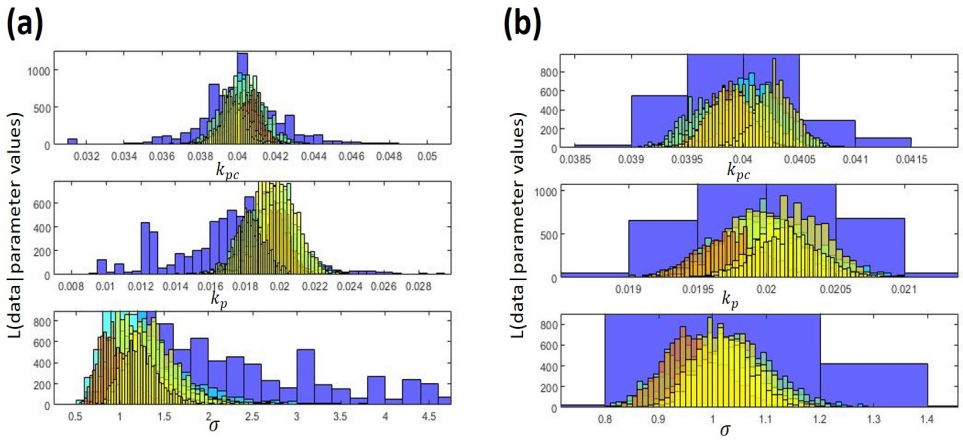

Figure 4.12: Histograms for the posterior distributions of $\theta = (k_{pc}, k_p, \sigma)$ where true inputted values are given by $k_{pc} = 0.04$, $k_p = 0.02$ and $\sigma = 1$ with 1 repeat (a) and 10 repeats (b). Histograms of different colours were simulated given different numbers of time points, where the back most (blue) histogram was made with 3 time points and each of the histograms in front of this were made using 1 extra time point per colour, the front most (yellow) histogram using 10 time points.

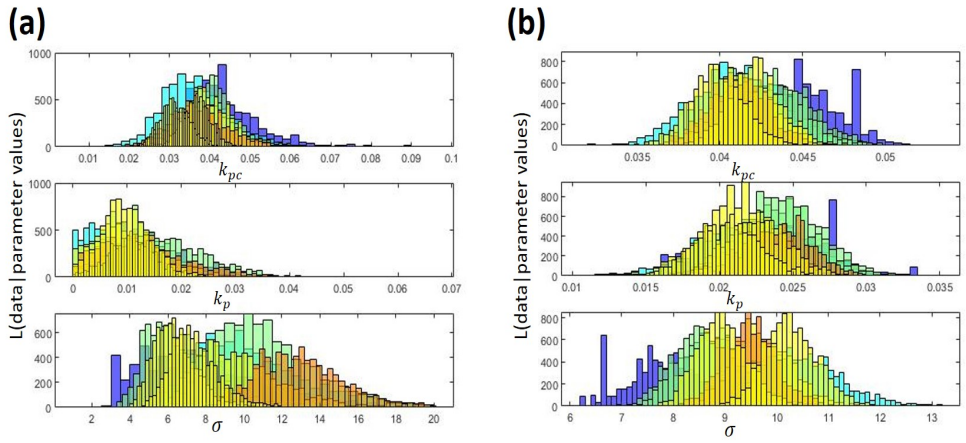

Figure 4.13: Histograms for the posterior distributions of $\theta = (k_{pc}, k_p, \sigma)$ where true inputted values are given by $k_{pc} = 0.04$, $k_p = 0.02$ and $\sigma = 10$ with 1 repeat (a) and 10 repeats (b). Histograms of different colours were simulated given different numbers of time points, where the back most (blue) histogram was made with 3 time points and each of the histograms in front of this were made using 1 extra time point per colour, the front most (yellow) histogram using 10 time points.

Figure 4.14 shows the difference between a simulation of the variable c with the parameters including σ given by the results of the Bayesian inference (blue) compared to their true values (red), with 3 time points and 1 repeat (a) and with 10 time points and 10 repeats (b). Here $\sigma = 15$ for the purpose of visualising the difference (σ needs to be fairly large to see this by eye). As seen, the simulation using the parameters obtained from the inference is more similar to the simulation using the true values when a higher number of both time points and repeats are used. Decreasing **either** the number of repeats or time points decreases this accuracy, however this is difficult to see by eye.

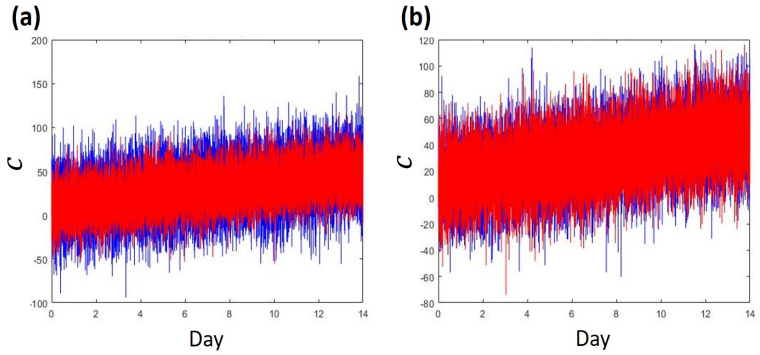

Figure 4.14: Simulated data from the model given by Equations (3.2) and (3.3) with random noise using true parameter values with $\sigma = 15$ (red) and parameters given through the inference (blue) with 3 time points and 1 repeat (a) compared to 10 time points and 10 repeats (b).

Finally, we show heat maps for the size of the IQR and the variance of the posterior distributions, given each combination of number of repeats and time points. Figure 4.15 shows the aforementioned statistics for the parameters k_p and k_{pc}, while Figure 4.16 shows the results for the inferred values of σ. Within each of these figures, we display results for $\sigma = 0.1$ (a and c) and $\sigma = 10$ (b and d). As expected, each of these figures show a gradual decrease in IQR/variance diagonally across the heat map from the highest IQR/variance when we have the smallest number of time points and repeats, to the lowest for the largest number of time points and repeats. We can also see that increasing the number of repeats improves the accuracy of the inferred distribution more quickly than by increasing the number of time points. Figure 4.15 (a and b), showing the IQR of parameter values k_p and k_{pc}, illustrates that for a small number of repeats (i.e. one or two), increasing the number of time points only improves the accuracy of the inference until a certain point (i.e even for a large number of time points, the IQR is still high).

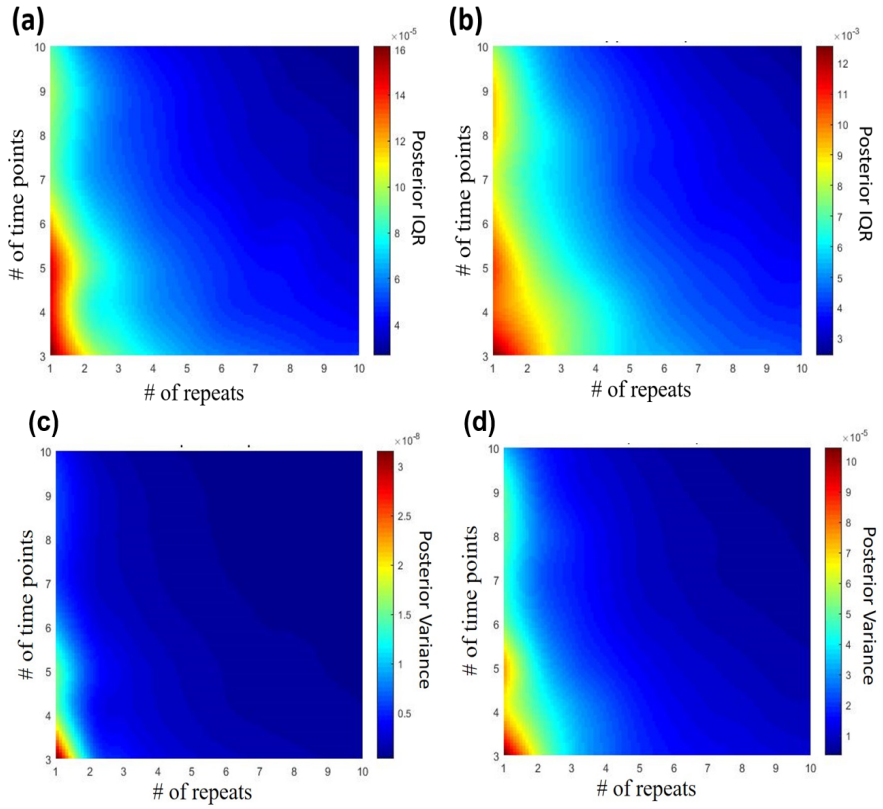

Figure 4.15: Heat maps showing the change in the IQR of the posterior distributions for parameters k_p and k_{pc} with $\sigma = 0.1$ (a) and $\sigma = 10$ (b) and the change in the variance of the posterior with $\sigma = 0.1$ (c) and $\sigma = 10$ (d), given different combinations of the number of experimental time points and experimental repeats.

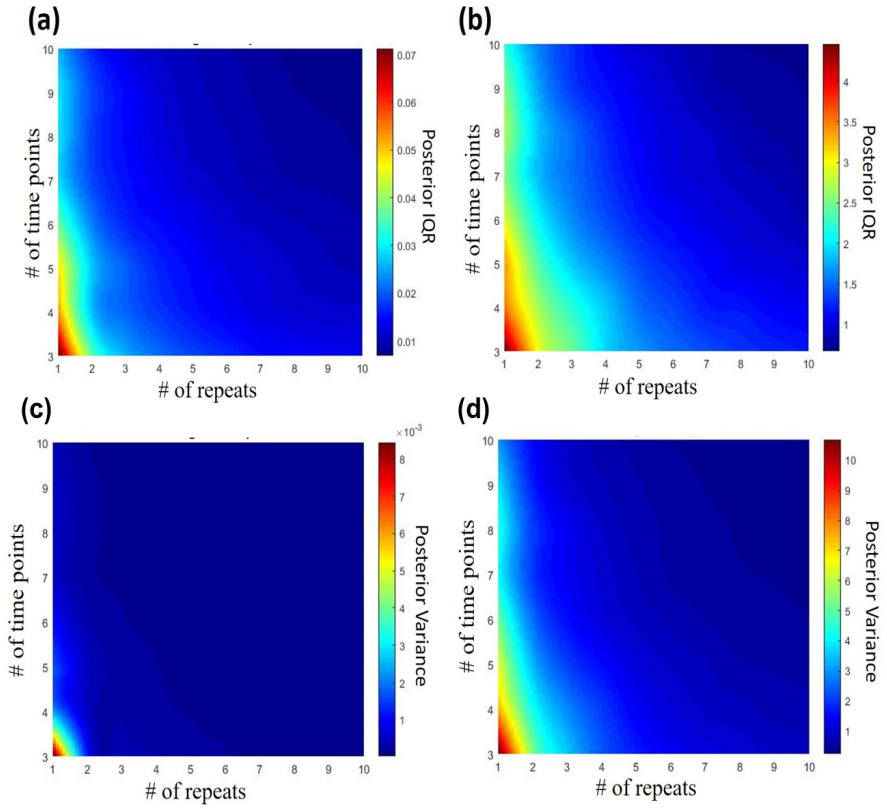

Figure 4.16: Heat maps showing the change in the IQR of the posterior distribution for σ with $\sigma = 0.1$ (a) and $\sigma = 10$ (b) and the change in the variance of the posterior with $\sigma = 0.1$ (c) and $\sigma = 10$ (d), given different combinations of the number of experimental time points and experimental repeats.

Furthermore, the analysis completed in this section can be used to decide on an optimal combination of experimental time points and experimental repeats to get a good model fit, and hence improve future experimental design. Although a large number of time points and repeats are always preferable (i.e. 10 time points and 10 repeats), this isn't always feasible for experimental protocols. In particular, collecting data at many time points can be very time consuming, and in the case of the TFM protocol, each extra time point puts the cells more at risk of infection. Instead, we can see that a reasonable accuracy can still be realised by collecting data at, for example, 5 time points but with 10 repeats (since a 96 well plate leaves room for many repeats).

4.5 SUMMARY

In fitting parameters to a reduced version of our ODE model using our own experimental data (Chapter 3), we find that we do not have enough experimental time points for a reliable fit, as it is likely that we would over-fit to the few data points we have. In this chapter, therefore, we use a Bayesian statistical approach to obtain distributions for the optimal parameter based on n data points. We generate synthetic data using our model equations, then use a Markov Chain Monte Carlo (MCMC) method to assess the impact of the number of experimental time points on the distribution of parameter estimates. When simulating this in a three-dimensional parameter space ($\theta = (k_{pc}, k_p, \sigma)$), however, we obtain poor mixing. To decrease the number of iterations before convergence, we improve this mixing property using an adaptive Metropolis-Hastings algorithm [28].

Having tested this method, we first use it to find the optimal parameter values for the data obtained in both experiment 1 and 2 (Table 3). In doing this, we also show that the posterior distributions tighten around the true

parameter value as the number of time points increases. When exploring the impact of changing the number of repeats, we find that a larger σ gives a higher variability in the distributions around the true parameter. Finally, we investigate the accuracy of posterior distributions given different combinations of time points and repeats. We show that increasing the number of repeats improves the accuracy of the inferred distribution more quickly than by increasing the number of time points. These results can be used to optimise experimental protocols so that the resultant data can be used to more accurately inform mathematical models.

5

CELL VERTEX MODEL: DEVELOPMENT AND TESTING

Our previous chapters concentrated on the temporal changes that occur during airway remodelling, with a focus on the function of ASM cells and the impact of an altered ECM. This involved conducting novel time course experiments *in vitro* using human ASM cells (Chapter 3), the results of which allowed us to quantify rate parameters in our ODE model (Chapter 2). The experimental results presented in Chapter 3 showed that, as the cells switch to a contractile phenotype, there is a change in the alignment of actin filaments (Figure 5.1) as well as an increase in the contractile force produced in response to an agonist (Figure 5.2). We used these data to fit parameters to the ODE model by inferring the spatially-averaged proportion of each cell phenotype over time. Bayesian analysis of a reduced version of the model then allowed us to determine the optimal number of experimental time points and repeats for future experiments (Chapter 4). The experiments undertaken using TFM (Section 3.2), however, also provided spatial-temporal data for the corresponding contractile forces involved.

In the current chapter, therefore, we extend our modelling of ASM to consider spatio-temporal aspects. In particular, we develop a biomechanical vertex-based model of the ASM monolayer in which cells are represented by a network of damped linear springs. We assume that cell shape changes are a result of local forces produced by cell-cell interaction and elasticity as well as phenotype switching and active contraction. This new model allows

us to simulate the TFM protocol (Section 3.2), with the corresponding ASM phenotype switching over the period of serum deprivation, as well as the response to a time-dependent addition of contractile agonist. Using this, we explore how the changes in cell shape and circularity align with the principle axis of stress, the impact this has on the force exerted by cells during ASM cell contraction and the resultant tissue-level properties that emerge from these processes.

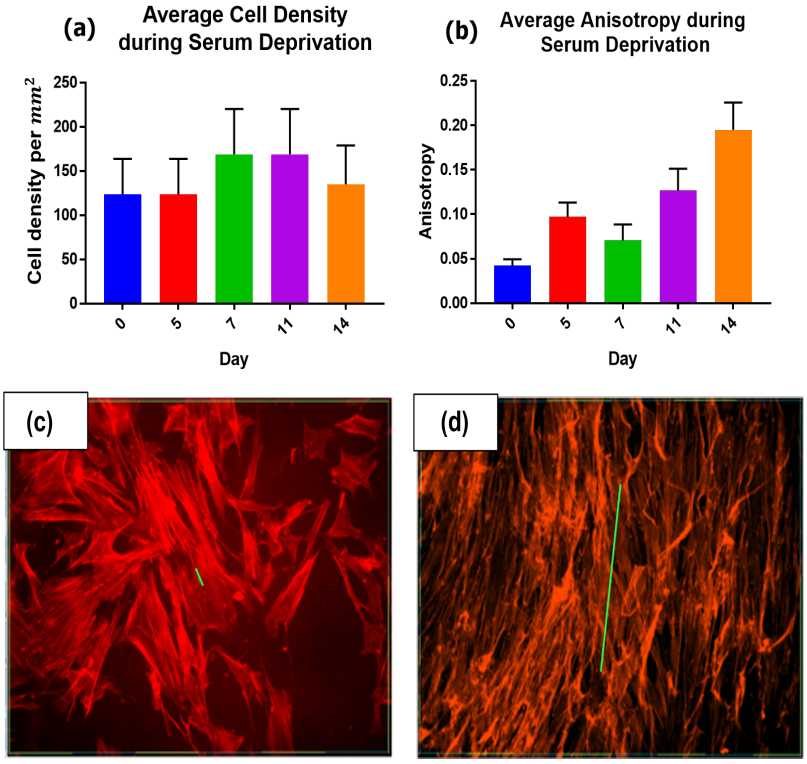

Figure 5.1: Reminder of the main results from experiment 1 using immunocytochemistry (presented in Section 3.1.5). Bar graphs showing (a) the change in average cell density over time using the nuclei stain counts (p-value of 0.9007) and (b) the change in anisotropy of cell fibres over time using the phalloidin stained images (p-value of < 0.0001). Phalloidin stained images (c) before and (d) after serum deprivation, where the length of the green line is proportional to the size of the anisotropy score.

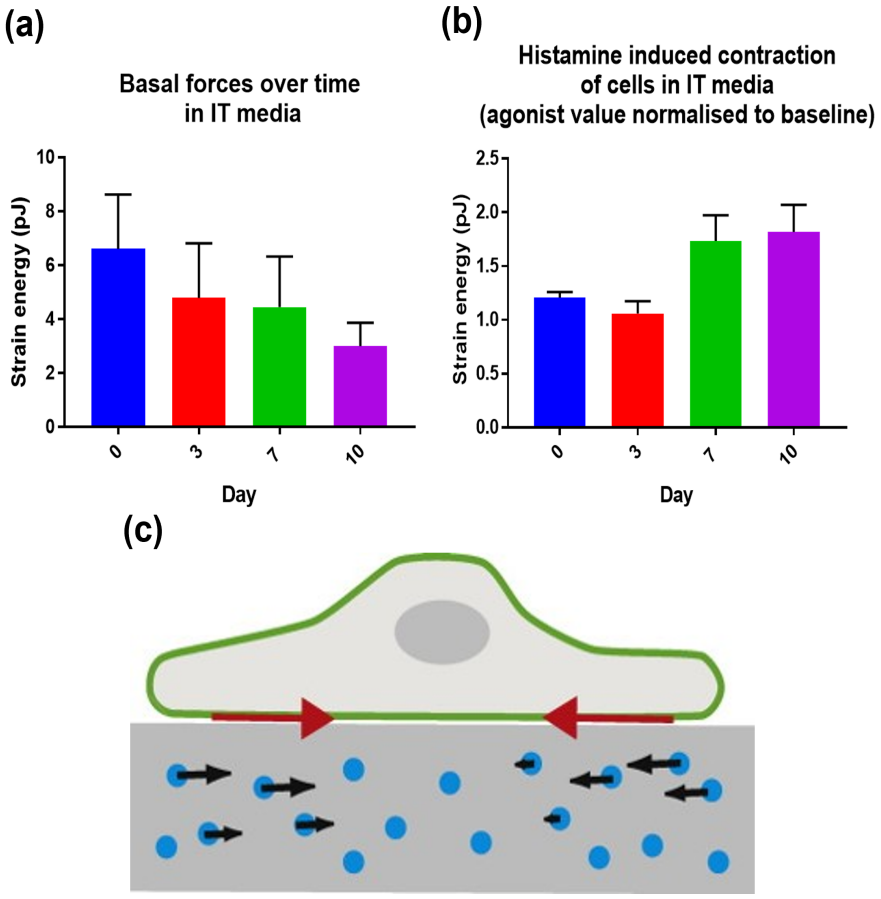

Figure 5.2: Reminder of the main results from experiment 2 using traction force microscopy (presented in Section 3.2.5). Bar graphs showing (a) changes in cell basal forces over time (p-value of 0.5403) and (b) changes in histamine induced contractile forces over time (p-value of 0.0111), both in serum deprived IT media. (c) shows a schematic representation of the TFM theory [71], where a cell contracts and displaces beads in the gel.

In this chapter we develop and test this new vertex-based model and briefly discuss its suitability for modelling ASM monolayers, such as those in our TFM experimental protocol. We start by introducing the lattice-free model set up used to represent the cell layer in each well of the TFM plate. We focus on lattice free models since we want to model continuous changes in the monolayer structure and we introduce vertex-model transitions to ensure the network remains biologically reasonable throughout the simulation. We evolve this network of cells such that the total energy in the system is continually being minimised. We then incorporate the different cellular phenotypes through differences in both cell shape and contractile ability (Section 5.1). In Section 5.2, we describe the implementation of this model in Matlab. We then analyse the simulated model mechanics at both the cellular and tissue level. To illustrate the impact that a contractile phenotype has on the local forces and dynamics within an ASM cell population, we first test a population with a small number of contractile cells and no switching (Section 5.3).

5.1 MODELLING APPROACH

In this section, we will describe: the basic set-up of our vertex-based cell model, the incorporation of an energy minimisation across the cellular network, the addition of phenotypic characteristics, and the measures we use to test and analyse simulated results.

As described in Section 1.5.2, an off-lattice framework is more biologically realistic than a lattice based model, since cell motion is not limited to the discrete spatial positions defined by a lattice. In an active network or cell-based model, cells can be represented by convex polygons (since concave polygons are less biologically realistic and lead to self intersecting cells with overlapping edges), where neighbouring cells share edges. We build our network of polygons from a set of randomly assigned generator points using a Voronoi

tessellation, described in detail in Section 1.5.2. This formulation is used widely in the literature for vertex-based cell models [5, 8, 46]. These models usually represent a confluent cell monolayer where there are no spaces between cells, as in our experimental protocol. By representing cell edges as damped linear springs and incorporating contractile machinery for cells of the associated phenotype, we are able to use this model framework to simulate the mechanics of ASM cell populations.

5.1.1 *Simple Vertex Model*

When time-stepping cell-centred models, one needs to re-define network edges between every time step (as discussed in 1.5.2). To avoid this and instead involve junctional mechanics within the cell layer, we choose to develop a vertex-based cell model. We therefore consider the balance of forces at each cell vertex using the Voronoi cell edges as our set of linear springs. We then have a network of N vertices joined by straight edges where cells that are neighbours share an edge.

A vertex-based approach allows gradual and continuous changes in cell shape as a direct result of the forces from neighbouring cells. In using this method, the cells remain connected in the same way (no re-meshing occurs) and so do not change their polygonal class unless a change is actively implemented under certain conditions. This represents a more biologically realistic monolayer compared to the cell-centred model, since tracking vertices and edges (rather than just cell centres) allows for the implementation of the effects of active forces at cell-cell junctions [5].

Following Nestor-Bergmann *et al.* [58], we describe the vertex-based cell network as follows: A cell α has Z_α vertices, a perimeter L_α, an area of A_α, an anticlockwise tangent $\mathbf{t}_\alpha^i$ from vertex i and a corresponding unit outward

normal $\mathbf{n}_\alpha^i$ as shown in Figure 5.3. Cell centre and vertex locations are denoted $\mathbf{R}_\alpha$ and $\mathbf{R}_\alpha^i$ respectively. The force generated by cell α on vertex i is denoted $\mathbf{f}_\alpha^i$ and the net force on each vertex $\mathbf{F}^i$ is given by the sum of the forces generated from the three cells surrounding that vertex.

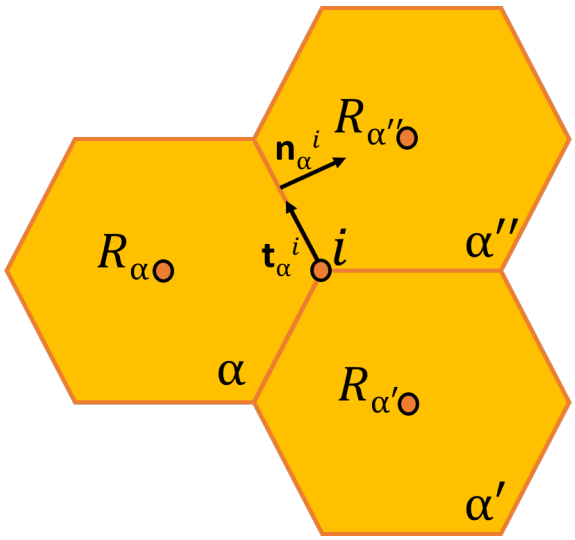

Figure 5.3: Representation of the geometry of the three cells, α, α' and α'', which surround vertex i. Their cell centres are denoted $\mathbf{R}_\alpha$, $\mathbf{R}_{\alpha'}$ and $\mathbf{R}_{\alpha''}$ Vertex i of cell α has an anticlockwise tangent given by $\mathbf{t}_\alpha^i$ and outward normal of $\mathbf{n}_\alpha^i$.

The majority of vertex-based models in the literature are used for epithelial cell monolayers, which are commonly represented by densely packed hexagonal cells for animal tissues, since this is the shape that is most often observed in microscopy [18, 23, 26]. While there is no specific evidence for this in ASM monolayers, hexagons still provide a reasonable approximation to confluent cells in general and so we adopt this strategy.

To represent intracellular structures and contractile machinery, we additionally incorporate internal springs for each cell in our model set up. These internal springs connect all cell centres with each of their vertices.

5.1.2 *Transitions*

Certain operations or transitions are widely used in the literature of vertex models in order to allow the evolution of a system while maintaining a monolayer of non-intersecting cells, each with the realistic polygonal shape. We chose to incorporate a so-called T1 transition for these reasons.

A T1 transition occurs if any cell edge becomes smaller than some d_{min} in length. This operation rearranges edges when two vertices are too close to each other (given a minimum threshold distance). The vertices are moved to be a length of $d_{sep} = k_{sep} d_{min}$ apart, where k_{sep} is a separation ratio and d_{min} and d_{sep} are the distances between the vertices before and after being separated respectively. A change in connectivity also occurs as seen in Figure 5.4. Out of the four cells involved, the two that originally contained both of the vertices in question lose one of them each and so their polygonal class decreases by one, while the other two cells involved gain these vertices. The T1 swaps ensure that vertices are always contained in exactly three cells when not on the boundary of the confluent cell layer, and that all cells keep their convex polygonal shape rather than self intersecting [24].

For some parameter regimes, transition problems arise such as repeated T1 flipping loops (where a transition keeps occurring back and forth for the same two small edges). To prevent this from happening, the separation edge is increased in length on each successive transition of that edge.

5.1.3 *Energy Minimisation*

Our cellular monolayer simulation without forcing (i.e. through an exacerbation as later discussed in Chapter 7) is essentially an optimization problem in that the network of springs is constantly aiming for the arrangement

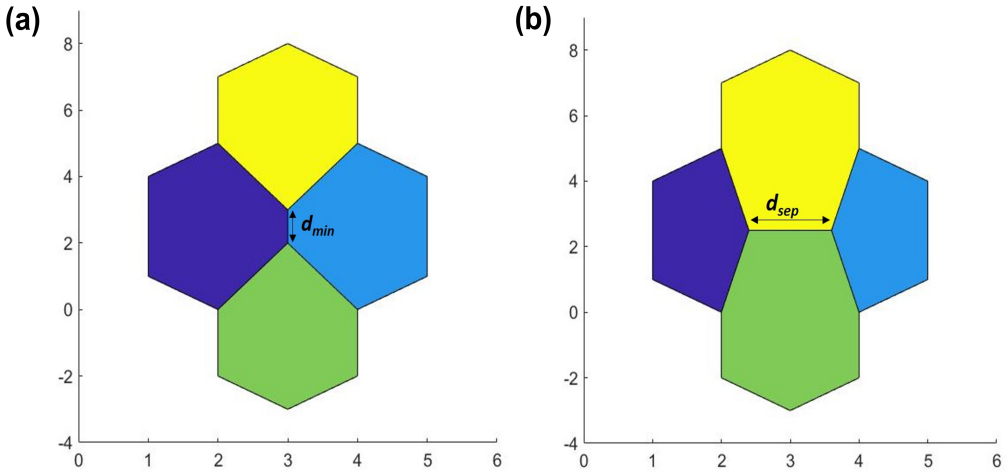

Figure 5.4: Four simulated cells undergoing a T1 Transition from (a) to (b).

with the lowest energy (its equilibrium position). In our case, this would be the formulation with all cells at their resting perimeter length $\tilde{L}_0$, internal spring lengths and area size $\tilde{A}_0$ (values are chosen such that this is possible). Since the cells are connected, however, and exert forces on one another when they move, this theoretical equilibrium may not be attainable. It is likely, therefore, that the system will evolve towards the theoretical equilibrium, but never reach it (as would occur in a biological monolayer).

The force of each spring is calculated using Hooke's law. In its most simple form, this is

$$F = -Kx, \tag{5.1}$$

where F is the magnitude of the force, K is the spring constant and x is the extension. The elastic potential energy stored in the spring can then be calculated as the area under the force-extension curve as

$$E = -\int_0^x F\,dx = \frac{1}{2}Kx^2. \tag{5.2}$$

For our system, we consider the resting quantities for both cellular area and perimeter and so the energy for each cell α is found as follows

$$\tilde{E}_\alpha = \frac{1}{2}\tilde{K}(\tilde{A}_\alpha - \tilde{A}_0)^2 + \frac{1}{2}\tilde{\Gamma}(\tilde{L}_\alpha - \tilde{L}_0)^2. \tag{5.3}$$

where $\tilde{K}$ is a constant for cell stiffness, $\tilde{\Gamma}$ is a perimeter spring constant for contractility and tildes denote dimensional variables.

Time Dependent Method

When using the `fminsearch` function in Matlab to implement this energy minimisation (discussed in Section 1.5.2), cells often end up overlapping. In order to prevent this from happening, we instead minimise the energy gradually using the time dependent method for evolving systems used by Nestor-Bergmann *et al.* in [58]. Here, they consider the resting perimeter of each cell L_0 to be governed by parameters $\tilde{\Gamma}$ and $\tilde{\Lambda}$, which tune the contractile strength and effective preferred cell perimeter respectively. Using $\tilde{L_0} = -\tilde{\Lambda}/2\tilde{\Gamma}$, Equation (5.3) therefore becomes

$$\tilde{E_\alpha} = \frac{1}{2}\tilde{K}(\tilde{A}_\alpha - \tilde{A}_0)^2 + \frac{1}{2}\tilde{\Gamma}\tilde{L}_\alpha^2 + \frac{1}{2}\tilde{\Lambda}\tilde{L}_\alpha + \frac{\tilde{\Lambda}^2}{8\tilde{\Gamma}}, \tag{5.4}$$

where $\tilde{K}$ remains the cell stiffness and tildes denote dimensional variables. This equation includes contributions from the bulk compressibility of the cell (given a resting area $\tilde{A}_0$) as well as cytoskeletal contractility. We non dimensionalise through scaling lengths with $\sqrt{\tilde{A}_0}$ using

$$\tilde{A}_\alpha = \tilde{A}_0 A_\alpha,\ \tilde{L}_\alpha = \sqrt{\tilde{A}_0} L_\alpha,\ \tilde{E} = \tilde{K}\tilde{A}_0 E \tag{5.5}$$

to obtain

$$E_\alpha = \frac{1}{2}K(A_\alpha - 1)^2 + \frac{1}{2}\Gamma L_\alpha^2 + \frac{1}{2}\Lambda L_\alpha + \Omega, \tag{5.6}$$

where

$$\Gamma = \frac{\tilde{\Gamma}}{\tilde{K}\tilde{A}_0},\ \Lambda = \frac{\tilde{\Lambda}}{\tilde{K}\tilde{A}_0^{\frac{3}{2}}},\ \Omega = \frac{\tilde{\Lambda}^2}{8\tilde{K}\tilde{\Gamma}\tilde{A}_0^2}. \tag{5.7}$$

Differentiating the vectorised version of Equation (5.2), we obtain $\mathbf{F} = -\nabla E$. We therefore take the gradient of Equation (5.6) term by term (as fully derived in Equations (3.8 – 3.11) of [58]) to obtain the force for cell α at vertex i as

$$\mathbf{f}_\alpha{}^i = T_\alpha \mathbf{q}_\alpha{}^i - P_\alpha \mathbf{p}_\alpha{}^i, \tag{5.8}$$

where $T_\alpha = \Gamma(L_\alpha - L_0)$ and $P_\alpha = A_\alpha - 1$ are the respective cell tension and pressure, and $\mathbf{q}_\alpha^i$ and $\mathbf{p}_\alpha^i$ are the respective cell inward and bulk compression force directions.

We now need to consider the contributions to this force from both cell edges and internal springs of all three cells surrounding each vertex in our monolayer (not just α). The resulting force $\mathbf{f}^j$ is the sum of each of these contributions

$$\begin{aligned}\mathbf{f}^j = {} & \mathbf{t}(T_\alpha + T_{\alpha''}) + \mathbf{t}'(T_{\alpha'} + T_\alpha) + \mathbf{t}''(T_{\alpha''} + T_{\alpha'}) \\ & + \bar{\mathbf{t}}(\overline{T}_\alpha + \overline{T}_{\alpha''}) + \bar{\mathbf{t}}'(\overline{T}_{\alpha'} + \overline{T}_\alpha) + \bar{\mathbf{t}}''(\overline{T}_{\alpha''} + \overline{T}_{\alpha'}) \\ & + \frac{1}{2}[\mathbf{n}(P_\alpha - P_{\alpha''}) + \mathbf{n}'(P_{\alpha'} - P_\alpha) + \mathbf{n}''(P_{\alpha''} - P_{\alpha'})],\end{aligned} \tag{5.9}$$

where $\mathbf{t}$ and $\mathbf{n}$ are the anticlockwise tangent and outward normal for each cell (as seen in Figure 5.3) and overlined measures represent those contributions from internal springs. The factor of $\frac{1}{2}$ occurs since the force due to pressure is split between the two vertices sharing each edge.

Finally, we know that the net force at each vertex $\mathbf{F}^j$ is made up of $\mathbf{f}^j$ minus the drag force on the displacement of that vertex (given as a function of area compared to polygonal class for each of the three surrounding cells) as follows

$$\mathbf{F}^j = \mathbf{f}^j - \left(\frac{A_\alpha}{Z_\alpha} + \frac{A_{\alpha'}}{Z_{\alpha'}} + \frac{A_{\alpha''}}{Z_{\alpha''}}\right)\dot{\mathbf{R}}^j, \tag{5.10}$$

where $\dot{\mathbf{R}}^j$ is the change in position of vertex j over time. Since the system evolves through balancing forces to reduce the energy, $\mathbf{F} = 0$ at equilibrium and so each iteration of the vertex position $\mathbf{R}_{t+1}^j$ is determined using

$$\mathbf{R}_{t+1}^j = \mathbf{R}_t^j + h\frac{\mathbf{f}^j}{\left(\frac{A_\alpha}{Z_\alpha} + \frac{A_{\alpha'}}{Z_{\alpha'}} + \frac{A_{\alpha''}}{Z_{\alpha''}}\right)}, \tag{5.11}$$

for some small time step h [58].

5.1.4 *Cell Phenotypes*

As in the ODE model of Chapter 2, we account for differences in the cell function and (in this case) cell shape, via the cell phenotype.

Cell Shapes

We saw in Chapter 1, and again in the immunocytochemistry experiment of Chapter 3, that ASM cell phenotypes have different morphologies. As described in Chapter 1, when ASM cells are cultured for experimental use, the addition of serum in the growth medium drives them to a proliferative phenotype, recognised by their less elongated, broader and flatter morphology [16, 32]. Contractile ASM cells, in contrast, are elongated and spindle-shaped, with a parallel alignment of actin filaments [16] (as shown in Figure 5.1) when the cells are in situ. We incorporate this elongation in our model by changing the resting lengths of internal springs based on the cellular phenotype. In a proliferative cell type, we set the resting lengths of these internal springs to be equal; however, under a switch to a contractile phenotype, the resting lengths of the internal springs in one randomly decided orientation are extended and the resting lengths for the remaining internal springs of that cell are reduced. Consequently, the resting areas of contractile cells are also different to proliferative cells, based on the calculation of area when considering a cell with resting edge lengths and resting internal spring lengths as just described. Figure 5.5 illustrates the impact that this would have on the cell shape.

Contractile Machinery

Contractile cells contain both actin and myosin contractile proteins. Phosphorylation of myosin allows myosin heads to attach to actin, enabling the sliding motion of these filaments causing the cells to shorten, and thus generate muscle contraction (see Chapter 1). We use an adaptation of the Hill model [34], one of the earliest and simplest muscle modelling approaches,

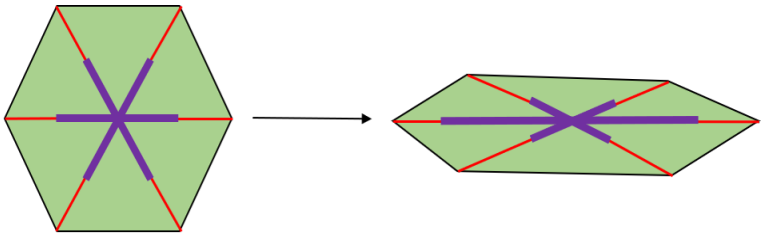

Figure 5.5: Diagram showing the way that different phenotypes are modelled in the vertex-based simulations. We start with regular hexagons to represent proliferative cells where the resting lengths of internal springs are all the same (purple lines in left cell). We then switch to a more elongated shape when a cell becomes contractile, where resting lengths of internal springs (purple lines in right cell) are longer in a given direction and shorter in all other directions.

to represent this contractile muscle machinery. The Hill model is based on the empirical observation that, when a muscle with a constant load contracts, the relationship between the force (or load) and the velocity of muscle shortening can be represented by the following force-velocity equation:

$$(F_c + a)v = -b(F_c - F_0). \tag{5.12}$$

In this equation, F_c and F_0 represent the contractile force and force at zero velocity (isometric force) respectively, while v is the muscle shortening velocity, and a and b are constants that are based on the fit of the force-velocity curve to experimental data. Here, we incorporate this relationship to model the contractile elements within an ASM cell after it switches from a proliferative to a contractile phenotype. We assume that the contractile element acts in parallel with elastic elements, as illustrated in Figure 5.6. This means that the length change of the cell is the same for both elastic and contractile elements and the total tension (T) is the sum of the forces produced by the two elements as follows

$$T = F_c + F_e, \tag{5.13}$$

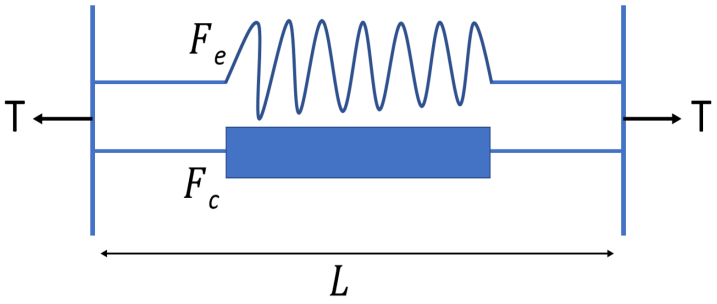

Figure 5.6: Schematic of the parallel elastic and contractile elements that we incorporate into cell internal springs using the Hill model [34]. The total tension (T) is separated into the contributions from contractile force (F_c) and elastic force (F_e), and the length of the muscle machinery (in our case an internal spring) is given by L.

where

$$F_e = k(L - L_0) \tag{5.14}$$

is the force of the elastic element given by Hooke's law.

The change in muscle length over time is determined by re-arranging Equation (5.12) and using $F_c = T - F_e$, based on Equation (5.13), to obtain

$$\frac{dL}{dt} = -v = \frac{b(T - F_e - F_0)}{T - F_e + a}. \tag{5.15}$$

Contractile machinery is therefore incorporated into our model by considering that the internal springs of contractile cells change length according to Equation (5.15). Since we are able to calculate the change in the length of internal springs, we can re-arrange Equation (5.15) to find the tension of an internal spring as follows

$$\overline{T} = \overline{F_e} + \frac{bF_0 + \frac{d\overline{L}}{dt}a}{b - \frac{d\overline{L}}{dt}}, \tag{5.16}$$

where once again, overlined measures represent contributions from an internal spring. Equation (5.16) is used to calculate the tensions of the internal springs for vertex j in each of the three cells surrounding that vertex ($\overline{T}_\alpha$,

$\overline{T}_{\alpha'}$ and $\overline{T}_{\alpha''}$), as used in Equation (5.9) in order to determine the net force at each vertex.

5.1.5 *Cellular Measures*

In order to analyse the dynamics of individual cells within an ASM cell layer, we first need to define several measures that will give an indication of the cell shape and stability to deformation based on surrounding forces and resting quantities.

Shape

Cell shape is important in this study since there is a significant difference in shape between each phenotype. It is therefore prudent to explore how a cell of each phenotype changes in shape and the impact this may have on neighbouring cells. We measure the circularity (c) of a cell α using the following equation:

$$c_\alpha = \frac{4\pi A_\alpha}{L_\alpha^2} \in [0, 1] \tag{5.17}$$

where A_α and L_α are the area and perimeter of a cell respectively. This would give $c_\alpha = 1$ for a perfect circle.

Square cells would result in a low measure of circularity using Equation (5.17), even though they are not an elongated shape (as one would assume when this measure is low). In order to address this flaw in measuring circularity, we additionally introduce a measure of elongation (e) of cell α as follows:

$$e_\alpha = \frac{\text{Major principle axis length}}{\text{Minor principle axis length}}, \tag{5.18}$$

using the `regionprops` function in Matlab, where the major axis length gives the longest diameter, and the minor axis length gives the shortest diameter for a given cell. The higher the value, the more elongated the cell (and again a value of $e_\alpha = 1$ represents a non-elongated cell).

Stress and Strain

In order to quantify cell deformation in a form that could be incorporated into macroscale models of tissue mechanics, we measure cell stress and strain. These are calculated for each cell using the following equations:

$$\text{Stress} = \frac{\sum_{j=0}^{N} F_{\alpha}^{j}}{A_{\alpha}}, \tag{5.19}$$

$$\text{Strain} = \frac{A_{\alpha} - A_{0}}{A_{0}}, \tag{5.20}$$

where the resting area A_0 is different for each phenotype (since we assume that an elongated contractile cell has a smaller area than a flat, round proliferative cell).

Stress Tensors

While our measure of stress in Equation (5.19) only considers the force at each vertex along with the cell area, we also consider the stress tensor of each cell in order to incorporate the impact of cellular shape on cell stress measures. To calculate the stress tensor, we must first define the effective cell pressure P_{α}^{eff} for each cell as follows (for this analysis refer to Section 3.3 of [58]):

$$P_{\alpha}^{eff} = P_{\alpha} + \frac{T_{\alpha} L_{\alpha}}{2A_{\alpha}}. \tag{5.21}$$

A cell (α) experiences net tension when the effective cell pressure is greater than zero and otherwise experiences net compression.

The stress tensor of a cell (σ_α) is also derived following the method in Section 3.3 of [58] and by considering the stress over each cell as uniform. This is calculated as

$$\sigma_\alpha = -P_\alpha^{eff} I + T_\alpha J_\alpha - \frac{1}{2}\dot{S}_\alpha, \tag{5.22}$$

where

$$J_\alpha = \frac{1}{A_\alpha}\left(\frac{1}{2}L_\alpha I - \sum_{i=0}^{Z_\alpha - 1} l_\alpha^i \hat{t}_\alpha^i \otimes \hat{t}_\alpha^i\right) \tag{5.23}$$

is the contribution to the cell stress resulting from asymmetries in cell shape (given that l_α^i is the length of an edge between vertex i and $i+1$ for cell α) and

$$S_\alpha = \frac{1}{Z_\alpha}\sum_{i=0}^{Z_\alpha - 1} \mathbf{R}_\alpha^i \otimes \mathbf{R}_\alpha^i. \tag{5.24}$$

is the cell shape tensor [58].

5.1.6 *Tissue-level Mechanics*

The properties of the cell population or tissue as a whole are important in understanding the dynamics that lead to a remodelled airway. Understanding how the distribution of different phenotypes impacts the cellular layer as a whole is also clearly important when considering the impact of an asthmatic exacerbation, as we later go on to do. To characterise the tissue mechanical properties, and in particular how these are altered by the proportions and patterns of the tissue phenotype make-up, we consider the stress-strain curve. Experimentally, stress-strain curves are measured through stretching a tissue by differing amounts and measuring the response. How we implement this in our simulated tissue is described in Section 5.2.5 below.

5.2 NUMERICAL IMPLEMENTATION

We first randomly or manually input a set of generating points. We then use the `Voronoin` function to tessellate these points. The output of this is a $2xN$ matrix of all N vertex 2D coordinates as well as a cell array where each cell contains a list of vertex matrix indices; the order in which they are listed tells us their anticlockwise connectivity. We disregard the 'open' Voronoi cells on the boundary of the monolayer (by removing these cells from the simulated tissue area) and so the cells on the outside of the resultant simulation have closed boundaries without the need for an enlarged convex hull. All simulations and other associated computations are implemented in Matlab.

5.2.1 *Boundary Conditions*

We impose periodic or Dirichlet boundary conditions depending on the focus of the specific test simulation. In most cases, we implement periodic boundary conditions to reduce edge effects such that our relatively small cell population produces dynamics that approximate the bulk ASM tissue. A simple way to impose periodic boundary conditions in this model is to first repeat our Voronoi seeding four times and choose the central region (a box of width w) as seen in Figure 5.7. This ensures that duplicate polygons are found on the boundaries of our chosen region. Vertices on the boundary are then coupled such that any vertex displacement also occurs to the corresponding vertex on the opposite boundary. Two examples of this can been seen in Figure 5.7 (black/white vertex found also on opposite boundary).
For specific test problems, such as in determining a stress-strain curve for simulated tissue (Section 5.2.5), we instead simulate stretching a tissue by displacing the vertices on the boundary of our chosen region and then fixing the positions of these outermost vertices (Dirichlet boundary conditions).

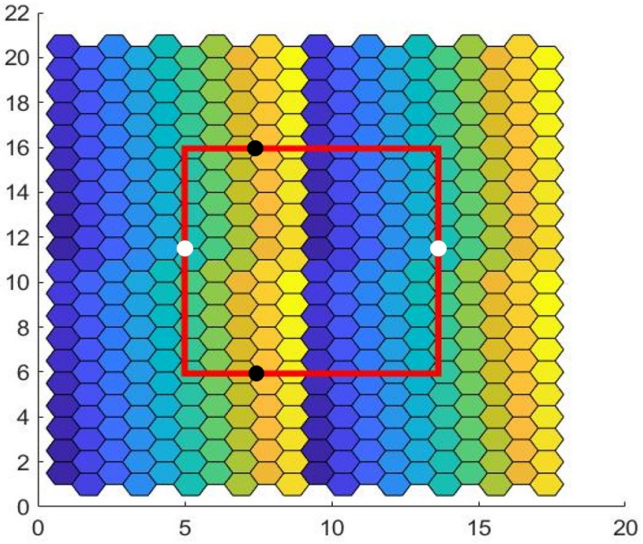

Figure 5.7: To implement periodic boundary conditions, we repeat the tessellation four times and then choose the box in the centre for our monolayer. Since the vertex geometry is repeated, we couple the boundary vertices and, upon removing vertices that are not contained in the box, the remaining monolayer has periodic boundary conditions.

5.2.2 *Initial Conditions*

In order to match our experimental protocol (described in Section 3.2), which begins with a full population of the proliferative phenotype, we begin with a population of regular hexagons and then perturb the vertex positions uniformly at random via $\alpha^i \to \alpha^i + \epsilon\gamma$ where $\gamma \sim U(0,1)$ and $\epsilon = 0.5$. All cells will then have near equal internal spring resting lengths and therefore a high circularity (which fits with the rounded morphology of this phenotype as discussed in Section 1.2.1).

5.2.3 *Time-stepping*

To calculate the change in vertex positions over time (using the method in Section 5.1.3), we calculate the net force at each vertex using Equation (5.9) and update the positions of vertices using Equation (5.11) with a small time step of $h = 0.001$ and parameters as in Table 4. Each time a vertex position is updated, it must be checked that all cells remain convex. This is done by using the `inpolygon` function along with vector geometry to move any point which makes a cell concave. T1 transitions (described in Section 5.1.2) are also implemented using the parameters d_{min} and d_{sep}, quantified in Table 4.

Parameter	Value	Description
$\tilde{L}_0$	3.4641	Resting length of cell perimeter
$\tilde{A}_0$	0.8660	Resting cell area
$\tilde{K}$	0.6	Cell stiffness
$\tilde{K_{int}}$	0.4	Stiffness of internal springs
$\tilde{\Lambda}$	0.15	Tunes cell contractile strength
d_{min}	0.05	Minimum cell edge length before a T1 transition
d_{sep}	0.25	New edge length following a T1 transition

Table 4: Parameter values used in the energy minimisation and T1 transitions.

5.2.4 *Cell Phenotypes*

As described in Section 5.1.4, a contractile cell starts with the same shape as a proliferative cell, but is elongated in a randomly determined orientation over time based on the increase of internal resting spring lengths. To do this, a single internal spring (between the cell centre and one of the vertices)

is first chosen uniformly at random. If the cell has an even number of vertices, the opposite internal spring is also chosen and their resting lengths are extended by L_{ext}. Should the cell have an odd number of vertices, the orientation of elongation is again decided randomly between the two opposite internal springs to the internal spring chosen first. With any change in resting length of internal springs, the resting area is also changed correspondingly. The effect of the contractile machinery is incorporated using the Hill force-velocity relationship described in Section 5.1.4. The parameters associated with these changes can be found in Table 5.

Parameter	Value	Description
L_{ext}	0.3	Extension in internal spring resting lengths
A_{c0}	0.2512	Resting area of elongated contractile cell
F_0	3	Isometric force (Hill model)
a	0.001	Tunes force velocity curve (Hill model)
b	0.001	Tunes force velocity curve (Hill model)

Table 5: Parameter values used in changing the shape of contractile cells and for incorporating the Hill Model to represent the cells internal contractile machinery.

5.2.5 *Stress-strain Curve*

To determine the stress-strain curve of ASM using our model, we simulate stretching our tissue by different amounts and, each time, measure the average cell stress and strain at the resultant equilibrium state. We simulate stretching the tissue by displacing the outermost vertices in the direction normal to the boundary, and fixing them at these new positions (as discussed in Section 5.2.1) to represent a sustained load. We then let the system relax to the new stretched equilibrium using the method described in

Section 5.1.3. We determine that this state has been reached when the average displacement of vertices for a given time step is < 0.0001 (i.e. when there is little to no further displacement of vertices within the system). Finally, we measure the average cell stress and strain across the tissue. This process is repeated with incremental increases in the distance of the vertex displacements (s) and therefore extent of the stretch, and the average cell stress and strain is recorded each time. We use this method to explore the impact of contractile population size and distribution in the tissue on the resultant stress-strain curve.

5.3 RESULTS

5.3.1 *Energy Minimisation*

Figure 5.8 shows that, when evolving the system in the time dependant manner discussed in this chapter, the cellular network slowly relaxes toward its minimum energy state over time and cells refrain from self intersection or overlapping during this time (as opposed to when using the Matlab function `fminsearch` in Figure 1.12).

5.3.2 *Cellular Measures*

We start this analysis by testing that individual simulated contractile cells within a proliferative population exhibit the structural and functional dynamics that we would expect for their phenotype based on literature and our TFM experimental findings. We therefore initialise 100 proliferative cells (as described in Section 5.2.2) and then "turn on" the contractile machinery and contractile-associated resting lengths of just four of these cells (that are widely spread-out), before simulating the population evolution over time. This means that the proliferative cells begin close to (but not

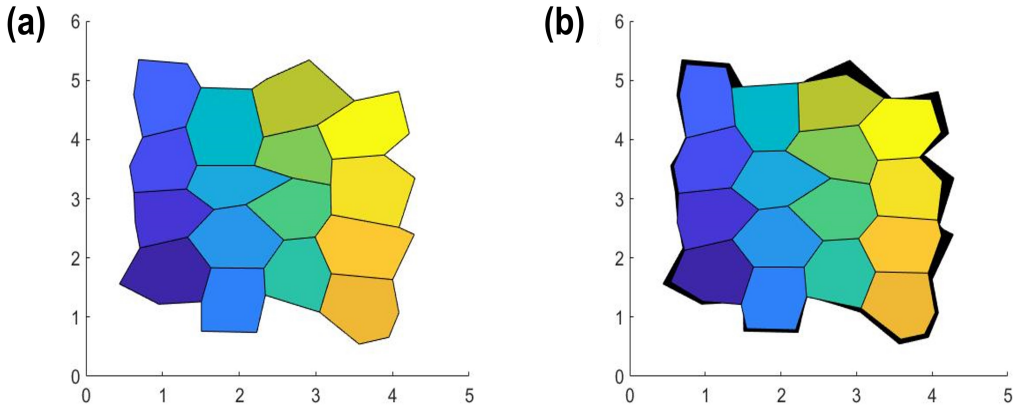

Figure 5.8: Vertex model (a) before and (b) after a time dependent energy minimisation on a small population of simulated cells, where black areas in (b) show the area initially occupied by the cells (as in (a)). Vertices are displaced using Equation (5.11).

at) their resting equilibrium state, while the contractile cells begin far from their equilibrium. We then measure the changes in cell circularity, elongation, stress and strain over the period of evolution. Our measures are taken for each contractile cell individually as well as the average of the contractile and proliferative populations (Figures 5.9 and 5.10).

Figure 5.9(a) shows the simulated population at the start and end of the simulation period. The contractile cells are coloured light blue, yellow, green and pink, as are their respective data points in Figures 5.9(b,c) and 5.10. We can see in Figure 5.9(a) that contractile cells are indeed elongated at $t = 1.72$ and that the proliferative cells (particularly those that neighbour the contractile cells) become less regular to allow for this.

Circularity and Elongation

As expected, Figure 5.9(b,c) shows that there is a significant decrease in contractile cell circularity over time as well as a corresponding increase in

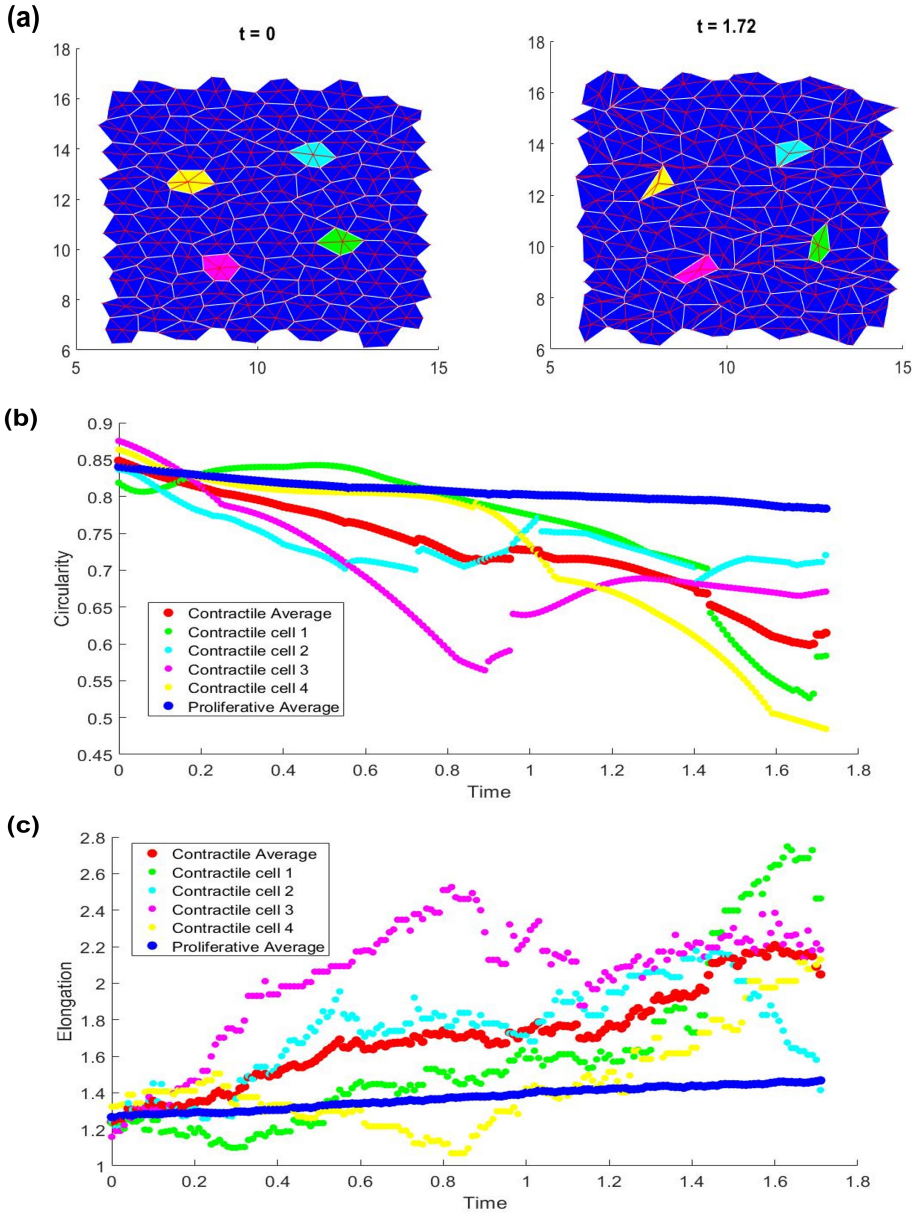

Figure 5.9: (a) Simulated ASM population before ($t = 0$) and after ($t = 1.72$) an energy minimisation, where each cell is represented by a white border and contains red internal springs. The proliferative cells are coloured dark blue and the remaining four coloured cells spread throughout this population are contractile. (b) Cell circularity (calculated using Equation (5.17)) and (c) elongation (found using Equation (5.18)) for each of the four contractile cells over this time period, as well as an average of the contractile (red) and proliferative (blue) populations.

elongation. The variability in individual contractile cells can be explained by the impact of transitions (discussed in Section 5.1.2) as the cells evolve towards their resting state. The circularity and elongation of proliferative cells on the other hand, varies only slightly throughout this period and, as can be observed in Figure 5.9(a), the changes are more significant when the cells in question neighbour contractile cells.

Stress and Strain

It can be seen in Figure 5.10(a) that, contractile cells experience higher stress than proliferative cells throughout the simulation. The average stress of the contractile population appears to decrease at the start of the simulation as the cells begin to elongate, however, there is large variability in average cell stress over the simulation period given this small population of contractile cells. The stress state of the proliferative population on the other hand, does not change significantly throughout the simulation. Moreover, the average stress of proliferative cells remains above zero since the system is unable to reach equilibrium. Figure 5.10(b) shows that the strain of proliferative cells remains at approximately zero throughout, and only rises slightly to allow for the changes in contractile cell shapes. As described above, contractile cells begin the simulation with a more rounded shape far from their equilibrium state, but as they elongate, the strain they are under decreases respectively.

5.3.3 *Tissue Measures*

Stress - Strain curve

We determine the stress-strain curve, using the method described in Section 5.2.5, for five different tissue types as follow.

TISSUE TYPE 1: has only 5 contractile cells that are spread out among a proliferative population (Figure 5.11(a)).

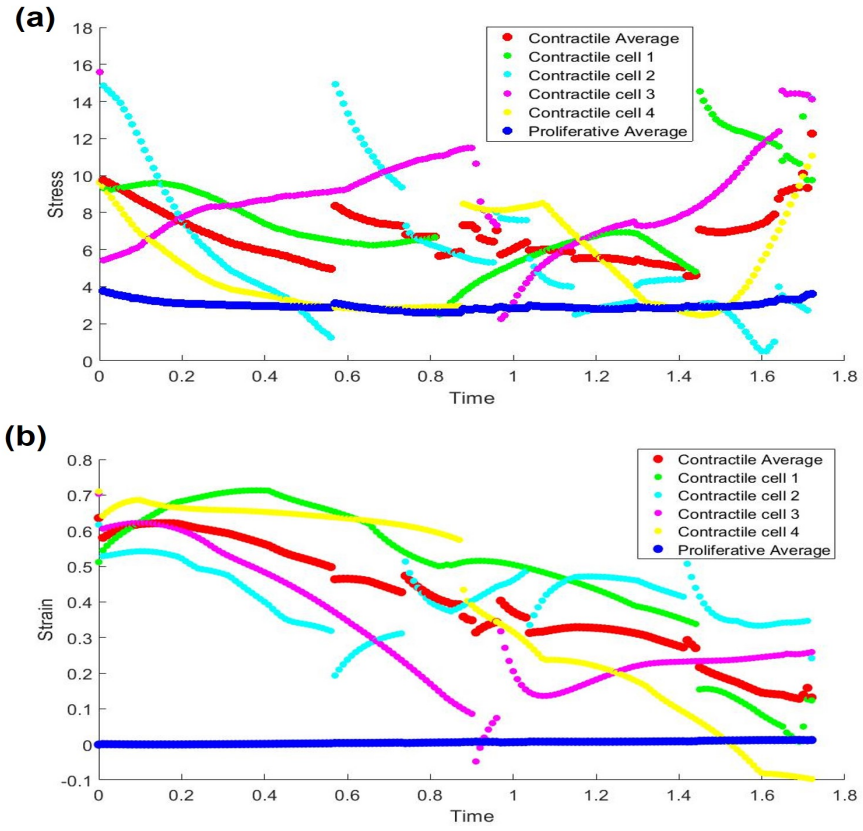

Figure 5.10: (a) Cell stress (calculated using Equation (5.19)) and (b) cell strain (found using Equation (5.20)) for each of the four contractile cells over the time period of Figure 5.9, as well as an average of the contractile (red) and proliferative (blue) populations.

TISSUE TYPE 2: has a larger proportion of 12 contractile cells that are similarly spread out within the proliferative population (Figure 5.11(b)).

TISSUE TYPE 3: has a still larger proportion of 17 contractile cells that are similarly spread out within the proliferative population Figure 5.11(c)).

TISSUE TYPE 4: is similar to Tissue type 2 in that it also has 12 contractile cells, but this time they are bunched in the centre of the proliferative tissue (Figure 5.11(d)).

TISSUE TYPE 5: has a large proportion of contractile cells surrounding a population of 12 proliferative cells bunched in the tissue centre (Figure 5.11(e)).

Each of the Figures 5.11(a–e) are shown at the stage where the outer vertices are first displaced, before the tissue has relaxed to a new equilibrium. As previously mentioned (Section 5.2.5), the corresponding stress-strain response curves (Figures 5.12 and 5.13) are the responses to deformation once at their new stretched equilibrium.

The average and variance of the stress and strain for each of the tissue types $1-3$ following relaxation after differing lengths of tissue stretch ($s = 0.2 - 2$) is shown in Figure 5.12(a–f) for each phenotype population separately (contractile in red and proliferative in blue). When comparing the changes for contractile and proliferative population stress (Figure 5.12(a, c and e respectively) and strain between tissue types 1–3 (Figure 5.12(b, d and f respectively), we find that there are few significant differences. One difference, however, is that the stress of the contractile population of tissue type 3 (Figure 5.12(e)) following a stretch of $0.6 < s < 2$ is significantly higher and has a larger range than that of tissue types 1 and 2. On the other hand, this difference in contractile stress does not appear to have an impact on the contractile strain (Figure 5.12(f)).

Figure 5.12(g) shows the stress-strain curve for each of the tissue types 1 (green), 2 (cyan) and 3 (pink), where the contractile population is spread out but the proportion of contractile cells differs. We can see that this difference in the proportion of contractile cells has a larger impact on the tissue properties for higher values of stress and strain. While the curves for tissue types 1 and 2 (green and cyan) look approximately linear, the curve for tissue type 3 (pink) shows non-linear features, suggesting some amount of strain-softening.

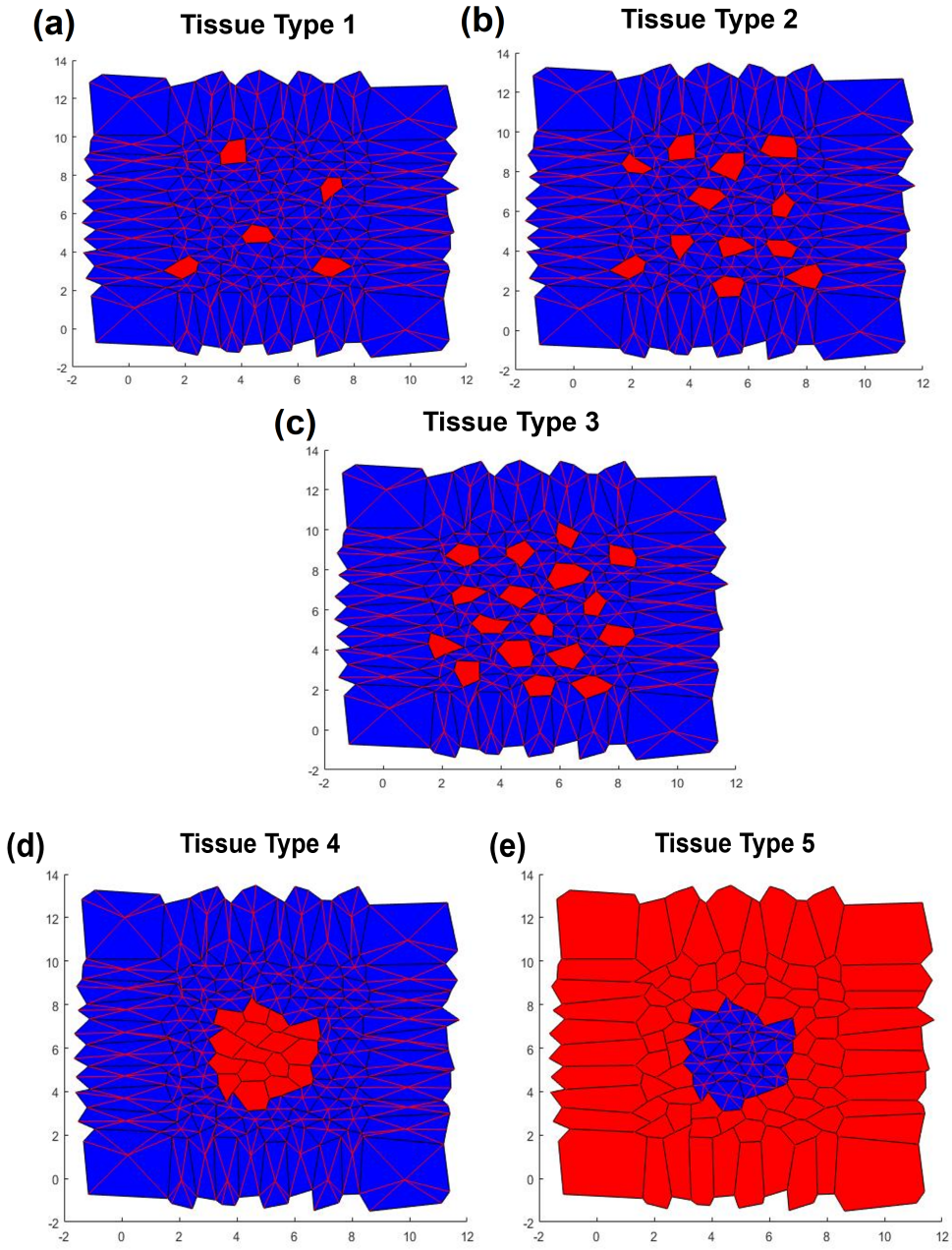

Figure 5.11: Five different simulated, non-periodic ASM tissue types shown after having been stretched but before relaxation to equilibrium. Contractile cells are coloured red and proliferative cells are blue.

The average and variance of the stress and strain for each of the tissue types 4 and 5 following relaxation after differing lengths of tissue stretch

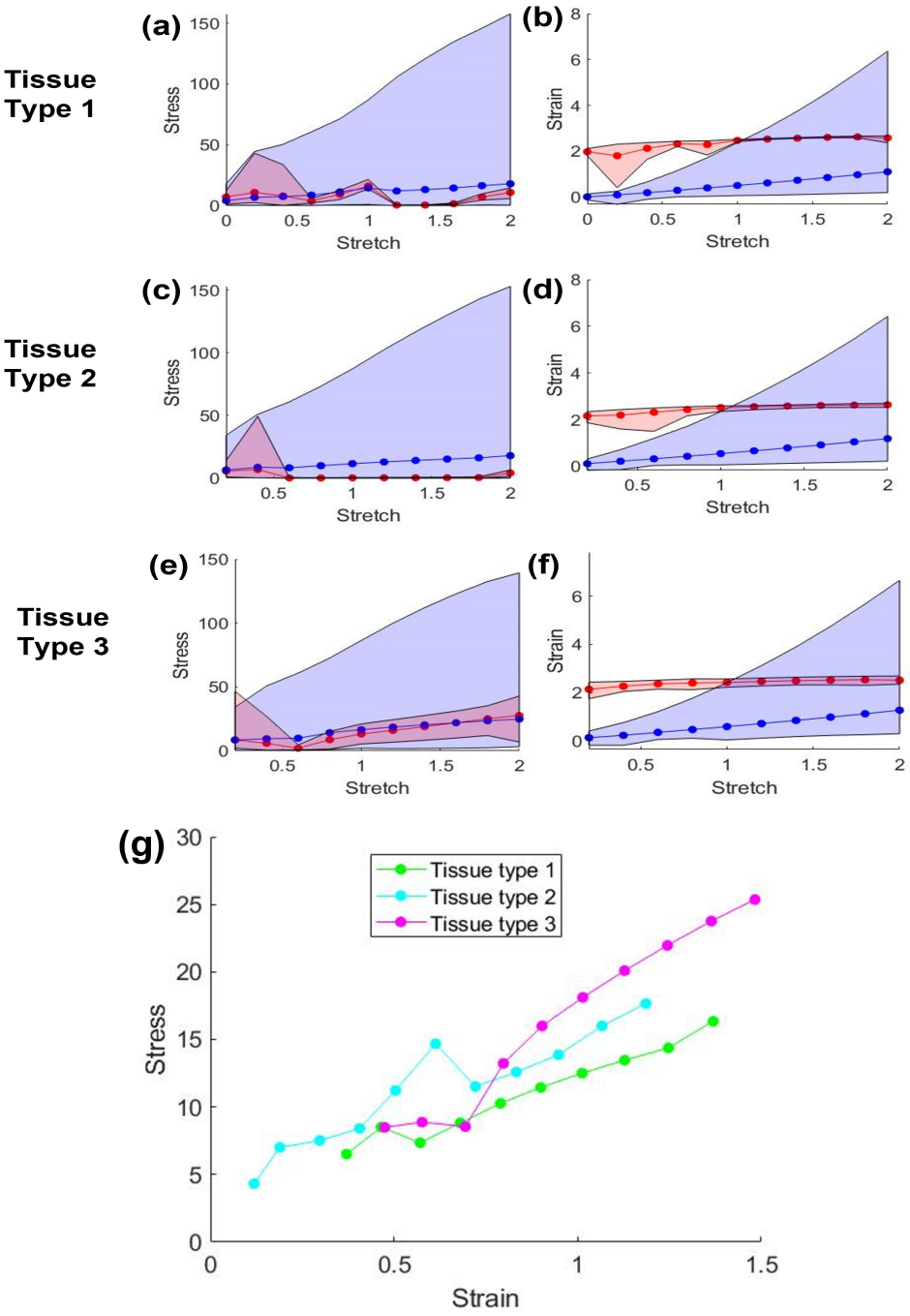

Figure 5.12: (a–f) Stress (left column) and strain (right column) as functions of stretch for the contractile (red) and proliferative (blue) populations of tissue types 1–3 (where shaded regions represent the variance); (g) stress-strain curves for each tissue type 1–3.

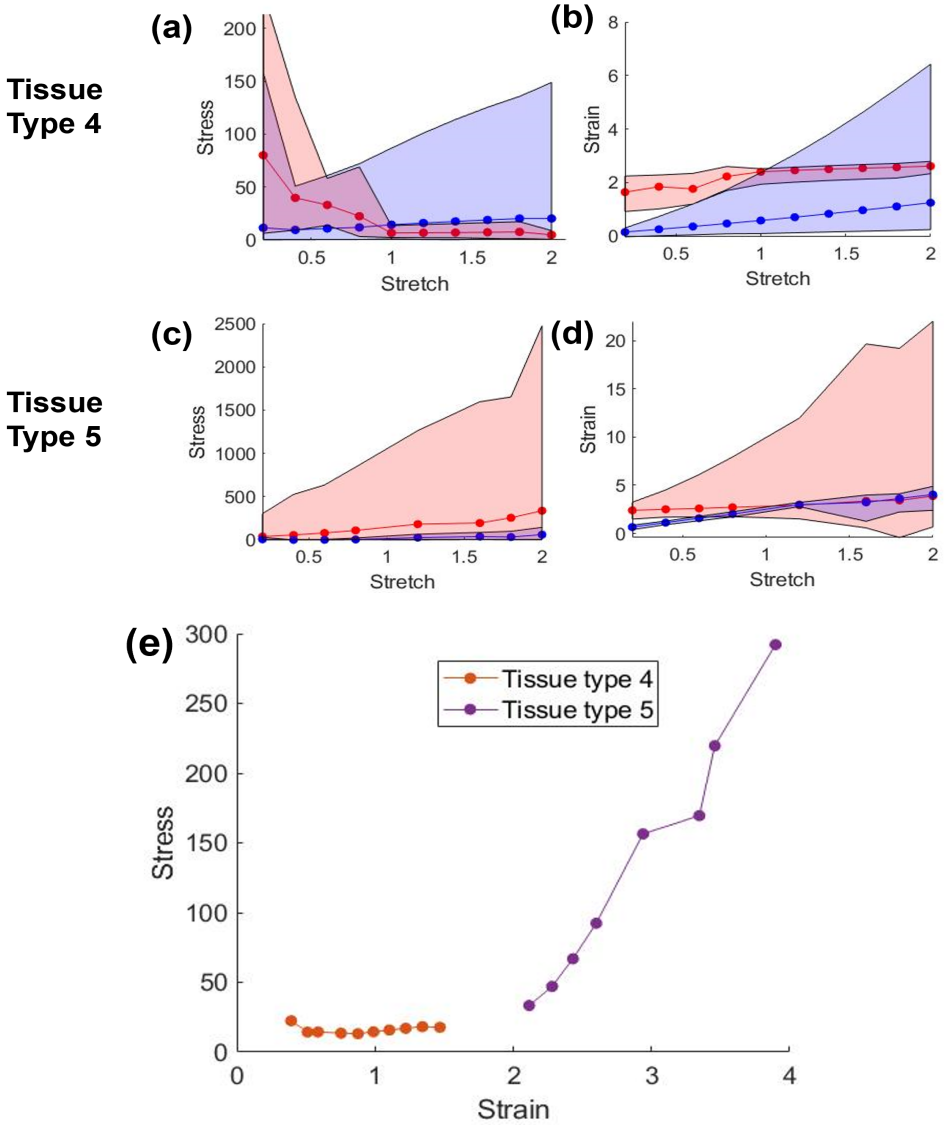

Figure 5.13: (a–d) Stress (left column) and strain (right column) as functions of stretch for the contractile (red) and proliferative (blue) populations of tissue types 4 and 5 (where shaded regions represent the variance); (e) stress-strain curves for each tissue type 4 and 5.

($s = 0.2 - 2$) is shown in Figure 5.13(a–d). In this case, however, there are very large differences in the stress and strain associated with each tissue type. For tissue type 4, both the range and average of cell stress values is high for low stretch lengths, but decreases to near zero once $s > 1$ (Fig-

ure 5.13(a)). For tissue type 5, contractile cell stress (average and variance) continues to increase as stretch is increased (Figure 5.13(c)). These trends in contractile cell value ranges are repeated for strain, though their average values remain fairly constant (Figure 5.13(b and d)).

Figure 5.13(e) shows the stress-strain curve for each of the tissue types 4 (orange) and 5 (purple), where there are 12 cells from each population respectively grouped in the centre of the tissue surrounded by the other phenotype. We see that this difference alters the tissue properties dramatically. Tissue type 5 exhibits a strain stiffening property, as seen by the sharp increase in stress with increasing strain (at larger deformations). *In vivo*, such stiffening is required for the alteration of ECM during mechanical deformation and is therefore important in order to maintain the structural support within the tissue [76]. Tissue type 4, however, seems to plateau such that there is an increasing strain, yet little to no change in the stress of the tissue. Most cells reside in a contractile phenotype when *in vivo* (unlike the cells in our *in vitro* experiments, which switch to the contractile phenotype only when serum is removed) and so exploring the properties of tissue type 5 is more relevant for understanding *in vivo* tissue.

We finally compare tissue types 2 and 4 (Figure 5.14) which both contain 12 contractile cells but are distributed throughout the tissue in different ways (spread out and gathered in the centre respectively). In this, we can see more clearly the impact of cell phenotype distribution throughout tissues and the impact this has on tissue properties. Interestingly, we see that the stress goes down in tissue type 4. The phenotype and corresponding location of cells within the tissue impacts their ability to rearrange and could therefore contribute to this observation. When the tissue stretch is small, the outer proliferative cells rearrange slightly, but the average cell stress remains high as cellular rearrangement is difficult for the contractile cells that are gathered in the centre of the tissue. As stretch increases, more contractile cells

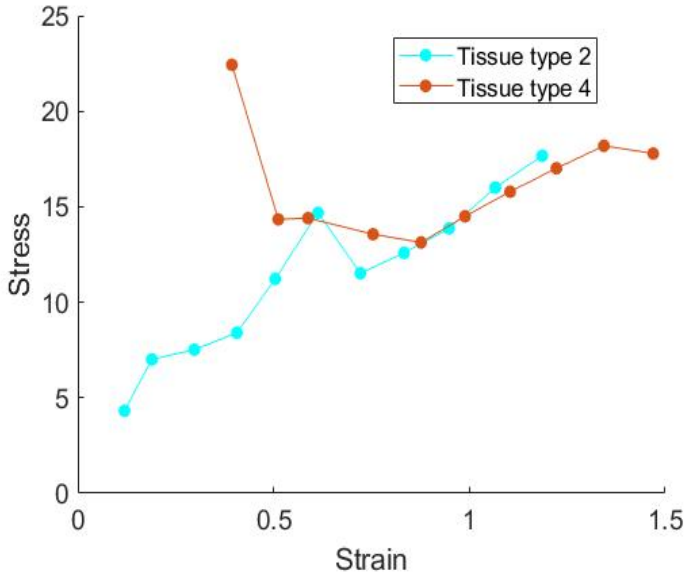

Figure 5.14: Stress-strain curve for 12 contractile cells distributed within a proliferative population in different ways (spread out for tissue type 2 and gathered in the centre for tissue type 4).

are able to rearrange to relieve stress and so the average cell stress reduces. Given that the variability is high for proliferative cells (Figure 5.13(a)), a few highly stressed cells may be dominating.

5.4 SUMMARY

In this chapter we have developed a new cell-based model of the mechanics of ASM cells in a monolayer. We represent cells as polygons formulated from a set of points using a Voronoi tessellation. We have chosen to use this vertex-based formulation in order to represent conveniently the interaction of cells at their boundaries. A shape and functional change associated with a switch in phenotype is modelled through the elongation of cells that have changed to a contractile phenotype, as well as the operation of contractile machinery contained within internal springs. A time dependent method of force balance and simulation is used, where we track the movements of

vertices based on the net force from its three surrounding cells.

To test this model, we explore the changes in both cellular and tissue measures for a small number of contractile cells in a largely proliferative population. We find that our model shows the increase in elongation/decrease in circularity of the contractile population over this simulated time period, as we would expect for contractile cells that have just switched from a proliferative phenotype. We also see an expected decrease in contractile strain as these cells elongate and a variable, non-zero stress. The proliferative population remains fairly constant throughout since all cells begin with a rounded, proliferative cell-like shape. Finally, stress-strain curves for different tissue types illustrate the impact that the distribution of contractile cells within a population has on the resulting non-linear mechanical properties of a tissue.

6

CELL VERTEX MODEL: PHENOTYPE SWITCHING

In this chapter, we further develop the vertex model presented in Chapter 5 by including the additional dynamics of ASM cell phenotype switching over a period of serum deprivation, in order to replicate the TFM experimental results. As in the population-level reduced ODE model of Chapter 3 (Section 3.3), the simulation time period is based on an experimental protocol in which *in vitro* ASM cells are deprived of serum. Thus, we expect that a sub-population of the initially fully proliferative cell population will gradually switch to the contractile phenotype over this period of serum deprivation. In Chapter 5 we demonstrated changes in the shape and mechanical properties of individual contractile cells in a proliferative population (Section 5.3.2), as well as the impact of different contractile population sizes and placements on stress-strain curves when stretching the simulated tissue (Section 5.3.3). Here we extend the model to capture the more biologically realistic dynamics of a randomly and continuously changing cellular population through the inclusion of phenotype switching.

We incorporate random phenotype switching over time (Section 6.2.1) and analyse the simulated results at both the cell level (Section 6.3.1) and the population level (Section 6.3.2). This allows us to explore our hypothesis that the mechanical environment of ASM cells and their neighbours drives changes in their structure and function, and hence is key in the phenotype

switching process.

We also explore the existence, length and cellular make-up of force chains throughout the population (Section 6.3.3). This is important as it gives an indication of the impact of emerging contractile populations on long distance mechanical communication across the tissue.

6.1 MODELLING APPROACH

6.1.1 *Stochastic Effects*

In our previously developed ODE model (Appendix A) which was extended in Chapter 2, we considered the deterministic change in ASM density and in other airway components over time. While the ODE approach was appropriate for modelling the average behaviour of a large number of cells, it does not account for the effects of interactions between individual cells. To include phenotype switching in our vertex-based model (developed in Chapter 5) therefore, we use a method that includes randomness when deciding on whether a switching event occurs for a given cell.

To ensure a dynamic equilibrium in which an *in vitro* serum-deprived population of cells consists of a small sub-population of contractile cells, both proliferative to contractile and contractile to proliferative switching rates have to be included. The latter is assumed to be very small; however, since the cells are serum deprived.

To accommodate for realistic phenotype switching rates, we assume the switching rate from contractile to proliferative is a function of the extent of cell elongation (i.e. it is less likely that a more elongated contractile cell will switch back to being proliferative). This represents the corresponding functional changes that occur in a contractile cell as it elongates, such as an

increase in quantities of contractile proteins and caveolae (as discussed in Section 1.2.1).

6.1.2 *Cell-based and Population-based Measures*

Model results in this chapter are quantified via the cellular measures (circularity, elongation, effective cell pressure, stress and strain) described in Section 5.1.5. Results from this model also give an indication of the dynamics of the cellular populations making up ASM tissues. This is important in order to gauge the impact that the contractile sub-populations have on the tissue as a whole, including the rearrangement of cells and the extent of mechanical communication between cells across the tissue. In view of this we introduce several new tissue measures as follows, and illustrated in Figure 6.1.

Bundles

We define bundles of contractile cells as groups of cells with more than three contractile cells neighbouring each other (as seen in Figure 6.1(a)).

Paths

Paths are found within bundles. These are defined to be chains of contractile cells connecting the cells in the bundle that are the furthest away (based on distances between cell-centres) as seen in Figure 6.1(b).

Force Chains

Bundles and paths of contractile cells within the ASM cell population, and the alignment of these cells, gives an indication of the rearrangement involved across the tissue over this period of serum deprivation. We also, however, aim to explore the mechanical communication throughout the tissue. The forces produced by cells regulate behaviours at the sub-cellular,

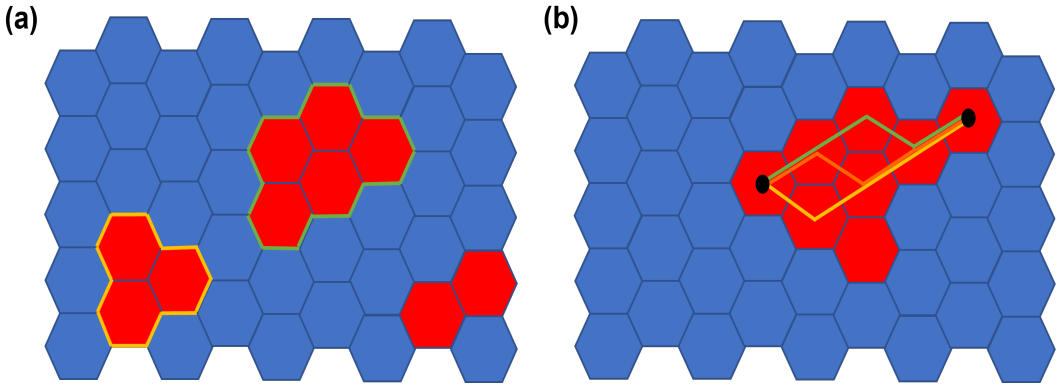

Figure 6.1: Schematics showing (a) two ASM bundles (outlined in yellow and green) and (b) three ASM paths (shown by yellow, orange and green lines between the cells furthest apart within the bundle, highlighted by a black centre).

cellular and tissue-level, and so are vital for many biological processes [82]. In order to measure the distance at which forces are transmitted across the tissue, and whether the size of the contractile cell population impacts this, we use the well defined notion of force chains (FCs). FCs represent chain-like groups of connected cells that exhibit a higher than average magnitude of stress [60].

6.2 NUMERICAL IMPLEMENTATION

6.2.1 *Random Phenotype Switching*

Based on the mechanisms incorporated into the ODE model discussed in Chapter 2, we first consider all the possible events that could occur for an ASM cell, namely: a proliferative cell divides, a contractile cell undergoes apoptosis, a proliferative cell switches to a contractile cell or a contractile cell switches to a proliferative cell. In an ODE setting, the change in density

of proliferative and contractile ASM cells respectively over time is described as follows:

$$\frac{dp}{dt} = k_{cp}c - k_{pc}p + k_p p, \tag{6.1}$$

$$\frac{dc}{dt} = k_{pc}p - k_{cp}c - k_{ca}c. \tag{6.2}$$

with rates k_{ij}, as in Chapter 2.

In our vertex-based cell model, however, we make the assumption that cell apoptosis (k_{ca}) is negligible, as in the reduced model of Chapter 3. For simplicity, with the focus being on the switching of cellular phenotypes during serum deprivation, we also assume that k_p is negligible. As described in Section 6.1.1, to obtain a dynamic equilibrium in which an *in vitro* serum-deprived population of cells consists of a small sub-population of contractile cells, we assume switching of ASM cells can occur in both directions. The possible events that could occur at each time-step, therefore, are either a proliferative cell switches to a contractile cell, or vice versa.

For each time step h for which we update the vertex positions (Equation 5.11), we first randomly choose a cell and then randomly choose the event that could occur for any given cell based on its current phenotype. For example, if the cell is proliferative, the cell could either switch to a contractile phenotype or stay in the proliferative phenotype. A given cell switches from a phenotype x to phenotype y with a transition probability given by $\alpha_{x\to y}$ as follows:

$$\alpha_{p\to c} = k_{pc}p, \tag{6.3}$$

$$\alpha_{c\to p} = k_{cp}c. \tag{6.4}$$

As mentioned in Section 6.1.1, we model the switching rate k_{cp} as a decreasing function of cell elongation. Here, we once again define elongation (e) as the ratio of the major axis length to the minor axis length, using the

`regionprops` function in Matlab. The modified transition probability for this switching event is then given as follows:

$$\alpha_{c\to p} = \frac{k_{cp}}{e^{15}}c. \tag{6.5}$$

6.2.2 *Initial Conditions*

Simulations in this chapter begin with a fully proliferative population of 100 cells, to mimic the experimental protocol in which we assume that all of the cells in media containing serum are proliferative. Parameters remain as stated in Tables 4 and 5 with the addition of switching rates $k_{cp} = 0.1$ and $k_{pc} = 0.005$, unless stated otherwise.

6.2.3 *Bundles*

We classify bundles using the following method:

1. For each contractile cell, create a group that consists of that cell and any of its neighbours that are also contractile (for Figure 6.2, groups are: [1 2 3], [2 1 3 4 5], [3 1 2 4], [4 3 2 5] and [5 2 4]).
2. Once a group has been identified for each contractile cell that also has contractile neighbours, compare groups and combine any that overlap (all the groups in Figure 6.2 overlap: [1 2 3 2 1 3 4 5 3 1 2 4 4 3 2 5 5 2 4]).
3. We then remove any repeated cells from each group (without repeats, the group in Figure 6.2 becomes: [1 2 3 4 5]) and, if the size of the group is still larger than 3 cells, it is classed as a bundle (group [1 2 3 4 5] in Figure 6.2 is a bundle).

We measure the alignment of cells within a contractile bundle by calculating the angle of the shape tensor axis, measured anticlockwise from the horizon-

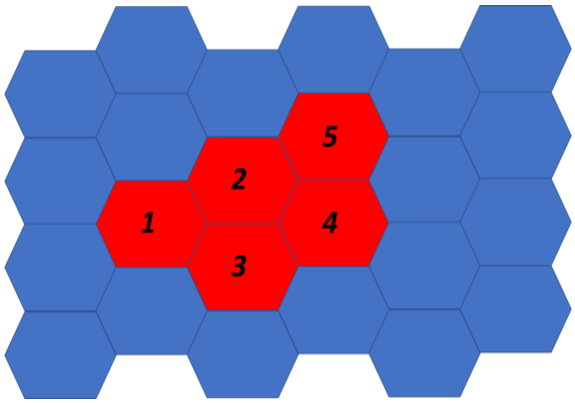

Figure 6.2: Defining a contractile bundle: through following the steps for defining a bundle, we find that contractile cells 1-5 indeed make up a bundle.

tal axis passing through the cell centre, and tracking the average variance between these angles. Since the arithmetic variance is not appropriate for angles, it is convenient to use the Kuramoto order parameter $V = |Z|$ as a measure of coherence where

$$Z = \frac{1}{N} \left| \sum_{n=1}^{N} e^{i\theta_n} \right|, \tag{6.6}$$

and θ_n is the angle in question. This gives us a value for the order parameter V of all the angles in a bundle of N cells, where $V = 1$ means that the angles are completely aligned and $V = 0$ means they are completely unaligned.

6.2.4 *Paths*

We classify paths using the following method. For each bundle, we first find the contractile cells that are the furthest away from one another (based on distances between cell centres); these cells are the path ends (for Figure 6.3, these are cells 1 and 6). For a randomly chosen path end, we add a neighbouring cell to the path if:

1. It is also contractile

2. It is not already part of the path

3. It only has one neighbour that is already a member of the path.

For Figure 6.3, the path is [1,2,4,5,6] or equivalently [6,5,4,2,1]. This method could result in several paths per bundle (as seen in Figure 6.1(b)); however, we choose to only measure the alignment of cells within the shortest path (measured by the distance between the cell centres of the path ends) for each bundle.

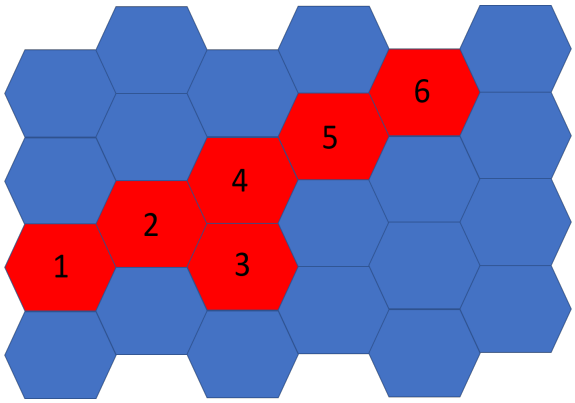

Figure 6.3: Defining a contractile path: through following the steps for defining a path, we find that contractile cells [1,2,4,5,6] make up the longest path.

6.2.5 *Force Chains*

Following the algorithm for Force Chains (FCs) defined by Peters *et al.* [60], we first find all cells that exhibit a stress tensor magnitude that is strictly larger than the average of the cell population as a whole (for Figure 6.4, these are cells 1–6, outlined in yellow). We then randomly choose a chain starter from one of these cells. For this example, we choose cell number 1 of Figure 6.4. Any neighbour of cell 1 is added to the chain if:

1. It has a larger than average stress tensor magnitude (defined in Chapter 5, illustrated by cells with a yellow outline in Figure 6.4). In this example, only cell number 2 satisfies this constraint.

2. The direction of the stress tensor (shown as a thick black line for each cell 1-6 in Figure 6.4) lies between θ degrees of the angle of the line between their centre and the centre of the previous cell in the chain (shown as a thin yellow line between cell centres in Figure 6.4). In this example, the direction of the stress tensor of cell 2 is within $\theta = \pi/4$ degrees of the direction of the line between the centres of cells 1 and 2, hence cell 2 satisfies this constraint.

3. The direction of the stress tensor of the previous cell in the chain lies between θ degrees of the angle of the the line between their centre and the centre of the previous cell in the chain (as in (2) but reversed). In this example, the direction of the stress tensor of cell 1 is also within $\theta = \pi/4$ degrees of the direction of the line between the centres of cells 1 and 2, cell 2 is therefore added to the chain.

For Figure 6.4, there is a force chain between cells [1,2,3,5]. Cell 4 has no neighbours that have a larger than average stress tensor magnitude so is, therefore, not included in a force chain. Although cell 6 neighbours cell 5, both angles referred to in criteria two and three above are larger than $\theta = \pi/4$ degrees and so this cell is not added to the force chain.

6.3 RESULTS

6.3.1 *Cellular measures*

To demonstrate the impact of the phenotype-associated cell shape change on the mechanics and alignment of cells, we first explore changes in the cellular pressures and the internal angle distributions for a population of

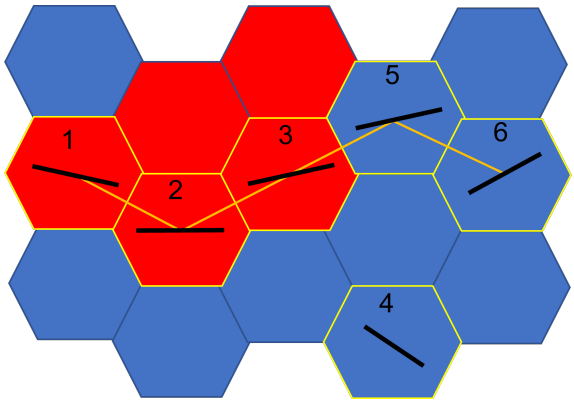

Figure 6.4: Defining a force chain: by following the steps for defining a force chain, we find that cells [1,2,3,5] make up the only force chain in this example.

cells. We simulate the vertex model developed in Chapter 5 (with periodic boundary conditions as discussed in Section 5.2.1 and initial conditions described in Section 6.2.2) and measure these metrics over the period of serum deprivation, for the populations we refer to as Tissue 1 and Tissue 2. Tissues 1 and 2 only differ by the initial random perturbation that was discussed in Section 5.2.2; i.e. the two tissues are two random instantiations. Over the period of serum deprivation, a sub-population of cells switch from a proliferative to contractile phenotype with associated cell shape changes, as in the TFM experiment.

Figure 6.5 illustrates the cellular shapes and positions that make up Tissues 1 and 2 before (Figure 6.5(a,c)) and after (Figure 6.5(b,d)) this time period. We observe that the simulated cells become much less rounded and more aligned following the serum deprivation (Figure 6.5(b,d)). There is also a significant reduction in the number of cells that are under net compression (green cells) and a corresponding increase in the number of cells that exhibit net tension (yellow cells). The cells that remain in a state of net compression, however, seem to be located in small groups or hot-spots. Under closer inspection, we observe that the axis of elongation (as seen by the alignment

of red internal springs) tends to align with that of cell neighbours.

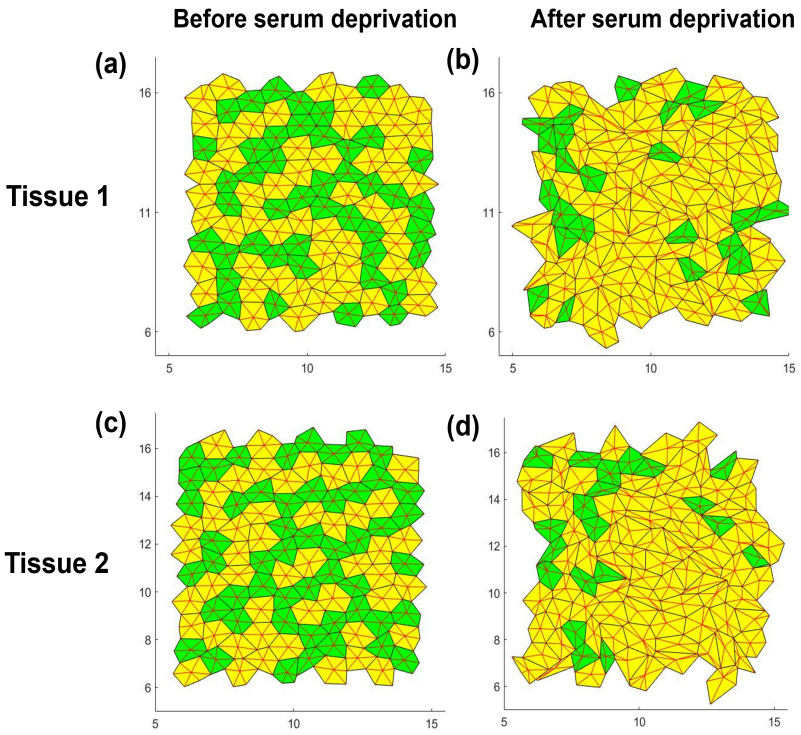

Figure 6.5: Simulated ASM cell monolayers using the vertex-based modelling approach with time dependent evolution. The structure of (a,b) Tissue 1 and (c,d) Tissue 2 (two random instantiations that do not differ otherwise) can be seen before (left column) and after (right column) a period of serum deprivation, under switching rates $k_{pc} = 0.01$ and $k_{cp} = 0.00001$ and with an internal spring extension of $L_{ext} = 0.8$. Cells under net compression are shown in green, while cells with net tension are yellow.

In Figure 6.6 we illustrate our hypothesis that for a population of predominantly proliferative cells (before serum deprivation), most cells are rounded and so the distribution of angles between adjacent vertices measured at the centre of each cell will be centred on 60°. As more cells switch to an elongated contractile phenotype, we expect the angle distribution to evolve (potentially to a bi-modal distribution). In our simulated results (Figure

6.7), the initial distribution of angles (Figure 6.7(a,c)) looks like a Gaussian distribution with a mean of approximately 60° in both Tissues 1 and 2. The distributions of these angles are then modified after the period of serum deprivation (Figure 6.7(b,d)). After serum deprivation, the angles have a higher variance and therefore a wider distribution that is consistent with our hypothesis, suggesting that more elongated cells are likely present.

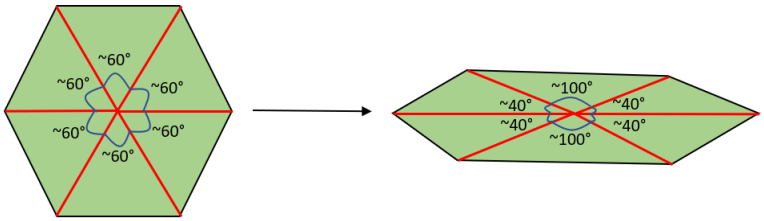

Figure 6.6: Diagram showing the way that proliferative cells (left) and contractile cells (right) are modelled in the vertex-based simulations; distributions of labelled angles are reported in Figure 6.7.

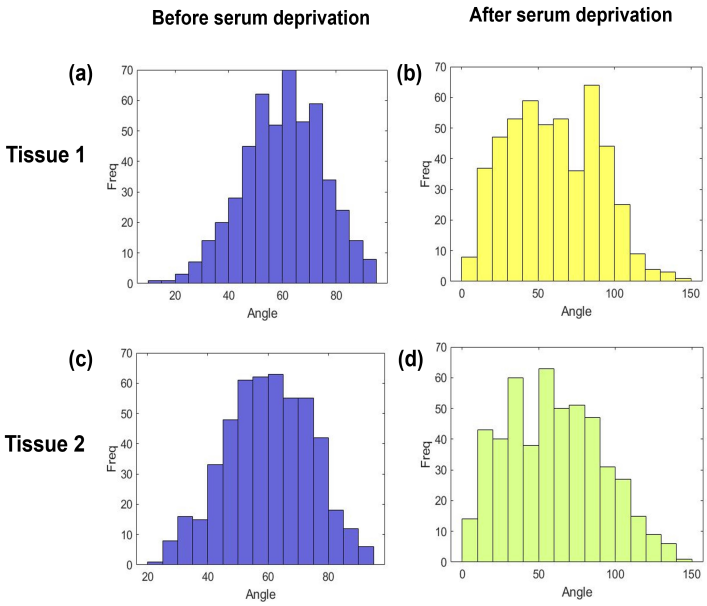

Figure 6.7: Distributions of all angles in each of the Tissues 1 and 2 described by Figure 6.6 before (a,c) and after (b,d) serum deprivation under switching rates $k_{pc} = 0.01$ and $k_{cp} = 0.00001$ and with an internal spring extension of $L_{ext} = 0.8$.

Next we simulate four random instantiations in order to measure the mean and variance of cell circularity and elongation (defined in Chapter 5) across phenotype populations at each time point. The results of the four instantiations are pooled in Figure 6.8. These clearly show that the proliferative population of cells change little in both mean circularity (Figure 6.8(a)) and mean elongation (Figure 6.8(b)) over this time period, with a small variance in their cell shapes across the tissue (most are fairly circular and not very elongated). The contractile cells, on the other hand, become more elongated and less circular over time on average, but have a much larger variance in cell shapes throughout their populations.

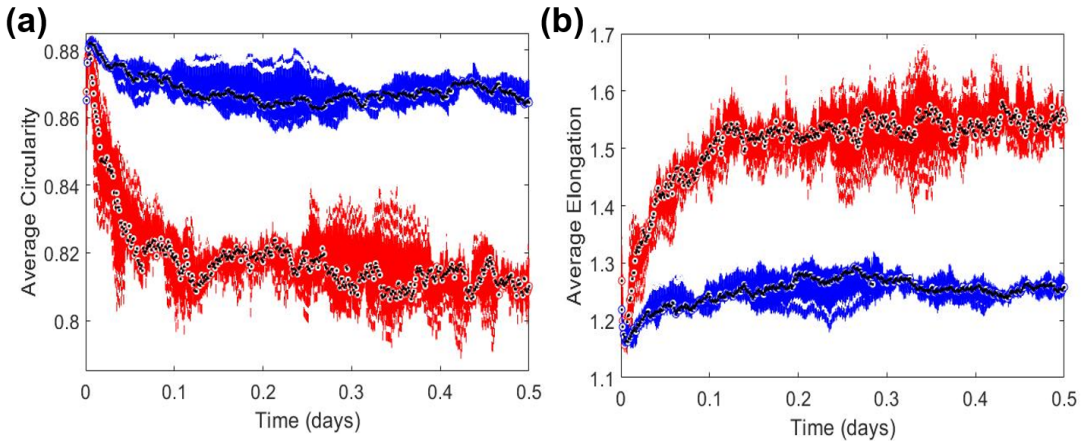

Figure 6.8: Change in the mean and variance of contractile (red) and proliferative (blue) cell circularity (a) and elongation (b) over time for four random instantiations of the simulated model developed in Chapter 5 with $k_{cp} = 0.05$ and $k_{pc} = 0.005$.

6.3.2 *Tissue measures*

In this section, we explore the changes in proportions and patterns of each cellular phenotype within the tissue over time and how this impacts cellular alignment.

Bundles

We track the average bundle size and alignment score over time, as cells switch phenotype with the corresponding shape and functional changes. We then plot an average alignment score over all bundles at each time point. Figure 6.9 shows these results for two different instantiations of simulated tissue (a) and (b). These examples show a clear increasing trend in cell alignment within contractile bundles after $t = 0.05$. This also fits with our observations of cell level elongation and angle distributions.

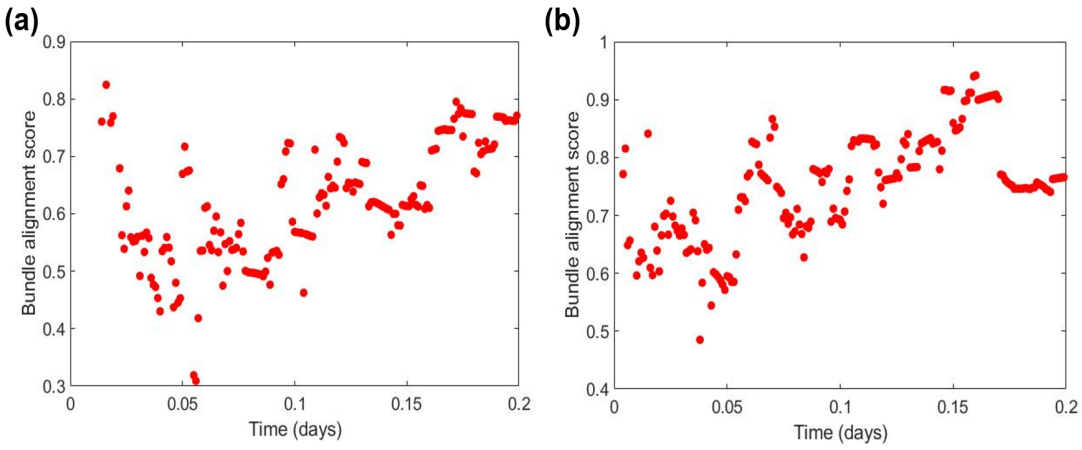

Figure 6.9: Average bundle alignment scores over time for two random instantiations of the simulated model developed in Chapter 5 with $k_{cp} = 0.05$ and $k_{pc} = 0.005$.

Paths

Although we are able to identify paths that travel through the whole simulated population (as in Figure 6.10), on analysis of the alignment within these paths, we find no evidence to indicate that the cells within paths become more aligned over time. In addition to exploring the alignment of cells within the path as a whole, we also analyse the pairwise alignment between neighbours within the path, and obtain similar results. We believe that this is due to the fact that, contractile cells do not remain contractile

long enough for the mechanical changes to occur before switching back to the proliferative phenotype.

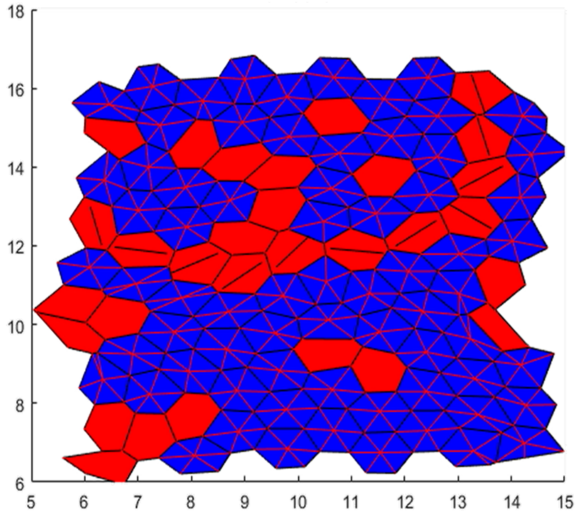

Figure 6.10: Simulated tissue, where phenotype switching has resulted in a long path of contractile cells. The shape tensor of cells in the chosen path are shown by a black line through each cell centre.

6.3.3 *Force Chains*

When analysing the make up of FCs we find that, although the lengths of FCs vary throughout the simulation, there is no significant trend in their length change over time (Figure 6.11(b)). We also demonstrate that the cells that make up these chains are mainly contractile (Figure 6.11(a)), thereby supporting the hypothesis that contractile cells cooperate in transmitting forces over long distances in tissues. In Figure 6.11(c), we can see that the most frequently observed FCs consist of just two contractile neighbours and, as both the FC length increases and the proportion of contractile cells decreases, the frequency with which they appear declines. This is likely a consequence of the switching rates that allow the saturation to a steady state

with a mixed population (hence contractile cells may not remain contractile long enough to reach their new resting state).

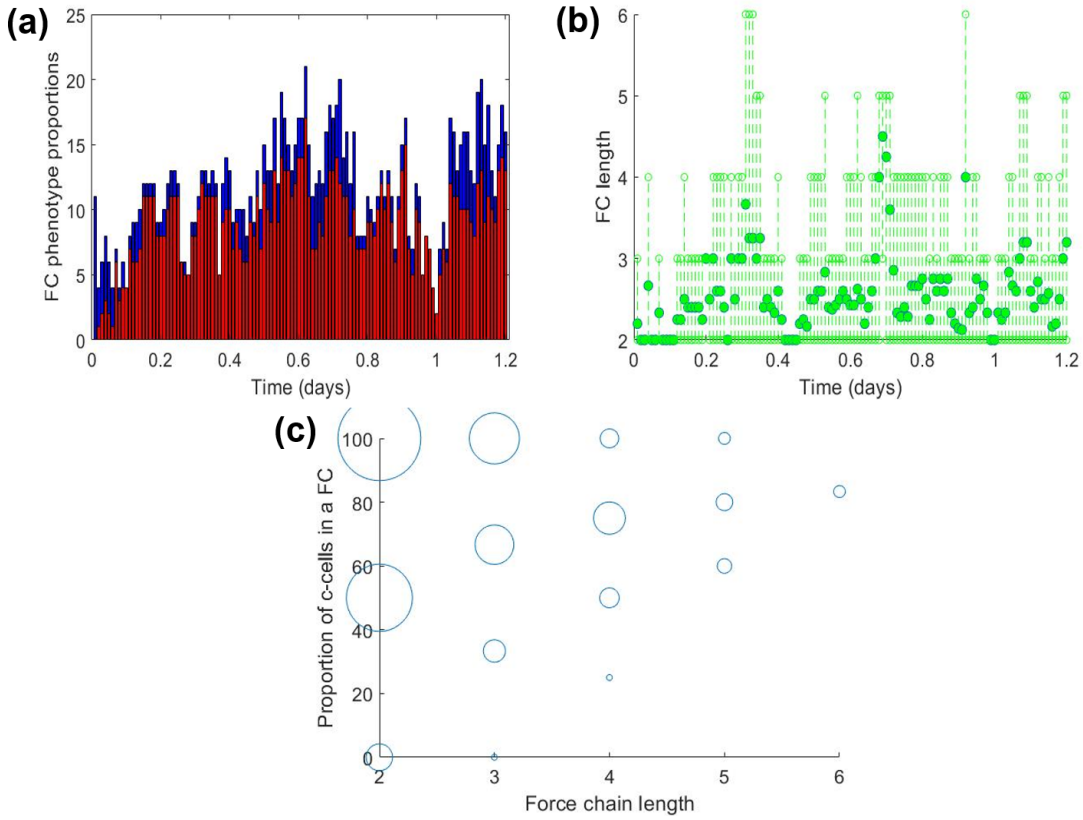

Figure 6.11: Force chain data plotted for every 10th time point over the simulation period. (a) The total number of cells in any FC at each time point and the proportion of those that are proliferative (blue) or contractile (red), (b) the average and variance in FC length at each time point, and (c) the corresponding total frequencies of each combination of these chain characteristics over the simulated time period, depicted by circles whose areas are proportional to frequency.

6.4 SUMMARY

ASM cell phenotype switching is incorporated into the vertex model in order to mimic cells in the experimental serum deprivation period. In the cellular results, we see a clear reduction in circularity, increase in elongation and an associated change in the distributions of cell internal angles throughout the period of serum deprivation. We also observe a reduction in the proportion of cells that experience net compression, with the few remaining compressed cells occurring in clumps.

In exploring tissue measures, we find that the cells within bundles align with one another during serum deprivation however this is not the case for paths that make up bundles or for pairs of contractile cells alone. We do, however, find long paths of contractile cells that traverse the whole cell layer. Finally, in our analysis of force chains across the tissue, we find that the majority of cells that make up these chains are contractile, the most frequent being made of just a contractile pair of cells.

While these simulations are set up to mimic experimental protocols, future work would consider accounting for more *in vivo* behaviour, in which longer force chains may arise more frequently. These simulations additionally do not account for the impact of contractile agonist, which will be explored in the next chapter.

7

CELL VERTEX MODEL: SIMULATING ASTHMATIC EXACERBATIONS

Following the development and testing of our mechanical vertex-based model for an ASM cell monolayer (Chapter 5), which was then further developed to incorporate cell phenotype switching (Chapter 6), we now use this model to simulate the impact of an asthmatic exacerbation. By illustrating the changes in cell and tissue properties during and post exacerbation, we aim to learn more about the mechanisms underlying multicellular mechanics that may occur *in vivo*.

In this chapter, we first discuss the modelling approach used to simulate an exacerbation. We then test this by investigating the impact of exacerbations on three different test cases: (i) a fixed ASM population (i.e. no phenotype switching); (ii) a toy model of a whole small airway surrounded by ASM cells without phenotype switching, and (iii) an ASM population undergoing phenotype switching. The final test case allows us to undertake a qualitative comparison of the simulated results to our TFM experimental data (discussed in Chapter 3).

7.1 MODELLING APPROACH AND IMPLEMENTATION

As previously described (Chapter 1), an exacerbation is caused by the recognition of an allergen in the airway, leading to the de-granulation of mast

cells which release contractile mediators like histamine. These mediators act as a stimulus which contributes to the generation of a contractile force in ASM cells.

For simplicity, we assume that increased contractile force can be represented by an increase in the isometric force F_0 in Equation 5.12 (the effect of this is shown in Figure 7.1(a)). During the time period of increased stimulus (where $A \leq t \leq B$), we therefore assume that F_0 is a time-dependent function represented by

$$F_0(t) = \alpha + \beta((\mathcal{H}(t - A) - \mathcal{H}(t - B)), \tag{7.1}$$

where $\mathcal{H}(t)$ is the Heaviside function, α is the baseline value of F_0 and β is the amount by which F_0 increases (Figure 7.1(b)). This will affect the load acting on each cell and hence the overall mechanical stress/strain.

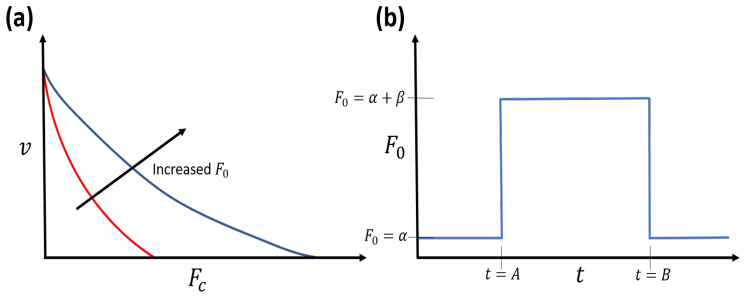

Figure 7.1: Schematics to show (a) the force velocity relationship given an increase in F_0 and (b) the change in F_0 for an increased stimulus in the period $A \leq t \leq B$.

7.2 EFFECT OF EXACERBATION IN A FIXED POPULATION

In the first test case, we simulate an asthmatic exacerbation in a mixed population of contractile and proliferative ASM cells that do not undergo phenotype switching. As in previous simulations, all cells begin as regular

hexagons that have been randomly perturbed such that each cell has near equal internal spring resting lengths and, therefore, a high circularity (as described in Section 5.2.2). While the population is fixed (so no phenotype switching will occur), the cells assigned as contractile in this simulation will need to elongate for their internal springs to reach their resting state.

We use a population with a small number of contractile cells (just 4 out of a total population of 100 cells), such that we are able to explore changes in individual contractile cells. The exacerbation is then simulated between $2 \leq t \leq 3$, hence F_0 increases by 20 during this period (shown by Figure 7.1(b) with $A = 2, B = 3, \alpha = 3$ and $\beta = 20$). We then measure the cellular circularity, elongation, stress and strain of each of these contractile cells (Figure 7.2).

7.2.1 *Results*

In the initial period (prior to exacerbation), the contractile cells within the population undergo a significant initial decrease in circularity (Figure 7.2(a)) and increase in elongation (Figure 7.2(b)), as expected. During this time, we can also see that the average cell stress (Figure 7.2(c)) and strain (Figure 7.2(d)) of the contractile population are higher than that of the proliferative population (which is close to zero). Furthermore, the strain of the contractile population decreases, while the stress of the contractile population varies in a non-monotonic fashion as the cells rearrange during this process.

During the exacerbation period, we see a large change in the cellular dynamics of the contractile population. The circularity stops decreasing and instead increases before levelling off (Figure 7.2(a)), while the elongation similarly stops increasing and instead decreases before levelling off (Figure 7.2(b)); both circularity and elongation appear to have reached a new equilibrium. These results are consistent with the expectation that elongated

contractile cells would shorten (and hence become more circular) under a contractile stimulus.

During this period of exacerbation, we can also see that the average cell stress of the contractile population has an initial large jump to a high level of stress (Figure 7.2(c)). The average stress then decreases throughout the period, returning to a similar level to that before the exacerbation was initiated. The average stress in the proliferative population follows a similar trend (albeit at lower levels) because of the altered load transmitted from contractile cells to neighbouring proliferative cells. The average contractile cell strain (Figure 7.2(d)), however, only gradually increases during this period.

After the contractile stimulus is removed (when $t > 3$), we see an initial small increase in circularity of contractile cells before a larger period of decrease, and then finally levelling off at approximately $t = 3.5$ (Figure 7.2(a)). The initial increase in circularity could be explained as an impact of our modelling choices, given that the direction of elongation is set (upon allocation as a contractile phenotype) and so the cell may need to move through a more rounded state before elongating in the given direction. Since the shape change of each of these cells has an effect on their neighbours and consequently the cell network as a whole, each of the contractile cells seem to reach the point at which they level off at around the same time ($t = 3.5$). Looking at the change in elongation after the contractile stimulus is removed, the contractile cells begin elongating once again, though at a slower rate than before the exacerbation (Figure 7.2(b)). The average stress and strain of contractile cells (Figure 7.2(c,d)) undergo a small change immediately after the stimulus is removed (for the same reason as for the initial increase in circularity discussed above). Both then stay fairly constant for the remaining period of the simulation, at a value significantly higher than

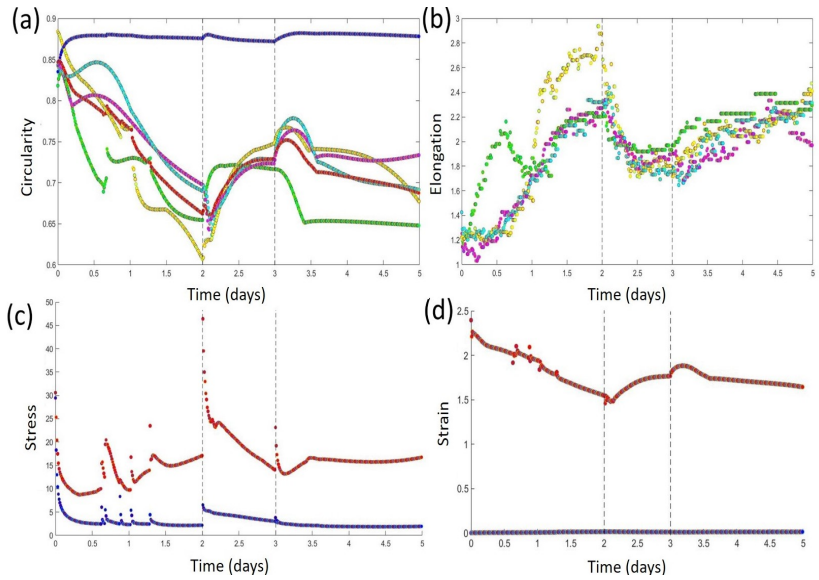

Figure 7.2: Simulation of the vertex-based model with no switching and an increase in stimulus to give $F_0 = 23$ between $2 \leq t \leq 3$ (Figure 7.1(b) with $A = 2, B = 3, \alpha = 3$ and $\beta = 20$). Results are shown for (a) circularity, (b) elongation, (c) stress and (d) strain of four individual contractile cells (marked in yellow, light blue, green and pink), as well as the average for a contractile (red) and proliferative (blue) population. Parameters are as in Table 4 except for the following: $\tilde{K} = 0.5$, $\tilde{K_{int}} = 0.5$, $a = 0.01$.

for the average of the proliferative population, as before.

The discontinuous parts of Figure 7.2 that occur for $t < 2$ (before the stimulus increases) or $t > 3$ (when the stimulus has been removed) are a result of the T1 transitions (discussed in Section 5.1.2).

7.3 MIMICKING THE CONTRACTION OF A SMALL AIRWAY

We next simulate an asthmatic exacerbation in a toy model of a small airway. We do this by forming a hole in our network where no cells exist; this represents the lumen of a small airway. We then assign the cells directly

adjacent to this hole to be of the contractile phenotype in order to mimic airway contractility, and the rest of the cells to be passive non-specific tissue (modelled in the same way as we do for proliferative ASM cells). As usual, all cells begin as regular hexagons that have been randomly perturbed. We therefore expect the contractile cells to elongate as they approach an equilibrium, until the exacerbation is initiated leading to an increase in F_0 by 20 at time $0.2 \leq t \leq 0.3$ (shown by Figure 7.1(b) with $A = 0.2, B = 0.3, \alpha = 3$ and $\beta = 20$), where we then expect to see their contraction. The time period for this exacerbation is for a smaller value of t than in our previous simulation. This is because, when a contractile cell is surrounded by proliferative cells (like those in Section 7.2), the proliferative cells reorganise over time to allow for contractile cell changes. Here, however, all contractile cells are connected and so are likely unable to evolve to their resting state. We therefore simulate the exacerbation at an earlier time, when the displacement of cells is already negligible.

7.3.1 *Results*

We observe changes in the shape of contractile cells at time points $t = 0$ (Figure 7.3(a)), $t = 0.19$ (immediately prior to exacerbation; Figure 7.3(b)), $t = 0.23$ (during the exacerbation period; Figure 7.3(c)) and $t = 0.35$ (after the exacerbation; Figure 7.3(d)). The most significant change in the shapes of contractile cells occurs between time points $t = 0.19$ and $t = 0.23$, which coincides with the initiation of the exacerbation at $t = 0.2$. We measure the lumen area and plot it as a function of time in Figure 7.4; we observe a significant decrease in area that we would expect during an exacerbation. Interestingly, the lumen area remains at this new, slightly smaller area even when the exacerbation has ended. This could be due to the rearrangement of the contractile cells adjacent to the lumen as the cells change shape (possibly undergoing transitions) during the exacerbation.

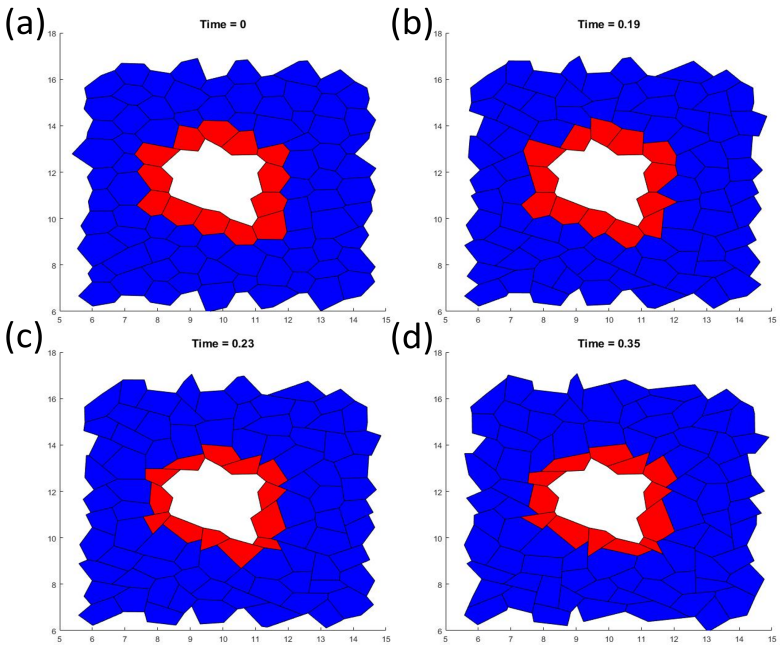

Figure 7.3: Toy vertex-based model of a small airway at (a) $t = 0$ days, (b) $t = 0.19$ days, (c) $t = 0.23$ days and (d) $t = 0.35$ days, where the exacerbation with an increase in F_0 by 20 occurs at $0.2 \leq t \leq 0.3$. Parameters are as in Table 4 except for $\tilde{K} = 0.4$.

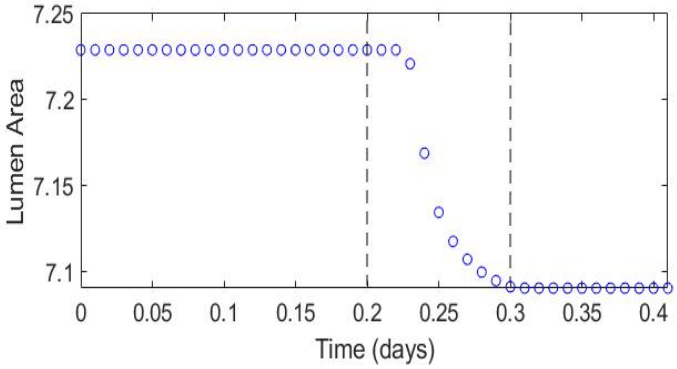

Figure 7.4: Area of the lumen in the toy airway model simulated in Figure 7.3 with an exacerbation at $0.2 \leq t \leq 0.3$.

7.4 MIMICKING THE EFFECT OF SERUM-DEPRIVATION ON FORCES IN ASM MONOLAYERS

Finally, we simulate a monolayer of ASM cells to mimic our experimental protocol from Section 3.2. This enables us to qualitatively compare simulated results to our experimental data. As mentioned at the beginning of Chapter 5, the development of a vertex-based model was motivated by the availability of spatial-temporal data for contractile forces that was collected during the TFM experiment (developed to characterise phenotype switching of ASM sub-populations during serum deprivation) but not required for the earlier ODE model. The TFM protocol involved imaging cells before and after the addition of a contractile stimulus on days 0, 3, 7 and 10 during a 10 day period of serum deprivation. An example of these results at each experimental time-point for a given image frame can be seen in Figure 7.5. We note that these images are only presented for illustrative purposes, to indicate how spatial aspects are represented in the data. The images in Figure 7.5 also show artefactual behaviour at the edges (due to the use of Fourier analysis when calculating tractions [14]), that should be disregarded in any analysis.

Now that we have developed a vertex-based model with phenotype switching, and tested the impact of an exacerbation for fixed populations, here we simulate a population with phenotype switching to match the switching initiated by serum deprivation in the experimental protocol.

Experimentally, confluent monolayers of ASM cells contain approximately 22,000 cells per well (given a well size of approximately 113mm^2) in the 96 well plates used in TFM. Given that the imaging area in this experiment is 732mm^2 $=$ 0.5358mm^2, we can estimate that there are approximately 105 cells within each image frame. We therefore simulate a population of 100 ASM cells that are initially all proliferative as described in Section 5.2.2.

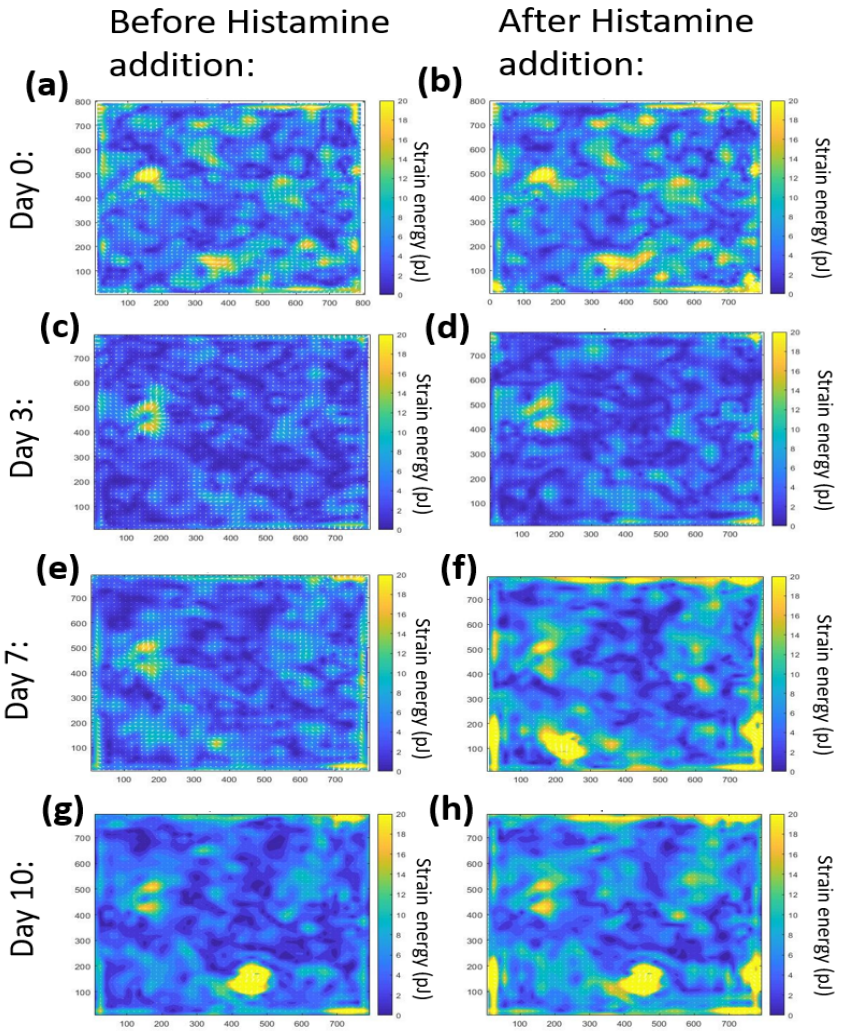

Figure 7.5: TFM experimental results showing heat-maps for the spatial changes in strain energy before (left column) and after (right column) the addition of the contractile stimulus at serum deprivation time points (a-b) day 0, (c-d) day 3, (e-f) day 7 and (g-h) day 10. The full experimental protocol and averaged results are shown in Section 3.2.

Phenotype switching is initiated from the start given that the serum was removed at day 0 in the experiment.

We impose switching rates of $k_{cp} = 0.0001$, $k_{pc} = 0.004$ to account for serum deprivation. These rates are chosen to create a sub-population of contractile cells within our simulation period, without all cells switching to the contractile phenotype, and with contractile cells remaining contractile long enough to elongate (hence k_{cp} is kept small). The time points of histamine additions are then chosen to illustrate the impact of stimulation at different points within the switching period from a fully proliferative population to a population of both proliferative and contractile cells, as in the experimental protocol. We therefore simulate histamine additions at $t = 0 - 0.014$, $t = 0.086 - 0.1$, $t = 0.152 - 0.166$ and $t = 0.214 - 0.216$. Each addition is represented by an increase in F_0 by 8 during these periods. We then measure the spatial-temporal changes in strain energy as a measure of contractile force as well as the changes in the average circularity, elongation, stress and strain of each population over time. We recall that we measure strain as the relative difference between a cells area and its resting area, whereas strain energy in the experimental protocol is calculated using the displacement field and Fourier transform traction cytometry (described in Section 1.4.2).

7.4.1 *Results*

Figure 7.6 shows heat-maps for the spatial changes in strain energy before and after each of the four simulated histamine additions, where contractile cells are marked with a red outline. We first note that Figure 7.6(a) shows a fully proliferative population at $t = 0$, therefore the high strain values are likely due to the initial random configuration of cells not having had sufficient time to reorganise towards their resting state. The number of contractile cells is shown to increase over time from 4 in Figure 7.6(b), to 33 in Figure 7.6(h). We see throughout that hotspots of both particularly high strain energy (cells with an area much larger than their resting area, shown in yellow) and particularly low strain energy (cells with an area much smaller than their resting area, shown in dark blue) coincide with the

contractile phenotype. We also see that it is these areas of larger magnitude that change the most during a histamine addition, with their strain energy values becoming more extreme afterwards. The strain of these areas seems to tend towards their pre-stimulated value during periods without histamine, but a combination of the changes to cell shape and the addition of new contractile cells results in a reorganised tissue following each histamine addition.

We now qualitatively compare our simulated results (Figure 7.6) to our experimental data (for which one image area can be seen in Figure 7.5), remembering that the artefactual behaviour at the edge of the field in the experimental results should be disregarded. We see that both sets of heatmaps display variable levels of low-magnitude strain across the simulation or image area, with a few small hotspots of strain energy with a larger magnitude. We also find that, for experimental results after day 0 (Figure 7.5(c–h)) and for simulated results up to histamine addition three (Figure 7.6(a–f)), each successive histamine addition results in a larger area of high strain energy. The strain energy after a histamine addition in Figure 7.6(h) is similar to that of Figure 7.6(f), possibly due to the fact that there is a much smaller increase in the number of contractile cells compared to between Figure 7.6(b–d) or between Figure 7.6(d–f).

In the averaged temporal experimental results, we found that basal forces decreased with cell culture time while histamine-induced traction force increased with culture time (Section 3.2.3). While our simulated results (Figure 7.6) indeed show an agonist-induced increase in energy over time, we do not see the decrease in basal forces over time, possibly due to contractile cells not having enough time after switching to relax to their altered resting state. The lack of time post stimulation was due to wanting to explore the impact of stimulation throughout the phenotype switching process. Waiting too long post-stimulation would mean that the contractile population

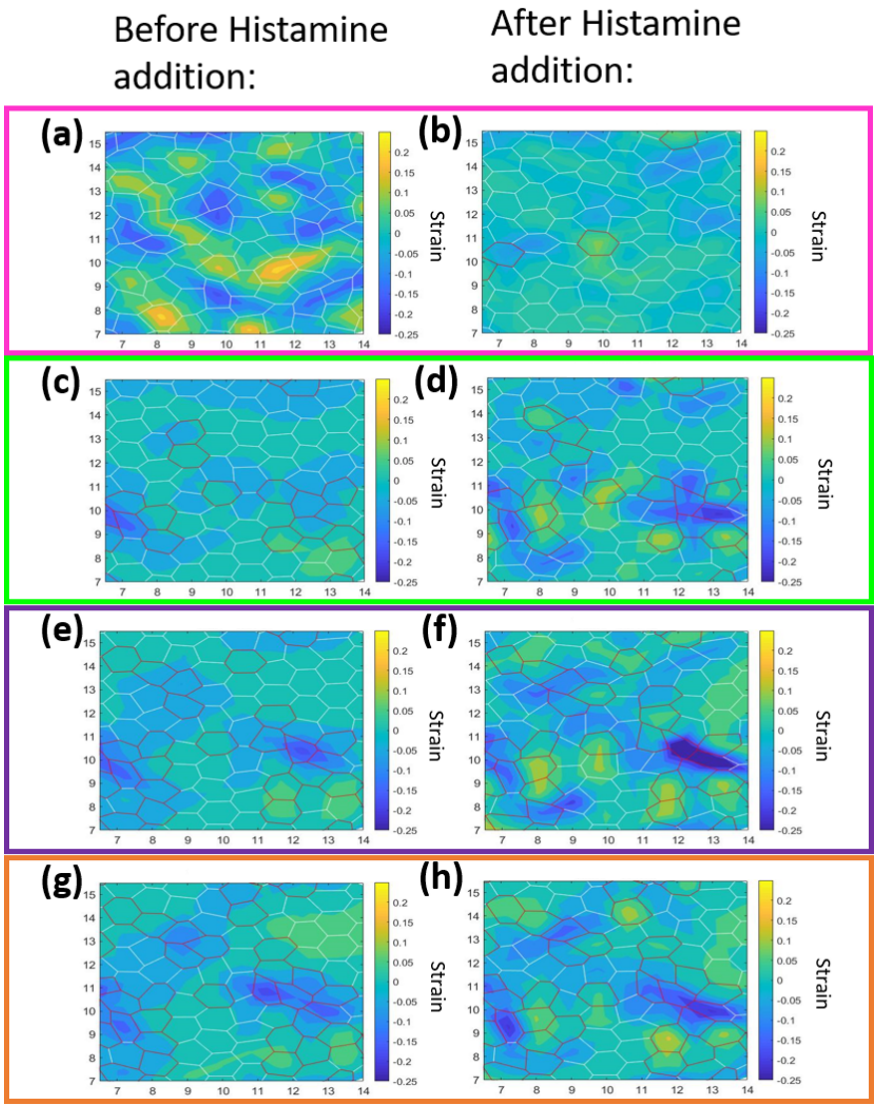

Figure 7.6: Heat-maps for strain energy of a simulated phenotype switching ASM population before and after four separate histamine additions at $t = 0 - 0.014$ (pink block), $t = 0.086 - 0.1$ (green block), $t = 0.152 - 0.166$ (purple block) and $t = 0.214 - 0.216$ (orange block). Contractile cells are shown by their red outline. Here, $h = 0.002$ and parameters are as in Table 4 except for $k_{cp} = 0.0001$ and $k_{pc} = 0.004$. F_0 increases by 8 during each histamine addition.

would grow too large. We can, however, see this result for our fixed popu-

lation in Figure 7.2(d).

Figure 7.7 shows changes in the average circularity (Figure 7.7(a)), elongation (Figure 7.7(b)), stress (Figure 7.7(c)), and strain (Figure 7.7(d)) over time, for the ASM cell population shown in Figure 7.6. The average values for the contractile population are shown in red and the proliferative population are in blue. The time period of each histamine addition is marked by the coloured block: pink for histamine addition one at $t = 0 - 0.014$, green for histamine addition two at $t = 0.086 - 0.1$, purple for histamine addition three at $t = 0.152 - 0.166$ and orange for histamine addition four at $t = 0.214 - 0.216$. As expected, the contractile agonist has a larger impact on the contractile population, the proliferative population only being affected through the re-adjustment of the entire monolayer to account for the load generated by the shortening contractile cells. Below we discuss changes to the contractile population in this simulation.

The first histamine addition (shown by the pink block) occurs at $t = 0$ in order to match experimental protocol. We see that average circularity increases (Figure 7.7(a)) and average elongation decreases (Figure 7.7(b)) during this period, as consistent with the results of the fixed population during stimulation (Figure 7.2(a,b)). During the other three histamine additions however, there is a rapid decrease in the average ASM cell circularity and increase in the average ASM cell elongation. Using videos to improve our understanding of why this happens, we pose that this could be due to contractile cells rapidly contracting along their axis of elongation but, in still needing to evolve toward their resting state, cells are forced to elongate in the direction perpendicular to their designated angle of elongation. Moreover, this could be the reason why basal forces do not appear to decrease over time in Figure 7.6; since cells would need extra time to re-elongate in their initially assigned direction, perpendicular to their elongation during a histamine addition. Further work would aim to investigate the change in

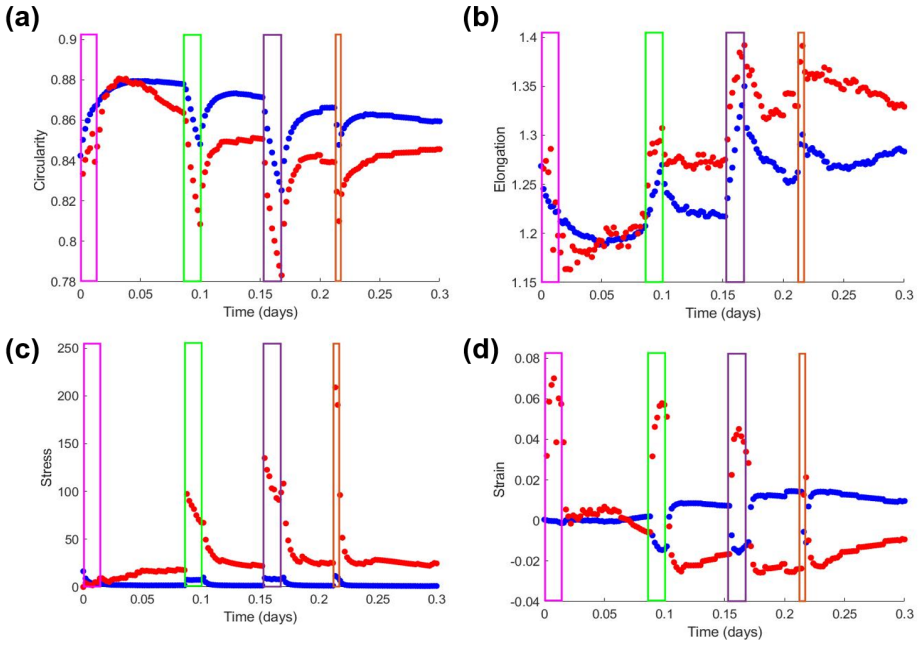

Figure 7.7: Average circularity (a), elongation (b), stress (c), and strain (d) for the contractile (red) and proliferative (blue) populations shown in Figure 7.6. Coloured blocks indicate the four time points during serum deprivation that histamine is added and match the four time points shown in Figure 7.6. Here, $h = 0.002$ and parameters are as in Table 4 except for $k_{cp} = 0.0001$ and $k_{pc} = 0.004$. F_0 increases by 8 during each histamine addition.

cell area distribution during contraction experimentally and implement a modelling approach to mimic this.

Immediately after the removal of histamine, average circularity increases and average elongation decreases. Following histamine additions two (green) and three (purple), the average circularity seems to level off at a value lower than its previous equilibrium prior to stimulation and the average elongation seems to level off at a value higher than its previous equilibrium prior to stimulation. Following histamine addition four (orange), both average circularity and elongation return to a value similar to that of before this

stimulation. This could be a result of the shorter period of stimulation.

Figure 7.7(c) shows that the average contractile ASM cell stress increases significantly immediately after the addition of histamine (except for in histamine addition one), then gradually decreases towards its pre-stimulation value during the period of histamine addition and continues to decrease towards this value post stimulation. Each successive histamine addition one–four results in a larger immediate increase in average stress, however, the stress seems to return to the same equilibrium after the removal of histamine each time.

Figure 7.7(d) shows that a histamine addition leads to a significant increase in the average contractile cell strain after a small delay. Following histamine addition one, the average contractile strain first returns to a value similar to that of the proliferative population (close to zero), before decreasing below zero due to contractile cells having a smaller area than their resting state. A higher magnitude of strain can therefore be seen in contractile cells compared to proliferative cells throughout. Following histamine additions two, three and four, the strain returns to this negative average strain.

Similarly to the observed changes in lumen area (Figure 7.4), the results of Figures 7.6 and 7.7 suggest a possibly irreversible cell rearrangement which could contribute to asthma pathology. This is because both measures of cell elongation do not return fully to their pre-exacerbation level after each exacerbation, hence each successive exacerbation results in a population with less circular, more elongated contractile cells, that will exert a larger force during contraction.

7.5 SUMMARY

In this chapter, we use the vertex-based ASM model developed in Chapters 5 and 6 to explore the changes in cellular dynamics during and after the simulation of an asthmatic exacerbation. Three test cases are used in order to investigate the cellular and population dynamics under different conditions.

In the first test case, we simulate a population of ASM cells with a small proportion of these having just switched to a contractile phenotype. The simulation then runs with no further phenotype switching so that the contractile cells are able to elongate towards their resting state without the possibility of switching again. During the exacerbation we see a significant increase in circularity, and decrease in elongation, of contractile cells. The average strain of contractile cells also increases during the exacerbation.

In the second test case, we simulate a toy model of a small airway where a hole in the network of cells represents the lumen of an airway. The results show that the lumen area decreases during an exacerbation and remains at the new, slightly smaller area even when the stimulus has been removed. This result shows a possible mechanism of tissue remodelling.

In the final test case, we mimic our TFM experimental protocol from Chapter 3 in order to simulate results that we can qualitatively compare to the spatial-temporal results obtained in this experiment. We see similarities in the distribution of strain energy across the monolayer (variable low levels with hotspots of high magnitude strain) and both experimental and simulated results show an increase in strain magnitude in these hotspots following histamine addition, as well as some evidence of increases in stimulus induced contraction with each successive exacerbation. Finally, by observing the average circularity, elongation, stress and strain of the simulated cell populations in this test case, we see changes to the contractile population

equilibrium following a histamine addition for several of these measures, further evidencing the existence of tissue remodelling.

8

CONCLUSIONS

In this thesis, we have used *in vitro* and *in silico* techniques in complement to learn about mechanisms of airway remodelling in asthma. In culture, ASM cells exhibit changes in cell shape and contractile ability between a spindle-shaped contractile phenotype and a more rounded proliferative phenotype with synthetic properties. The link between phenotype switching and corresponding changes in structure, function and relative biomechanical abilities *in vivo* is currently unclear, but is key to understanding remodelling. Our aim was to develop both mathematical models and novel *in vitro* experimental protocols, to combine their insights, and to use them to understand the role of ASM phenotype switching in the thickening of the airways responsible for fatal attacks in severe asthmatics. To our knowledge this work is the first to model the specific pathway of remodelling discovered by Naveed *et al* [56], uses novel experiments designed specifically based on model results, and presents the only vertex-based model for ASM cells with phenotype specific dynamics including active contraction. In Section 8.1, we summarise the main findings of this work. Section 8.2 then discusses areas of interest for future work.

8.1 SUMMARY OF MAIN FINDINGS

In Chapter 1 we reviewed the literature surrounding asthma (in particular asthmatic airway remodelling), the *in vitro* experimentation methods that

we go on to use in Chapter 3, and previous mathematical modelling techniques (either that explore airway remodelling or that we use for this purpose). Mathematical models in combination with *in vitro* methods allows for a deeper exploration of the mechanisms involved, as well as the ability to make predictions about the future dynamics of a system. There have been relatively few attempts at modelling asthmatic airway remodelling and a very small number that consider ASM phenotypes. Those that do, show an increase in ASM mass over time that is consistent with airway remodelling and this is often reliant on parameters relating to agonistic/inflammatory magnitude and resolution [17, 33]. We finally found that cell-based models enable the incorporation of cellular forces into models and are used widely to explore mechanical properties of epithelial tissues [24, 53]. While several methods have been developed, we found vertex-based models to best represent the properties of cellular monolayers as a whole including cell–cell functional mechanics [53, 58].

Chapter 2 was an extension of my Masters Dissertation (Appendix A), in which we developed an ODE model based on a newly discovered pathway of airway remodelling involving the activation of MMP-1. We first recapitulated the formulation, analysis and main results from that work (Section 2.1). The main findings of this project include the discovery of a mechanism of remodelling (through model bifurcation analysis, Figure 2.5) and the identification of the phenotype switching rates as the most important model parameters to accurately quantify (through parameter sensitivity analysis, Figure 2.4). We went on to develop this model to improve the biological realism and undertook further analyses to explore system dynamics following the addition of an exacerbation stimulus (Section 2.2). We maintained the observation of this mechanism of remodelling for some parameter set, as well as finding some interesting possibilities of limit cycle behaviour.

In Chapter 3, we used the results from Chapter 2 to inform the design of two novel *in vitro* experimental protocols that aimed to quantify phenotype switching rates in ASM cells. Both experiments used serum deprivation as a way of initiating a switch in human ASM cell phenotype in culture, from proliferative to contractile. In experiment 1 (Section 3.1), immunocytochemistry was used to measure the change in cell numbers (as a measure of proliferation) and the actin alignment (as a measure of contractility) over the period of serum deprivation. The results of this experiment (Figure 3.4) showed a four-fold increase in anisotropy over the period of serum deprivation and, along with total cell counts, were used to infer the proportion of each phenotype at each of our experimental time points.

In experiment 2 (Section 3.2), we measured contractility directly using traction force microscopy at different time points within the period of serum deprivation. This work was undertaken at Harvard Medical School with the help of Dr Ramaswamy Krishnan. We found that basal HASM cell force decreased with cell culture time, while histamine-induced contraction increased with culture time (Figure 3.6). This is consistent with the switch from a proliferative to a contractile population, and this data is again used as a measure of the proportion of each phenotype out of the whole population over time. We additionally explored the impact of adding activated mast cell supernatant to certain wells within this experiment, the results of which (Figure 3.7) further confirmed the importance of mast cell tryptase in airway remodelling, as discussed in Section 1.3 and incorporated in our ODE model. Following both experiments, the ODE model from Chapter 2 was reduced to match the experimental system and this enabled us to fit parameters to our data using a least squares method (Section 3.3.1).

Since experiments 1 and 2 contained relatively few time points, a Bayesian statistical analysis was undertaken in Chapter 4, with the aim of optimising further experiments for fitting parameters to our respective models. In order

to utilise the Bayesian approach, we first synthesised data using our reduced ODE model. We then used a Markov Chain Monte Carlo (MCMC) method to assess the impact of the number of time points on the distribution of parameter estimates. We show that the posterior distributions tighten around the true parameter value as the number of time points increases. When undertaking this analysis to assess the impact of the number of experimental repeats (by fitting an additional parameter representing the standard deviation of the noise of our simulated data), we found poor mixing and a need for a much higher number of iterations before converging. We hence went forward using an adaptive covariance to improve mixing. The optimised method was used to find parameter values for experimental data from both our experiments, as summarised in Table 3. It was also used to show that the same accuracy can be realised by collecting data at slightly fewer time points but with a larger number of repeats (which is more practical for these experimental protocols, Section 4.4).

In Chapter 5, we made use of the spatial-temporal data for contractile forces obtained during experiment 2 (Section 3.2), by developing a bio-mechanical cell-based model of the ASM mono-layer. A vertex-based approach was chosen due to it best representing important cell–cell junctional mechanics. Our cellular network of damped linear springs (where each cell is represented by a polygon), was created using a Voronoi tessellation and maintained as biologically reasonable though transitions (Section 5.1). We incorporated ASM cell phenotypes in this model through assigning differences in their shape and contractile machinery (Section 5.1.4). Simulations of this model for a population comprising of a small number of contractile cells in a largely proliferative population, showed that contractile cell elongation increases (Figure 5.9) and strain decreases (Figure 5.10) during the period of simulation. We also plotted stress-strain curves for different phenotypic tissue make-ups and found that the resulting non-linear mechanical properties of a tissue can be significantly effected by the size and distribution of a con-

tractile population.

In Chapter 6, we further developed our vertex model to match our experimental protocol by adding the process of gradual cell phenotype switching over the simulation period (representing the experimental time period for which the cells were deprived of serum), with rates chosen such that we obtained a small contractile sub-population. Upon evolving initial populations of 100 proliferative cells, we found that there was a reduction in the proportion of cells that experienced net compression over the simulation period (in which cell phenotypes were switching), with the few remaining compressed cells found together in clumps.

In Section 6.3.2, we explored the changes in tissue-level measures (including bundles, paths and force chains) in order to test our hypothesis that the mechanical environment of ASM cells and their neighbours drives changes in their structure and function, and hence is key in the phenotype switching process. Over the simulation period representing serum deprivation, we found: cellular alignment within bundles (Figure 6.9), paths of contractile cells that traverse the whole tissue (Figure 6.10) and that the phenotypic make-up of force chains is mainly contractile (with the most frequent being pairs of contractile cells, Figure 6.11). These results give an important indication of the impact of phenotype switching on long distance mechanical communication within ASM tissue.

Finally, in Chapter 7, we used the vertex-based model developed and tested in Chapters 5 and 6 to investigate the impact of an asthmatic exacerbation on the dynamics of the simulated ASM tissue, and illustrated how this compares to the results obtained in the TFM experiment of Chapter 3. We undertook three test cases to explore the population dynamics following an exacerbation under different tissue conditions. The first test (Section 7.2) consisted of a fixed population of mixed phenotype and showed that the

elongation of contractile cells (that occurs during serum deprivation) is reversed during the addition of a contractile stimulus (as they contract) but then continues following a short delay after the removal of the stimulus. In the second test case (Section 7.3), we simulated an exacerbation on a toy model of a whole airway and found a resultant decrease in the area of the airway lumen, which interesting remained after the removal of the stimulus (much like the results from our ODE model as seen in Figure 2.6).

In the final test case (Section 7.4), we simulated the model under conditions that mimicked the TFM experimental protocol, and found similarities between simulated and experimental results in both the distribution of strain energy across the monolayer as well as the increase in stimulus induced contraction with each successive exacerbation (Figure 7.6). We additionally found further evidence of tissue remodelling through changes in cell shape that compounded after each successive exacerbation rather than reversing upon the removal of the contractile stimulus (Figure 7.7).

8.2 SCOPE FOR FUTURE WORK

The results presented in this thesis suggests several directions for future work in this area. We conclude by discussing the scope for future work including: additional experimentation, further model analysis and validation, and model extensions.

8.2.1 *Additional experimentation*

Firstly, the Bayesian statistical analysis undertaken in Chapter 4, resulted in our knowledge of the optimal combination of experimental time points and repeats for a run of each of our experimental protocols in order to best

fit parameters to our ODE model while retaining practical feasibility. Further experimentation could make use of this information to more accurately quantify ASM phenotype switching rates in general, without over-fitting the model to a single experimental run. Furthermore, following the TFM experiment of Chapter 3 (experiment 2, Section 3.2), discussions with Dr Ramaswamy Krishnan and his team at Harvard Medical school involved several potential alterations to the protocol to optimise their ability to inform mathematical models. Examples include: collecting explicit cell numbers, using ISOproterenol to test if cells are contractile before the addition of an agonist and doing measurements for both collagen and fibronectin ligands to explore focal adhesion-based signalling.

In experiment 2 of Chapter 3 (Section 3.2), we explored the impact of the addition of activated (and inactivated) mast cell media, based on the presence of activated mast cells in the signalling pathway [56] used to develop the ODE model discussed in Chapter 2. While we found that activated mast cell supernatant led to an increase in histamine induced ASM contraction over the period of serum deprivation (agreeing with our ODE model formulation, Section 2.1), the experiment does not provide us with any information about the signalling steps between mast cell activation and ASM contraction. Interesting additional experiments would therefore include exploring the intermediate steps of the signalling pathway used to develop our ODE model, including MMP-1 activation and structural changes to ECM. The first of these additions could be incorporated relatively easily by adding an MMP-1 inhibitor to some of the mast cell supernatant treated wells.

Another hypothesis gained as a result of our TFM experimental data that could be tested using additional TFM experimentation, is: as we deprive ASM cells of serum (and therefore initiate the switch to a contractile phenotype), there is more cooperation between inter-cellular stresses and that this cooperation is enhanced further with activated mast cell media.

8.2.2 *Further model analysis and validation*

In Section 2.2, we extend our ODE model to include a baseline production value of mast cell tryptase. This results in the observation of three steady states for a certain range of parameter values. Following the simulation of a time course with the addition of an exacerbation (Figure 2.8), we find that the system is driven to the higher steady state following the addition of the stimulus, irrespective of which of the two lower steady states it begins sufficiently close to. We predict, however, that there may be a parameter space in which an exacerbation would drive the system beginning at the lower steady state to the intermediate state for which a further exacerbation would then result in the system reaching the highest state. This would be more representative of the gradual airway remodelling process. Further analysis of this model could use two-parameter bifurcation diagrams to explore the parameter space further, in order to discover such behaviour.

Our vertex-based model, developed and tested in Chapters 5-7, provides a framework that can be exploited in many different ways to learn more about ASM cell interactions and the impact of phenotype switching. For example, it could be used to explore whether cell signalling changes the shape and function of cells which then drives the phenotype change, or whether the change in phenotype is what initiates these changes (an important question that is left unanswered by experimentation alone). Another example would be to use the model to further explore cell patterning and orientation to find how the global structure of the monolayer affects the rate of contraction. Moreover, combining this model with other multiscale approaches could give a wider insight on the impact of changes in ASM cell structure and function on whole airway mechanics.

While the vertex-based model is currently useful for exploring the mechanistic behaviour of ASM cell monolayers during serum deprivation and

upon stimulation with a contractile agonist, the model would require further validation to be used for any of its predictive capabilities. A good place to begin with this validation would be to undertake parameter-fitting and uncertainty-quantification using TFM data, in order to fit mechanical model parameters.

8.2.3 *Model extensions*

There are a plethora of avenues for the extension of this vertex model, many of which expand on the models physiological detail. Based on the signalling pathway of airway remodelling discussed in this thesis and used to develop our ODE model discussed in Chapter 2, it would be useful to incorporate into the model the presence of mast cell tryptase, MMP-1 and ECM and impact of their activated/altered forms. The first of these is particularly significant considering the availability of TFM data for cells in media with activated mast cell supernatant (Figure 3.7). Under the inclusion of ECM in this model, the model could be exploited to learn more about ASM-ECM connections [62] in a remodelled airway and how this impacts the contractile force produced during an exacerbation.

BIBLIOGRAPHY

[1] An, S.S., Kim, J., Ahn, K., Trepat, X., Drake, K.J., Kumar, S., Ling, G., Purington, C., Rangasamy, T., Kensler, T.W. and Mitzner, W., 2009. Cell stiffness, contractile stress and the role of extracellular matrix. *Biochemical and biophysical research communications*, **382**(4), pp.697-703.

[2] Andersen, C.L., Jensen, J.L. and Ørntoft, T.F., 2004. Normalization of real-time quantitative reverse transcription-PCR data: a model-based variance estimation approach to identify genes suited for normalization, applied to bladder and colon cancer data sets. *Cancer research*, **64**(15), pp.5245-5250.

[3] Araujo, B.B., Dolhnikoff, M., Silva, L.F., Elliot, J., Lindeman, J.H.N., Ferreira, D.S., Mulder, A., Gomes, H.A., Fernezlian, S.M., James, A. and Mauad, T., 2008. Extracellular matrix components and regulators in the airway smooth muscle in asthma. *E*uropean Respiratory Journal, **32**(1), pp.61-69.

[4] Asthma, U.K., Slipping through the net. The reality facing patients with difficult and severe asthma, 2018. [Online]. [Accessed 4 March 2023]. Available from: https://www.asthma.org.uk/6fc29048/globalassets/get-involved/external-affairs-campaigns/publications/severe-asthma-report/auk-severe-asthma-gh-final.pdf

[5] Barton, D.L., Henkes, S., Weijer, C.J. and Sknepnek, R., 2017. Active vertex model for cell-resolution description of epithelial tissue mechanics. *PLoS computational biology*, **13(6)**, p.e1005569.

[6] Bayes, T., 1763. LII. An essay towards solving a problem in the doctrine of chances. By the late Rev. Mr. Bayes, FRS communicated by Mr. Price, in a letter to John Canton, AMFR S. *Philosophical transactions of the Royal Society of London*, (53), pp.370-418.

[7] Blume, C. and Davies, D.E., 2013. In vitro and ex vivo models of human asthma. European Journal of Pharmaceutics and Biopharmaceutics, **8**4(2), pp.394-400.

[8] Bock, M., Tyagi, A.K., Kreft, J.U. and Alt, W., 2010. Generalized voronoi tessellation as a model of two-dimensional cell tissue dynamics. *Bulletin of mathematical biology*, **72(7)**, pp.1696-1731.

[9] Boudaoud, A., Burian, A., Borowska-Wykręt, D., Uyttewaal, M., Wrzalik, R., Kwiatkowska, D. and Hamant, O., 2014. FibrilTool, an ImageJ plug-in to quantify fibrillar structures in raw microscopy images. *N*ature protocols, **9**(2), p.457.

[10] Brodland, G.W. and Veldhuis, J.H., 2002. Computer simulations of mitosis and interdependencies between mitosis orientation, cell shape and epithelia reshaping. *Journal of Biomechanics*,**35**(5), pp.673-681.

[11] Brook, B.S., Peel, S.E., Hall, I.P., Politi, A.Z., Sneyd, J., Bai, Y., Sanderson, M.J. and Jensen, O.E., 2010. A biomechanical model of agonist-initiated contraction in the asthmatic airway. *R*espiratory physiology & neurobiology, **1**70(1), pp.44-58.

[12] Brooks, S., 1998. Markov chain Monte Carlo method and its application. *Journal of the royal statistical society: series D (the Statistician)*, **47**(1), pp.69-100.

[13] Burry, R.W., 2011. Controls for immunocytochemistry: an update.*J*ournal of Histochemistry & Cytochemistry, **5**9(1), pp.6-12.

[14] Butler, J.P., Tolic-Nørrelykke, I.M., Fabry, B. and Fredberg, J.J., 2002. Traction fields, moments, and strain energy that cells exert on their

surroundings. *A*merican Journal of Physiology-Cell Physiology,**2**82(3), pp.C595-C605.

[15] Chan, V., Burgess, J.K., Ratoff, J.C., O'connor, B.J., Greenough, A., Lee, T.H. and Hirst, S.J., 2006. Extracellular matrix regulates enhanced eotaxin expression in asthmatic airway smooth muscle cells. *A*merican journal of respiratory and critical care medicine, **1**74(4), pp.379-385.

[16] Chang, S., Song, S., Lee, J., Yoon, J., Park, J., Choi, S., Park, J.K., Choi, K. and Choi, C., 2014. Phenotypic modulation of primary vascular smooth muscle cells by short-term culture on micropatterned substrate. *P*LoS One, **9**(2), p.e88089.

[17] Chernyavsky, I.L., Croisier, H., Chapman, L.A., Kimpton, L.S., Hiorns, J.E., Brook, B.S., Jensen, O.E., Billington, C.K., Hall, I.P. and Johnson, S.R., 2014. The role of inflammation resolution speed in airway smooth muscle mass accumulation in asthma: insight from a theoretical model. *PloS one*,**9**(3), pp.e90162.

[18] Classen, A.K., Anderson, K.I., Marois, E. and Eaton, S., 2005. Hexagonal packing of Drosophila wing epithelial cells by the planar cell polarity pathway. *Developmental cell*, **9**(6), pp.805-817.

[19] Dobrin, A., 2005. A review of properties and variations of Voronoi diagrams. *Whitman College*, pp.1949-3053.

[20] Eisenberg, E. and Levanon, E.Y., 2013. Human housekeeping genes, revisited. *Trends in Genetics*, **29**(10), pp.569-574.

[21] Eliason, S.R., 1993. *Maximum likelihood estimation: Logic and practice* (No. 96). Sage.

[22] Elshaw, S.R., Henderson, N., Knox, A.J., Watson, S.A., Buttle, D.J. and Johnson, S.R., 2004. Matrix metalloproteinase expression and activity in human airway smooth muscle cells. *British journal of pharmacology*, **142**(8), pp.1318-1324.

[23] Escudero, L.M., Costa, L.D.F., Kicheva, A., Briscoe, J., Freeman, M. and Babu, M.M., 2011. Epithelial organisation revealed by a network of cellular contacts. *Nature communications*, **2**(1), pp.1-7.

[24] Fletcher, A.G., Osborne, J.M., Maini, P.K. and Gavaghan, D.J., 2013. Implementing vertex dynamics models of cell populations in biology within a consistent computational framework. *Progress in biophysics and molecular biology*, **113**(2), pp.299-326.

[25] Freyer, A.M., Johnson, S.R. and Hall, I.P., 2001. Effects of growth factors and extracellular matrix on survival of human airway smooth muscle cells. *American journal of respiratory cell and molecular biology*, **25**(5), pp.569-576.

[26] Gibson, M.C., Patel, A.B., Nagpal, R. and Perrimon, N., 2006. The emergence of geometric order in proliferating metazoan epithelia. *Nature*,**442(7106)**, pp.1038-1041.

[27] Gillespie, D.T., 1977. Exact stochastic simulation of coupled chemical reactions. *T*he journal of physical chemistry, **8**1(25), pp.2340-2361.

[28] Haario, H., Saksman, E. and Tamminen, J., 2001. *A*n adaptive Metropolis algorithm. Bernoulli, 7(2), pp.223-242.

[29] Hai, C.M. and Murphy, R.A., 1988. Cross-bridge phosphorylation and regulation of latch state in smooth muscle. *A*merican Journal of Physiology-Cell Physiology,**2**54(1), pp.C99-C106.

[30] Halayko, A.J., Camoretti-Mercado, B., Forsythe, S.M., Vieira, J.E., Mitchell, R.W., Wylam, M.E., Hershenson, M.B. and Solway, J., 1999. Divergent differentiation paths in airway smooth muscle culture: induction of functionally contractile myocytes. *A*merican Journal of Physiology-Lung Cellular and Molecular Physiology, **2**76(1), pp.L197-L206.

[31] Halayko, A.J., Tran, T. and Gosens, R., 2008. Phenotype and functional plasticity of airway smooth muscle: role of caveolae and caveolins. *Proceedings of the American Thoracic Society*, **5**(1), pp.80-88.

[32] Hassan, M., Jo, T., Risse, P.A., Tolloczko, B., Lemière, C., Olivenstein, R., Hamid, Q. and Martin, J.G., 2010. Airway smooth muscle remodeling is a dynamic process in severe long-standing asthma. *J*ournal of Allergy and Clinical Immunology, **1**25(5), pp.1037-1045.

[33] Hill, M.R., Philp, C.J., Billington, C.K., Tatler, A.L., Johnson, S.R., O'Dea, R.D. and Brook, B.S., 2018. A theoretical model of inflammation-and mechanotransduction-driven asthmatic airway remodelling. *B*iomechanics and modeling in mechanobiology, **1**7(5), pp.1451-1470.

[34] Hill, A.V., 1938. The heat of shortening and the dynamic constants of muscle. *Proceedings of the Royal Society of London. Series B-Biological Sciences*, **126**(843), pp.136-195.

[35] Hiorns, J.E., Jensen, O.E. and Brook, B.S., 2014. Nonlinear compliance modulates dynamic bronchoconstriction in a multiscale airway model. *B*iophysical journal, **1**07(12), pp.3030-3042.

[36] Honda, H., 1978. Description of cellular patterns by Dirichlet domains: the two-dimensional case.*Journal of theoretical biology*, **72**(3), pp.523-543.

[37] Irons, L. and Brook, B.S., 2022. The role of mathematical models in designing mechanopharmacological therapies for asthma. *Frontiers in Systems Biology*, 2.

[38] Johnstone, R.H. 2018. *Uncertainty characterisation in action potential modelling for cardiac drug safety*. Ph.D. thesis, University of Oxford.

[39] Keglowich, L.F. and Borger, P., 2015. The three A's in asthmaˇ airway smooth muscle, airway remodeling & angiogenesis. *The open respiratory medicine journal*, **9**, p.70.

[40] Koch, K.R., 1990. Bayes' theorem. *Bayesian Inference with Geodetic Applications*, pp.4-8.

[41] Krishnamoorthy, B. and Tropsha, A., 2003. Development of a four-body statistical pseudo-potential to discriminate native from non-native protein conformations. *Bioinformatics*, **19**(12), pp.1540-1548.

[42] Krishnan, R., Klumpers, D.D., Park, C.Y., Rajendran, K., Trepat, X., Van Bezu, J., Van Hinsbergh, V.W., Carman, C.V., Brain, J.D., Fredberg, J.J. and Butler, J.P., 2010. Substrate stiffening promotes endothelial monolayer disruption through enhanced physical forces. *American Journal of Physiology-Cell Physiology*, **300**(1), pp.C146-C154.

[43] Krishnan, R., Tambe, D., Steward Jr, R., Hardin, C., Butler, J. (2015). Traction Microscopy. 10.1201/b18184-5.

[44] Kruschke, J.K. 2015. *Doing Bayesian data analysis: A tutorial with R, JAGS, and Stan*. 2nd edition. Academic Press.

[45] Kuo, C., Lim, S., King, N.J., Johnston, S.L., Burgess, J.K., Black, J.L. and Oliver, B.G., 2011. Rhinovirus infection induces extracellular matrix protein deposition in asthmatic and nonasthmatic airway smooth muscle cells. *American Journal of Physiology-Lung Cellular and Molecular Physiology*, **300**(6), pp.L951-L957.

[46] Kursawe, J., Baker, R.E. and Fletcher, A.G., 2017. Impact of implementation choices on quantitative predictions of cell-based computational models. *Journal of Computational Physics*, **345**, pp.752-767.

[47] Lambert, B. 2018. *A Student's Guide to Bayesian Statistics*. SAGE Publications Ltd.

[48] Martinez, FD and Vercelli, D. 2013. Asthma. *The Lancet*, **382**(9901), pp.1360-1372.

[49] Mathematics in Medicine. 2011. *Study Group Report: Mathematical modelling of airway smooth muscle cell proliferation and apoptosis in asthma*. [Online]. [Accessed 4 March 2023]. Available from: https://mmsg.mathmos.net/uk/2011/asthma/

[50] Meineke, F.A., Potten, C.S. and Loeffler, M., 2001. Cell migration and organization in the intestinal crypt using a lattice-free model. *Cell proliferation*, **34**(4), pp.253-266.

[51] Melan, M.A., 1994. Overview of cell fixation and permeabilization. In Immunocytochemical Methods and Protocols (pp. 55-66). Humana Press.

[52] Metropolis, N., Rosenbluth, A.W., Rosenbluth, M.N., Teller, A.H. and Teller, E., 1953. Equation of state calculations by fast computing machines. *The journal of chemical physics*, **21**(6), pp.1087-1092.

[53] Mosaffa, P., Rodríguez-Ferran, A. and Muñoz, J.J., 2018. Hybrid cell-centred/vertex model for multicellular systems with equilibrium-preserving remodelling. *International journal for numerical methods in biomedical engineering*, **34**(3), p.e2928.

[54] Murdoch, J.R. and Lloyd, C.M., 2010. Chronic inflammation and asthma. *Mutation Research/Fundamental and Molecular Mechanisms of Mutagenesis*, **690**(1-2), pp.24-39.

[55] Nagai, T.A.T.S.U.Z.O. and Honda, H.I.S.A.O., 2006. Wound healing mechanism in epithelial tissues cell adhesion to basal lamina.*WSEAS Transactions on Biology and Biomedicine*,**3**(6), p.389.

[56] Naveed, S.U.N., Clements, D., Jackson, D.J., Philp, C., Billington, C.K., Soomro, I., Reynolds, C., Harrison, T.W., Johnston, S.L., Shaw, D.E. and Johnson, S.R., 2017. Matrix metalloproteinase-1 activation contributes to airway smooth muscle growth and asthma severity. *American journal of respiratory and critical care medicine*, **195**(8), pp.1000-1009.

[57] Nelder, J.A. and Mead, R., 1965. A simplex method for function minimization. *The computer journal*, **7**(4), pp.308-313.

[58] Nestor-Bergmann, A., Goddard, G., Woolner, S. and Jensen, O.E., 2017. Relating cell shape and mechanical stress in a spatially disordered epithelium using a vertex-based model. *Mathematical medicine and biology: a journal of the IMA*, **35**(Supplement 1), pp.i1-i27.

[59] Park, C.Y., Zhou, E.H., Tambe, D., Chen, B., Lavoie, T., Dowell, M., Simeonov, A., Maloney, D.J., Marinkovic, A., Tschumperlin, D.J. and Burger, S., 2015. High-throughput screening for modulators of cellular contractile force. *Integrative Biology*, **7**(10), pp.1318-1324.

[60] Peters, J.F., Muthuswamy, M., Wibowo, J. and Tordesillas, A., 2005. Characterization of force chains in granular material. *Physical review E*, **72**(4), p.041307.

[61] Plotnikov, S.V., Sabass, B., Schwarz, U.S. and Waterman, C.M., 2014. High-resolution traction force microscopy. *Methods in cell biology*(Vol. 123, pp. 367-394). Academic Press.

[62] Polio, S.R., Stasiak, S.E., Jamieson, R.R., Balestrini, J.L., Krishnan, R. and Parameswaran, H., 2019. Extracellular matrix stiffness regulates human airway smooth muscle contraction by altering the cell-cell coupling. *Scientific reports*, **9**(1), pp.1-12.

[63] Politi, A.Z., Donovan, G.M., Tawhai, M.H., Sanderson, M.J., Lauzon, A.M., Bates, J.H. and Sneyd, J., 2010. A multiscale, spatially distributed model of asthmatic airway hyper-responsiveness. *Journal of theoretical biology*, **266**(4), pp.614-624.

[64] Potten, C.S. and Loeffler, M., 1987. A comprehensive model of the crypts of the small intestine of the mouse provides insight into the mechanisms of cell migration and the proliferation hierarchy. *Journal of Theoretical Biology*,**127**(4), pp.381-391.

[65] Puga, J., Krzywinski, M. and Altman, N. Bayes' theorem. *Nat Methods* **12**, 277–278 (2015).

[66] Rajah, R.O.O.P.M.A.T.H.Y., Nunn, S.E., Herrick, D.J., Grunstein, M.M. and Cohen, P.I.N.C.H.A.S., 1996. Leukotriene D4 induces MMP-1, which functions as an IGFBP protease in human airway smooth muscle cells. *American Journal of Physiology-Lung Cellular and Molecular Physiology*, **271**(6), pp.L1014-L1022.

[67] Rajah, R., Nachajon, R.V., Collins, M.H., Hakonarson, H., Grunstein, M.M. and Cohen, P., 1999. Elevated levels of the IGF-binding protein protease MMP-1 in asthmatic airway smooth muscle. *American journal of respiratory cell and molecular biology*, **20**(2), pp.199-208.

[68] Roberts, G.O., Gelman, A. and Gilks, W.R., 1997. Weak convergence and optimal scaling of random walk Metropolis algorithms. *The annals of applied probability*,**7**(1), pp.110-120.

[69] Rogers, N.K., Clements, D., Dongre, A., Harrison, T.W., Shaw, D. and Johnson, S.R., 2014. Extra-cellular matrix proteins induce matrix metalloproteinase-1 (MMP-1) activity and increase airway smooth muscle contraction in asthma. *PloS one*, **9**(2), p.e90565.

[70] Russell, W.M.S. and Burch, R.L., 1959. *The principles of humane experimental technique*. Methuen.

[71] Schwarz, U.S. and Soiné, J.R., 2015. Traction force microscopy on soft elastic substrates: A guide to recent computational advances. *Biochimica et Biophysica Acta (BBA)-Molecular Cell Research*, **1853**(11), pp.3095-3104.

[72] Shewchuk, J.R., 1994. An introduction to the conjugate gradient method without the agonizing pain.

[73] Soltanpour, A., Nahavandchi, H. and Featherstone, W.E., 2006. The use of second-generation wavelets to combine a gravimetric quasigeoid model with GPS-levelling data. *Journal of Geodesy*, **80**(2), pp.82-93.

[74] Staddon, M.F., Cavanaugh, K.E., Munro, E.M., Gardel, M.L. and Banerjee, S., 2019. Mechanosensitive junction remodelling promotes robust epithelial morphogenesis. *bioRxiv*, p.648980.

[75] Stone, J.V., 2013. Bayes' rule: a tutorial introduction to Bayesian analysis.

[76] Storm, C., Pastore, J.J., MacKintosh, F.C., Lubensky, T.C. and Janmey, P.A., 2005. Nonlinear elasticity in biological gels. *Nature*, **435(7039)**, pp.191-194.

[77] Theocharis, A.D., Skandalis, S.S., Gialeli, C. and Karamanos, N.K., 2016. Extracellular matrix structure. *Advanced drug delivery reviews*, **97**, pp.4-27.

[78] Voronoi, G., 1908. Nouvelles applications des paramètres continus à la théorie des formes quadratiques. Premier mémoire. Sur quelques propriétés des formes quadratiques positives parfaites. *Journal für die reine und angewandte Mathematik (Crelles Journal)*, **1908(133)**, pp.97-102.

[79] Wadsworth, S.J., Yang, S.J. and Dorscheid, D.R., 2012. IL-13, Asthma and Glycosylation in Airway Epithelial Repair. In: *Carbohydrates-Comprehensive Studies on Glycobiology and Glycotechnology*. InTech.

[80] Walker, J.M., 1994. The bicinchoninic acid (BCA) assay for protein quantitation. In Basic protein and peptide protocols (pp. 5-8). Humana Press.

[81] Wang, I., Politi, A.Z., Tania, N., Bai, Y., Sanderson, M.J. and Sneyd, J., 2008. A mathematical model of airway and pulmonary arteriole smooth muscle. *Biophysical journal*, **94**(6), pp.2053-2064.

[82] Weaver, V.M., 2017. Cell and tissue mechanics: the new cell biology frontier. *Molecular biology of the cell*, **28**(14), pp.1815-1818.

[83] Wright, S. and Nocedal, J., 1999. Numerical optimization. *Springer Science*, **35**(67-68), p.7.

[84] Wright, D.B., Trian, T., Siddiqui, S., Pascoe, C.D., Johnson, J.R., Dekkers, B.G., Dakshinamurti, S., Bagchi, R., Burgess, J.K., Kanabar, V. and Ojo, O.O., 2013. Phenotype modulation of airway smooth muscle in asthma. *Pulmonary pharmacology & therapeutics*, **26**(1), pp.42-49.

[85] Yoshie, H., Koushki, N., Kaviani, R., Tabatabaei, M., Rajendran, K., Dang, Q., Husain, A., Yao, S., Li, C., Sullivan, J.K. and Saint-Geniez, M., 2018. Traction force screening enabled by compliant PDMS elastomers. *Biophysical journal*, **114**(9), pp.2194-2199.

[86] Zhang, M.Q. and Timmerman, H., 1997. Mast cell tryptase and asthma. *Mediators of Inflammation*, **6**(5-6), pp.311-317.

A

MASTERS DISSERTATION

An in silico study of altered airway smooth muscle and extracellular matrix structure and function in the remodelled asthmatic airway

G14MBD

MSc Dissertation in

Mathematical Medicine and Biology

2016/17

School of Mathematical Sciences

University of Nottingham

Sarah Kirsty Brown

Supervisor: Dr. Bindi Brook

I have read and understood the School and University guidelines on plagiarism. I confirm that this work is my own, apart from the acknowledged references.

Abstract

This project studies the airway remodelling involved in the chronic lung disease of asthma. We formulate and refine a mathematical model to represent the complete signalling pathway from asthmatic exacerbation event to remodelled airway. The model at each of its stages is analysed to find steady states, stability and bifurcation behaviour. Our final refined model suggests a possible mechanism by which the irreversible remodelling of airways occurs. We are also able to identify possible therapeutic targets through blocking interactions between variables in the system.

Contents

1 Introduction

The lung disease of asthma is often not considered to be a serious condition, but having asthma creates a lifetime burden which can become life threatening if not treated properly. The key hallmarks of asthma are airway inflammation, hyper-responsiveness (rapid narrowing of the airways in response to a low dose of stimulus) and remodelling. Airway remodelling involves several irreversible changes to the structure of airway smooth muscle (ASM) bundles including increases in both extracellular matrix (ECM) and total ASM mass. New information suggests that the pathway that leads to this process involves the activation of Matrix Metalloproteinase-1 (MMP-1) by the inflammatory mast cell tryptase. Uncertainty in the value of *in vivo* experiments alone to gain insight into airway remodelling has given the need for *in silico* techniques, however, very few of these currently exist. The aim of this project therefore, is to generate a mathematical model for airway remodelling in asthma which incorporates the biological discoveries concerning the involvement of MMP-1. By developing a model for a complete signalling pathway from exacerbation event to remodelled airway, we can investigate the dynamics of all the interactions in the system and use this to find possible therapeutic targets. In doing this, we develop a model that shows the mechanism by which an asthmatic exacerbation could lead to an irreversible change in the structure of an airway.

Section 2 begins by explaining the biological context of this work. The pathology involved in the disease asthma is described, in particular the process of airway remodelling. The recent discoveries regarding the involvement of MMP-1 in the pathway that leads to remodelling are also discussed. Section 3 first briefly looks at a few previous mathematical models for changes to the airways and then goes on to explain in detail a particular model on ASM growth developed by Chernyavsky *et al* [6]. In section 4 we formulate the basis of the model which is refined throughout this paper. The system of ordinary differential equations is non-dimensionalised and parameter values are asigned to the dimensionless system based on order of magnitude estimates and by using data from Naveed *et al* [16]. We consider the model under 3 situations; the case of a healthy control, the case of an asthmatic patient who has not recently experienced an asthmatic exacerbation event and the case of an asthmatic patient who is undergoing an exacerbation event. This model

is simulated in each of these cases using Matlab and we examine the dynamics of each of the time courses. We also analytically calculate the steady states of this system and determine their stability. Section 5 then makes the first refinement to the model in order to include a variable switching rate between proliferative and contractile ASM phenotypes. We again simulate this model and find the number of steady states, this time using a numerical technique. In section 6, a further refinement is made to the model to include inhibition of ASM apoptosis as an affect of the survival signal produced by ECM. We use parameter sensitivity anaylsis here in order to find appropriate parameters for use in bifurcation diagrams produced with XPP. When adding pathology to this model, we see a change in steady state. Section 7 interprets the results obtained in the context of airway remodelling in asthma and compares these to the conclusions made by Chernyavsky *et al* [6]. Here we additionally critically evaluate our models and suggest some possible further work. Finally, in section 8 we draw together our conclusions.

2 Biological Background

Asthma is a chronic lung disease that affects approximately 5.4 million people across the UK. The majority of asthma patients have moderate cases that are easily diagnosed and managed, however 250,000 people in the UK are severely affected by this disease, and this severity often co-occurs with another collection of lung diseases; chronic obstructive pulmonary disease (COPD) [2, 13]. Though in the public mind asthma is not always seen as being a serious disease, for severe asthma patients, doing simple daily tasks like walking to the shops can leave them fighting for breath and in the UK there is an average of 3 deaths each day as a direct impact of asthma [2]. No prevention strategies have yet been identified for this disease. Treatment is based on combining regular corticosteroid inhalation (to reduce inflammation), bronchodilators (to reopen airways during an attack) and environmental controls [13]. Many researchers are currently working to enhance both diagnosis and treatment techniques, and to ultimately find a cure [2].

In this section we first give an introduction into the pathology behind this disease; specifically the process of airway remodelling and what this means for the patient. We then review some recent evidence regarding the activation of an enzyme involved in this

remodelling process and how this new knowledge could lead to the possibilities of new drug targets.

2.1 Asthma Pathology

There is no one way to define asthma; this disease is instead often characterised by many processes that occur in the airways of patients, which account for their well-known occurrences of wheezing and loss of breath. Asthma patients experience recurrent exacerbations in which their airways are narrowed as an effect of contraction of ASM. Exacerbations may occur in response to aero-allergens such as dust mites and histamine inducing pollen [14]. When the allergen is recognised an acute inflammatory response is induced, bringing inflammatory cells such as mast cells, eosinophils, macrophages and T-helper cells to the area. These cells release mediators such as histamines, proteases and cytokines as well as many growth factors, which in turn leads to the structural remodelling of the airways [13, 6].

2.2 Airway Remodelling

The accumulation of all the changes to the airways, as a result of the inflammation involved in asthma exacerbations, leads to airway remodelling. It is thought that the process begins in patients early in life and is irreversible. Remodelling progresses through each exacerbation event leading to the advancement of the disease and can eventually cause severe breathing difficulties [16].

A remodelled airway is characterised by epithelial desquamation (shedding of the airway epithelial layer), hyperplasia of goblet cells (increases in the quantity of cells which secrete mucus) and increases in reticular basement membrane (RBM) thickness, together with increases in the amount of ECM and the amount of ASM [14, 16]. The differences between a healthy airway and a remodelled airway of a severe asthma patient is shown in Figure 1. In particular, the image highlights the increase in ASM mass and the thickening of the RBM in the asthmatic airway [20].

The ECM from an asthma patient differs from a healthy ECM critically in its structure and amount [18]. Specifically, there are significant changes in the quantities of several

proteins; there are increases in proteins such as fibronectin, lumican, collagen I II and V and tenasin C whereas elastin and collagen IV are reduced [10]. This altered ECM profile has a crucial impact on ASM cell function. It has been shown that this altered ECM gives both higher migration and proliferation of ASM cells [10]. Rises in collagen and fibronectin specifically, also leads to enhances in synthetic function [4] and changes in contractile capacity [1]. These changes in ASM cells in turn increases bronchial hyper responsiveness and the likelihood of airway obstruction causing exacerbations to be more threatening [16].

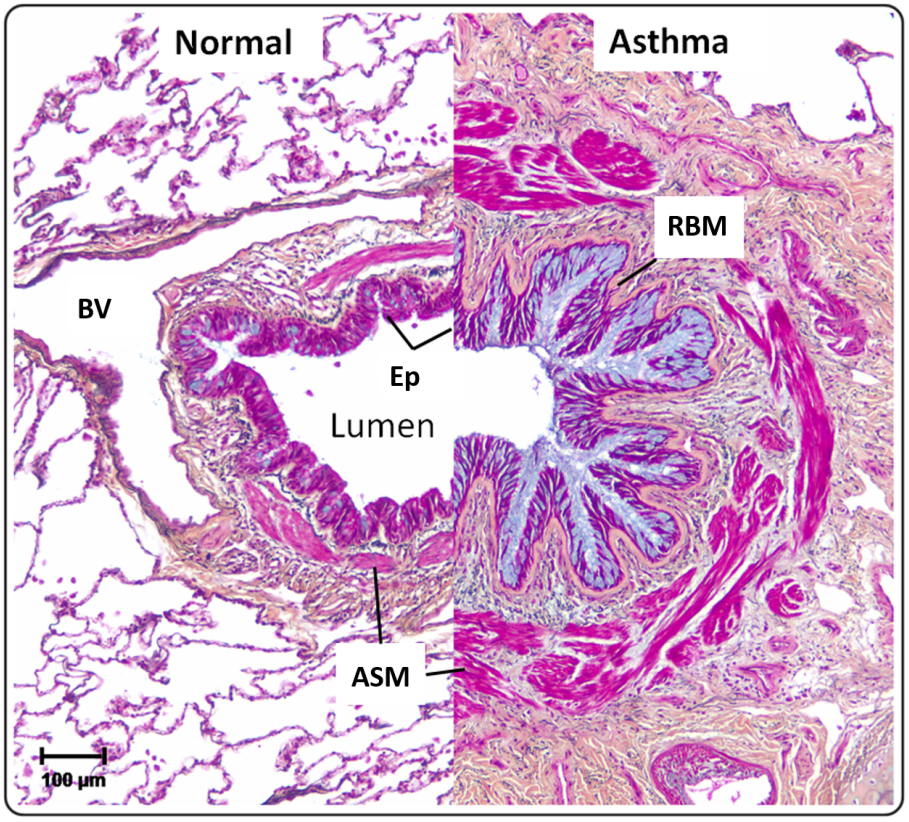

Figure 1: Cross-sectional image of a stained normal healthy airway (left) and a remodelled airway of a severe asthma patient (right). The blue staining shows the difference in amount of goblet cells in the epithelial (Ep) layer. Differences in the thickness of RBM and amount of ASM can also be seen. This image is open sourced and was taken from [20].

2.3 Matrix Metalloproteinase-1

In this section we describe the findings of Naveed *et al* [16], which provides new information on the role of an enzyme called Matrix Metalloproteinase-1 (MMP-1) in the remodelling of ECM in the ASM bundle. It was descovered that MMP-1, which is made by ASM cells, is activated by tryptase; an enzyme that is released from inflammatory mast cells. Naveed *et al* [16] used enzyme-linked immunosorbent assays (ELISAs) and western blots of bronchial washings from asthmatic patients and controls to find that there is more MMP-1 in the airways of asthmatics compared to controls. Additionally, under the inflammatory conditions present during an asthma exacerbation, airway mast cells increase in quantity, hence there is more mast cell tryptase present for activation of pro MMP-1 (the inactivated form of the enzyme). This was tested by inoculating asthma patients with rhinovirus in order to stimulate an exacerbation. It was shown that an exacerbation led to a significant increase in active MMP-1. The active form of MMP-1 changes the structure of the ECM into its altered proproliferative form described in section 2.2. This was found using treatments of active mast cell supernatants on ECM samples. This altered ECM now contains a substrate which promotes the proliferative form of ASM hence giving a significant rise in the overall ASM cell population. Furthermore, it was shown that the enzyme kinetics of MMP-1 increases within an exacerbation event and that there is a strong association between the expression of activated MMP-1 and the reduction of airway calibre [16].

This evidence was first obtained in *in vitro* studies and was later confirmed in human airways using asthma and control groups. This knowledge can henceforth be used to further research in airway remodelling. Ultimately it may be shown that preventing interactions between certain cells within an ASM bundle, for example mast cells and ASM derived products like pro MMP-1, could lessen remodelling of airways and therefore asthma severity [16].

3 Mathematical Background

While there have been several hopeful drug treatments for prevention of disease development through airway remodelling, which have proved successful when tested on animals, none of these have been appropriate for human use. These issues bring out the uncertainty in the value of *in vivo* experimentation alone in this area and the need for more combinations with *in silico* solutions such as mathematical modelling [14].

In this section, we discuss some previous mathematical models of the airways, focussing in particular on a model by Chernyavsky *et al* [6] that takes into account the inflammation involved in an asthma exacerbation and its effect on accumulation of ASM mass.

3.1 Previous Airway Mathematical Models

There have been few attempts to develop mathematical models for airway remodelling. Until fairly recently, the majority of airway models have focussed on expiratory airflow interacting with its structural properties, for example as in [11]. In the past decade however, there has been an increase in the number of models to predict functional changes in the airways as an effect of ASM contraction. In 2008, Wang et al [21] published a model based on the Hai-Murphy cross bridge model which looks at the effect of changes in calcium concentration on contraction of ASM cells and therefore airway hyper-responsiveness. These molecular level dynamics where later incorporated in a multiscale model in order to examine the impact of hyper-responsiveness on the lung as a whole [17]. Another model focusses on the mechanics of airways [3]; in particular ASM cells, through the use of a continuum method that considers the amount of connective tissue relative to ASM. Results from this model agree well with data from experimentation on lung slices and show the increase in ASM by remodelling and the resulting increase in heterogeneity of local stress patterns. This is the first model which incorporates the changes in the airway response as an effect of cellular events and structural remodelling by considering associations between local stress and proliferation of ASM cells.

3.2 Model of ASM Cell Growth in Asthma

In 2014, Chernyavsky *et al* developed a model which examines specifically the impact of the inflammation involved in asthma exacerbations on the accumulation of ASM mass. This model assumes that ASM cells can be of two different phenotypes, proliferative or contractile (non-proliferative). These phenotypes are hence used as variables in the system, $p(t)$ and $c(t)$ respectively, in order to model their change in quantities over time. Contractile ASM can switch to proliferative with the associated rate λ_{cp} and visa versa with the rate λ_{pc} (see Fig. 2). Only the p population proliferates and here, it does so logistically, with a rate λ_p and maximum quantity V. It is assumed that the switching rate λ_{pc} is much faster than the proliferation rate λ_p hence the cells are only in state p for a short amount of time. Only the c population degrades, so the p cells must switch back to being in the c state for their degradation. This occurs with a rate λ_a which is taken to be significantly slower than the proliferation rate. The system of ordinary differential equations (ODEs) for this model is given below [6]:

$$\frac{dp}{dt} = \lambda_p p\left(1 - \frac{p+c}{V}\right) - \lambda_{pc}p + \lambda_{cp}c, \tag{3.1}$$

$$\frac{dc}{dt} = \lambda_{pc}p - (\lambda_{cp} + \lambda_a)c. \tag{3.2}$$

As can be seen in the schematic in Figure 2, the system also has another variable $\mu(t)$. μ takes into account the inflammation involved in an exacerbation event for an asthmatic patient and modifies the value of the switching rate from state c to p: λ_{cp}. The equation for the change in μ over time is as follows [6]:

$$\frac{d\mu}{dt} = -\lambda_d\mu + af(t;w), \quad f(t;w) = \sum_i \delta(t - t_i), \quad w = \frac{1}{E[t_{i+1} - t_i]} \tag{3.3}$$

Where λ_d is the degradation rate of the inflammation and a is a parameter that represents the magnitude of each peak in inflammation given by the function $f(t;w)$, an environmental stimulus. An exacerbation occurs at each time t_i and w gives the rate of recurrence of these events [6].

There are three outcomes of an exacerbation event depending on the value of μ relative to two different thresholds. This therefore leads to three corresponding values of λ_{cp}. If

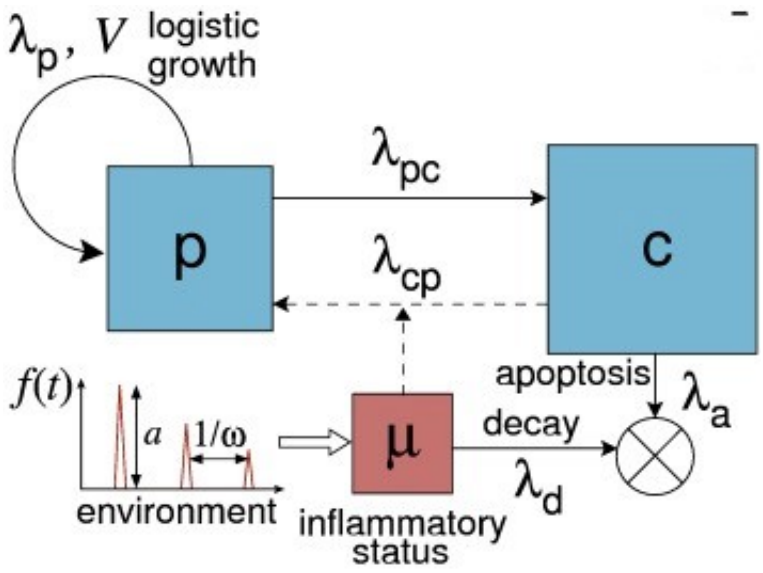

Figure 2: Schematic representation of the ASM growth model made by Chernyavsky *et al*, showing the interactions between the three varaibles c, p and μ and the relavance of the environmental stimulus $f(t)$. This image was taken from the open access article; [6].

μ is below the first threshold, λ_{cp} is slower than both the rate of proliferation and the opposite switching rate but faster than the apoptosis rate of ASM cells. If μ is in between the two threshold values, λ_{cp} increases to approximately the same rate as λ_p but is still smaller than λ_{pc}. For the highest values of μ above both threshold values, λ_{cp} rises further so that it is approximately the same as λ_{pc}, the fastest rate. Each of these three possibilities give a different modelling outcome which corresponds to the diagnosis of a patient being healthy, having mild asthma or having severe asthma respectively [6].

This model predicts that the increase in quantities of ASM cells is fundamentally reliant on the normalised parameters: $a/(\text{"}\textit{lower threshold of}\ \mu\text{"})$, w/λ_p and λ_d/λ_p which gives the rate of inflammation resolution. The latter of these is shown to be the parameter of highest importance in remodelling. This is because slow resolution leads to a build-up of inflammation from previous events giving a bigger impact on total ASM growth. Furthermore, results of this model show that the primary goal should be to increase this resolution speed in asthma patients before decreasing frequency and magnitude of exacerbation events [6].

4 Model 1: Role of MMP-1 in alteration of ECM and ASM accumulation

In this project, we develop an ODE model in order to simulate the dynamics of an ASM bundle in both a normal and an asthmatic airway over time, where an external input at given times represents an inflammatory exacerbation. We base part of this new mathematical model on ideas proposed by Chernyavsky *et al* [6], but we also include a significant number of new variables and parameters to account for the advancement in biological knowledge in this area. The model in [6], while including an effect of inflammation directly on the rate of switching between contractile and proliferative ASM cells, does not account for the pathway that leads to this change in rate directly. We therefore develop a model to give a more complete signalling pathway from exacerbation event to ASM growth. By including new information relating to the airway remodelling process, the hope is to learn more about effects of different interactions in the system and to ultimately find an interaction that, when blocked, halts further remodelling.

4.1 Model Formulation

To our knowledge, the model we develop is the first one to incorporate MMP-1 activation and its impact on airway remodelling as discussed in section 2.3. This model must therefore include:

1. The increase in mast cell tryptase as an effect of an exacerbation event,
2. The activation of MMP-1 by mast cell tryptase,
3. The effect of active MMP-1 on altering the ECM,
4. The impact that the altered ECM has on the switching rate from contractile to proliferative ASM cells and on the rate of proliferation.

To do this, we first decided that there are 7 significant variables in this system; mast cell tryptase (Y), inactivated (pro) MMP-1 (M), activated MMP-1 (Q), ECM (E), altered ECM of asthmatic airways (A), contractile ASM (C) and proliferative ASM (P). As in

[6], we consider the 2 different states of ASM cells, contractile and proliferative, as being separate variables. It has been shown using western blots that changes in these variables are inversely related to the expression of one another [7]. We also consider the exacerbation event to be an environmental stimulus as a function of time.

The interactions between the variables in this system were then considered and a signalling network was formulated to show their impact on one another, as shown in Figure 3. Pro MMP-1 is produced by both proliferative and contractile ASM cells with a rate k_{PM} and k_{CM} respectively. Mast cell tryptase is assumed to have an environmental input $S(t;w)$ during an exacerbation event due to the sharp increase in inflammatory cells that this causes. When mast cell tryptase is present, it binds to MMP-1 in order for this to be activated with a rate $k_{MQ}(Y)$. ECM is also produced by ASM cells with rates k_{PE} and k_{CM}. Active MMP-1 binds to ECM which leads to it changing into its altered form with a rate $k_{EA}(Q)$; this altered ECM has a significant impact on ASM function. Altered ECM both increases the rate $k_{CP}(A)$ for switching from the contractile to proliferative state and increases the proliferation rate $k_P(A)$. As in [6], proliferative ASM cells also switch back to contractile, here with a rate k_{PC}. Pro MMP-1, ECM and proliferative ASM all have small amounts of baseline production through variables not included in this model. These are given by λ_M, λ_E and λ_P respectively. Each variable (i) additionally exhibits apoptosis or decay with a rate k_{ia}, except for proliferative ASM cells which revert back to their contractile form before degrading. Full tables of the parameter descriptions can be found in Appendix 1.

4.2 System of ODEs

To generate the system of ODE's, we make use of the theory of mass action and use Hill functions to describe threshold and saturation effects. Mass action kinetics are used when describing the activation of a single variable as this chemical reaction occurs with a rate proportional to the quantity of the inactivated species [5]. To describe the binding of variables, which in this model lead to many of these chemical reactions, we use Hill functions. This is because binding of ligands and receptors are known to follow a saturating curve which commonly has a sigmoidal shape [19]. An assumption made in formulating this

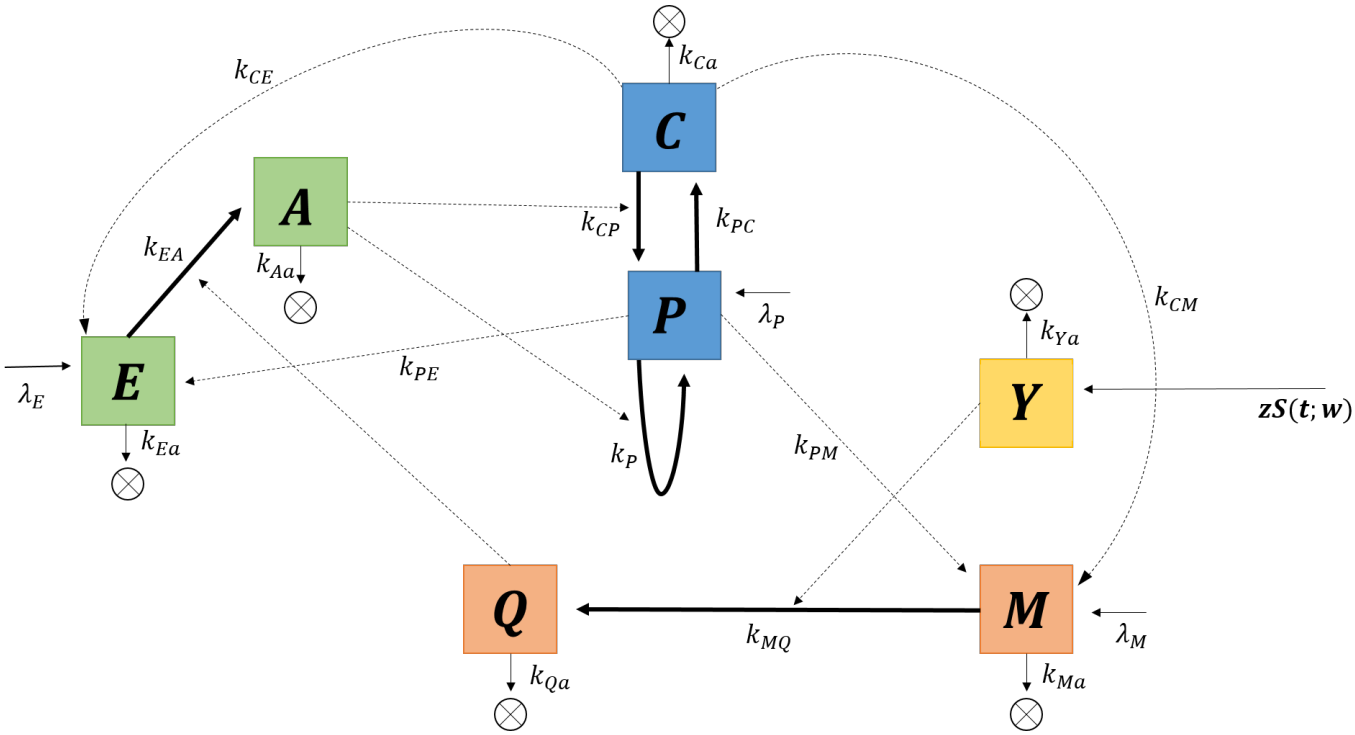

Figure 3: A schematic representation of the new model, showing all 7 variables within an ASM bundle and their interactions with one another, as well as the impact of an environmental stimulus $zS(t;w)$ which accounts for the inflammation involved in an exacerbation event. Solid thick black lines represent a variable being converted to another variable, solid thin black lines represent baseline productions and degradations, and dashed lines show variables that enhance production of other variables without being lost themselves.

system of equations is that the variable p grows logistically where, as in [6], V represents the maximum possible size of population p.

The system of 7 ODEs is hence formulated as follows:

$$\frac{dY}{dt} = zS(t;w) - k_{Ya}Y, \tag{4.1}$$
$$\frac{dM}{dt} = k_{PM}P + k_{CM}C - k_{MQ}(Y)M - k_{Ma}M + \lambda_M, \tag{4.2}$$
$$\frac{dQ}{dt} = k_{MQ}(Y)M - k_{Qa}Q, \tag{4.3}$$
$$\frac{dE}{dt} = k_{PE}P + k_{CE}C - k_{EA}(Q)E - k_{Ca}E + \lambda_E, \tag{4.4}$$
$$\frac{dA}{dt} = k_{EA}(Q)E - k_{Aa}A, \tag{4.5}$$
$$\frac{dC}{dt} = k_{PC}P - k_{CP}(A)C - k_{Ca}C, \tag{4.6}$$
$$\frac{dP}{dt} = k_{CP}(A)C - k_{PC}P + k_P(A)P\left(1 - \frac{P+C}{V}\right) + \lambda_P. \tag{4.7}$$

where

$$\begin{aligned} k_{MQ}(Y) &= \frac{J_{MQ}Y^n}{\mu + Y^n}, \\ k_{EA}(Q) &= \frac{J_{EA}Q^n}{\gamma + Q^n}, \\ k_{CP}(A) &= \hat{k}_{CP} + \frac{J_{CP}A^n}{\beta + A^n}, \\ k_P(A) &= \hat{k}_P + \frac{J_PA^n}{\alpha + A^n}. \end{aligned} \tag{4.8}$$

and

$$S(t;w) = \sum_i \delta(t - t_i) \tag{4.9}$$

The stimulus of the system is given by the function $S(t;w)$. This function models the effect of an asthma patients' exacerbation event which leads to an inflammatory response and therefore a corresponding increase in mast cell tryptase of magnitude z. δ represents the delta dirac function and t_i is the time of each exacerbation event. This time dependant input will be discussed in more detail in section 4.9.

Equations (4.8) all include Hill functions. J_{MQ}, J_{EA}, J_{CP} and J_P represent the maximum respective rates of these functions, α, β, γ and μ give the switching values at which the rate is at half of its maximum and n is the common Hill coefficient. The existence of baseline values $\hat{k}_{CP}$ and $\hat{k}_P$ mean that there is still some rate of switching from C to P and some non-zero proliferation rate even when no altered ECM is present. It is assumed however, that there is no activation of pro MMP-1 without any mast cell tryptase and

no alteration of ECM without any active MMP-1. An example of the dynamics of the function $k_{MQ}(Y)$ with different values of the Hill coefficient can be seen in Figure 4. As can be seen, the higher the Hill coefficient, the steeper the switch is from the original rate to its maximum value.

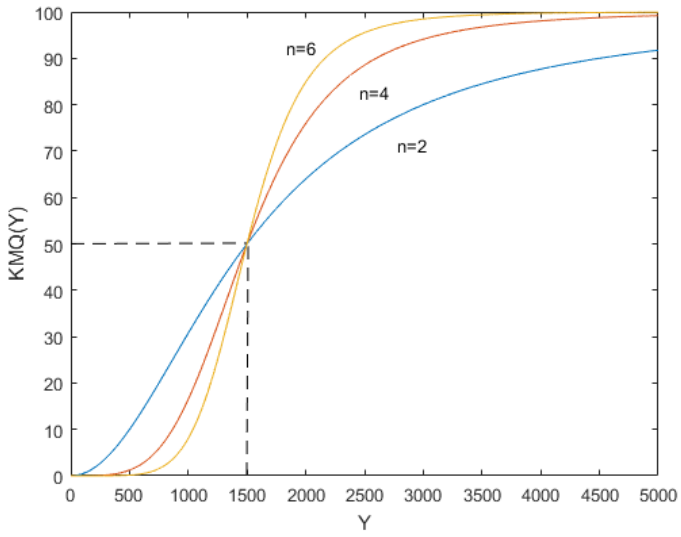

Figure 4: Graph showing the rate of MMP-1 activation as a function of mast cell tryptase ($k_{MQ}(Y)$) for different Hill coefficients. Here we set the maximum rate $J_{MP} = 100$ and the switching value at which the rate $k_{MQ}(Y)$ is at half of its maximum $\mu = 1500^n$. We then look at the dynamics of this rate function for different Hill coefficients: $n = 2$ (blue curve), $n = 4$ (red curve) and $n = 6$ (orange curve).

We first look at the non-pathological case, whereby $S(t; w) = 0$, in order to see how an asthma patients' airway, without having had a exacerbation, compares to that of a healthy control and ultimately, to that of the pathological case. We also use no stimulus originally, in order to check that the model gives biologically sensible predictions of variables at the steady state. We therefore begin by non-dimensionalising the system and then discuss the assigning of parameter values for both the case of an asthmatic patient and a healthy control. We numerically simulate this model using Matlab to examine the dynamics of the time course. Steady states of the model are calculated and we determine their stability followed by a bifurcation analysis in order to see if this stability ever changes. Finally we will add in the pathology of an exacerbation event and see how this affects the dynamics of the system.

4.3 Non-Dimensionalisation

We non-dimensionalise the system of equations 4.1-4.8, without stimulus, using lower case letters to show the dimensionless variables and an upper case T to represent dimensionless time. Each variable, x say, is therefore non-dimensionalised using $X = x\bar{X}$, where $\bar{X}$ is a scaling constant. Time is scaled with what is assumed to be the fastest rate in the system: the switching rate from proliferative to contractile ASM cells, hence we use $t = \frac{T}{k_{PC}}$. New dimensionless parameters $K_1 - K_{12}$, $\sigma_1 - \sigma_9$, $j_1 - j_4$, $\phi_1 - \phi_4$ and $\psi_1 - \psi_3$ are introduced to represent dimensionless groupings as shown in Tables 1 - 3. The non-pathological dimensionless equations are therefore as follows:

$$\frac{dy}{dT} = -K_1 y, \tag{4.10}$$

$$\frac{dm}{dT} = K_2\sigma_1 p + K_3\sigma_2 c - j_1\left(\frac{y^n}{\phi_1 + y^n}\right)m - K_4 m + \psi_1, \tag{4.11}$$

$$\frac{dq}{dT} = j_1\sigma_3\left(\frac{y^n}{\phi_1 + y^n}\right)m - K_5 q, \tag{4.12}$$

$$\frac{de}{dT} = K_6\sigma_4 p + K_7\sigma_5 c - j_2\left(\frac{q^n}{\phi_2 + q^n}\right)e - K_8 e + \psi_2, \tag{4.13}$$

$$\frac{da}{dT} = j_2\sigma_6\left(\frac{q^n}{\phi_2 + q^n}\right)e - K_9 a, \tag{4.14}$$

$$\frac{dc}{dT} = \sigma_7 p - K_{10} c - j_3\left(\frac{a^n}{\phi_3 + a^n}\right)c - K_{11} c, \tag{4.15}$$

$$\frac{dp}{dT} = K_{10}\sigma_8 c + j_3\sigma_8\left(\frac{a^n}{\phi_3 + a^n}\right)c - p + p(K_{12} + j_4\left(\frac{a^n}{\phi_4 + a^n}\right))\left(1 - \frac{p + \sigma_8 c}{\sigma_9}\right) + \psi_3. \tag{4.16}$$

4.4 Parameter Values

Estimated dimensionless parameter values are given in Tables 1 - 3 for both an asthmatic patient and a healthy control. These values were assigned using order of magnitude estimations where possible, based on data from [16]. Some parameters were difficult to quantify, however, due to little data being available, hence theoretical estimates are given. As can be seen in Table 1, normalised dimensionless value K_3 is set to be very small compared to other parameters. This is because pro MMP-1 is mainly produced as an effect of the pathology, through the altered ECM creating more proliferative ASM cells. We also assign a relatively large value for the normalised apoptosis rate of active

MMP-1 (K_5) which is significantly faster than the degradation of altered ECM. The ASM apoptosis rate (k_{Ca}), base rate of change $\hat{k}_{CP}$ and the base proliferation rate $\hat{k}_P$ without any disease are very small compared to the rate k_{PC} hence K_{10}, K_{11} and K_{12} are small. These estimations were based on the literature-based and estimated parameter values in Table 1 of [6].

Non dimensional parameter	In terms of dimensional parameters	Value for asthma patient	Value for healthy control
K_1	k_{Ya}/k_{PC}	ε^2	-
K_2	k_{PM}/k_{PC}	ε	ε^3
K_3	k_{CM}/k_{PC}	ε^2	ε^4
K_4	k_{Ma}/k_{PC}	ε	1
K_5	k_{Qa}/k_{PC}	1	-
K_6	k_{PE}/k_{PC}	ε	ε^2
K_7	k_{CE}/k_{PC}	ε	ε^2
K_8	k_{Ea}/k_{PC}	ε	ε^2
K_9	k_{Aa}/k_{PC}	ε	-
K_{10}	$\hat{k}_{CP}/k_{PC}$	ε^2	ε^3
K_{11}	k_{Ca}/k_{PC}	ε^2	$\varepsilon^3(0.005)$
K_{12}	$\hat{k}_P/k_{PC}$	ε^2	ε^3

Table 1: Dimensionless parameters shown in terms of their dimensional parameter groupings plus their reference values for an asthmatic patient and for a healthy control for the system of equations 4.10-4.16. Y, Q and A are zero in the healthy case hence rates involving them are not applicable.

4.4.1 Differences between an Asthmatic and a Healthy Airway

The system of ODEs remains the same for both an asthma patient and a healthy control, however, the dimensionless parameter values and initial conditions vary significantly. Firstly, it is assumed that values of mast cell typtase, active MMP-1 and altered ECM are very small in comparison to the other variables in the system for a healthy individual, so their initial conditions are all taken as zero for simplicity. This means that any parameters involved in Hill functions are no longer applicable as all of them are functions of variables that are zero in the healthy case. In a Western blot conducted by Naveed *at al* [16], no

Non dimensional parameter	In terms of dimensional parameters	Value for asthmatic patient	Value for healthy control
σ_1	$\bar{P}/\bar{M}$	ε	1
σ_2	$\bar{C}/\bar{M}$	1	100
σ_3	$\bar{M}/\bar{Q}$	100	0
σ_4	$\bar{P}/\bar{E}$	ε	ε^2
σ_5	$\bar{C}/\bar{E}$	1	1
σ_6	$\bar{E}/\bar{A}$	100	0
σ_7	$\bar{P}/\bar{C}$	ε (0.3)	ε^2(0.08)
σ_8	$\bar{C}/\bar{P}$	10	100
σ_9	$V/\bar{P}$	100	100

Table 2: Dimensionless parameters shown in terms of their dimensional parameter groupings plus their reference values for an asthmatic patient and for a healthy control for the system of equations 4.10-4.16.

MMP-1 activity was found in control subjects without asthma. Any small amounts of active MMP-1 that is found in healthy airways, acts as a collagenase in order to help break down ECM and so is included into the ECM degradation term. It was also found that pro MMP-1 is significantly higher in asthmatics than in healthy controls therefore its production rates (k_{CM}, k_{PM}) are smaller, its baseline production value (ψ_1) is assumed zero and the degradation rate (k_{Ma}) is faster in the healthy case. Quantities of ECM and contractile ASM are similar between the two cases but both are slightly higher in the asthmatic case to account for the thicker basement membrane and larger total ASM population of asthmatics respectively. Finally, the quantity of proliferative ASM cells is higher in asthmatics hence the baseline value (ψ_3) is taken to be zero and the switching rate k_{PC} is taken as being faster in the healthy case. As the latter is the parameter that the majority of other parameter values are scaled by when non-dimensionalising, these dimensionless variables are all an order of magnitude smaller in the healthy case. Values for σ's additionally take into account the approximate difference in magnitudes between variables in each case.

Non dimensional parameter	In terms of dimensional parameters	Value for asthmatic patient	Value for healthy control
j_1	J_{MQ}/k_{PC}	1	-
j_2	J_{EA}/k_{PC}	ε	-
j_3	J_{CP}/k_{PC}	10	-
j_4	J_P/k_{PC}	1	-
ϕ_1	$\mu/\bar{Y}^n$	10^n	-
ϕ_2	$\gamma/\bar{Q}^n$	10^n	-
ϕ_3	$\beta/\bar{A}^n$	10^n	-
ϕ_4	$\alpha/\bar{A}^n$	10^n	-
ψ_1	$\lambda_M/k_{PC}\bar{M}$	ε^2	0
ψ_2	$\lambda_E/k_{PC}\bar{E}$	ε^2	ε^3
ψ_3	$\lambda_P/k_{PC}\bar{P}$	ε^2	0

Table 3: Dimensionless parameters shown in terms of their dimensional parameter groupings plus their reference values for an asthmatic patient and for a healthy control for the system of equations 4.10-4.16. All values involved in Hill functions (j's and ϕ's) are not applicable for the healthy case as are always functions of variables that are zero.

4.5 Numerical Simulations

We numerically simulate the system of equations 4.10-4.16, for both a healthy and an asthmatic case, using the ode45 solver in Matlab. The healthy and asthmatic cases are as described in section 4.4.1, where an asthmatic case is that of a patient who is not currently exhibiting an exacerbation. The results of this can be seen in Figures 5 and 6 respectively. We can see that, in the healthy case of Figure 5, mast cell tryptase, active MMP-1 and altered ECM remain at zero throughout. The number of pro MMP-1s instantly jumps to approximately half of their initial amount and then gradually declines to their steady state value of 3.4 over a remodelled time scale of about $T = 1000$. ECM and contractile smooth muscle populations both start with a significantly higher initial amount and hence are seen to smoothly decrease until reaching their steady states, which again, are a lot higher than the other variables due to these populations dominating in an ASM bundle. Proliferative smooth muscle initially jumps up to approximately 1.75 of its starting amount, overshooting its steady state, then declines gradually, like the other

variables, until reaching steady state.

In comparison, when looking at the asthmatic case of Figure 6, we consider a system that begins with a small amount of mast cell tryptase that may be in the airway, whether this be still present from a previous exacerbation event or just using the fact that asthmatics in general have a higher number of mast cells in the airway. This means that pro MMP-1 is able to be converted to active MMP-1. Hence we can see that pro MMP-1 remains approximately constant until a remodelled time of about $T = 120$, while in that time, active MMP-1 instantly jumps to 100 and then quickly declines back to zero. When active MMP-1 is back to being zero, pro MMP-1 then rises quickly to its steady state which is significantly higher than that of the healthy case. As active MMP-1 is instantly fairly high in quantity, this means that ECM is able to be converted into altered ECM. We can therefore see that, after a short lag, altered ECM also increases significantly and then declines back to zero before reaching $T = 100$. In this time, normal ECM decreases to nearly zero and then increases quickly to its steady state, which is slightly higher than that of the healthy case, once altered ECM is back to zero. Similarly, as altered ECM becomes non-zero, this means that it can have the effect of both increasing the change from contractile to proliferative ASM and increasing the amount of proliferation. This can be seen as the proliferative population jumps to about 250 straight away and remains there until about $T = 120$ and in that time, the contractile population jumps to and stays at nearly zero. After this time, there is a small peak in the proliferative population followed by a fast decay so that it reaches its steady state before $T = 200$. This steady state is again higher than that of the healthy case. While the proliferative population declines to its steady state, the contractile population increases to theirs.

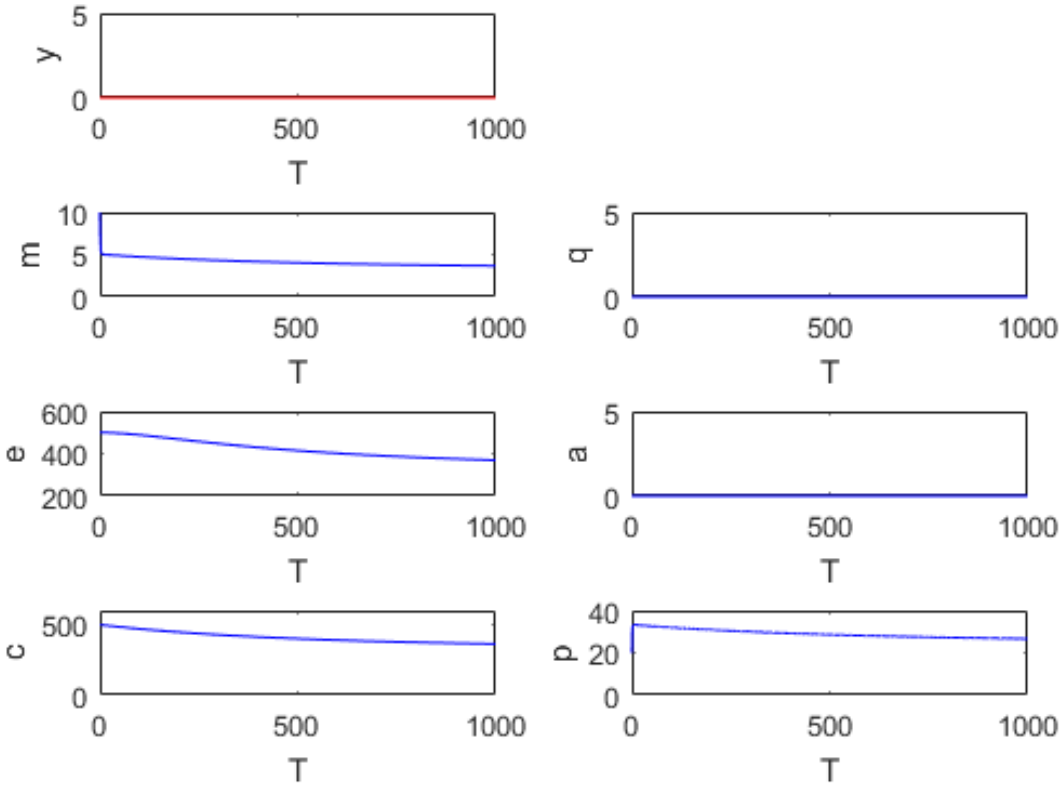

Figure 5: Matlab simulation for the change in each variable of the dimensionless system over time for a healthy control subject with inital conditions $[y_0, m_0, q_0, e_0, a_0, c_0, p_0] = [0, 10, 0, 500, 0, 500, 20]$, parameters as in Tables 1 - 3 and the Hill coefficient $n = 4$.

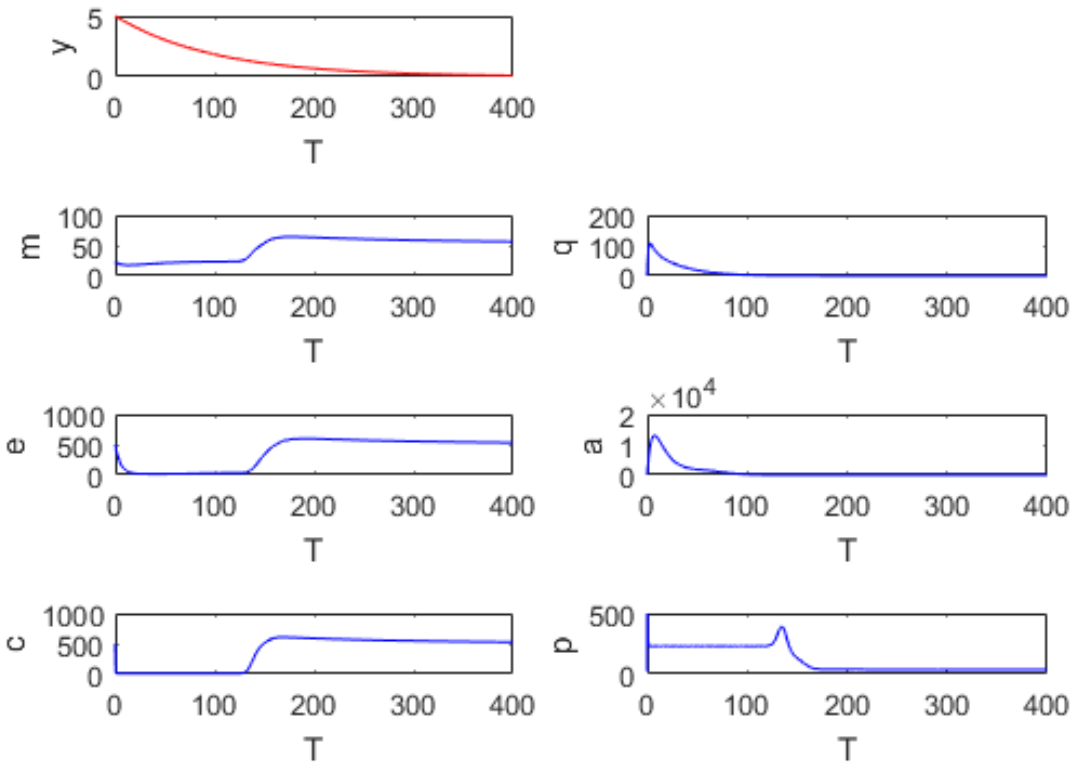

Figure 6: Matlab simulation for the change in each variable of the dimensionless system over time for an asthmatic patient with initial conditions $[y_0, m_0, q_0, e_0, a_0, c_0, p_0] = [5, 20, 0, 500, 0, 500, 20]$ and no further stimulus. Parameters are as in Tables 1 - 3 and the Hill coefficient $n = 4$.

While all previous and future simulations use a Hill coefficient of $n = 4$, we briefly look at the results of a time course where a much higher Hill coefficient of $n = 15$ is used. The results for this, for the asthmatic case are shown in Figure 7. As can be seen, there is a much smaller affect of the mast cell tryptase on active MMP-1 and therefore altered ECM and ASM growth. This means that pro MMP-1 and normal ECM only increase to their steady states and both contractile and proliferative ASM populations look to remain constant at their steady state values throughout.

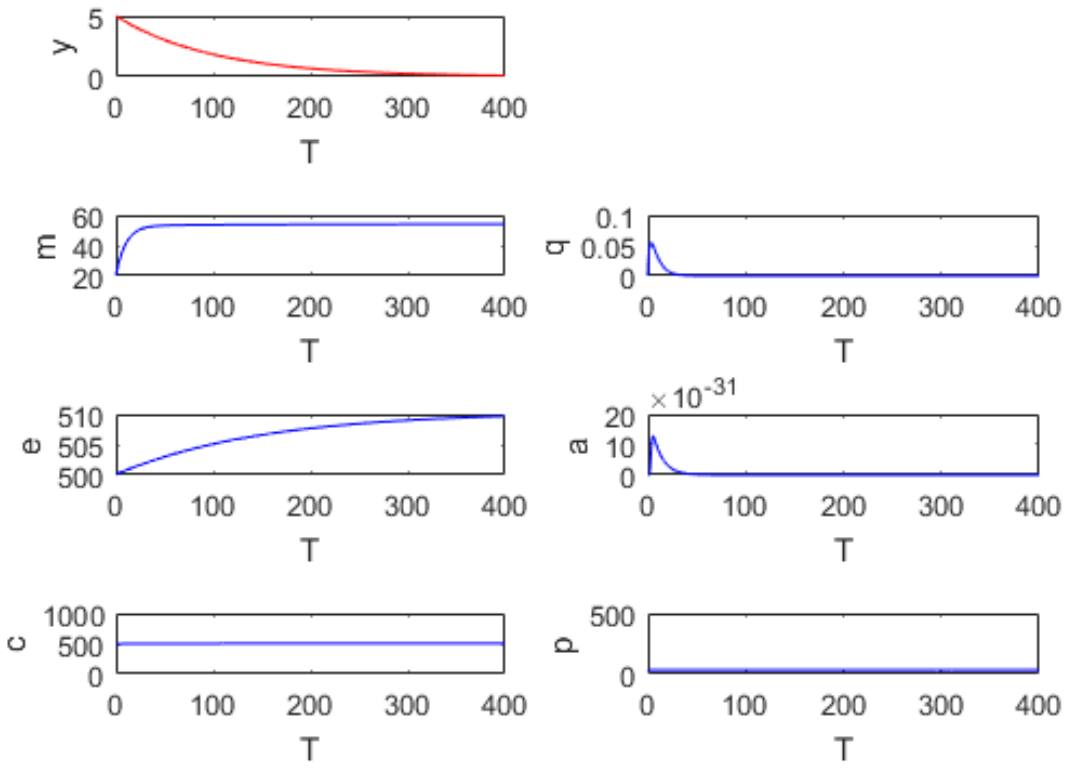

Figure 7: High Hill coefficient: Matlab simulation for the change in each variable of the dimensionless system over time for an asthmatic patient with initial conditions $[y_0, m_0, q_0, e_0, a_0, c_0, p_0] = [5, 20, 0, 500, 0, 500, 20]$ and no further stimulus. Parameters are as in Tables 1 - 3 and here, the Hill coefficient $n = 15$.

4.6 Steady States

The steady states of this system are determined by setting each time derivative of the non-dimensional system (equations 4.10-4.16) to equal zero. It is found that $y^* = q^* = a^* = 0$ at the steady state always. The steady states of the remaining variables are as follows:

$$m^* = \frac{K_2\sigma_1 p^* + K_3\sigma_2 c^* + \psi_1}{K_4}, \tag{4.17}$$

$$e^* = \frac{K_6\sigma_4 p^* + K_7\sigma_5 c^* + \psi_2}{K_8}, \tag{4.18}$$

$$c^* = \frac{\sigma_7 p^*}{K_{10} + K_{11}}, \tag{4.19}$$

where, with use of the quadratic formula,

$$
\begin{aligned}
p^{*}\pm = \Bigg(& \sigma_7\sigma_8\sigma_9K_{10} + \sigma_9K_{12}(K_{10}+K_{11}) - \sigma_9(K_{10}+K_{11}) \\
& \pm \Bigg(\big(\sigma_7\sigma_8\sigma_9K_{10} + \sigma_9K_{12}(K_{10}+K_{11}) - \sigma_9(K_{10}+K_{11})\big)^2 \\
& + 4\sigma_9\psi_3(K_{10}^2K_{12} + K_{11}^2K_{12} + 2K_{10}K_{11}K_{12} + \sigma_7\sigma_8K_{12}(K_{10}+K_{11}) \Bigg)^{\frac{1}{2}} \Bigg) \\
& \Bigg(2K_{12}(K_{10}+K_{11}+\sigma_7\sigma_8) \Bigg)^{-1}.
\end{aligned}
\tag{4.20}
$$

Due to the fact that all the parameter values are positive, when looking at the quadratic equation ($\frac{-b\pm\sqrt{b^2-4ac}}{2a}$) for p^*, $4ac$ is always negative no matter the values of parameters. This means that the quantity under the square root is always positive. The roots of this equation therefore are always real and $\sqrt{b^2-4ac} > b$. Hence irrespective of whether b is positive or negative, there is always one positive steady state for p^* and one negative one. If p^* is positive (or negative), m^*, e^* and c^* will also be positive (or negative).

With the parameter values as described in Tables 1 - 3, we get the steady state values as follows. For the healthy case, $y^* = 0$, $m^* = 3.4$, $q^* = 0$, $e^* = 334.4$, $a^* = 0$, $c^* = 334.1$ and $p^* = 25.1$ is the positive steady state. For the asthmatic case, $y^* = 0$, $m^* = 54.2$, $q^* = 0$, $e^* = 510.4$, $a^* = 0$, $c^* = 506.9$ and $p^* = 33.8$ is the positive steady state. We are only interested in the positive steady states as the negative ones represent biologically impossible outcomes. Though in the asthmatic case, there are some initial quantities of mast cell typtase, active MMP-1 and altered ECM, without further stimulus these variables eventually decay to zero.

4.7 Stability Analysis

Linear stability of the steady states is found by obtaining the Jacobian matrix and hence the eigenvalues of the system for each steady state. The Jacobian evaluated at the steady state $(y, m, q, e, a, c, p) = (0, m^*, 0, e^*, 0, c^*, p^*)$ is given below:

$$J = \begin{pmatrix} -K_1 & 0 & 0 & 0 & 0 & 0 & 0 \\ 0 & -K_4 & 0 & 0 & 0 & K_3\sigma_2 & K_2\sigma_1 \\ 0 & 0 & -K_5 & 0 & 0 & 0 & 0 \\ 0 & 0 & 0 & -K_8 & 0 & K_7\sigma_5 & K_6\sigma_4 \\ 0 & 0 & 0 & 0 & -K_9 & 0 & 0 \\ 0 & 0 & 0 & 0 & 0 & -(K_{10}+K_{11}) & \sigma_7 \\ 0 & 0 & 0 & 0 & 0 & (K_{10}\sigma_8 - \frac{K_{12}\sigma_8 p^*}{\sigma_9}) & (-1+K_{12}-\frac{2K_{12}p^*}{\sigma_9}-\frac{K_{12}\sigma_8 c^*}{\sigma_9}) \end{pmatrix}$$

This directly gives the eigenvalues $\lambda_1 = -K_1, \lambda_2 = -K_4, \lambda_3 = -K_5, \lambda_4 = -K_8, \lambda_5 = -K_9$. λ_6 and λ_7 can then be calculated from the following characteristic equation:

$$\big(-(K_{10}+K_{11})-\lambda\big)\big(-1+K_{12}-\frac{2K_{12}p^*}{\sigma_9}-\frac{K_{12}\sigma_8 c^*}{\sigma_9}-\lambda\big)-(K_{10}\sigma_7\sigma_8-\frac{K_{12}\sigma_7\sigma_8 p^*}{\sigma_9}) = 0, \quad (4.21)$$

which gives the quadratic equation:

$$\begin{aligned} &\lambda^2 + \lambda(K_{10}+K_{11}+1-K_{12}+\frac{2K_{12}p^*}{\sigma_9}+\frac{K_{12}\sigma_8 c^*}{\sigma_9}) \\ &+ (K_{10}+K_{11})(1-K_{12}+\frac{2K_{12}p^*}{\sigma_9}+\frac{K_{12}\sigma_8 c^*}{\sigma_9}) - (K_{10}\sigma_7\sigma_8 - \frac{K_{12}\sigma_7\sigma_8 p^*}{\sigma_9}) = 0 \end{aligned} \quad (4.22)$$

From this quadratic, we find that λ_6 and λ_7 are both always negative for any positive value of p^* (and therefore c^*), hence the positive steady state is always stable. We can see this by looking again at the quadratic formula with use on equation 4.22, where $\frac{-b+\sqrt{b^2-4ac}}{2a} = \lambda_+$ and $\frac{-b-\sqrt{b^2-4ac}}{2a} = \lambda_-$. We vary parameters that are likely to affect the stability of the positive steady state and look at the sign of λ_+ and λ_-. Results for the effect of varying the parameters K_{10} (baseline switching rate from C to P relative to the switching rate back to C from P) and K_{12} (baseline proliferation rate relative to the switching rate from P to C) can be seen in Figures 8 and 9 respectively. We can hence see that for any value of these parameters up to 50 (with other parameters fixed as in Tables 1 - 3), we get both eigenvalues as being negative. This is because, though there are negative multiples of parameter values in this quadratic, we find that both b and c from the quadratic formula are always positive here (and $a = 1$). If we increase the

negative parameter values relative to the others in this equation, this leads to a subsequent increase in the positive values due to the change in the steady state values p^* and c^*. This means we always have $\frac{-b\pm\sqrt{b^2-4c}}{2}$ where b is positive and $b > \sqrt{b^2-4ac}$, hence giving a negative value for both λ_+ (λ_6) and λ_- (λ_7). We have already shown that λ_1-λ_5 are always negative therefore all eigenvalues are negative and so the steady state is stable. In the non-biological case where p^* and c^* are both negative however, there is always at least one positive eigenvalue hence this steady state is unstable.

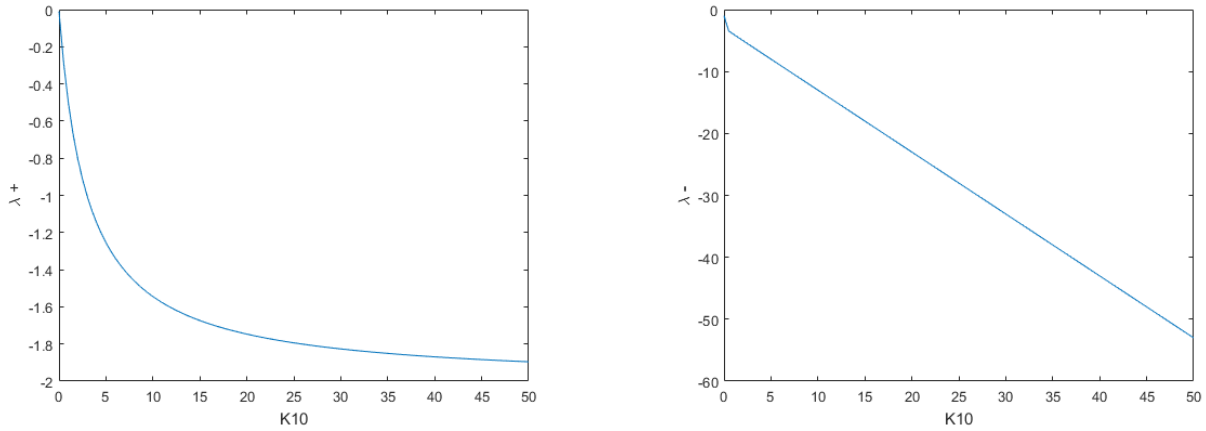

Figure 8: $\lambda_+ = \frac{-b+\sqrt{b^2-4ac}}{2a}$ (left) and $\lambda_- = \frac{-b-\sqrt{b^2-4ac}}{2a}$ (right) for the characteristic equation 4.22 as a function of K_{10}. Both λ_+ and λ_- are always negative for these values of K_{10}.

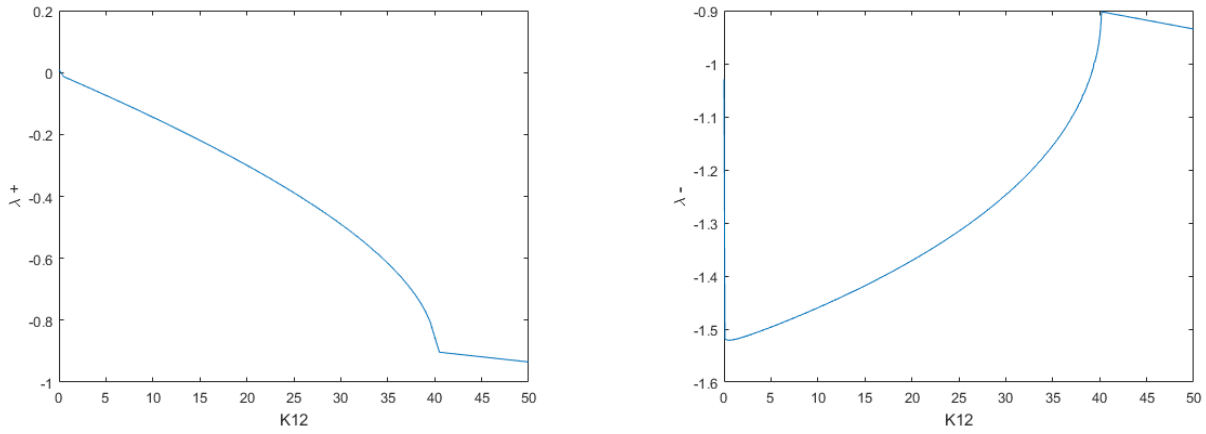

Figure 9: $\lambda_+ = \frac{-b+\sqrt{b^2-4ac}}{2a}$ (left) and $\lambda_- = \frac{-b-\sqrt{b^2-4ac}}{2a}$ (right) for the characteristic equation 4.22 as a function of K_{12}. Both λ_+ and λ_- are always negative for these values of K_{12}. The abrupt change in these curves at $K_{12} = 40$ occurs as, at that point, $b^2 < 4ac$ so the eigenvalues become complex, however matlab continues to only plot the real parts. These complex eigenvalues mean that the solution becomes ocsillatory but the real parts remain negative so that the steady state is still always stable.

4.8 Bifurcation Analysis

We can also see that the positive steady state of the system always remains stable through producing bifurcation diagrams using XPP. Looking at [6], as described in section 3.2, resolution rate was shown to have a significant impact on airway remodelling. We may therefore expect that the parameters involved in this (here this includes the decay rate of mast cell tryptase and the ASM proliferation rate), might have an impact on the steady state value. A bifurcation diagram for the change in c^* as K_{11} is varied, is shown in Figure 10 and that for the change in p^* as a function of K_{12}, is illustrated in Figure 11. The remaining parameters in these figures were kept as the values for the asthmatic case as shown in Tables 1-3. As can be seen, both of these steady states remain stable throughout. These diagrams also show, however, that increasing these parameters decreases the steady state value for the amount of c and p ASM cells. We could therefore use this is order to find an optimal value for these rates so that we get a lower, more healthy amount of ASM cells for an asthmatic patient at steady state.

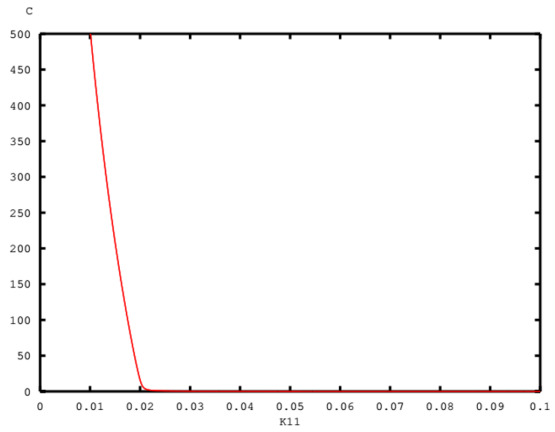

Figure 10: Bifurcation diagram for the variable c as parameter K_{11} is altered. The other parameters remain as stated in Tables 1-3 for the asthmatic case. The red line represents a stable steady state.

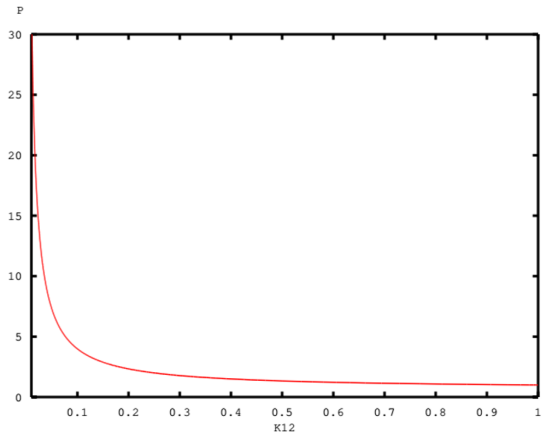

Figure 11: Bifurcation diagram for the variable p as parameter K_{12} is altered. The other parameters remain as stated in Tables 1-3 for the asthmatic case. The red line represents a stable steady state.

4.9 Pathology

We now add in the stimulus to the model, $S(t;w)$, to represent each asthmatic exacerbation event. This, therefore, only ever occurs for an asthmatic patient; there is never any stimulus for the model of a healthy control. We non-dimensionalise as before, giving us the dimensionless system as in equations 4.10-4.16 but with equation 4.10, for the change in mast cell tryptase over time, now given as:

$$\frac{dy}{dT} = \hat{z}S(t;w) - K_1 y, \tag{4.23}$$

where $\hat{z}$ is the dimensionless parameter given by

$$\hat{z} = \frac{z}{K_{PC}\bar{Y}}. \tag{4.24}$$

As mentioned in section 2.1, when an allergen is recognised in the airway of an asthma patient, an acute inflammatory response occurs almost instantaneously leading to an influx of mast cells (as well as other inflammatory cells). This is called an exacerbation. Like in [6], we choose to model this environmental time dependent stimulus, $\hat{z}S(t;w)$, using a Gaussian function to represent each event. This can be seen in Figure 12, where

exacerbation events occur with with a magnitude of $\hat{z}$ and a recurrence time of $\frac{1}{w}$. The individual events are taken to be given by

$$S(t;w) = \sum_i \exp\left(-\sigma(t-t_i)^2/2\right) \tag{4.25}$$

where $\sigma = 0.01$.

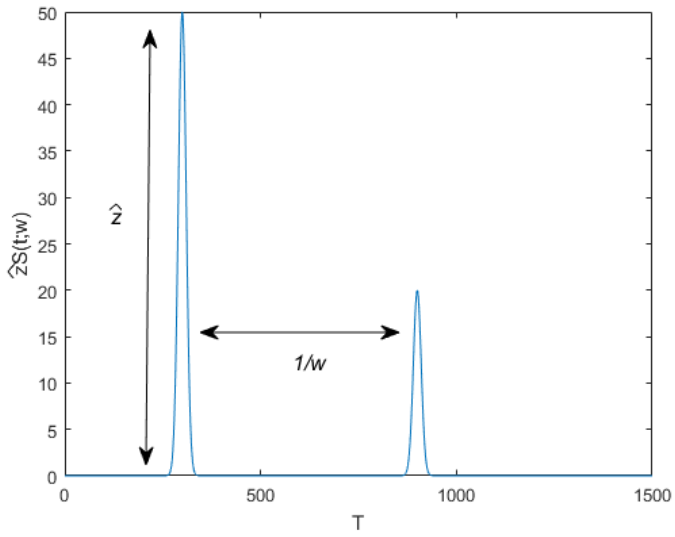

Figure 12: Dynamics of the environmental stimulus taken to represent the influx of inflammatory cells to the airway during an asthmatic exacerbation. Here the function $\hat{z}S(t;w)$ is simulated over time using equation 4.9 with $i = 2$. $\hat{z} = 50$ for the first event at $t_1 = 300$ and $\hat{z} = 20$ in the second event at $t_2 = 900$.

The red curves in Figures 13 and 14 then illustrate the impact that this environmental stimulus has on the dynamics of the variable y. Here, we are assuming that the quantity of mast cell tryptase (y) is directly proportional to the amount of mast cells present, which increases significantly under the inflammatory response involved in an exacerbation event.

4.9.1 Numerical Simulation

We simulate this model in Matlab in the same way as the non-pathological case, but here with a stimulus as described in Figure 12. The time course is shown in Figure 13. We can see that this looks incredibly different to the simulations that were done for the system

without pathology, by comparing it with Figure 6. Where in the non-pathological case there are smooth changes, here the graphs look very sporadic. The two peaks in mast cell tryptase can be seen as subsequent increases in active MMP-1, altered ECM and proliferative ASM and equivalent decreases in pro MMP-1, normal ECM and contractile ASM. While the second, smaller peak in mast cell tryptase can be seen as a small increase in active MMP-1, this increase is not enough to create another peak in altered ECM and hence proliferative ASM. If the pathological variables (y, q and a) have enough time to decay to zero between exacerbation events, then the non-pathological variables quickly increase to approximately their steady state value before they have to decrease again to allow increases in the pathological variables.

In Figure 14, we test the impact of reducing resolution speed, as investigated in [6], on the dynamics of y and hence the other variables in the system. We can see from this that a reduction in resolution speed, as an affect of reducing the decay rate of y, leads to a build up of mast cell tryptase. This build up means that the non-pathological variables (m, e and c) rapidly decline to near zero, while the pathological variables (q, a and p) jump to a higher value where they remain untill the pathology is removed. Chernyavsky *et al* [6] have shown that this build up in inflammatory cells can then result in an increase in total ASM growth.

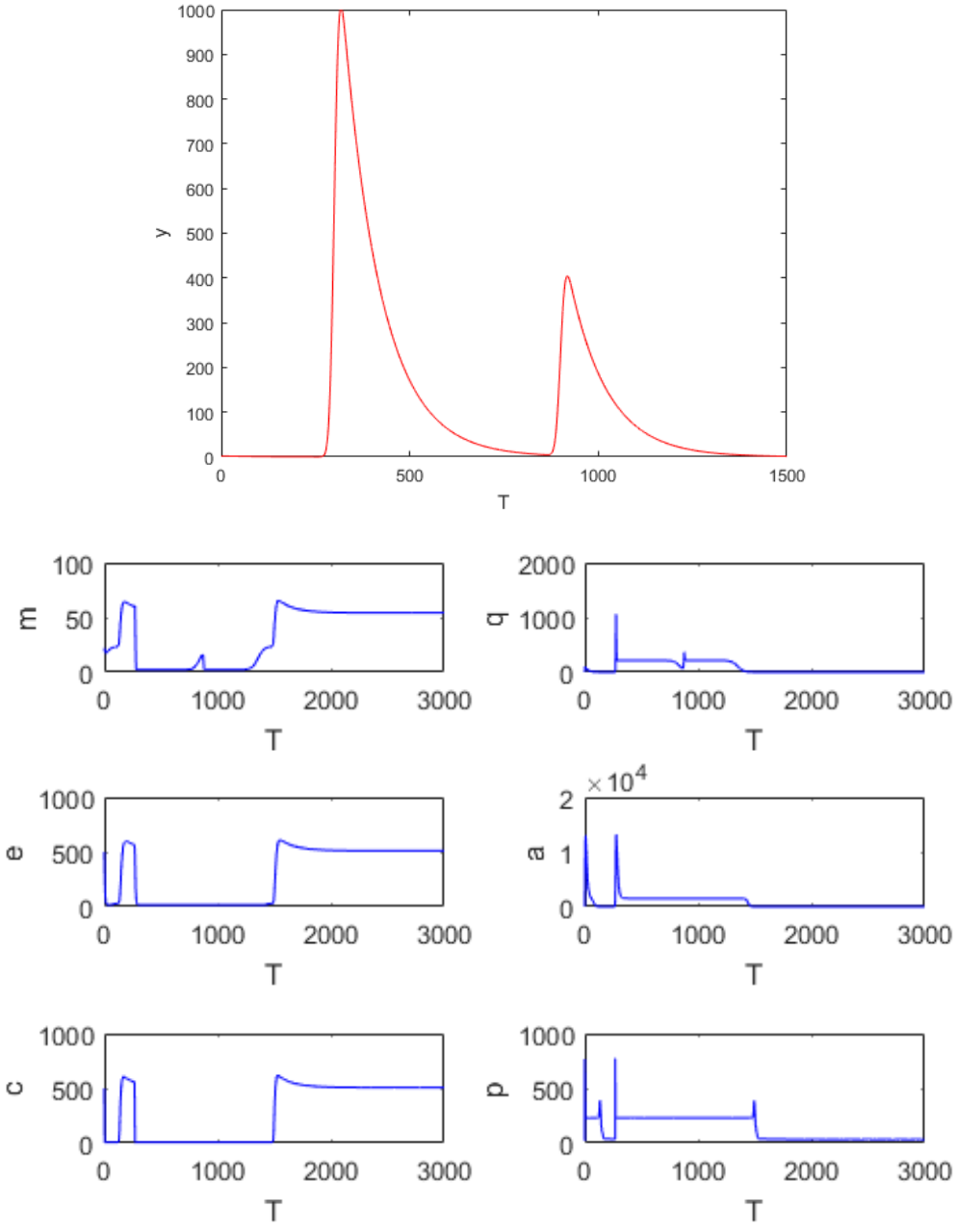

Figure 13: Top (red): Dynamics of y when stimulated using the input as modelled in Figure 12. Bottom (blue): Simulation of the change in each of the other variables in the dimensionless system over time, as an impact of the change in y. This is for an asthmatic patient with initial conditions $[y_0, m_0, q_0, e_0, a_0, c_0, p_0] = [5, 20, 0, 500, 0, 500, 20]$. Parameter values are as in Tables 1 - 3 with a Hill coefficient of $n = 4$.

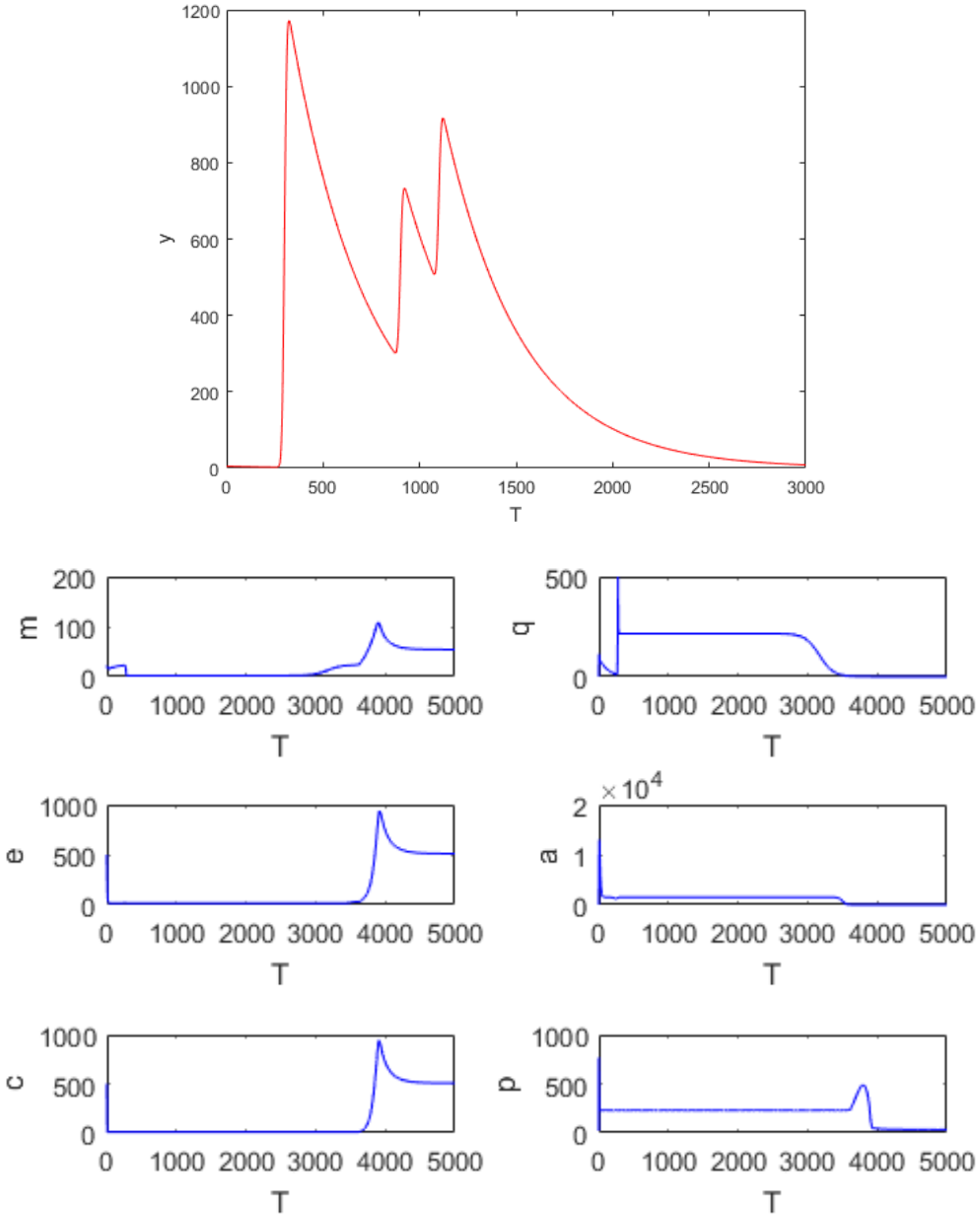

Figure 14: Top (red): Dynamics of y with a slow resolution speed due to a reduction in the decay rate of y to $K_1 = 0.0025$. Here, y again has the input $\hat{z}S(t; w)$, which is simulated over time using equation 4.9 with $i = 3$. Again, $\hat{z} = 50$ for the first event at $t_1 = 300$ and $\hat{z} = 20$ in the second event at $t_2 = 900$ but here there is a further event of $\hat{z} = 20$ at $t_3 = 1100$. A build up of y can be seen. Bottom (blue): Simulation of the change in each of the other variables in the dimensionless system over time, as an impact of the change in y. This is for an asthmatic patient with initial conditions $[y_0, m_0, q_0, e_0, a_0, c_0, p_0] = [5, 20, 0, 500, 0, 500, 20]$. Parameter values are as in Tables 1 - 3 with a Hill coefficient of $n = 4$.

4.9.2 Steady States

Adding the pathology of an exacerbation event to an asthmatic time course does not have an impact on the steady state of the system. This is because, once the stimulus is removed, y will eventually decay to zero as before, and so we obtain the same steady state for large T. We could, however, consider there to be a pathological, temporary steady state of which the variables tend to for a given magnitude of inflammation $\hat{z}$. This can be seen in Figure 13, for variables e, a, c and p for a time around $T = 1000$ and, more clearly, in Figure 14 for $T = 1000 - 3000$. We can therefore see that a slow resolution speed gives the temporary pathological steady state for longer. If the environmental input for this pathology is sustained, then these values act as a steady state for each variable during this time.

5 Model 2: Variable switching rate between proliferative and contractile ASM populations

We now make our first refinement to Model 1 in order to make the system more biologically realistic by adding a variable switching rate between proliferative and contractile ASM populations. Ultimately by making this alteration, we want to find out if more positive steady states exist, and if a change in a parameter value could lead to a change in stability to generate a new stable steady state. Knowing this information means that, if changing a particular parameter value gives a steady state where the quantities of variables are similar to that of the healthy case, we could target this respective parameter to induce this change in asthmatic patients.

5.1 Model Formulation

The model remains similar to Model 1 in most aspects but in order to refine it we now assume that the switching rate from P to C is not constant but a function of the amount of P. This can be seen in a zoom of the new schematic in Figure 15 where the rest of the signalling network remains as in Figure 3. While there is a significant amount of

research behind the switching of ASM cells from a contractile to a proliferative phenotype in response to growth factors produced by altered asthmatic ECM *in vitro*, there is less information about the switch back to their original contractile state from being proliferative. In both cases, it is not known whether this type of switching occurs *in vivo*. Here, we assume that the rate at which this switch occurs increases with an increase in quantity of the proliferative population up until a point where the rate increases no further. As before, where we used Hill functions to represent the binding of molecules leading to a change in rate $k_{MQ}(Y)$, $k_{EA}(Q)$ and so on, we now introduce the function $k_{PC}(P)$ as follows.

$$k_{PC}(P) = \hat{k}_{PC} + \frac{J_{PC}P^n}{\zeta + P^n}. \tag{5.1}$$

Here, $\hat{k}_{PC}$ is taken as being the same as k_{PC} from the previous model, J_{PC} is the maximum rate of switching from P to C and ζ is the switching point at which the rate is at half of its maximum. Hence the dimensional equations 4.1-4.5 from the original system of Model 1 remain the same but 4.6 and 4.7 are altered to the following:

$$\frac{dC}{dt} = k_{PC}(P)P - k_{CP}(A)C - k_{Ca}C, \tag{5.2}$$

$$\frac{dP}{dt} = k_{CP}(A)C - k_{PC}(P)P + k_P(A)P\left(1 - \frac{P+C}{V}\right) + \lambda_P. \tag{5.3}$$

We can non-dimensionalise these equations and the rest of the system as before using $t = \frac{T}{\hat{k}_{PC}}$, $C = c\bar{C}$ and $P = p\bar{P}$. The dimensionless system therefore comprises of equations 4.10-4.14 whereby the dimensionless parameters are now relative to the rate $\hat{k}_{PC}$, and equations for the change in c and p as seen below.

$$\frac{dc}{dT} = \sigma_7 p + j_5\sigma_7\left(\frac{p^n}{\phi_5 + p^n}\right)p - K_{10}c - j_3\left(\frac{a^n}{\phi_3 + a^n}\right)c - K_{11}c, \tag{5.4}$$

$$\begin{aligned}\frac{dp}{dT} = {} & K_{10}\sigma_8 c + j_3\sigma_8\left(\frac{a^n}{\phi_3 + a^n}\right)c - p - j_5\sigma_7\left(\frac{p^n}{\phi_5 + p^n}\right)p \\ & + p(K_{12} + j_4\left(\frac{a^n}{\phi_4 + a^n}\right))\left(1 - \frac{p + \sigma_8 c}{\sigma_9}\right) + \psi_3,\end{aligned} \tag{5.5}$$

where $j_5 = \frac{J_{PC}}{\hat{k}_{PC}}$ and $\phi_5 = \frac{\zeta}{P^n}$.

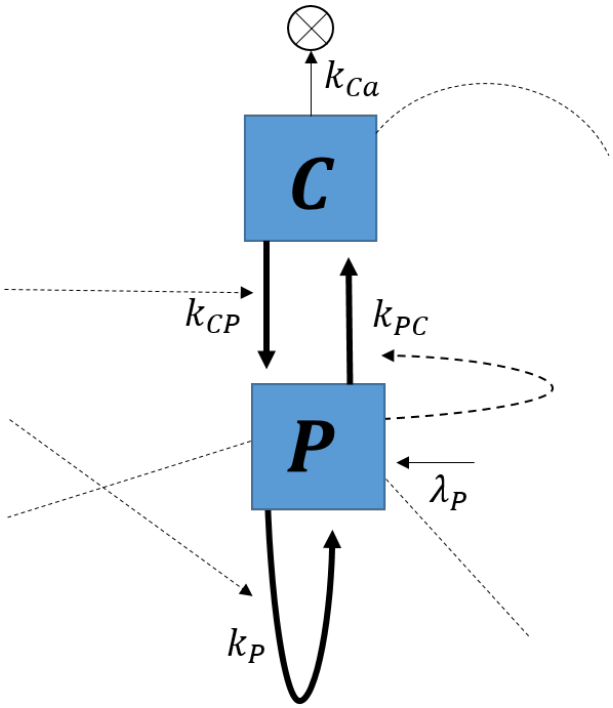

Figure 15: Zoom of the model schematic as shown in Figure 3 with the added alteration for Model 2 shown. The parts of the signalling network not shown are the same as in Model 1.

5.2 Numerical Simulation

We simulate Model 2 over time, as we did with Model 1, in order to compare the dynamics of each of the variables in the system for an asthmatic patient, and to see if this refined model better represents the time course we would expect (see Fig.16 for Model 2 as compared to Fig.6 for Model 1). All parameter values for the Model 2 simulation are the same as in Tables 1-3 and as described, the only difference from Model 1 is that the switching rate from p to c is now a function of p. The dynamics of y are therefore identical to that of Model 1. We notice however, that quantitatively, there is an approximate 10 fold increase in the steady state values of m, e and c and a 2 fold increase in p when comparing them to Model 1, whereas the values of q and a remain similar to those of Model 1. There is little to no data available on the relative quantities of these non-pathological variables (m, e and c) to the pathological variables (q, a and p), hence it is currently difficult to know which of Model 1 and Model 2 are the most realistic in this regard. Qualitatively, the time courses are very similar, except, where in Model 1 the variables m, e and c begin

low and then quickly increase to their steady state once the pathological variables are zero, in Model 2, they increase towards their steady state but then decrease again before increasing to saturate at their steady state.

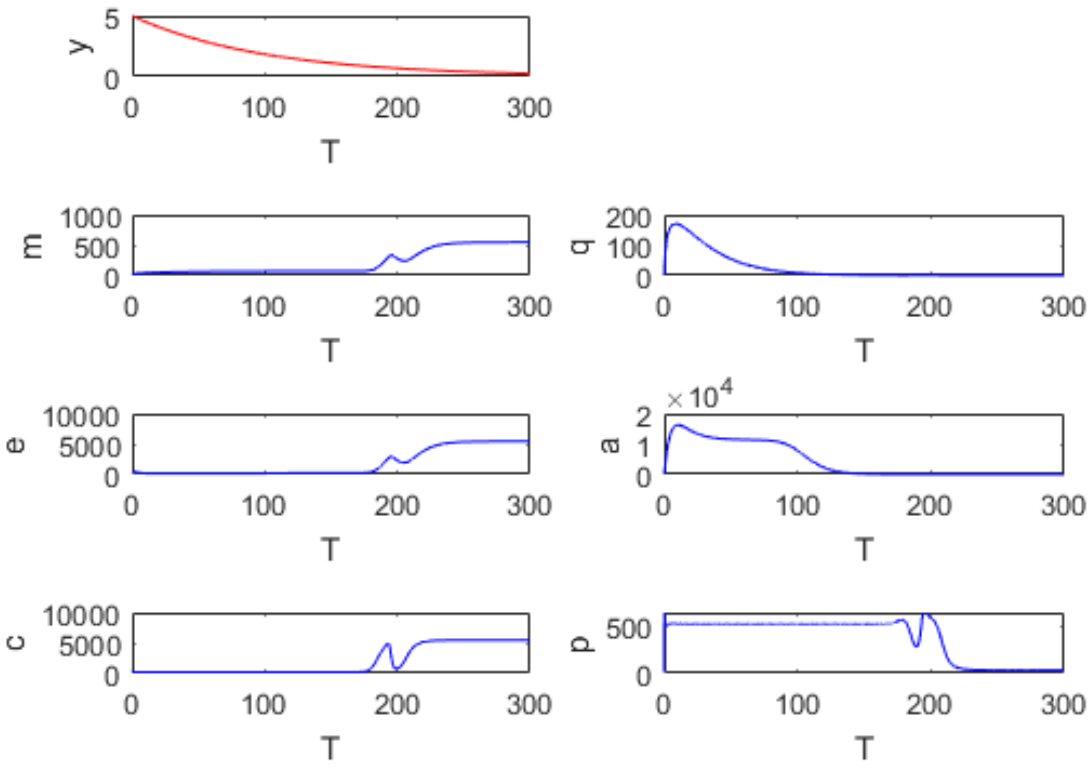

Figure 16: Matlab simulation for the change in each variable of Model 2 over time for an asthmatic patient with initial conditions $[y_0, m_0, q_0, e_0, a_0, c_0, p_0] = [5, 20, 0, 500, 0, 500, 20]$ and no further stimulus. Parameter values are as in Tables 1 - 3.

5.3 Steady States

When looking at the steady states of this model, we again get $y^* = q^* = a^* = 0$. We also get m^* and e^* as in equations 4.17 and 4.18, where now,

$$c^* = \frac{\sigma_7 p^* + j_5 \sigma_7 \left(\frac{p^n}{\phi_5 + p^n}\right) p^*}{K_{10} + K_{11}}, \tag{5.6}$$

and p^* is found to satisfy the $(n+2)$ degree polynomial shown below.

$$
\begin{aligned}
&p^{n+2}(K_{12}(\sigma_7\sigma_8 + K_{10} + K_{11} + \sigma_7\sigma_8 j_5) \\
&+ p^{n+1}((K_{10} + K_{11})\sigma_9 - K_{10}\sigma_7\sigma_8\sigma_9(1 + j_5) - (K_{10} + K_{11})(K_{12}\sigma_9 + j_5\sigma_9)) \\
&+ p^n(\psi_3(K_{10} + K_{11})) + p^2(K_{12}(\sigma_7\sigma_8\phi_5 + \phi_5(K_{10} + K_{11}) \\
&+ p(\phi_5\sigma_9(-K_{10}\sigma_7\sigma_8 K_{10}K_{12} - K_{11}K_{12} + K_{10} + K_{11}) \\
&+ \psi_3\phi_5(K_{10} + K_{11}) = 0
\end{aligned} \tag{5.7}
$$

5.3.1 Hypersurface Analysis

As it would be difficult to find p^* analytically as we did previously, here we instead gain an understanding of steady states by looking at the qualitative nature of the nullclines of the system. By rearranging the nullcline equations for $\frac{dc}{dt} = 0$ and $\frac{dp}{dt} = 0$, we can find equations for the respective hypersurfaces given below:

$$
c = \frac{p\big(\sigma_7 + j_5\sigma_7\left(\frac{p^n}{\phi_5 + p^n}\right)\big)}{K_{10} + K_{11}} \tag{5.8}
$$

$$
c = \frac{-K_{12}p^2 + p(K_{12}\sigma_9 - \sigma_9 - j_5\sigma_9\left(\frac{p^n}{\phi_5 + p^n}\right)) + \psi_3}{\sigma_8(K_{12}p - K_{10}\sigma_9)} \tag{5.9}
$$

As these two equations given for c are both in terms of p only, we can simulate their dynamics for varying values of parameters and the two curves will cross at any steady state values. We did this for a number of parameters that are likely to affect the nature of these hypersurfaces the most (using equations 5.8 and 5.9). Equation 5.8 for c is linear looking. Equation 5.9 tends to infinity when $p = \frac{K_{10}\sigma_9}{K_{12}}$ hence varying the parameters that affect this is a good place to start. We also consider which rates would have the biggest impact biologically, for example, we would expect that the apoptosis rate K_{11} would have a big effect. Examples of these graphs are shown in Figure 17, where we vary parameters K_{10}, K_{12} and j_5 while keeping all the other parameters fixed for both $K_{11} = 0.01$ and $K_{11} = 0.1$. This Figure shows that for each of these combinations of parameters, the two nullclines only ever cross at zero and one positive steady state value. Hypersurfaces for e and m are both linear and in terms of p and c only, hence their steady states follow to give only one positive steady state value for the system.

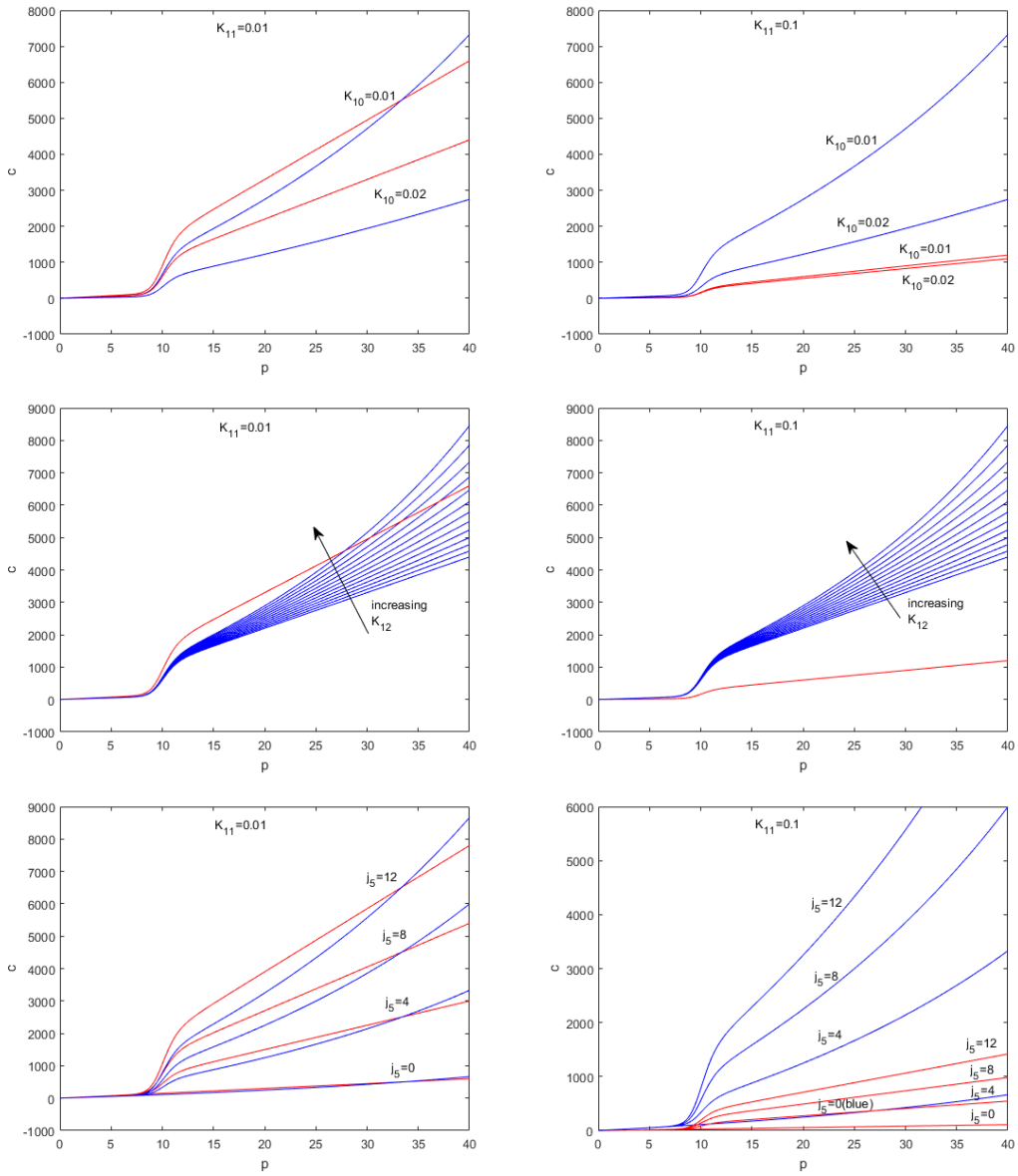

Figure 17: Graphs showing the two c nullclines in terms of p as in equations 5.8 (as shown by the red lines) and 5.9 (as shown by the blue lines). The left hand column of graphs shows simulations with $K_{11} = 0.01$ and the right hand coloumn has $K_{11} = 0.1$. Within each graph we also alter a single parameter; K_{10} in the top two graphs, K_{12} in the middle two and j_5 in the bottom pair. These changes are shown by plotting the new nullclines for each change in value. When altering K_{10} and j_5, both the nullclines change, however, only the blue c nullcine is altered for a change in K_{12}. Each of the corresponding red and blue curves cross eachother at the steady states. This only occurs at zero and one other positive state.

As this system, again, only gives one positive steady state, this means that we are unable to use Model 2 to gain an insight into possible changes that can be made in order to alter the system so that it tends to a more healthy steady state value. It also means that when we add pathology to the system from an environmental input, as we did in section 4.9 with Model 1, as soon as the external stimulus is removed, the system will tend back to the only steady state.

6 Model 3: Inhibition of ASM apoptosis

We will now make a further refinement to the model to add some complexity which makes the system even more biologically realistic. Though the amount of ASM cells in an ASM bundle is determined by both the division and apoptosis of these cells, the models so far have concentrated only on the effect that the altered ECM has on the proliferative capacity of ASM cells. We now consider the additional effect of altered ECM on change in apoptosis rates of smooth muscle cells in asthmatic airways.

Freyer *et al* [8] have investigated the impact that ECM has on the survival or relative apoptosis of ASM cells. It was discovered that ASM cells are robust to apoptosis as a result of a survival signal released to them from interacting ECM and β1-integrins. They additionally found that the proteins that are more abundant in the altered ECM, as a result of the airway remodelling explained in 2.2, are important in the production of this signal. For example, it was found that adding fibronectin to cells that can not produce any matrix proteins alone, creates this survival signal, and blocking the recognition site of fibronectin, destroys it. As mentioned previously, fibronectin (and other proteins involved in the production of this signal) increases in an altered ECM of an ASM bundle and so this survival signal is enhanced in an asthmatic airway. Freyer *et al* [8] therefore conclude that asthmatic ASM growth is partially explained by this strong signal produced by altered ECM, and that this increase in ASM cells leads to further production of ECM and hence a cycle which eventually leads to the narrowing of the airways. This has also been confirmed *in vivo*, as it has been shown that both rises in proliferation and decreases in apoptosis of ASM cells occur in an infected Brown Norway rat model [12].

6.1 Model Formulation

We therefore incorporate this survival signal into our model to create Model 3. We do this by adding some inhibition to the model (Models 1 and 2 only exhibit activation). Increasing the survival of ASM cells, in turn, means reducing their apoptosis. This means that, in this model, apoptosis of C is inhibited by both E and A, with a rate $k_{Ca}(E, A)$. This can be seen in a zoom of the full model schematic as seen in Figure 18, where the switching rate from P to C and the rest of the signalling network remains as in Model 2 (as described in section 5). Looking at this schematic, we can see a clear positive feedback loop. This occurs as the inhibition of ASM apoptosis by ECM leads to growth of ASM and, in turn, further production of ECM. We set $k_{Ca}(E, A)$ to be another Hill function but this time, one that decreases from its maximum at a rate depending on the values of both E and A as shown in the equation below:

$$k_{Ca}(E, A) = \hat{k}_{Ca} + (J_{Ca} - \hat{k}_{Ca}) \left(\frac{1}{1 + \frac{E^n}{\omega}} \right) \left(\frac{1}{1 + \frac{A^{n+1}}{\upsilon}} \right) \tag{6.1}$$

Here, $\hat{k}_{Ca}$ represents the very low rate of apoptosis that occurs when both E and A are at their maximum and so $(J_{Ca} - \hat{k}_{Ca})$ is the maximum rate of ASM cell death which occurs when E and A are both negligible. ω and υ are the switching parameters at which the apoptosis rate, as a function of E and A respectively, is at half of its maximum. As can be seen, A has a higher Hill coefficient and so its switching gradient is more steep (as we saw in Figure 4). The dimensional equations 4.1-4.5 for the change in Y, M, Q, E and A from the original system of Model 1 therefore remain the same, equation 5.3 for P stays as in Model 2 and 5.2 for C is altered to the following:

$$\frac{dC}{dt} = k_{PC}(P)P - k_{CP}(A)C - k_{Ca}(E, A)C. \tag{6.2}$$

Non-dimensionalising, we get

$$\begin{aligned} \frac{dc}{dT} =& \sigma_7 p + j_5 \sigma_7 \left(\frac{p^n}{\phi_5 + p^n} \right) p - K_{10} c - j_3 \left(\frac{a^n}{\phi_3 + a^n} \right) c - K_{13} c \\ & - j_6 \left(\frac{1}{1 + \frac{e^n}{\phi_6}} \right) \left(\frac{1}{1 + \frac{a^{n+1}}{\phi_7}} \right) c, \end{aligned} \tag{6.3}$$

where $K_{13} = \frac{\hat{k}_{Ca}}{\hat{k}_{PC}}$, $j_6 = \frac{(J_{Ca} - \hat{k}_{Ca})}{\hat{k}_{PC}}$, $\phi_6 = \frac{\omega}{\bar{E}^n}$ and $\phi_7 = \frac{v}{\bar{A}^{n+1}}$ are dimensionless constants.

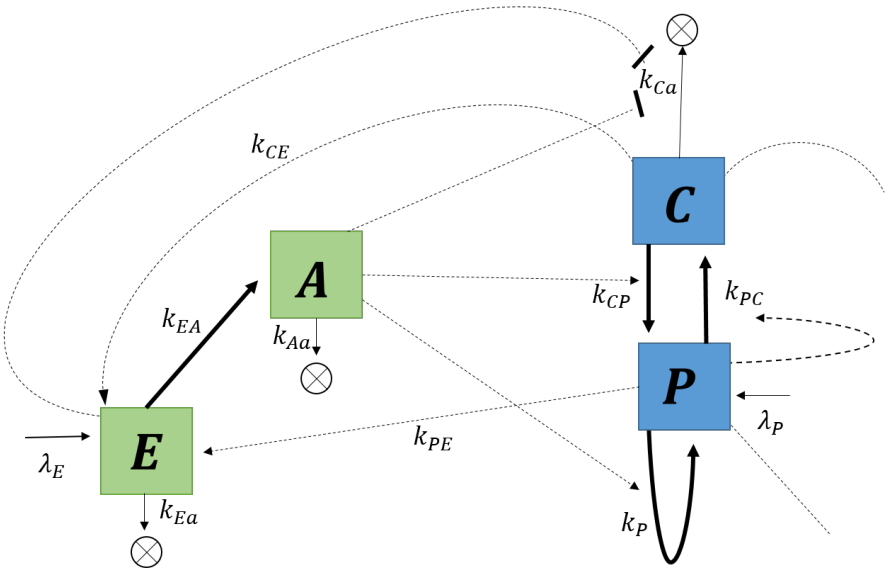

Figure 18: Zoom of the model schematic as shown in Figure 3 with the added alterations for Models 2 and 3 shown. The parts of the signalling network not shown are the same as in Model 1.

6.2 Numerical Simulation

We simulate Model 3, as shown in Figure 19 and compare the results of this to the dynamics seen previously in Model 1 and Model 2. The dynamics of the time course for Model 3 can be seen to be extremely similar to that of Model 2, the difference being that the variables m, e and c increase to their steady state values (after the pathological variables have decayed to zero) much more slowly than in Model 2. The steady state value, at which these variables eventually saturate, is again significantly higher than in the previous model.

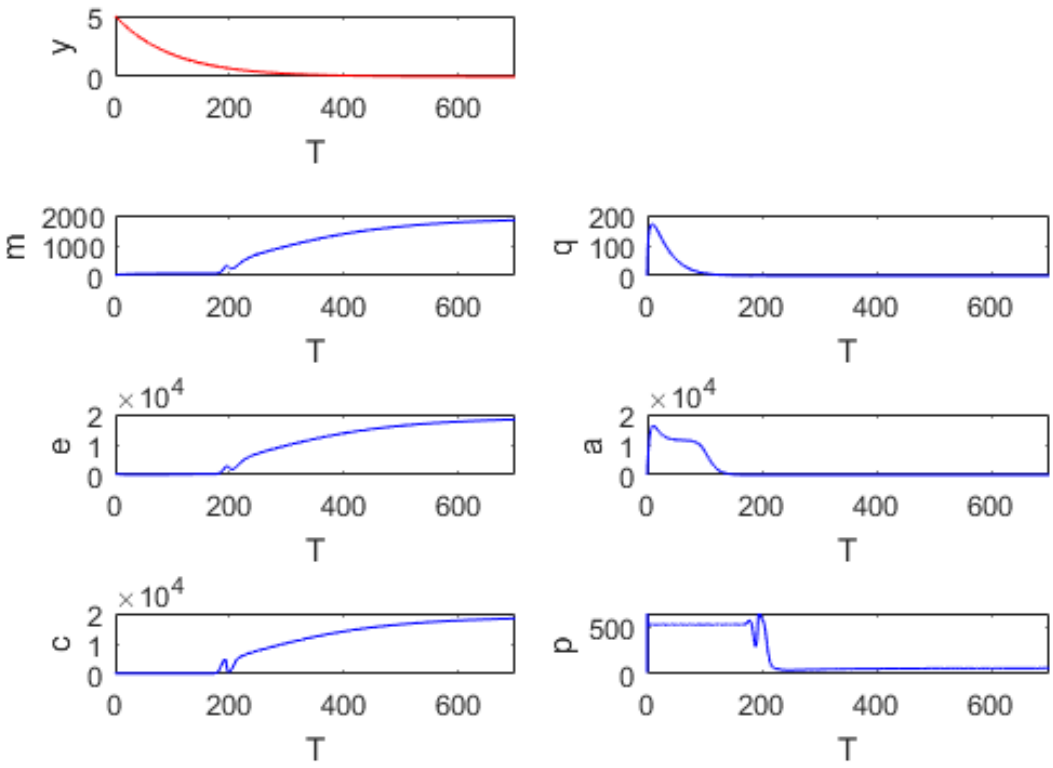

Figure 19: Matlab simulation for the change in each variable of Model 3 over time for an asthmatic patient with initial conditions $[y_0, m_0, q_0, e_0, a_0, c_0, p_0] = [5, 20, 0, 500, 0, 500, 20]$ and no further stimulus. Parameter values are as in Tables 1 - 3.

6.3 Parameter Sensitivity Analysis

We perform a parameter sensitivity analysis using COPASI in order to find the parameters that the steady state of the system is most sensitive to, and hence those that are likely to lead to bifurcations. We want to identify any bifurcations in order to determine if adding pathology to the system could change the stable steady state to being of a more unhealthy value, as we would expect. This information could also be used in order to find the rates that are most suitable to be targeted in any therapies as, just a small change in these parameter values, gives a big change in the dynamics of the system. Additionally, in the formulation of this model, parameter values were assigned using order of magnitude estimates, but their actual values are mostly unknown. Sensitivity analysis can therefore

tell us the importance of knowing accurate values of certain parameters or if estimates are sufficient. COPASI calculates this analysis using the finite differences method [15]. A delta factor value of 0.001 is used here so that the sensitivities we see are the percentage change in the steady state value for a 0.1% change in parameter value. The sensitivity of the steady state to the rates $K_1 - K_{13}$ can be seen in Figure 20. It is clear from this bar chart that K_{12} and K_{13} are the most sensitive parameters. The percentage change in steady states as an affect of changing these parameters may be so large due to the fact that the parameter baseline values are very small. This means that any percentage changes for these parameters get amplified. We therefore conduct our bifurcation analysis with a focus on these parameters.

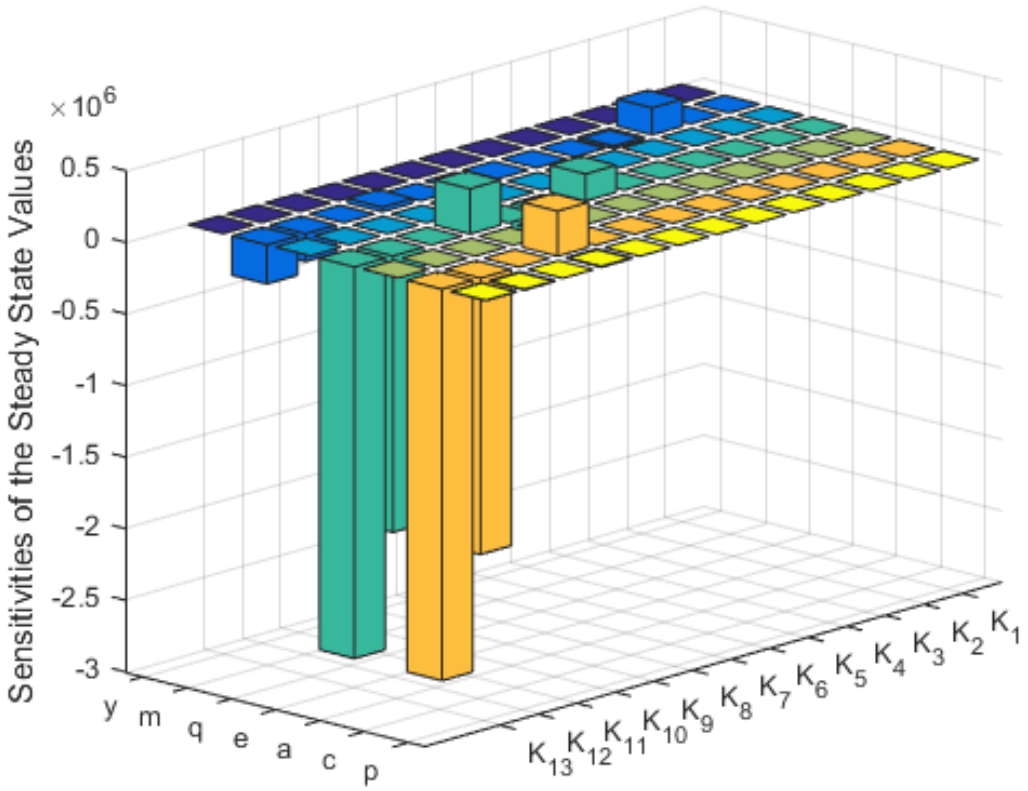

Figure 20: Bar graph showing the sensitivity of the steady state to a 0.1% change in parameter values of $K_1 - K_{13}$. Sensistivities were calculated using COPASI.

6.4 Bifurcation Analysis

In this section we analyse the bifurcation behaviour in Model 3 by varying sensitive parameters using XPP. In doing this, we observe multiple saddle node bifurcations, whereby two steady states collide and disappear at a limit point (LP). Figure 21 shows the change in c when varying K_{10}. It can be seen that there are two saddle node bifurcations, one with negative c for very small values of K_{10} and the other with a positive value of c that increases as K_{10} increases. For the system to be biologically relevant however, we see that K_{10} needs to be greater than approximately 0.0005. In between the positive and negative saddle nodes, the stable steady state which cannot be seen in Figure 21 is extremely negative and so is also irrelevant in our analysis. Figure 22 shows the change in p when varying K_{13}. Here, we again see two saddle nodes bifurcations, this time with the irrelevant (negative) branch being for higher values of K_{13}. Similarly, in between the two saddle nodes we find a very negative stable steady state that isn't shown in the figure.

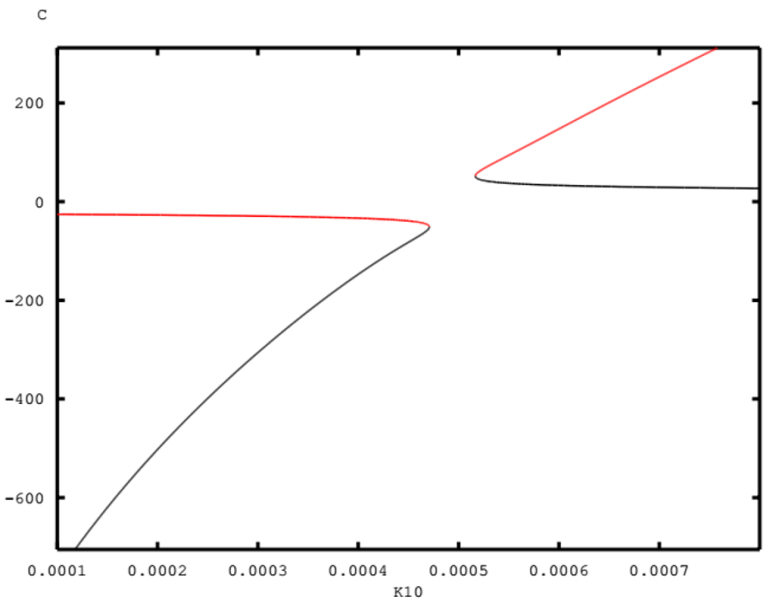

Figure 21: Bifurcation diagram for the variable c as parameter K_{10} is altered in Model 3. The other parameters remain as stated in Tables 1-3 for the asthmatic case. The red line represents a stable steady state and the black line an unstable steady state. Saddle-node bifurcations can be seen.

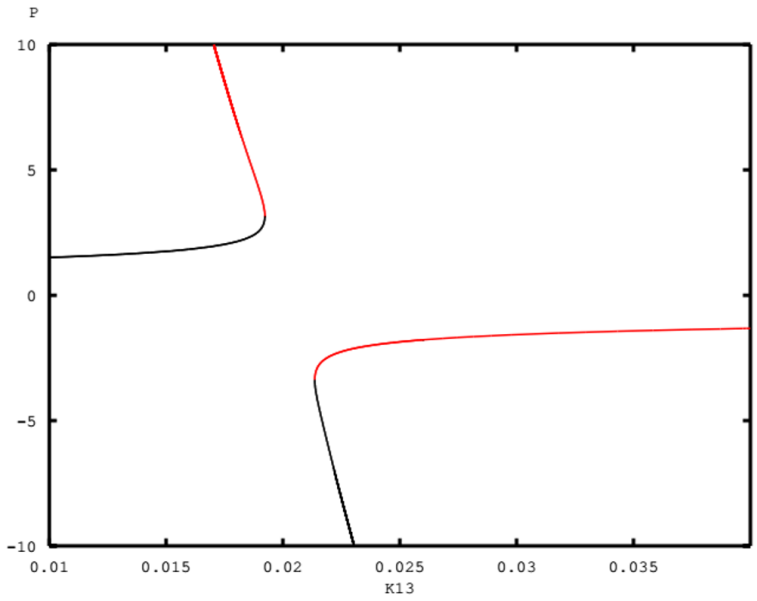

Figure 22: Bifurcation diagram for the variable p as parameter K_{13} is altered in Model 3. The other parameters remain as stated in Tables 1-3 for the asthmatic case. The red line represents a stable steady state and the black line an unstable steady state. Saddle-node bifurcations can be seen.

Figure 23 illustrates the change in p when varying K_{12}. We can see that, while again there are two saddle node bifurcations, here these saddle nodes overlap so that for a region between $K_{12} \approx 0.78$ and $K_{12} \approx 1.17$, there are four steady states (two stable and two unstable). Figure 24 shows this more clearly, by zooming in on the area at which the stable steady states overlap. It can be seen that, for $K_{12} < 0.78$, there are just 2 steady states with the stable steady state higher than the unstable one. For $0.78 < K_{12} < 1$ two more steady states arise; a new higher stable steady state and an unstable steady state in between this and the original stable steady state. When $K_{12} = 1$, the unstable steady state from the top branch crosses the two lower steady states and at the same time, the stable and unstable parts of this lower branch cross over. This means that for $1 < K_{12} < 1.17$, the two stable steady states are still separated by an unstable steady state with an additional unstable steady state below. When $K_{12} \approx 1.17$, the two original steady states coalesce and disappear at their LP so that only the other two steady states remain. We can also see that for $K_{12} = 0.8013$ and $K_{12} = 0.782$, Hopf bifurcations (HB) occur for the two higher steady states. This suggests that these steady states have a complex

conjugate pair of eigenvalues which, at this point, change to being only imaginary. The stable steady state therefore becomes unstable and limit cycles arise. The two unstable steady states then collide at their LP where $K_{12} = 0.78$ and disappear. Furthermore, using Figure 23, we can see that hysteresis occurs. This is because if K_{12} began low and was increased, the stable steady state would stay on its original lower branch until reaching its LP and jumping up to the higher stable steady state. If K_{12} began high and was decreased however, the stable steady state would stay on the upper branch until reaching its LP and jumping down to the lower stable steady state. These are two different paths, thus for the region of K_{12} with two possible steady states, its state depends on its history.

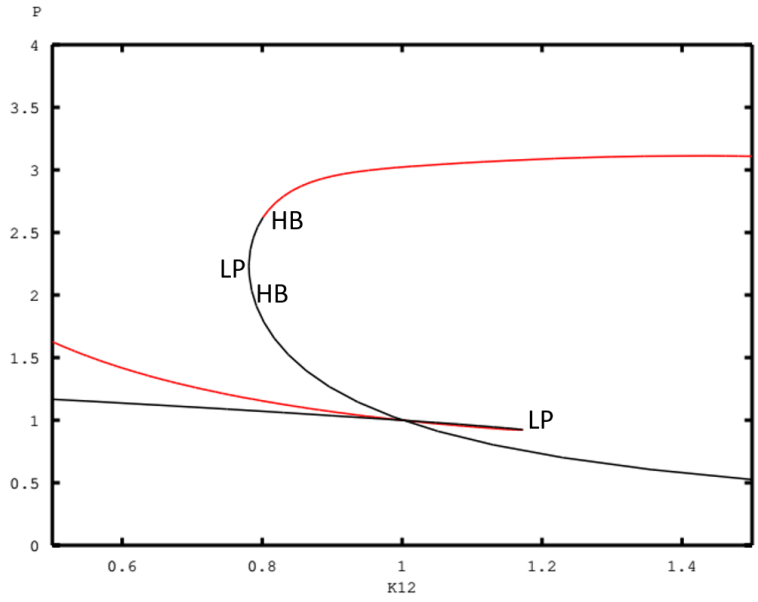

Figure 23: Bifurcation diagram for the variable p as parameter K_{12} is altered in Model 3. The other parameters remain as stated in Tables 1-3 for the asthmatic case. The red line represents a stable steady state and the black line an unstable steady state. Limit points (LP) of saddle node bifurcations and Hopf bifurcations (HB) can be seen.

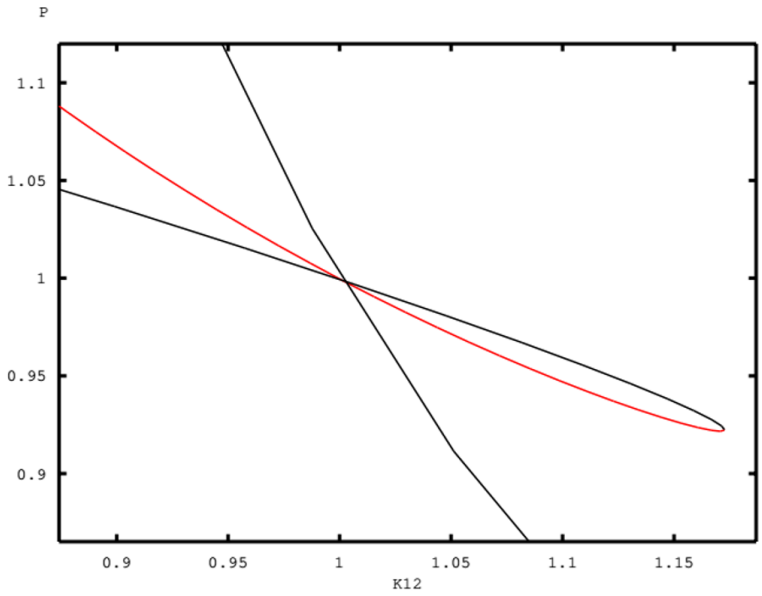

Figure 24: Zoom of Figure 23 to show the dynamics at the point where $K_{12} = 1$ and the unstable steady state (black) of the upper branch crosses the stable (red) and unstable steady states of the lower branch.

In Figure 25 we can see the same range of K_{12} values, where we now look at their impact on the value of variable c. Just as with p, for the small region between $K_{12} \approx 0.78$ and $K_{12} \approx 1.17$, there is bistability of c. We see again the LP's of each saddle node bifurcation and two HB's this time on the lower branch. The stable part of the lower branch becomes negative before the HB occurs however, so that this is biologically irrelevant. The same bifurcation behaviour also occurs for the variables e and m as can be seen in Figures 26 and 27 respectively.

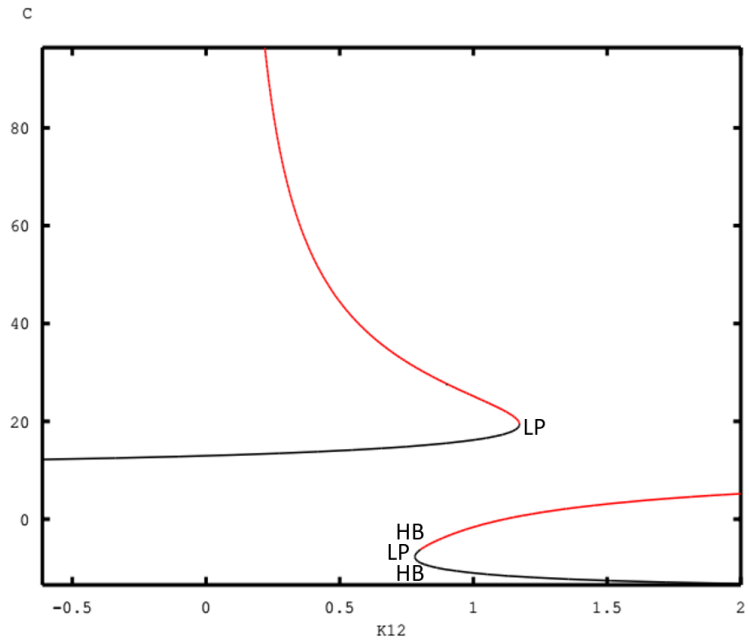

Figure 25: Bifurcation diagram for the variable c as parameter K_{12} is altered in Model 3. The other parameters remain as stated in Tables 1-3 for the asthmatic case. The red line represents a stable steady state and the black line an unstable steady state. Limit points (LP) of saddle node bifurcations and Hopf bifurcations (HB) can be seen.

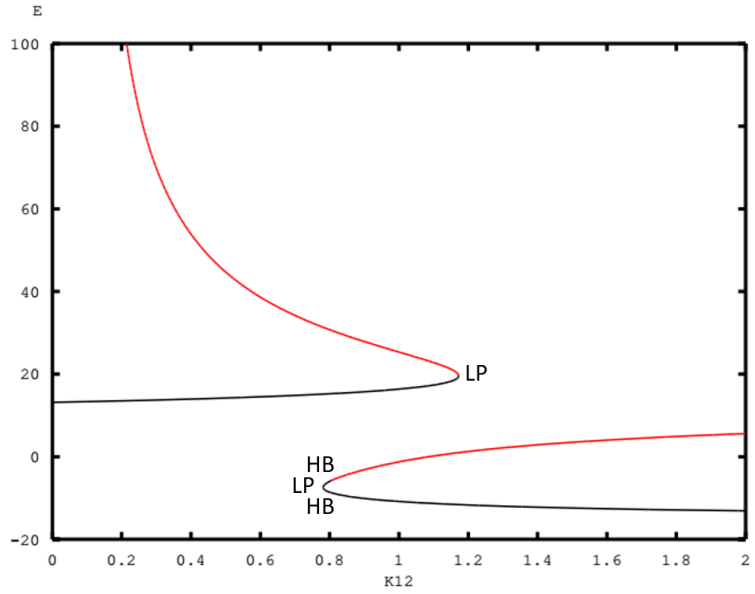

Figure 26: Bifurcation diagram for the variable e as parameter K_{12} is altered in Model 3. The other parameters remain as stated in Tables 1-3 for the asthmatic case. The red line represents a stable steady state and the black line an unstable steady state. Limit points (LP) of saddle node bifurcations and Hopf bifurcations (HB) can be seen.

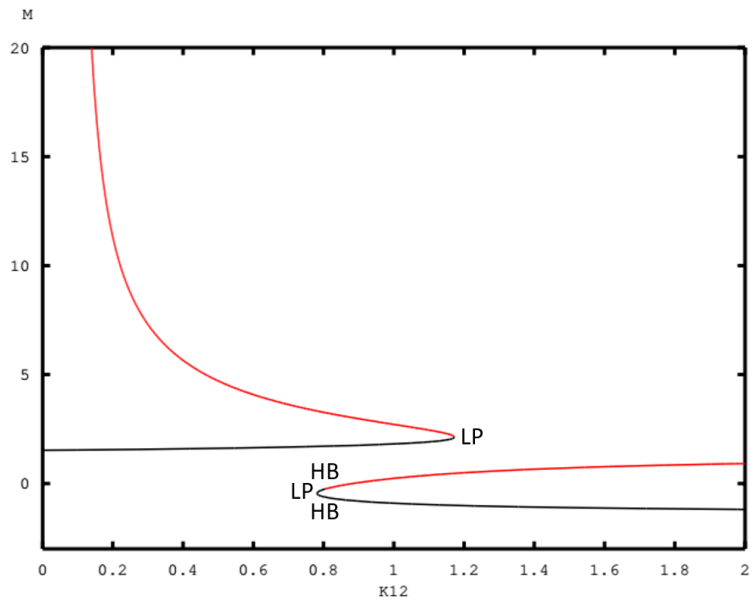

Figure 27: Bifurcation diagram for the variable m as parameter K_{12} is altered in Model 3. The other parameters remain as stated in Tables 1-3 for the asthmatic case. The red line represents a stable steady state and the black line an unstable steady state. Limit points (LP) of saddle node bifurcations and Hopf bifurcations (HB) can be seen.

As the range of K_{12} for which there are two positive steady states is only small in Figures 23-27, we undertake a two parameter bifurcation analysis in order to find a combination of parameter values for which this region is widened. It would also be interesting to find out if there is a point at which the two saddle nodes coalesce. We do this by grabbing the LP's in XPP and continuing them in a two parameter space as seen in Figure 28 with K_{10} being varied as well as K_{12}. From this we can see that for $0 < K_{10} < 0.042$ and $0 < K_{12} < 2.2$, there are two limit points of K_{12} for each value of K_{10}. At $K_{10} \approx 0.00338$ and $K_{12} \approx 0.61064$ the two LP's coalesce, however this occurs at such a precise value that it is unable to be found in a one parameter bifurcation diagram with XPP. Using Figure 28 we are able to see that the largest vertical distance between LP's for a given value of K_{10} occurs at $K_{10} \approx 0.025$. When using this value for K_{10} in a one parameter bifurcation diagram for c against K_{12} as before, we obtain the wider region of bistability we were looking to find (see Fig.29).

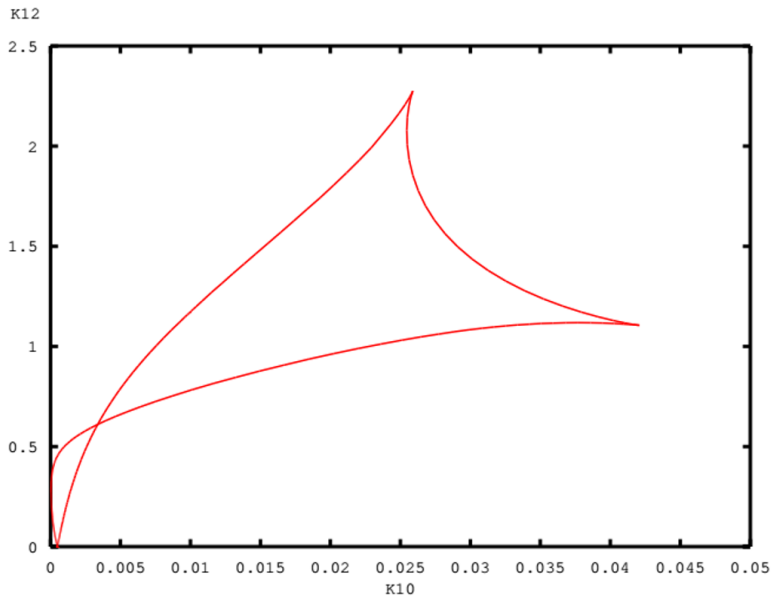

Figure 28: Two parameter bifurcation diagram: continuation of the saddle node limit point for varying K_{10} and K_{12}.

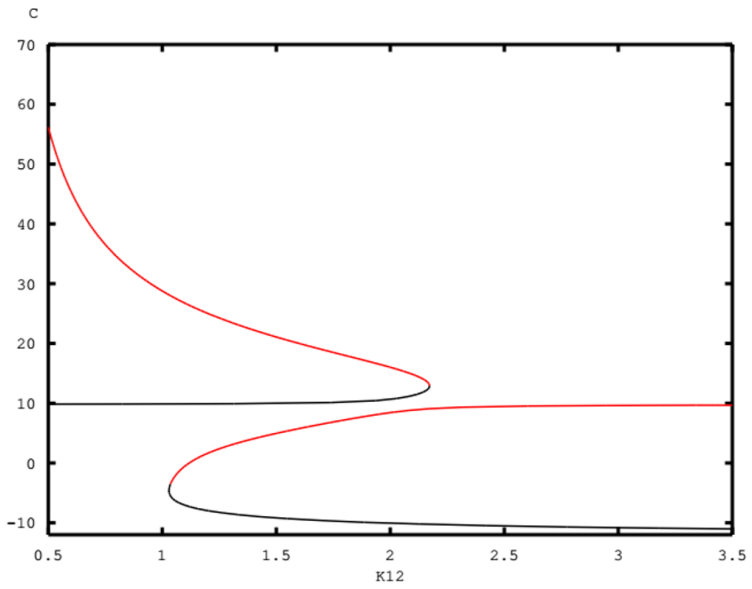

Figure 29: Widened region of bistability: Bifurcation diagram for the variable c as parameter K_{12} is altered in Model 3 with $K_{10} = 0.025$. The other parameters remain as stated in Tables 1-3 for the asthmatic case. The red line represents a stable steady state and the black line an unstable steady state.

6.5 Pathology

In this section we look at the results of the simulation of Model 3 when adding in the pathology of an asthmatic exacerbation event as we did for Model 1 in section 4.9. Looking at the bifurcation diagrams from the previous section, we know that for a particular range of values for K_{12}, there are two positive stable steady states separated by an unstable steady state. Henceforth, we now use a value for K_{12} within this region for all simulations. Using Figure 29, we can see that if we begin a time simulation with initial conditions such that the value of c is below the unstable steady state, then the system will tend to the lower stable steady state of c (see Fig.30). We now add the stimulus of a single exacerbation event of magnitude $\hat{z} = 50$ at a time of $T = 300$ and examine the dynamics of the time course, as well as the values of the steady states.

Figure 31 shows the impact of this exacerbation event. As noticed when adding pathology to Model 1, the pathological variables q and a increase rapidly in response to an increase in y and remain at a temporary pathological steady state until y has decayed to zero, where they then rapidly decline back to zero. Unlike in the time course simulations we have previously seen however, here, due to the initial conditions being so low, the non-pathological variables m, e and c also rapidly increase at $T = 300$ though this is by a smaller amount than the pathological variables. When the pathological variables begin to decline, the non-pathological variables increase further, but as the pathological variables reach zero, the non-pathological variables begin to decline until they saturate at their steady state. The steady state of the pathological case, even when the pathology is removed, is different to the steady state of the non-pathological case. This is because, looking back at Figure 29, once the pathology has pushed c above the unstable steady state, it is then in a new attractor region for the higher stable steady state and so this is where it remains.

It is clear that the values of the variables we test here are fairly biologically unrealistic. For example, all variables are at very low values and the amount of p at the non-pathological steady state is higher than that of other other variables (which is unlikely). However, here we have shown the mechanism by which an asthmatic exacerbation can lead to an irreversible change in the airways. Model 3 shows that, when an exacer-

bation occurs, the steady states for m, e and c increase. These increases coincide with research on airway remodelling which tells us that exacerbations can lead to an increase in levels of MMP-1, ECM and total ASM mass.

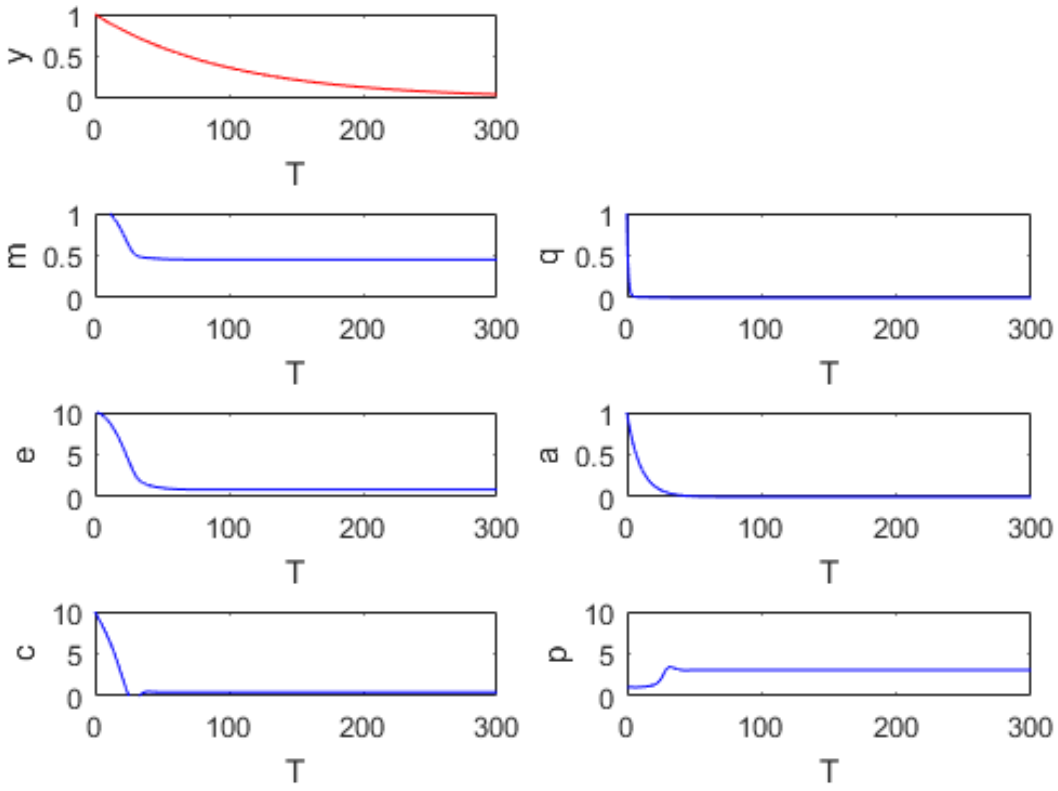

Figure 30: Matlab simulation for the change in each variable of Model 3 over time for an asthmatic patient with initial conditions $[y_0, m_0, q_0, e_0, a_0, c_0, p_0] = [1, 1, 1, 10, 1, 10, 1]$ and no further stimulus. Parameter values are as in Tables 1 - 3 except here $K_{12} = 1.158$. The Hill coefficient $n = 4$.

When testing different magnitudes of exacerbation events ($\hat{z}$), it was found that any non-zero magnitude was enough stimulus to enable this change in steady state. All values of magnitude therefore gave the same steady state values, because once the variables have increased enough such that their value is above their unstable steady state, they are now in the basin of attraction for the only other stable steady state. This suggests that, although the exacerbation event leads to remodelling, the severity of the event has no impact on the amount of remodelling that occurs.

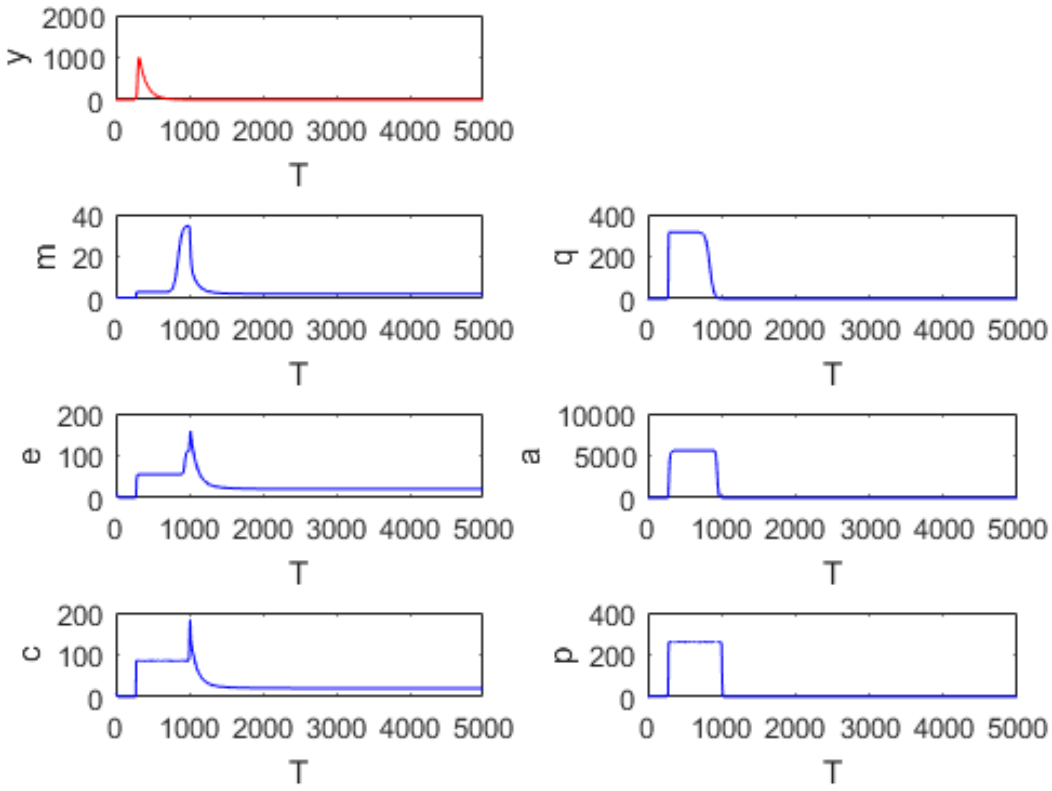

Figure 31: Matlab simulation for the change in each variable of Model 3 over time for an asthmatic patient with initial conditions $[y_0, m_0, q_0, e_0, a_0, c_0, p_0] = [1, 1, 1, 10, 1, 10, 1]$ and the single exacerbation input $\hat{z}S(t; w)$ at $t_1 = 300$ with $\hat{z} = 50$. Parameter values are as in Tables 1 - 3 except here $K_{12} = 1.158$. The Hill coefficient $n = 4$.

As the knowledge on the involvement of MMP-1 in the pathway that leads to airway remodelling is fairly new, there is very little data available in literature of which to compare our results to. The only data that is able to be compared to our results therefore, is taken from Naveed *et al* [16]. We can see that, in our results for Model 3, the steady state for pro MMP-1 is 3.9 fold greater after the exacerbation event (see Fig.32). This is exactly the same as the fold difference obtained by Naveed *et al* [16] for the change in mean MMP-1 activity after inoculating patients with a virus in order to simulate an exacerbation event. Hence, though here we are only considering pro MMP-1 (as at the steady state of this model, active MMP-1 is zero) it could be thought that there is an equivalent increase in overall MMP-1 quantities. Naveed *et al* [16] also show that, when both control and

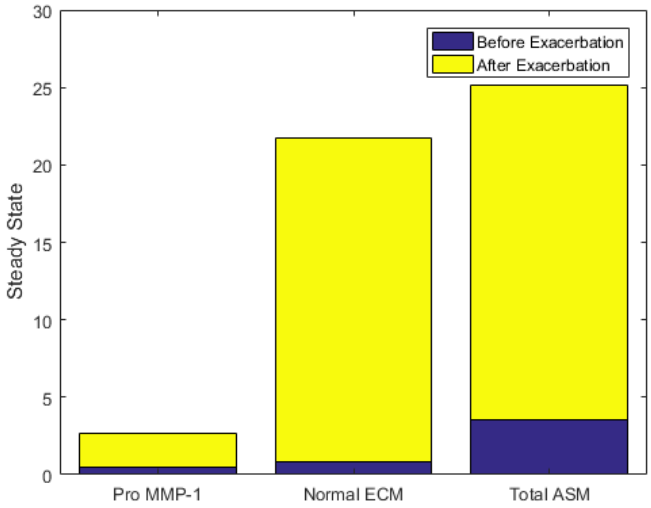

Figure 32: Difference between steady state values before and after an exacerbation event using Model 3.

asthmatic ASM is treated with active mast cell supernatants, there is respective 0.73 and 0.78 fold increase in the ASM cell numbers. In our Model 3, there is a 5.13 fold increase in total ASM mass (c+p) at the steady state after an exacerbation event. Hence our results, while showing an increase in total ASM mass as expected, are giving a much larger affect of pathology then this data suggests.

7 Discussion

We started this project with the aim of generating and developing a mathematical model for airway remodelling in asthma which incorporates recent biological discoveries concerning the involvement of MMP-1. Our original model (Model 1) was formulated based on a signalling network we put together using data from Naveed *et al* [16]. This data was also used to assign sensible values for parameters in the system. Using Model 1, we were able to compare the dynamics of a time simulation for a healthy control and an asthmatic patient. It was found that there are only two steady states in this model; a positive one which is always stable and a biologically irrelevant negative one which is always unstable. An exacerbation event was considered as the pathology that can be added to the system as an input, which is a function of time. Having already found that there is only one

positive steady state and that this is always stable, it was not a surprise to find that while the pathology gave a temporary pathological steady state which was of a more "unhealthy" value, as soon as the stimulus was removed, the system went back to the original steady state. Based on the research conducted in asthma and airway remodelling, it can be assumed that, while this model shows some of the dynamics we would expect, it is unrealistic for the model to only have one positive steady state, as this would suggest that the airways of asthmatic patients do not change in the long term. This also means that a change in resolution speed, as investigated in [6], would indeed have a bigger impact on ASM growth during an exacerbation, but would have no longer term effects. In doing our analysis on Model 1 however, we found that increasing the relative rate of baseline ASM apoptosis and proliferation to the switching rate from a proliferative to a contractile phenotype, significantly decreases the amount of contractile and proliferate ASM cells respectively. Hence if we could increase these rates to an optimal value, we could change the number of ASM cells for an asthmatic patient to a lower and so more healthy amount.

Model 2 was then developed as a refinement to Model 1 to include a variable switching rate between proliferative and contractile ASM phenotypes based on the amount of proliferative ASM mass. Hypersurface analysis was undertaken in order to find any steady states due to this model being less analytically tractable than Model 1. It is found that, even when varying parameters that would be expected to have a large impact on the system, for example those involved in resolution speed, there are only ever steady states at zero and one positive value. This means that again, when stimulus is added to the model, as soon as mast cell tryptase has decayed back to zero, the system returns to its only positive stable steady state. Hence this model is also unable to show the results we would expect for airway remodelling.

In Model 3, we made a further refinement to the original model by adding inhibition of ASM apoptosis to account for the survival signal released by normal and altered ECM. Through performing parameter sensitivity analysis, we found the parameters that most affect the steady state values of the system and hence use these to look for bifurcations in the model. The parameters which impact the steady state the most are those for the baseline ASM proliferation rate and the baseline ASM apoptosis rate, both non-

dimensionalised relative to the switching rate from a proliferative to contractile ASM phenotype. As the former is an important parameter involved in resolution speed, as discussed in [6], our results therefore agree with the conclusion made by Chernyavsky *et al* [6] that parameters involved in resolution speed are the most important in remodelling. Several saddle node bifurcations were found including a critical region where, for a small range of parameter values, there is bistability. A two parameter bifurcation diagram enabled us to widen this region of bistability as well as finding a point at which the two saddle node limit points coalesce. When simulating time courses for Model 3 with the the value of this parameter (the baseline ASM proliferation rate relative to the switching rate from a proliferative to contractile ASM phenotype) within this critical region, we can see a change in the steady state of the system after pathology is added. This gives a possible representation of the sort of mechanism involved in airway remodelling which leads to an irreversible change in airway structure. The impact of the exacerbation event on the steady states includes an increase in pro MMP-1, normal ECM and contractile ASM. While little data is available to compare our results to, increases in these variables agrees with the general consensus in literature that airway remodelling in asthma leads to an increase in ECM and total ASM mass.

An unexpected result given in Model 3 however, is that after pathology is added, the new steady state for the proliferative ASM phenotype is actually lower than the steady state before the exacerbation occurs. We have been unable to find any data to quantify the changes in these sub-populations of ASM, hence, though we believe it to be unlikely for the proliferative ASM population to decrease after pathology is added, we only consider the ASM population as a whole in which there is indeed an overall increase as expected. We also observe that, in our model, the magnitude of exacerbation events are irrelevant to the size of the new steady state. This is because, there is only one other positive stable steady state, and the pathology only needs to push the value of each variable above the respective unstable steady state for the system to be attracted to the new higher steady state. This tells us that the severity of exacerbation events has no impact on the amount of remodelling that occurs in the airway as an affect of this. Again, there is little data to tell us if exacerbation severity impacts the amount of remodelling that occurs after each

event, however, the model developed by Chernyavsky *et al* [6] predicts that the amount of increased ASM mass is indeed influenced by inflammation magnitude as well as resolution.

Overall, using all our models, we can see that blocking several interactions between variables could give us possible therapeutic solutions to prevent airway remodelling. Disrupting the signals between mast cell tryptase and pro MMP-1, active MMP-1 and ECM and altered ECM and ASM, could halt the remodelling at any of these respective stages of the pathway. For example, if we were to block mast cell tryptase from activating pro MMP-1, then ECM is unable to be altered and so ASM mass will not increase. Doing this could therefore reduce the overall disease severity.

For further work, we would make yet another refinement to the model developed in this project by adding in a baseline value of mast cell tryptase. This would make the model more biologically realistic as data suggests that, while being significantly lower amounts than in asthmatics, controls also have some mast cell tryptase and active MMP-1 in their ASM bundles. Naveed *et al* [16] find total MMP-1 levels of approximately 0.25ng/ml in controls as compared to aproximately 1.6ng/ml in asthmatics. This alteration would have a significant impact on the dynamics of the system. This is because, at steady state, mast cell tryptase would become non-zero and hence so would active MMP-1 and altered ECM. As these variables are involved in the Hill functions in this model, this therefore suggests the strong likely-hood of multiple positive steady states arising as well as interesting bifurcation behaviour. This model refinement to ignore the previous assumption that healthy values of mast cell tryptase are insignificant, would also mean that we could then more easily compare fold differences in data to the results of the model steady states between a normal and an asthmatic case, or before and after an exacerbation event. Data from [16] shows that active MMP-1 has a 3.9 fold increase after the patient has been stimulated with rhinovirus. This is something that we are unable to accurately compare to the results of our current model as active MMP-1 will always return to zero however, with this further work, we will be able to gain a better insight into the validity of the model.

All three models we have developed are formulated based on several assumptions. One

of these is that all the changes that are occurring are uniform in space. It has been found however that migration of ASM cells could be a contributing factor which leads to the accumulation of ASM mass in a particular ASM bundle. Hirst *et al* [9] hypothesise that, just as vascular smooth muscle (VSM) cell migration has found to lead to an increased VSM mass in atherosclerosis, migration of ASM cells could give the increased ASM mass we see in asthma. It is also possible that cells such as myofibroblasts which surround the ASM bundles could migrate into the bundles and, at the same time, change their phenotype to be similar to that of ASM and so contribute to their total mass. Additionally, while our work has been based on the assumption that proliferative cell types increase as an effect of pathology, some studies have found that there is no observable increase in these proliferation markers in ASM cells [9].

8 Conclusions

This project has led to several conclusions. Firstly, it is evident that more mathematical models are needed as tools for predicting airway remodelling in order to find possible drug targets. This would reduce the need for as many *in vivo* experiments. In order to do this however, we first need more data to base these models on, in particular, more knowledge on the structural changes that occur after each exacerbation event in terms of the changes in quantities of each of the variables in the system. Secondly, we conclude that while Models 1 and 2 show possible realistic dynamics in time simulations, they do not account for the irreversible changes involved in airway remodelling. Our third model, however, shows the mechanism by which exacerbation events could lead to airway remodelling. Results from this model agree with the hypotheses from literature that the airway remodelling involved in asthma gives structural changes to ASM bundles, including increases in the amount of ECM and total ASM. With a more accurate model of this type, for example one with baseline values of mast cell tryptase and spatial aspects included, one could use the results of the model to make sure that the critical rate in which bistability occurs, is never reached. This would mean that after an exacerbation event has occurred, the airway will just return to its previous state. Finally it is clear that disrupting the interactions between the variables in this system, in particular that of mast cell tryptase and pro

MPP-1, could give a possible therapeutic target in order to halt remodelling.

References

[1] An, S.S., Kim, J., Ahn, K., Trepat, X., Drake, K.J., Kumar, S., Ling, G., Purington, C., Rangasamy, T., Kensler, T.W. and Mitzner, W., 2009. Cell stiffness, contractile stress and the role of extracellular matrix. *Biochemical and biophysical research communications*, **382**(4), pp.697-703.

[2] AsthmaUK. 2015. *Media centre: Asthma facts and statistics*. [Online]. [Accessed 2 July 2017]. Available from: https://www.asthma.org.uk/about/media/facts-and-statistics/

[3] Brook, B.S., Peel, S.E., Hall, I.P., Politi, A.Z., Sneyd, J., Bai, Y., Sanderson, M.J. and Jensen, O.E., 2010. A biomechanical model of agonist-initiated contraction in the asthmatic airway. *Respiratory physiology & neurobiology*, **170**(1), pp.44-58.

[4] Chan, V., Burgess, J.K., Ratoff, J.C., O'connor, B.J., Greenough, A., Lee, T.H. and Hirst, S.J., 2006. Extracellular matrix regulates enhanced eotaxin expression in asthmatic airway smooth muscle cells. *American journal of respiratory and critical care medicine*, **174**(4), pp.379-385.

[5] Chellaboina, V., Bhat, S.P., Haddad, W.M. and Bernstein, D.S., 2009. Modeling and analysis of mass-action kinetics. *IEEE Control Systems*, **29**(4).

[6] Chernyavsky, I.L., Croisier, H., Chapman, L.A., Kimpton, L.S., Hiorns, J.E., Brook, B.S., Jensen, O.E., Billington, C.K., Hall, I.P. and Johnson, S.R., 2014. The role of inflammation resolution speed in airway smooth muscle mass accumulation in asthma: insight from a theoretical model.*PloS one*,**9**(3), pp.e90162.

[7] Dekkers, B.G., Naeimi, S., Bos, I.S.T., Menzen, M.H., Halayko, A.J., Hashjin, G.S. and Meurs, H., 2015. l-Thyroxine promotes a proliferative airway smooth muscle phenotype in the presence of TGF-1. *American Journal of Physiology-Lung Cellular and Molecular Physiology*, **308**(3), pp.L301-L306.

[8] Freyer, A.M., Johnson, S.R. and Hall, I.P., 2001. Effects of growth factors and extracellular matrix on survival of human airway smooth muscle cells. *American journal of respiratory cell and molecular biology*, **25**(5), pp.569-576.

[9] Hirst, S.J., Martin, J.G., Bonacci, J.V., Chan, V., Fixman, E.D., Hamid, Q.A., Herszberg, B., Lavoie, J.P., McVicker, C.G., Moir, L.M. and Nguyen, T.T.B., 2004. Proliferative aspects of airway smooth muscle. *Journal of Allergy and Clinical Immunology*,**114**(2), pp.S2-S17.

[10] Kuo, C., Lim, S., King, N.J., Johnston, S.L., Burgess, J.K., Black, J.L. and Oliver, B.G., 2011. Rhinovirus infection induces extracellular matrix protein deposition in asthmatic and nonasthmatic airway smooth muscle cells. *American Journal of Physiology-Lung Cellular and Molecular Physiology*, **300**(6), pp.L951-L957.

[11] Lambert, R.K., Wilson, T.A., Hyatt, R.E. and Rodarte, J.R., 1982. A computational model for expiratory flow. *Journal of applied physiology*, **52**(1), pp.44-56.

[12] Martin, J.G. and Ramos-Barbn, D., 2003. Airway smooth muscle growth from the perspective of animal models. *Respiratory physiology & neurobiology*, **137**(2), pp.251-261.

[13] Martinez, FD and Vercelli, D. 2013. Asthma. *The Lancet*, **382**(9901), pp.1360-1372.

[14] Mathematics in Medicine. 2011. *Study Group Report: Mathematical modelling of airway smooth muscle cell proliferation and apoptosis in asthma.* [Online]. [Accessed 2 July 2017]. Available from: http://www.maths-in-medicine.org/uk/2011/asthma/report.pdf

[15] Mendes, P., Hoops, S., Sahle, S., Gauges, R., Dada, J. and Kummer, U., 2009. Computational modeling of biochemical networks using COPASI. *Systems Biology*, pp.17-59.

[16] Naveed, S.U.N., Clements, D., Jackson, D.J., Philp, C., Billington, C.K., Soomro, I., Reynolds, C., Harrison, T.W., Johnston, S.L., Shaw, D.E. and Johnson, S.R., 2017. Matrix metalloproteinase-1 activation contributes to airway smooth muscle growth

and asthma severity. *American journal of respiratory and critical care medicine*, **195**(8), pp.1000-1009.

[17] Politi, A.Z., Donovan, G.M., Tawhai, M.H., Sanderson, M.J., Lauzon, A.M., Bates, J.H. and Sneyd, J., 2010. A multiscale, spatially distributed model of asthmatic airway hyper-responsiveness. *Journal of theoretical biology*, **266**(4), pp.614-624.

[18] Rogers, N.K., Clements, D., Dongre, A., Harrison, T.W., Shaw, D. and Johnson, S.R., 2014. Extra-cellular matrix proteins induce matrix metalloproteinase-1 (MMP-1) activity and increase airway smooth muscle contraction in asthma. *PloS one*, **9**(2), p.e90565.

[19] Santilln, M., 2008. On the use of the Hill functions in mathematical models of gene regulatory networks. *Mathematical Modelling of Natural Phenomena*, **3**(2), pp.85-97.

[20] Wadsworth, S.J., Yang, S.J. and Dorscheid, D.R., 2012. IL-13, Asthma and Glycosylation in Airway Epithelial Repair.In:*Carbohydrates-Comprehensive Studies on Glycobiology and Glycotechnology*. InTech.

[21] Wang, I., Politi, A.Z., Tania, N., Bai, Y., Sanderson, M.J. and Sneyd, J., 2008. A mathematical model of airway and pulmonary arteriole smooth muscle. *Biophysical journal*, **94**(6), pp.2053-2064.

Appendices

Parameters

Parameter	Description
k_{Ya}	Decay rate of mast cell tryptase
k_{PM}	Rate of production of pro-MMP-1 by proliferative ASM cells
k_{CM}	Rate of production of pro MMP-1 by contractile ASM cells
k_{Ma}	Decay rate of mast pro MMP-1
k_{Qa}	Decay rate of active MMP-1
k_{PE}	Rate of production of ECM by proliferative ASM cells
k_{CE}	Rate of production of ECM by contractile ASM cells
k_{Ea}	Decay rate of ECM
k_{Aa}	Decay rate of altered ECM
k_{PC}	Rate of switch from a proliferative ASM phenotype to a contractile phenotype
k_{Ca}	Decay rate of contractile ASM
$\hat{k}_{CP}$	Base rate of switch from a contractile ASM phenotype to a proliferative phenotype
$\hat{k}_P$	Base rate of proliferation of ASM cells

Parameter	Description
J_{MQ}	Maximum rate of activation of pro MMP-1
J_{EA}	Maximum rate of change of ECM to altered ECM
J_{CP}	Maximum rate of change of contractile ASM to proliferative ASM
J_P	Maximum proliferation rate
α	Switching point of the hill function for $k_P(A)$
β	Switching point of the hill function for $k_{CP}(A)$
γ	Switching point of the hill function for $k_{EA}(A)$
μ	Switching point of the hill function for $k_{MQ}(A)$
n	Hill exponent
λ_M	Baseline value of pro MMP-1
λ_E	Baseline value of ECM
λ_P	Baseline value of proliferative ASM
V	Total capacity of ASM cells

Table 4: Descriptions of the parameters in the original dimensional system (equations 4.1-4.7).

B

EXPERIMENTAL METHODS

B.1 CELL CULTURE PROTOCOL

The below describes the common process of culturing HASM cells which is used in this project in order to undertake the experiments in Chapter 3.

B.1.1 *Materials*

- Primary HASM cells
- Dulbecco's Modified Eagle Medium (DMEM) with 10% Fetal Bovine Serum (FBS)
- Trypsin
- Dimethyl sulfoxide (DMSO)

B.1.2 *Method*

HASM cells are thawed and transferred to a universal containing 10ml of warmed media (containing 10% FBS). This is then centrifuged at 200g for 5 minutes at room temperature. The media is then aspirated, leaving just the cell pellet in the tube. 10ml of fresh media is then added to the universal making sure to disrupt the pellet and this cell suspension is then

transferred to a T75 flask. This is then incubated at 37°C. The media in the flask is changed every 2-3 days or when it has changed colour/contains debris (aspirate media and replace with 10ml of new warmed media). The cells are passaged when a flask is 70-90% confluent. To do this, we aspirate the media from the flask and replace with 10ml of trypsin. Once we observe the cells becoming detached from the flask, we agitate the flask to detach the cells that are still stuck and then transfer this cell suspension to a universal containing 10ml of fresh media. We spin this in the centrifuge using a speed of 200g for 5 minutes and then aspirate the media leaving just the cell pellet. The pellet is re-suspended in 20ml of warmed media and this is disrupted evenly into 4 fresh flasks. Finally we add an extra 5ml of media to each flask so that they all contain 10ml in total and place these in the incubator to grow. In order to freeze a confluent flask of cells, repeat the process of passaging cells above until we have the pellet of cells. We then add 1ml of freezing media (1/10 DMSO in FBS) making sure that the pellet is dispersed, and transfer this to a cryovial to freeze at -80°C.

B.2 EXPERIMENT 1: OPTIMISATION STEPS

1. **C**hamber slides.

   We found that healthy cells would stick to each other and not glass hence polylysine coated chamber slides were used going forward.

2. **C**ell densities.

   Cell densities of 3000, 6000, 12000 and 24000 cells per well were initially tested and it was found that somewhere in the middle of this range was best (3000 was not dense enough and 24000 was too dense).

3. **A**ntibody dilutions.

   PCNA antibody dilutions of 0.25mg/ml, 0.5mg/ml, 0.75mg/ml and 1mg/ml were tested as well as controls for secondary only and no antibody. Since there was little difference, 0.25mg/ml was used going

forward. Ki67 dilutions of 1/400, 1/600, 1/800 and 1/1000 were also tested and again 1/1000 was adequate for our use.

4. **P**halloidin V Anti-Actin, α -Smooth Muscle - Cy3^{TM} antibody
   It was found that phalloidin gave a much stronger signal.

5. **F**ixation methods.
   3 different fixation methods were tested on cells in serum. (1) Fix in 4% formaldehyde (FA) for 10 minutes, permeabilise with 0.1% Triton X-100 in PBS, block. (2) Fix in 1% FA for 10 minutes, rinse with PBS, fix in 100% methanol in the freezer for 10 minutes, don't permeabilise, block. (3) Fix in 100% methanol in the freezer for 10 minutes, don't permeabilise, block. The results can be seen in Figure B.1. It was found that method (1) gave the strongest signal for phalloidin but no signal for the antibodies and method (3) gave the strongest signal for the antibodies but the phalloidin was sequested in the nucleus. We therefore chose to separate the two stains onto different slides that can be fixed using the corresponding optimal method.

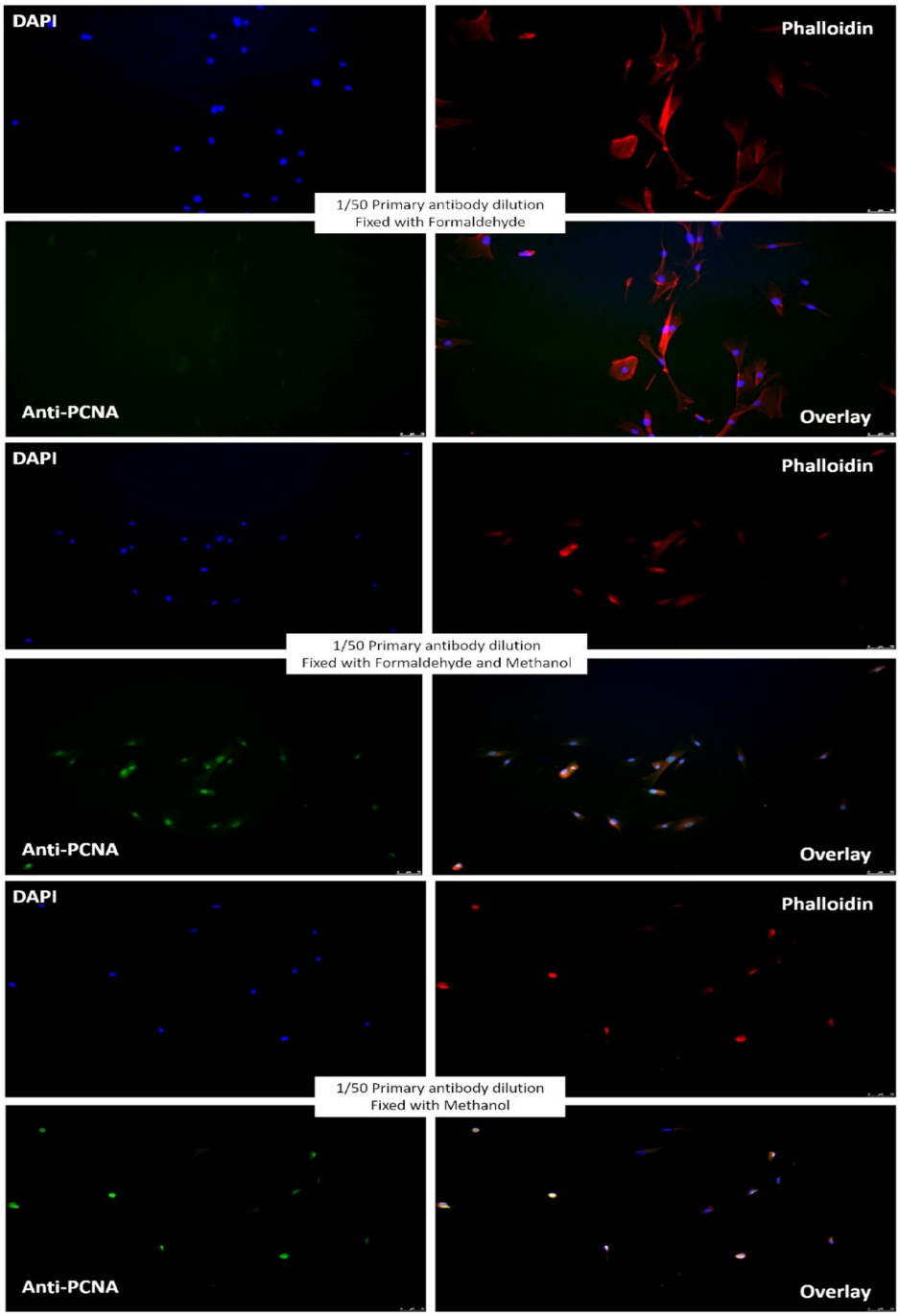

Figure B.1: Fixation method optimisation. Each box is stained as labeled with formaldehyde fixation (top), formaldehyde and methanol fixation (middle) and methanol only fixation (bottom).

B.3 EXPERIMENT 2: MAST CELL ACTIVATION PROTOCOL

Experiment 2 in Section 3.2 requires the collection of activated and inactivated mast cell supernatant as follows (this method was provided by Roya Babaei-Jadidi, Division of Respiratory Medicine, University of Nottingham). Mast cells differ from ASM cells in that they are suspension cells and do not stick to the bottom of the flask in a monolayer.

B.3.1 *Materials*

- HMC-1 cells
- Phorbol 12-myristate 13-acetate (PMA)
- Calcium ionophore (A23187)
- Complete media (IMDM + 1% pen/strep + 1% glutamine plus 10% FBS when serum present)

B.3.2 *Method*

HMC-1 cells were recovered in 2 flasks with complete medium and 10% FBS for 1-2 days. We then removed the serum for 1 day. Since HMC-1s are suspension cells, to change the media we had to centrifuge at 100g for 5 minutes and then resuspend in the new serum free media. After the serum had been removed for 1 day, we added 50ng/ml PMA and 25ng/ml calcium ionophore to only the flask that was being activated and left for 16 hours. After this, we spun down both the activated and non-activated cell suspensions at 1200rmp for 5 minutes to pellet the cells. The activated supernatant was then sterile-filtered and aliquoted into cryovials to be frozen at -80. For the control supernatant, 50ng/ml PMA and 25ng/ml calcium

ionophore were added to the inactivated media (with no cells) before being sterile-filtered and aliquoted as above.